Diffusion Weighted Imaging of the Hepatobiliary System

Techniques and Clinical Applications

Celso Matos
Nickolas Papanikolaou
Editors

Springer

Diffusion Weighted Imaging of the Hepatobiliary System

Celso Matos • Nickolas Papanikolaou
Editors

Diffusion Weighted Imaging of the Hepatobiliary System

Techniques and Clinical Applications

Springer

Editors
Celso Matos
Department of Radiology
Champalimaud Foundation
Lisbon
Portugal

Nickolas Papanikolaou
Department of Radiology
Champalimaud Foundation
Lisbon
Portugal

ISBN 978-3-319-62976-6 ISBN 978-3-319-62977-3 (eBook)
https://doi.org/10.1007/978-3-319-62977-3

This Springer imprint is published by the registered company Springer Nature Switzerland AG
The registered company address is: Gewerbestrasse 11, 6330 Cham, Switzerland

Contents

DW MRI: Techniques, Protocols and Post-processing Aspects

1

Thierry Metens and Nickolas Papanikolaou

1.1 Introduction

Diffusion is the process of random motion of water molecules in a free medium. For human tissues, water mobility can be assessed in the intracellular, extracellular and intravascular spaces. All media have a different degree of structure and thus pose a variant level of difficulty in water mobility that is called "diffusivity". A sequence sensitized to microscopic water mobility by means of strong gradient pulses can be utilized to provide insights in the complexity of the environment which in turn can reveal information related to tissue microarchitecture.

A major requirement in diffusion imaging is to select ultrafast pulse sequences that may freeze macroscopic motion in the form of respiration, peristalsis or patient motion in general. For this reason, Echo Planar Imaging (EPI) sequences modified with the addition of two identical strong diffusion gradients are routinely used to provide diffusion information. The amplitude and duration of the diffusion gradients is represented by the "*b*-value" (measured in s/mm^2), an index used to control the sensitivity of DWI contrast to water mobility.

T. Metens
Department of Radiology, Hôpital Erasme, MRI Clinics, Bruxelles, Belgium
e-mail: thierry.metens@erasme.ulb.ac.be

N. Papanikolaou (✉)
Oncologic Imaging, Computational Clinical Imaging Group, Champalimaud Foundation, Centre for the Unknown, Lisbon, Portugal
e-mail: nickolas.papanikolaou@research.fchampalimaud.org; npapan@npapan.com

C. Matos, N. Papanikolaou (eds.), *Diffusion Weighted Imaging of the Hepatobiliary System*, https://doi.org/10.1007/978-3-319-62977-3_1

1.2 Formal Definition of Diffusion

Molecules are involved in a thermal random motion called the Brownian motion, according to the observation in 1827 by Robert Brown [1773–1858] of the erratic translation movement of pollen in water, a random movement with no net ensemble displacement. This situation was further studied in 1908 by Paul Langevin [1872–1946] [1] and by Albert Einstein [1879–1955] [2]. This microscopic movement is due to thermal agitation and occurs for water molecules in a bath of pure water (self-diffusion) or in a viscous liquid medium.

For the free three-dimensional diffusion, considering the Brownian motion under thermal agitation, Albert Einstein derived in 1905 the relation between the mean quadratic displacement, the diffusion coefficient and the diffusion time t:

$$\left\langle r^2 \right\rangle = 6Dt \tag{1.1}$$

In other words, starting from a position r_0 after a time t the particles reach a standard deviation position located on the surface of a sphere of radius $(6Dt)^{1/2}$. The value of the diffusion coefficient D depends on the temperature T and the friction F (that is proportional to the viscosity) of the medium.

In living tissues, diffusion is restricted by many other factors like intracellular metabolites, the presence of cell membranes, the extracellular architecture, the relative size of cells and extracellular compartment. Therefore, the measured diffusion coefficient is called apparent diffusion coefficient (ADC). The apparent diffusion coefficient value is in general reduced if cells expand because of cytotoxic oedema, or when the cell density is more elevated, like in most malignant tissues. The link between the ADC and tissue cellularity seems quite complex and is still under investigation [3].

In biological tissue, water diffusion can be spatially restricted by the presence of ordered structures; therefore, diffusion becomes anisotropic where the mathematical description requires a diffusion tensor $\underline{\mathbf{D}}$ to be introduced. However, in abdominal organs like the liver or the pancreas the overwhelming majority of studies deals with the isotropic part of the diffusion tensor, i.e. the average diffusion measured in three orthogonal directions, called the average diffusivity or the mean diffusion. In what follows we shall simply refer to it as the diffusion coefficient.

1.3 Diffusion-Weighted Magnetic Resonance Imaging

1.3.1 The Stejskal–Tanner Sequence, Image Contrasts, and Basic Image Processing

Following the seminal works on MR and diffusion by Carr and Purcell [4], Torrey [5] and Woessner [6], in 1965 Stejskal and Tanner [7] have shown that the MR signal can be made sensitive to diffusion by the addition of supplementary gradients, called diffusion gradients (Fig. 1.1). Diffusing spins (moving spins) travelling at

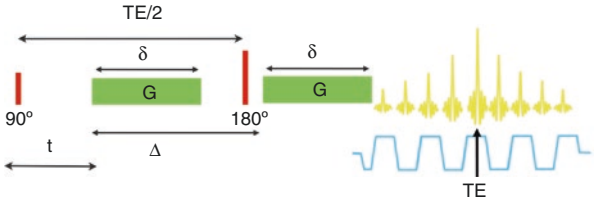

Fig. 1.1 Stejskal–Tanner SE diffusion sequence with EPI reading (only the diffusion sensitized gradients are shown in green, these gradients are aligned along one spatial direction. *G* is the gradient amplitude, Δ is the delay between successive diffusion gradients and δ is the duration of the diffusion gradients, the 90° and 180° RF pulses are used to generate a spin echo in order to minimize $T2^*$ effects. Note that after the 180°RF pulse, the effective gradient sign is changed

least partially along the direction of the diffusion gradients will accumulate a net dephasing and this results into a signal attenuation, while stationary spins will be identically dephased and rephased with no signal loss. The Stejskal–Tanner gradients are generally used within a Spin Echo Echo Planar Imaging (SE-EPI) sequence, allowing to acquire diffusion-weighted images (DWI). The signal of the SE Stejskal–Tanner sequence can be calculated as:

$$S(\mathrm{TE}) = S(\mathrm{TE}=0,\, b=0)\mathrm{e}^{-\mathrm{TE}/\mathrm{T2}}\mathrm{e}^{-bD} \tag{1.2}$$

with the diffusion control parameter *b* (in s/mm^2):

$$b = (\gamma G\delta)^2(\Delta - \delta/3) \tag{1.3}$$

with γ the proton gyromagnetic ratio, *G* the gradient amplitude, Δ is the delay between successive diffusion gradients and δ is the duration of the diffusion gradients. The signal of the Stejskal–Tanner sequence is thus both T2-weighted and diffusion-weighed, the *b* factor controls the diffusion-weighting and TE controls the T2-weighting (Fig. 1.2). The product of the two exponential attenuations explains the inherent low signal to noise ratio (SNR) of DWI, the spatial resolution is generally kept low in order to compensate for the otherwise low SNR.

Equation (1.2) accounts for diffusion in one particular direction in space and shows that increased water mobility results in substantial signal attenuation on diffusion-weighted images. Conversely, water molecules with reduced mobility will present with significantly lower signal attenuation comparing to water molecules with increased mobility leading to a relative higher signal on high *b* value images, as shown on Fig. 1.2d, where the liver tumour presents with higher signal to surrounding liver parenchyma due to reduced water mobility within the lesion. We emphasize that the signal intensity in DW images is not only affected by the *b* factor and the diffusion of water but also by the T2 and $T2^*$ relaxation time of the tissues because the Stejskal–Tanner diffusion "carrying sequence" is a SE-EPI. In a tissue with a long T2 relaxation coefficient, a relatively high signal intensity can be maintained mimicking restricted diffusion patterns, the so-called "T2 shine-through" effect (Fig. 1.3). On the contrary, a tissue with a very low T2 value will appear dark,

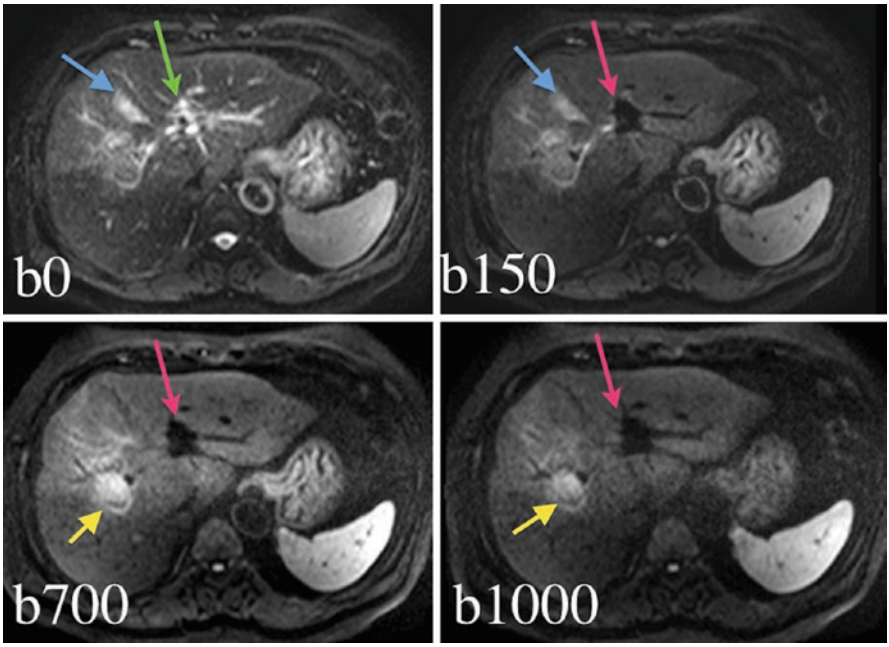

Fig. 1.2 DW images acquired at fixed TE with $b = 0$, 150, 700, 1000 s/mm^2 and showing various degrees of diffusion-weighting (blue arrow: gallbladder, yellow arrow: liver tumour, green and red arrows: portal blood flow). Note the black blood effect in the aorta and portal system

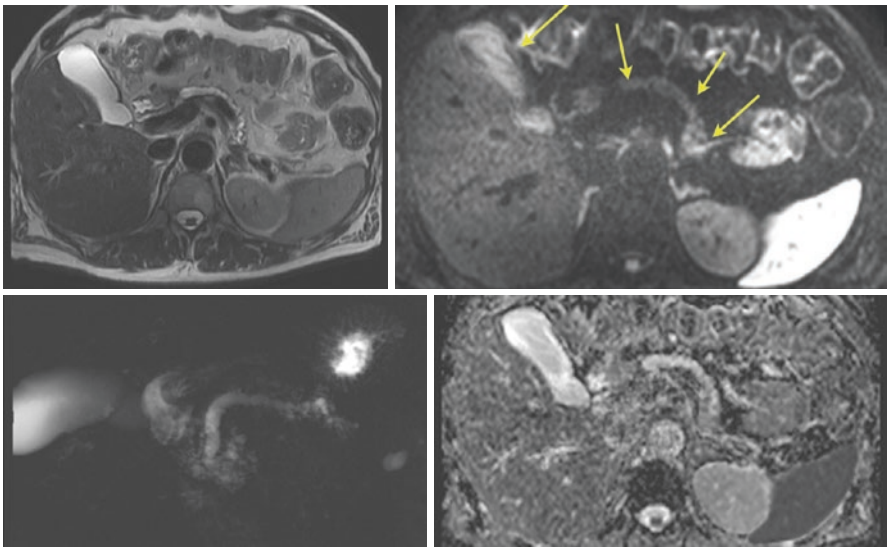

Fig. 1.3 TSE T2-weighted (top left), $b = 900$ s/mm^2 SE-EPI DWI (top right), MRCP (bottom left) and ADC map (bottom right) illustrating the T2-shine-through effect from the long T2 bile fluid in the gallbladder and from the pancreatic fluid in the enlarged Wirsung duct (hypersignal, arrows on the $b = 900$ s/mm^2 image). The ADC map however demonstrates the relatively high value of their diffusion coefficient

the so-called "T2 shading effect". It is important to avoid such confusion by comparing DW images with T2-weighted images.

In many clinical situations, visual interpretation of DW images is not enough and further quantification of ADC is considered mandatory. This calculation involves at least the acquisition of two signals $S1$ and $S2$ from acquisitions with different b factors, i.e. b_1 and b_2 factors and by computing:

$$\mathrm{ADC} = \mathrm{Ln}\left(S1/S2\right)/\left(b_2 - b_1\right) \tag{1.4}$$

If more than two b value images are involved, a linear regression of the logarithms $\mathrm{Ln}[S(b)/S(0)]$ in function of the b values will provide the ADC value (i.e. − slope of the regression line). When this is performed for each pixel, a calculated image of the ADC, called the ADC map, is reconstructed. More generally, the ADC map can be reconstructed by considering one or a combination of several diffusion directions and several b values, while the correct choice of the regression points is influencing the final ADC value. The calculated numerical ADC value depends on many parameters, and therefore we emphasize the "apparent" denomination.

The diffusion sequence must be repeated using diffusion gradients oriented in at least three orthogonal directions. The geometric mean of three orthogonal diffusion-weighted images with the same b amplitude gives the isotropic diffusion image (where directional effects have been eliminated by definition):

$$\begin{aligned} I\left(b\right) &= S\left(0\right)\mathrm{e}^{-\left({}^{b}xx\,{}^{D}xx + {}^{b}yy\,{}^{D}yy + {}^{b}zz\,{}^{D}zz\right)/3} \\ &= S\left(0\right)\mathrm{e}^{-b\left({}^{D}xx + {}^{D}yy + {}^{D}zz\right)/3} = S\left(0\right)\mathrm{e}^{-b\,\mathrm{MD}} \end{aligned} \tag{1.5}$$

The derivation of Eq. (1.2) is based on the hypothesis that the diffusion is the single source of intravoxel incoherent motion (IVIM). However in living tissue, micro-perfusion represents another potential source of IVIM: the blood flow appears indeed random as it follows the randomly oriented capillaries and during the diffusion time spins in the capillary blood flow might have changed their direction several times, or different spins will flow along different directions in differently oriented capillaries. This micro-perfusion phenomenon constitutes a pseudo-diffusion movement and will be discussed in detail below. Another complication arises from the fact that the pixel size in DWI is large compared to the various tissue compartments with different diffusivity and partial volume effects might result, again justifying the apparent character of the diffusion coefficient measured in tissue.

1.4 Pulse Sequences Considerations

The Stejskal–Tanner SE-EPI sequence is acquired using a single EPI echo train, providing an image in the so-called "single shot" mode. In a segmented acquisition (multi-shot mode), the signal phase of the different k-space segments can interfere destructively causing an irremediable signal loss in the final image. This severe

segmental dephasing occurs in the strong diffusion gradients because of several physiologic factors like heart pulsation and organ movement occurring in-between consecutive k-space segments acquisitions. Segmented approaches are possible but require adequate phase corrections that are often difficult to be implemented. The SE-EPI sequence requires fat suppression to avoid the large water-fat shift in the EPI phase encoding direction. Moreover, $T2^*$ image blurring and spatial distortions due to the high EPI echo train length (ETL) related artefacts are mostly present along the phase encoding direction (Fig. 1.4).

The spatial resolution of abdominal clinical DW imaging is in general relatively lower comparing to that of conventional MRI sequences like T1 or T2. However, multichannel high-performance abdominal coils are nowadays available and do allow the use of parallel imaging with high acceleration factors to minimize geometric distortions and $T2^*$ blurring (Fig. 1.5). High *b* value images suffer from poor SNR and therefore more averages than in the low *b* values, may be acquired to compensate for the limited signal (Fig. 1.6). Depending on the specificities of the coil, the phase encoding direction, the size and shape of the object of interest, the static magnetic field strength and the image SNR, acceleration factors of 2–4 are used. Recent progress has been provided by the multislice simultaneous excitation technique, that allows diffusion-weighted imaging of the liver accelerated by a factor two in addition to parallel imaging [8, 9].

The availability of 3 T magnets equipped with fast gradient systems makes possible to acquire complete abdominal studies with high spatial resolution images of excellent quality (Fig. 1.7a–c). Several new DW sequences have been proposed including Resolve, a high-resolution DW readout segmented EPI sequence with two spin echoes. This sequence uses the second echo data from a 2D navigator acquisition to perform a nonlinear phase correction and to control the real-time reacquisition of unusable data that cannot be corrected [10].

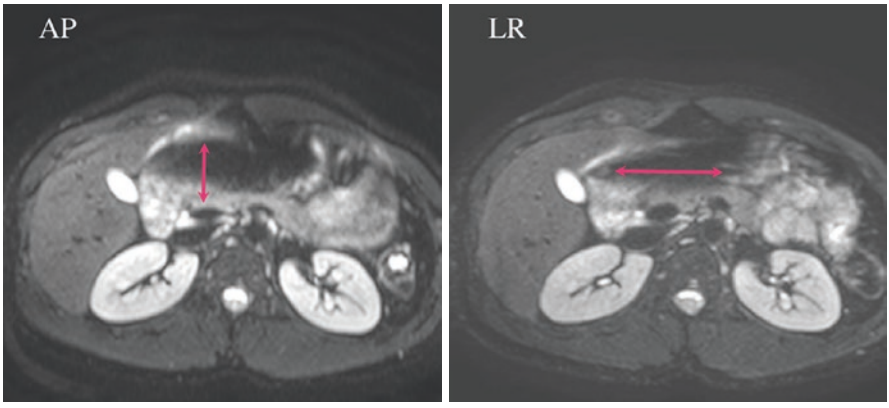

Fig. 1.4 DW images acquired at 3 T with b 10 s/mm^2 with phase encoding in the anterior to posterior direction (left) and in the left to right direction (right), the red arrows indicate the corresponding EPI spatial distortions

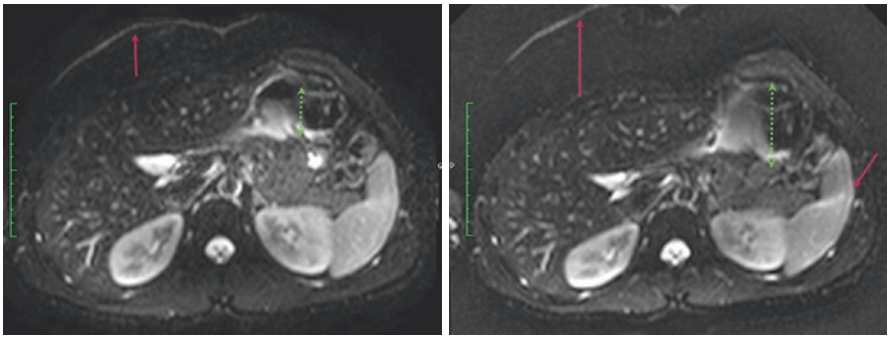

Fig. 1.5 SE-EPI images acquired at 3 T (same image matrix and TR,TE, with $b = 0$ s/mm^2) with anterior to posterior phase encoding direction, respectively with EPI ETL of 41 (left) and 95 (right, with more blurring and larger distortions). The red arrows indicate the water-fat shift (distance between the skin and the liver, suboptimal fat suppression) and the green dotted arrow suggests the amplitude of the EPI spatial distortion. High parallel imaging acceleration factors enable lower ETL and deliver images with less artefacts

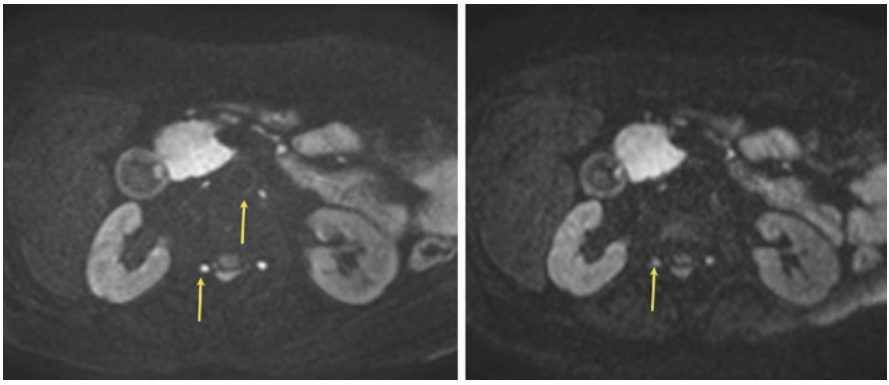

Fig. 1.6 Respiratory-triggered DW SE-EPI images acquired at 3 T with $b = 1000$ s/mm^2, with a 1200 ms expiration sampling window and using a 16-channel coil. Left: image acquired with the phase encoding in the left to right direction, using a parallel imaging (sense) acceleration factor 4, ETL 69, TE 86 ms, with high spatial resolution, acquisition voxel size 1.8 × 1.9 × 5 mm, acquisition duration 420 s. Right: image acquired with anterior to posterior phase encoding direction using a sense acceleration factor 2, ETL 47, TE 77 ms, with moderate spatial resolution, acquisition voxel size 2.2 × 2.7 × 5 mm, acquisition duration 288 s. Note the conspicuity of the lymph nodes and the aorta wall on the high-resolution image (left)

1.5 Diffusion Modelling in Abdominal Organs

Liver, pancreas and kidneys are organs with a strong perfusion component. The capillary random movement through the diffusion gradients constitutes an intravoxel incoherent motion, IVIM, dephasing the Stejskal–Tanner signal. An adequate

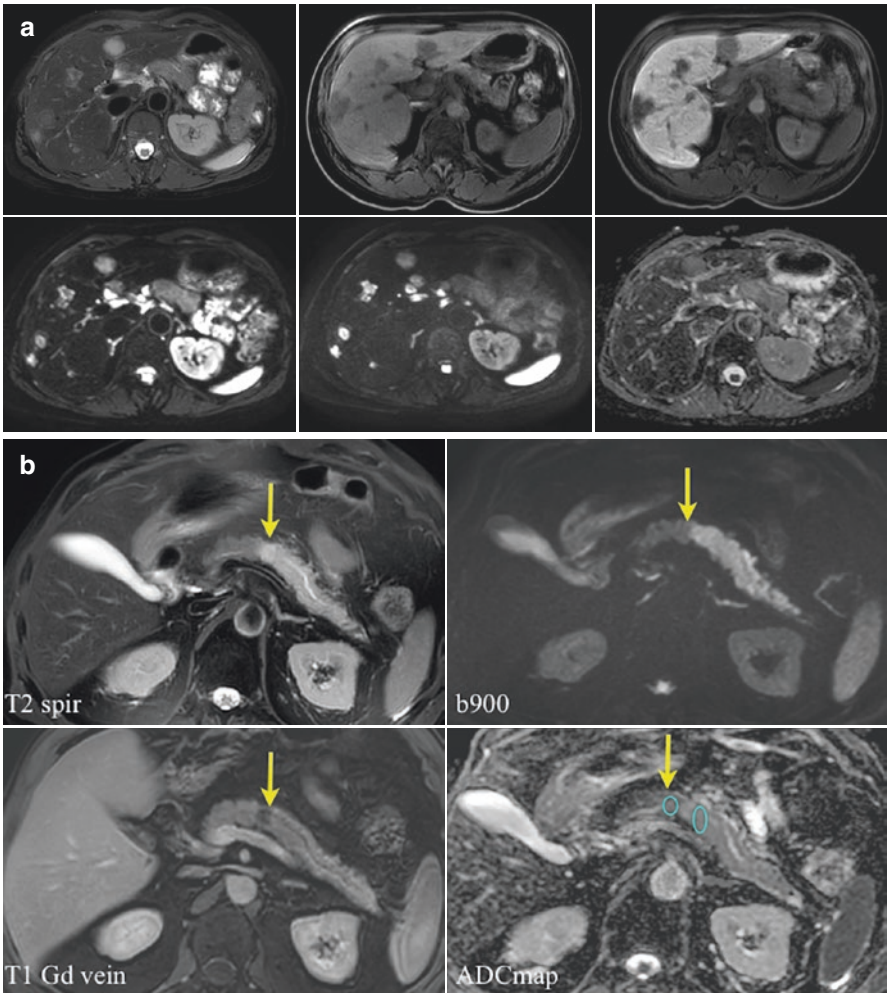

Fig. 1.7 (**a**) Example of a 3 T liver study involving (clockwise from top left). Fat suppressed T2-weighted TSE Propeller; Dixon water image before and after administration of hepatospecific contrast agent (gadoxetic acid) the b = 0 s/mm^2 and b 900 s/mm^2 high-resolution DW images and the ADC map. The relatively high spatial resolution of DW images deliver an ADC map with enough resolution to enable ADC quantification of subcentimetric lesions. (**b**) High spatial resolution diffusion-weighted imaging is mandatory for the analysis of pancreatic tumours (arrows). In this patient, the tumour was responsible for a pancreatitis in the tail of the pancreas affecting the ADC values: tumour ADC = 1200 × 10^{-6} mm^2/s, pancreas tail ADC = 1400 × 10^{-6} mm^2/s. Courtesy of Dr. M Pezzullo, ULB Erasme Brussels. (**c**) This rare pancreatic Schwannoma (arrows) was depicted on T1 and T2 weighted images, the high-resolution 3 T diffusion-weighted sequence was needed to provide an accurate ADC map for quantification (Tumour ADC = 914 × 10^{-6} mm^2/s pancreas ADC = 1350 10^{-6} mm^2/s). (Courtesy of Dr. M. Pezzullo, ULB Erasme Brussels)

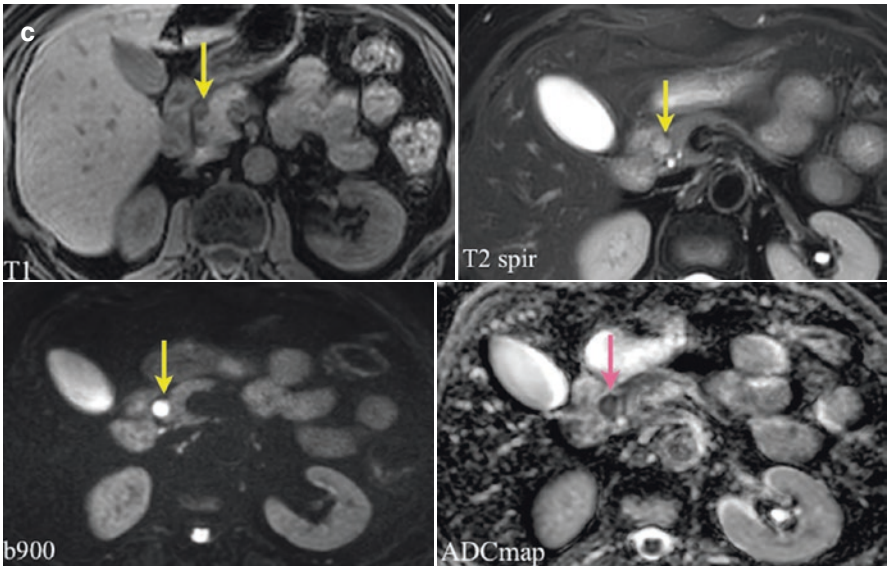

Fig. 1.7 (continued)

model should thus take into account both water diffusion and the pseudo diffusion from blood capillary flow. One approach is provided by the bi-exponential model [11–17]:

$$S(b)/S(0) = f\,\mathrm{e}^{-bD^*} + (1-f)\,\mathrm{e}^{-bD} \tag{1.6}$$

where f is the micro-perfusion fraction, D^* is the pseudo-diffusion coefficient linked to micro-perfusion and D is the water true diffusion coefficient in the tissue. The major disadvantage that prohibits routine clinical applications of IVIM is that the bi-exponential model is very prone to signal fitting errors. However, fortunately, in general $D^* \gg D$ and there exists a value b^* such that:

$$\text{for } b > b^* : \mathrm{e}^{-bD^*} \simeq 0 \tag{1.7}$$

meaning that for $b > b^*$ the attenuation comes from pure diffusion D only. Thus, instead of trying at once to fit the bi-exponential model with three parameters f, D^* and D, an approximate strategy called "partial fitting" comprises D calculation by fitting a mono-exponential model to the signal of 2 or more images with b values larger than b^*, typically $b^* = 150$ s/mm^2:

$$\mathrm{Ln}\left[S(b)/S(0)\right] \sim \mathrm{Ln}(1-f) - bD = \beta - bD \tag{1.8}$$

where β is the intercept of the linear regression and:

$$f = 1 - \mathrm{e}^{\beta} \tag{1.9}$$

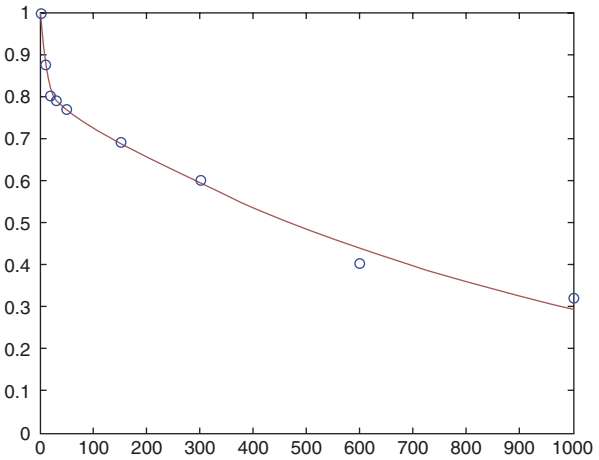

Fig. 1.8 Liver bi-exponential relative signal attenuation $S(b)/S(0)$ in function of b values (in s/mm^2) This fit provides the following values: $f = 0.20$, $D^* = 95{,}677 \times 10^{-6}$ mm^2/s, $D = 1001 \times 10^{-6}$ mm^2/s

Alternatively, in a stepwise procedure, the previous approximate values obtained for b and D can be used as initial guessed values of the bi-exponential fit. Figure 1.8 shows the liver bi-exponential signal attenuation in function of b values. The bi-exponential character of the liver (or the pancreas) apparent diffusion explains why mono-exponential ADC maps obtained with different sets of b value images provide ADC values that are different. In case of all b value from $b = 0$ to $b = 1000$ s/mm^2 inclusion to the calculation, a mixture of perfusion-related pseudo-diffusion effects (D^*) and true water diffusion (D) will result in a higher ADC value than the ADC value obtained by considering only b values superior to b^* ($b^* = 150$ s/mm^2) for which the sole true water diffusion D will be effectively probed (Figs. 1.9 and 1.10). Another possible source of IVIM comes from the blood flow in macroscopic veins or arteries. The parabolic velocity profile in veins, the pulsatile accelerated velocity profile in arteries and the turbulent blood flow in more pathologic vascular conditions all result in an intravoxel velocity distribution responsible for a strong signal dephasing by the diffusion gradients and this phenomenon is observed even at very low b values. The image contrast with low b values (around 10–50 s/mm^2) shows the so-called black blood effect (Fig. 1.11) and is convenient to differentiate small lesions from liver vessels. Note that bile ducts are not erased because of the absence of bile movement (Fig. 1.12). Studies have demonstrated to utility of low b DWI for the detection of focal hepatic lesions [18, 19], Fig. 1.13 compares the contrast between the liver and a focal lesion between conventional TSE T2-weighted sequence and low b DWI.

Many studies have been devoted to other diffusion models, including the stretched-exponential model [20]:

$$S(b)/S(0) = \exp - (b\,\mathrm{DDC})^{\alpha} \tag{1.10}$$

involving the distributed diffusion coefficient (DDC) and the stretching parameter α.

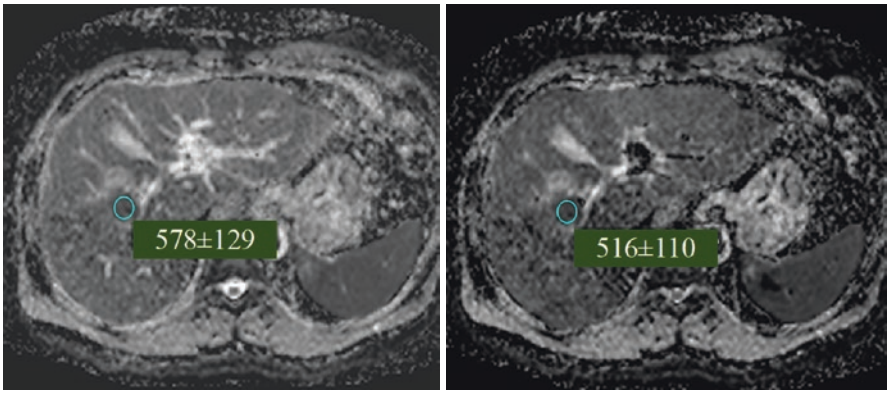

Fig. 1.9 ADC maps obtained by signal fitting using b = 0–150–500–1000 s/mm^2 (left image, ROI 578 × 10^{-6} mm^2/s) and by signal fitting using b = 150–500–1000 s/mm^2 (right image, ROI 516 × 10^{-6} mm^2/s). The ADC ROI value measured in a lesion on the left map is more elevated because it is influenced by the large pseudo-diffusion coefficient D^*. Note that when ADC is derived from images using b = 150–500–1000 s/mm^2 (right), the blood in the portal vein is attributed a paradoxical "zero" ADC value, while we expect that blood, a fluid, would have a relatively high ADC value. Due to the vascular black blood effect, this region had no signal (signal values close to zero, in the noise floor) on DW images with $b > 0$ s/mm^2 (see Fig. 1.2). Thus taking into account only these images for the ADC calculation, there is virtually no signal attenuation and the obtained ADC is zero. On the contrary using b = 0–150–500–1000 s/mm^2 images, since the signal of portal blood is quite high on the $b0$ image, and quasi zero on all other images, the obtained ADC value seems very high, however not accurate!

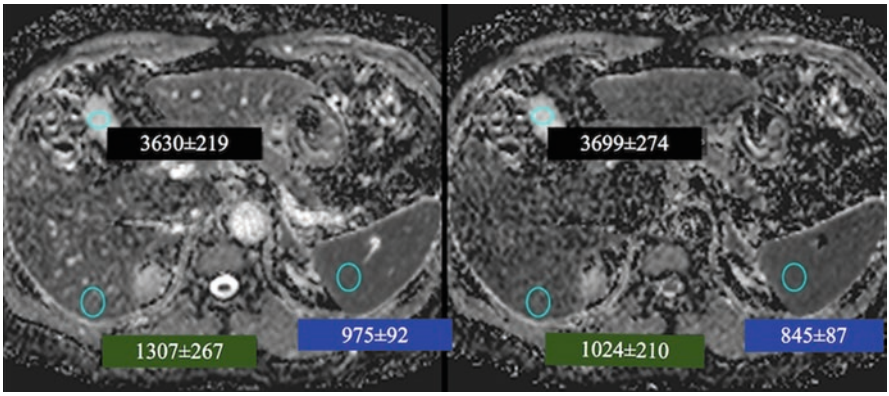

Fig. 1.10 ADC maps (units 10^{-6} mm^2/s) obtained by signal fitting using b = 0–150–500 s/mm^2 (left image) and by signal fitting using b = 150–500 s/mm^2 (right image). The ADC value measured on the image on the left is more elevated in the liver and in the spleen because it is influenced by the large pseudo-diffusion coefficient D^*, while no significant difference is recorded in the gallbladder, containing no blood vessels. Note again the paradoxical of the black blood effect on the aortic blood ADC; on the right image the ADC has an apparent zero value, while it appears to be very high on the left image

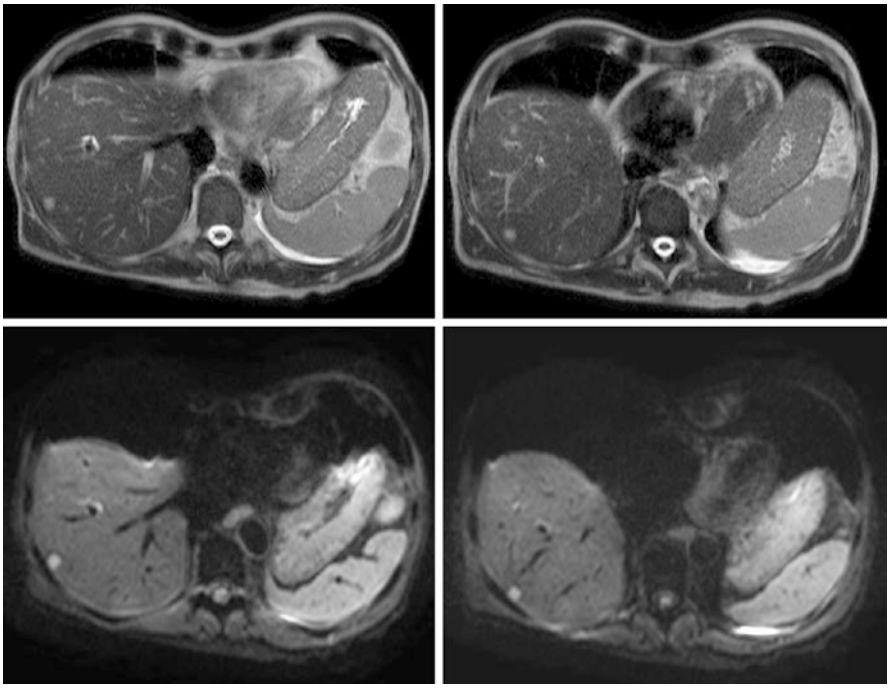

Fig. 1.11 Single Shot TSE T2-weighted images (right) compared with $b = 10$ s/mm^2 SE-EPI DW images (left). On DW images the black blood effect (elimination of vascular signal) increases significantly lesion conspicuity

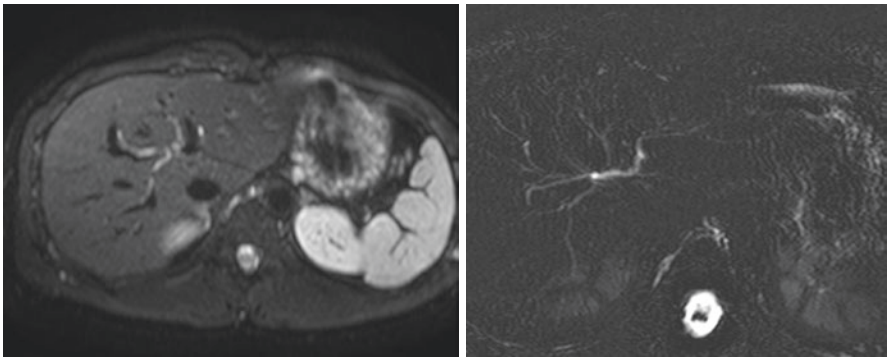

Fig. 1.12 $b = 10$ s/mm^2 SE-EPI DW image (left) compared to MRCP (right) demonstrates that black blood does not affect static bile in ducts

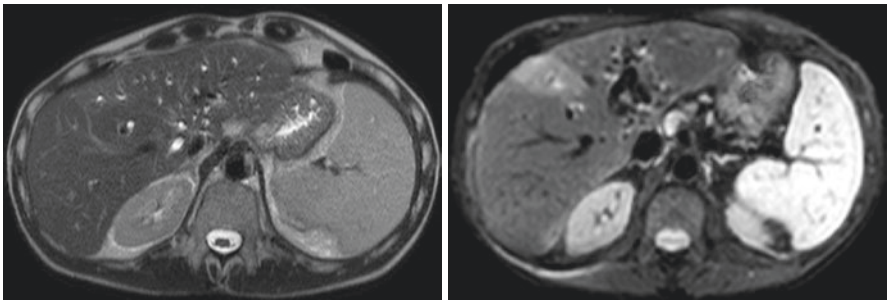

Fig. 1.13 Comparison of lesion to liver image contrast between a conventional TSE T2-weighted sequence (TE:80 ms) and a $b = 50$ s/mm^2 SE-EPI DWI (fat suppression, TE:51 ms)

The kurtosis model is another non mono-exponential decay of the diffusion-weighted signal [21]:

$$S(b)/S(0) = \exp-\left(bD + b^2D^2K/6\right) \tag{1.11}$$

Since diffusion is a process that takes place in four dimensions we need to utilize a displacement distribution function that will predict the position of each water molecule at a certain time point. In a homogeneous medium, the molecular displacement distribution can be Gaussian, where the width is proportional to the diffusion coefficient. In heterogeneous tissues, the water molecular displacements significantly differ from the true "Brownian motion" defined for free molecules because water molecules bounce, cross and interact with cell membranes and other microstructural components. In the presence of those obstacles, the actual diffusion distance is reduced compared to free water, and the displacement distribution is no longer Gaussian (Fig. 1.14). In other words, while over very short times diffusion reflects the local intrinsic viscosity, at longer diffusion times the effects of the obstacles become predominant.

Several more sophisticated models have been introduced recently. The VERDICT model includes three compartments, namely the intracellular, extracellular and intravascular [22]. The Filter Exchange Imaging is based on a double pulse gradient spin echo technique and takes into consideration the water exchange time between two compartments with different diffusion characteristics [23]. Currently, these sequences are not available on clinical MR scanners, and further studies are needed to unveil in what circumstances these models will be adequate and whether they can be clinically useful.

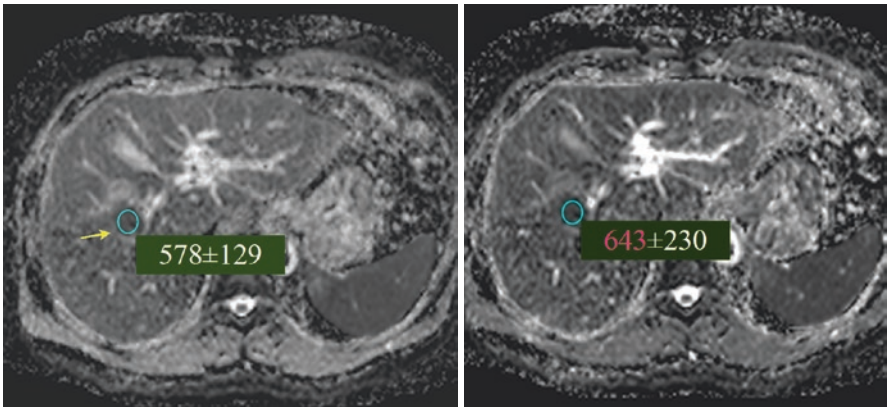

Fig. 1.14 Kurtosis coefficient (*K*) maps in a normal volunteer presenting the liver, pancreas and spleen with high *K* values that are compatible with increased deviation from Gaussian behaviour, while the kidneys, gallbladder and stomach presents with low *K* values

1.6 Factors Influencing the ADC Value

The ADC value, most often derived from a mono-exponential model, depends on the signal fitting, and the available SNR. Artefacts might also, significantly influence the fit quality. The slope calculated by the linear regression, giving the ADC, will inevitably be influenced by the signal value measured for each point, especially the points corresponding to the highest *b* values because these have the most attenuated signal and lowest SNR, therefore are more prone to noise (Fig. 1.15). The fit can be performed pixel by pixel to generate an ADC map but can also be based on ROI signal measurement and of course the definition of the ROI (size, position, homogeneous region or not) plays a crucial role [24]. Note that the mean ADC value in the ROI drawn on the ADC map is not identical to the ADC value computed from the mean signal of the same ROI drawn in all separate *b* value images because Eq. (1.4) is nonlinear. Globally we can expect a better fit quality if an increasing number of *b* values are used, at the cost of a longer acquisition duration. At fixed *b* value and diffusion direction, the acquisition might be repeated, providing an average from a higher number of samples. The number of *b* values or *b* directions might also be increased at acquisition; the choice of the *b* values involved in the fit will finally influence the ADC quantification (Fig. 1.15).

Several studies have suggested the interest of using ADC histograms as a surrogate marker of chemotherapy response [25] or to differentiate low-grade from high-grade clear cell renal cell carcinoma [26]. Another more novel approach consists of analyzing texture parameters of abdominal DWI or ADC maps [27].

In the clinical setting, a compromise must be found considering the number of slices, the spatial resolution, the use of trigger methods or a breath-hold approach. Of course, a central question is whether the examination aims at lesion detection (ADC map with enough contrast between the lesion and the surrounding tissue) or aims at a precise quantification with low variability, required in the case of a

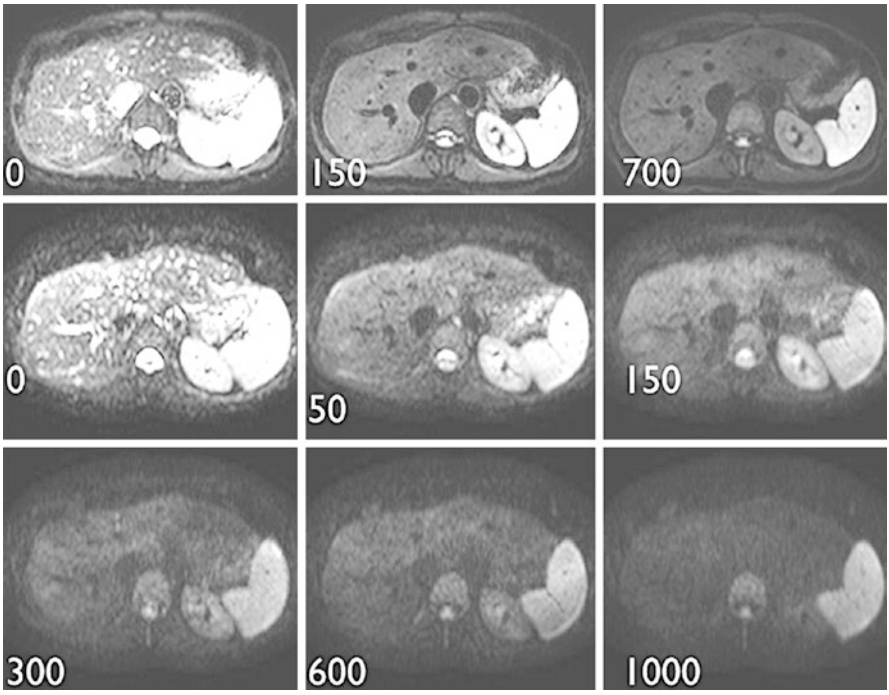

Fig. 1.15 ADC maps obtained by signal fitting using four images with b = 0–150–500–1000 s/mm^2 (left image, lesion ROI ADC 578 ± 129 × 10^{-6} mm^2/s) and by signal fitting using three images b = 0–150–500 s/mm^2 (right image, lesion ROI ADC 643 ± 230 × 10^{-6} mm^2/s). When less b values are involved, the fit is based on less points and thus is more prone to individual point value fluctuations. In these conditions, the ADC standard deviation (i.e. the uncertainty of the ADC in an otherwise rather homogeneous region) increases (in this example ±230 × 10^{-6} mm^2/s compared with ±129 × 10^{-6} mm^2/s). However when the highest b value increases from 500 to 1000 s/mm^2, the signal value is relatively more attenuated and often has a lower SNR. If the SNR gets too low, the noise signal adds substantially to the expected signal and the measured signal appears artificially less attenuated, resulting in a lower regression slope, thus an artificially lower ADC value (in this example 578 × 10^{-6} mm^2/s compared with 643 × 10^{-6} mm^2/s)

longitudinal study meant to detect a change due to the natural evolution of the disease or being the signature of a response to a treatment.

1.7 Factors Influencing the SNR and Artefacts in DWI

ADC quantification accuracy depends on the available SNR of DW images. The SNR itself depends on many parameters like the amplitude of the main field $B0$ (Fig. 1.16), the voxel size or section thickness (Fig. 1.17), the acquisition duration via the number of signal averages and the number of phase encoding steps. An elevated parallel imaging acceleration factor results in less image distortion; however, a too high acceleration factor leads to the failure of the parallel imaging

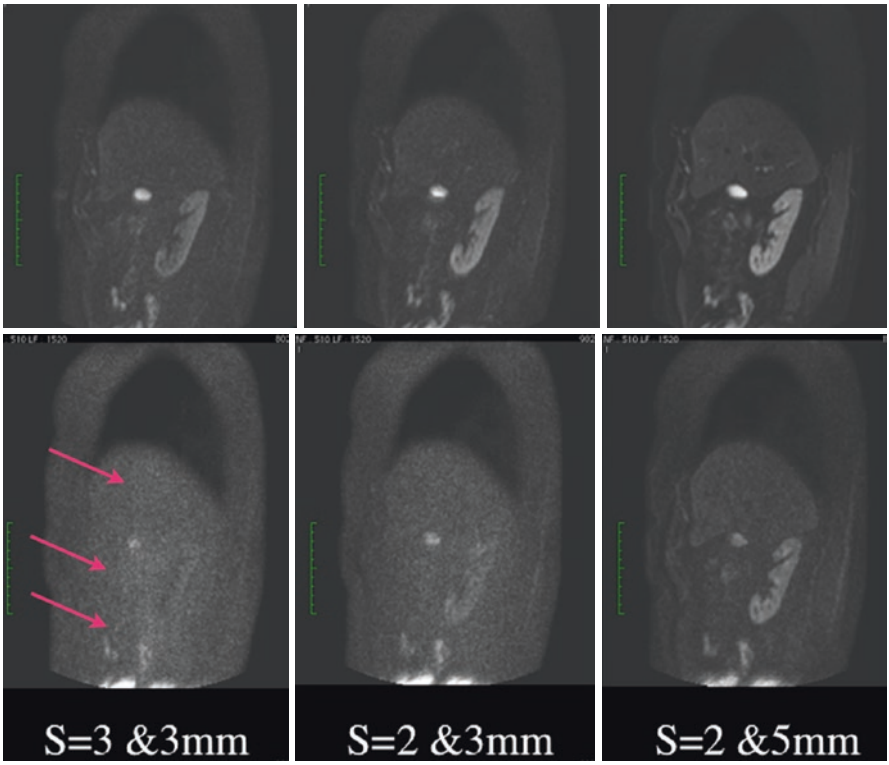

Fig. 1.16 Images obtained in the same individual at 3 T (top row, acquisition 2.4 s per slice, 2.2 × 2.5 × 5 mm TE 61 ms, ETL 47) and 1.5 T (centre and bottom row, acquisition 2.6 s per slice, 2.3 × 2.7 × 5 mm TE 70 ms, ETL 61) with the corresponding *b* values in s/mm^2. Obviously, the SNR is higher at 3 T with higher gradient performances compared with the 1.5 T system

reconstruction and degrades the image quality due to increased noise (Fig. 1.17). The coefficient of variation (COV) of the liver ADC is minimized when measured on the ADC map derived from images with the highest SNR.

In the absence of respiratory synchronisation, in general the different *b* value images will not be located exactly at the same anatomic position due to the respiratory movement of the liver (Fig. 1.18a, b) and this might affect the precision of the ADC; the effect is becoming more significant when multiple *b* value images are acquired (several different *b* values, Fig. 1.19). The misalignment of different *b* value or *b* direction images can seriously impact the ADC values. For example, in Fig. 1.20, one *b*500 image that was misaligned compared with the two other *b*500 images, is shown depicting the high signal intensity from a lesion responsible for an artificially reduced ADC value compared to the ADC obtained from images with an efficient respiratory triggering and without partial volume effect (Figs. 1.21 and 1.22). The respiratory triggering or the use of cardiac triggering may help to avoid these drawbacks.

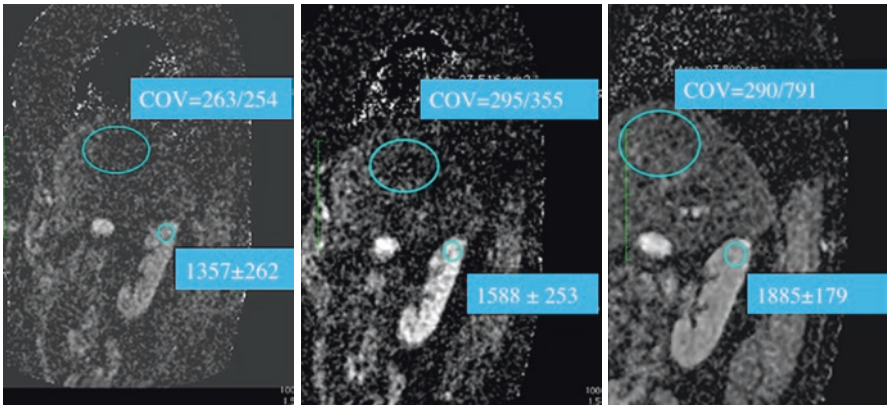

Fig. 1.17 Sagittal DW 1.5 T images (top row: *b* 100 s/mm^2, bottom row: *b* 800 s/mm^2) acquired respectively with (left) Sense factor 3, section thickness 3 mm, TE 69 ms, fixed TR 6100 ms; (middle) Sense factor 2, section thickness 3 mm, TE 75 ms, fixed TR 6100 ms; (right) Sense factor 2, section thickness 5 mm, TE 74 ms TR according to the respiratory triggering. In the left images the sense factor is too high and a vertical band of noise appears through the image centre (red arrows). Visually the images with 5 mm section thickness provide the best SNR

Generally, images with the same *b* value but with different diffusion sensitized directions are not reconstructed, instead, their geometric average, the isotropic or trace diffusion images, are provided directly. If so, the observer has no opportunity to identify a possible mismatch in the anatomic position of the separate directions and a possible deleterious impact on the ADC quantification might be hidden. An alternative solution consists in reconstructing and displaying all *b* value images in all diffusion sensitized directions, followed by a sorting operation discarding all misaligned images. A ROI is then drawn on the remaining images and the ROI ADC value can be computed off line by fitting a linear regression of the logarithms Ln[$S(b)/S(0)$] in function of the *b* values.

A more spurious artefact in DW images of the abdomen comes from the pulsatile heart motion that is transmitted to the abdominal organs and is at the source of an intravoxel incoherent motion that mimics and overcome diffusion especially at moderate or high *b* values [28] (Fig. 1.23). The phenomenon has an impact on the ADC quantification: without cardiac triggering ADC values in healthy subjects are significantly higher in the left lobe of the liver compared to the right lobe [29–31]. It is however possible to predefine individually an optimum cardiac triggering delay minimizing these artefacts; further, using this sequence, residual artefacts can be filtered out at ADC calculation [32]. ADC values in the left and the right lobes of the liver are not anymore significantly different when derived from the images acquired with the optimum cardiac triggering delay (Fig. 1.24). Moreover, when comparing ADC obtained in these optimal conditions with the ADC derived from a non-cardiac-triggered sequence, the ADC value appears to be lower and more reproducible in both lobes of the liver and in the spleen and the range of ADC values obtained from different individuals is narrower. For example, the intra individual left liver

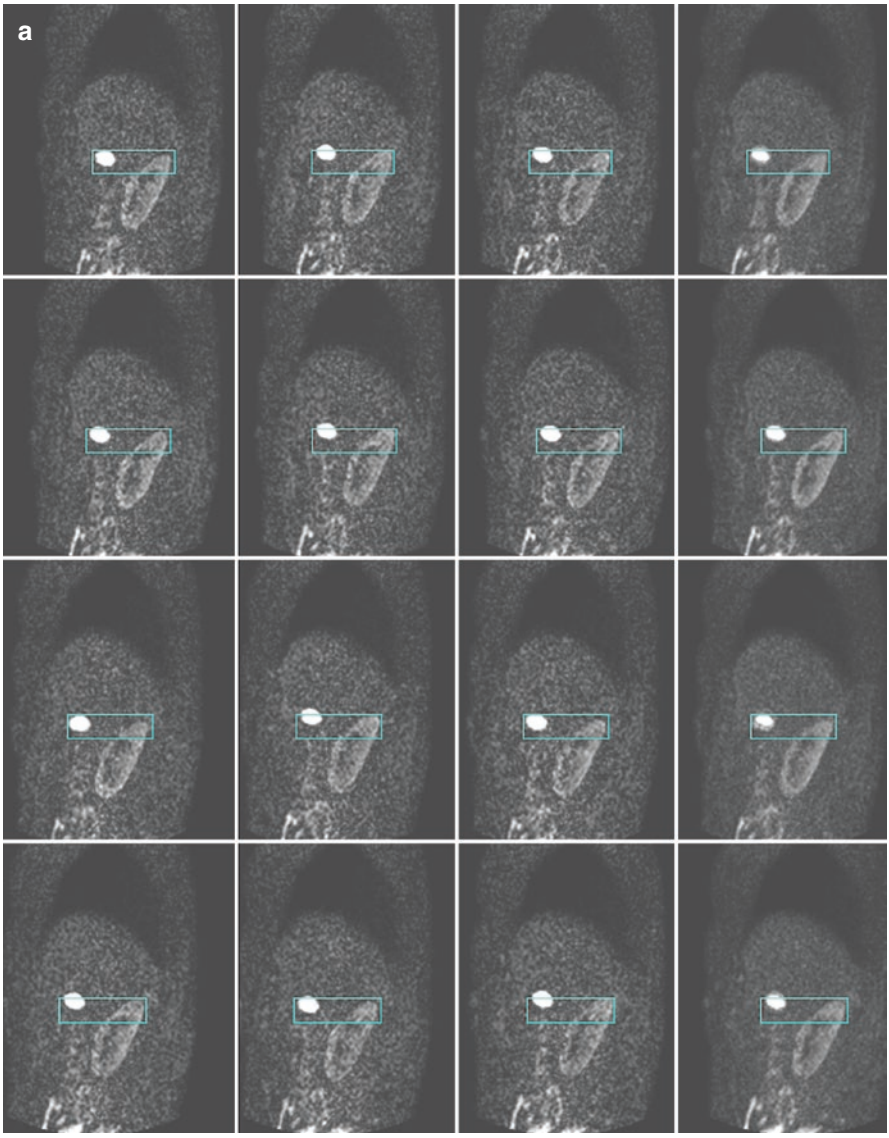

Fig. 1.18 (**a**) Dynamic repetition of the acquisition of b 100 s/mm^2 DW images, 3 mm thickness without respiratory triggering (each row shows DW images in three orthogonal directions and their isotropic geometric average, from top to bottom: four repetitions). The blue rectangle is a fixed position and is used to illustrate the liver, gallbladder, and kidney movements along the respiration. Averaging from all images (and more generally for several *b* value images) will result in a high SNR mean image however affected by the movement blurring and thus affecting the ADC quantification. (**b**) Dynamic repetition of the acquisition of *b* 100 s/mm^2 DW images, 5 mm thickness with respiratory triggering (each row shows DW images in three orthogonal directions and their isotropic geometric average, from top to bottom: four repetitions). The blue rectangle is a fixed position and is used to illustrate the liver, gallbladder and kidney movements along the respiration. Compared with (**a**) the anatomic position of the different images is more stable

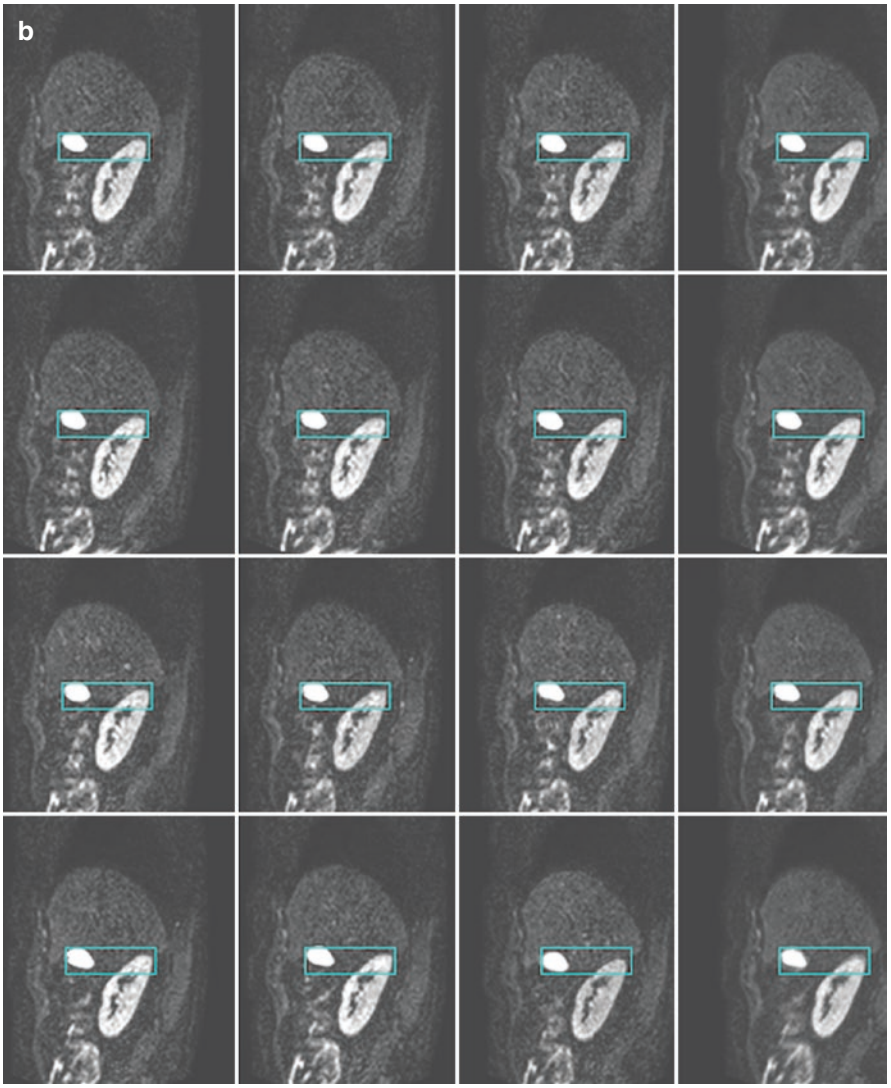

Fig. 1.18 (continued)

ADC limit of agreement (LOA) considering the averaged of three 1 cm^2 ROI's from four acquisitions was $\pm 835 \times 10^{-6}$ mm^2/s without cardiac triggering and dropped to $\pm 315 \times 10^{-6}$ mm^2/s with optimal cardiac triggering and to $\pm 152 \times 10^{-6}$ mm^2/s after further signal filtering. In the right liver, the ADC LOA were $\pm 392 \times 10^{-6}$ mm^2/s without cardiac triggering and $\pm 172 \times 10^{-6}$ mm^2/s with optimal cardiac triggering.

Many authors have studied various aspects of ADC variability in the abdomen in normal liver and in lesions. One of these studies was devoted to the comparison of several non-cardiac-triggered techniques: breath-hold, respiratory-triggered,

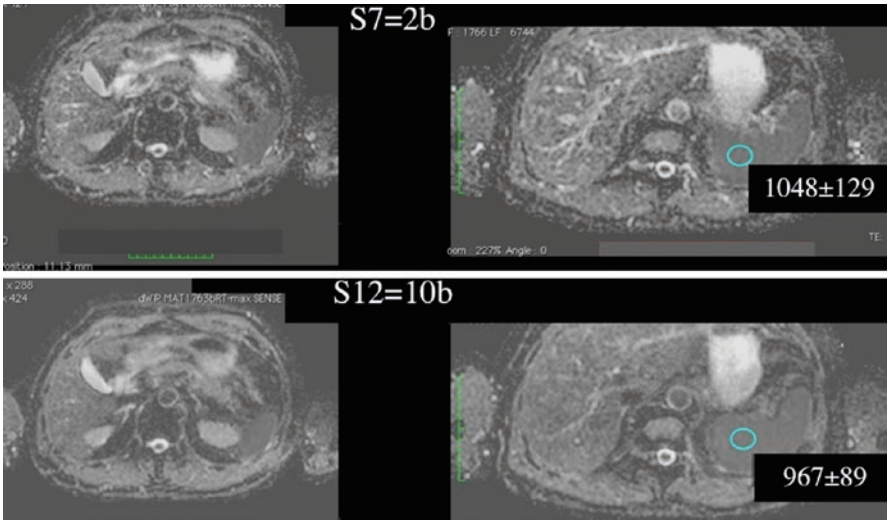

Fig. 1.19 ADC maps (units 10^{-6} mm^2/s) acquired at 1.5 T with TE = 81 ms and fixed TR = 6100 ms, involving respectively 2 *b* values (top row, 0 and 800 s/mm^2) and 10 *b* values (bottom row, 0, 10, 20, 50, 75, 100, 150, 300, 600, 800 s/mm^2). Each *b* value image was sampled in three diffusion sensitized orthogonal directions. The bile duct system appears a little more blurred on the 10 *b* value ADC map reconstruction, because these images were more sensitive to the different actual anatomic section positions of different *b* value images along the respiratory cycle. However, the Spleen ROI mean ADC and standard deviation are lower due to less noise contribution

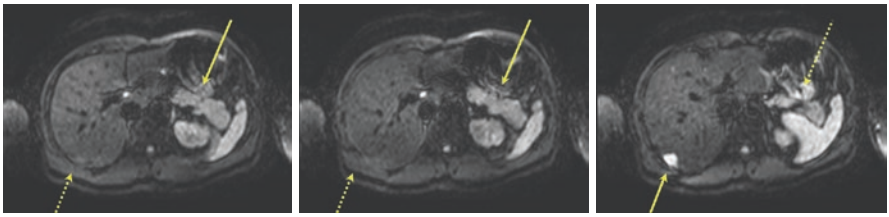

Fig. 1.20 Individual *b* = 500 s/mm^2 images in the three orthogonal diffusion directions. The acquisition was performed with respiratory triggering in a subject with an irregular respiratory cycle, resulting in a variation of the anatomic level across the acquisition of the different images. The solid arrow points to the tail of the pancreas that is well visible only on the two first images from the left. The dotted arrow on the left and central images points to a haemangioma, visible only on the last image to the right (solid arrow). A subsequent ADC calculation will be blurred by this effect (see Fig. 1.21)

navigator-triggered and free breathing [31] and demonstrated again a significantly larger ADC value in the left liver compared with the right liver, additionally the LOA for ADC measured in several locations in the right liver were in between 325–440 × 10^{-6} mm^2/s, while the ADC LOA for ADC measured in several locations in the left liver were in between 360–810 × 10^{-6} mm^2/s. Even more importantly, the LOA for acquisition repeatability using a respiratory triggering sequence were 315 × 10^{-6} mm^2/s in the right liver and 515 × 10^{-6} mm^2/s in left liver. Considering the

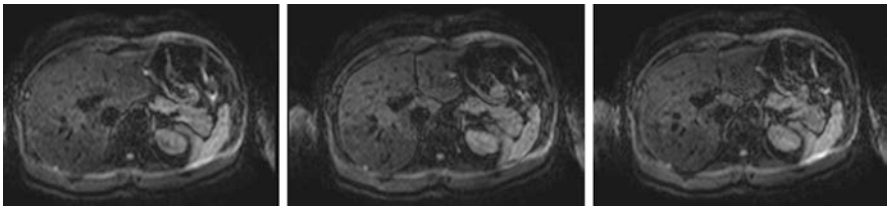

Fig. 1.21 Individual b = 500 s/mm^2 images in the three orthogonal diffusion directions in the same subject as in the previous figure. The acquisition was performed with a tracking diaphragmatic navigator, enabling the section level to be acquired in the same anatomic position (including the tail of the pancreas) for the different images

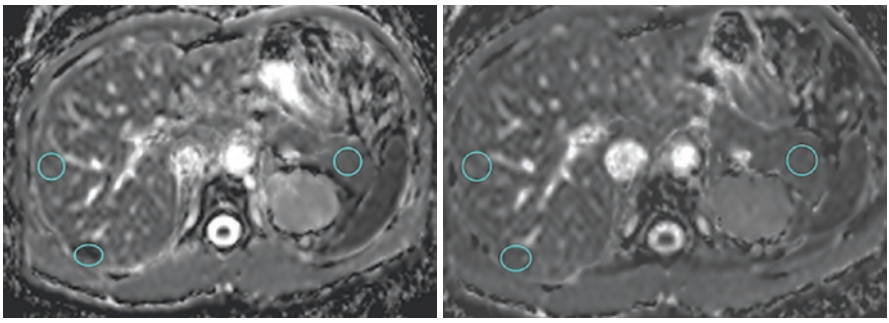

Fig. 1.22 ADC map (left) derived from images shown in Fig. 1.19, with liver signal contaminated with lesion hyperintense signal on one of the b500 images providing an ADC = $866 \pm 506 \times 10^{-6}$ mm^2/s, compared with the ADC map (right) derived from images shown in Fig. 1.20 without misalignment with the liver ADC = $1215 \pm 344 \times 10^{-6}$ mm^2/s

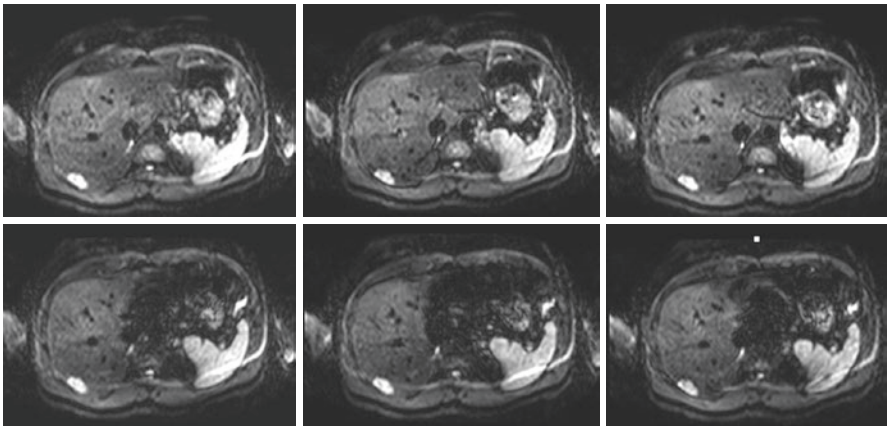

Fig. 1.23 Individual b = 500 s/mm^2 images in the three orthogonal diffusion directions in the same subject as Figs. 1.19–1.21. The acquisitions were performed with cardiac triggering respectively 921 ms (top row) and 121 ms after the VCG signal (bottom row). On the bottom row image series, a huge signal loss occurred in the left lobe of the liver and is due to the IVIM pseudo diffusion from the transmission of the pulsatile heart movement to the liver

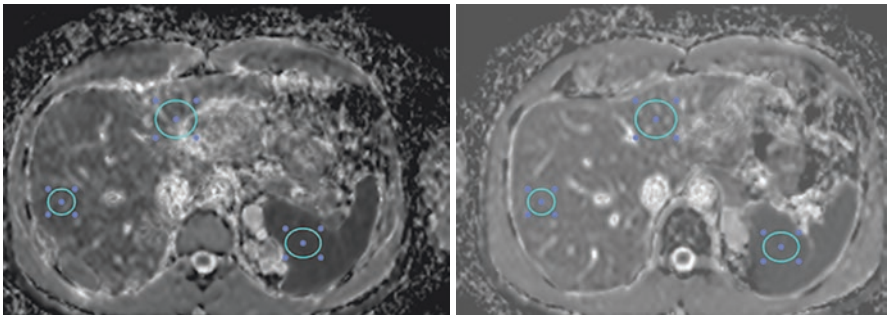

Fig. 1.24 ADC maps from a respiratory-triggered sequence without cardiac triggering (left) and from a respiratory- and cardiac-triggered sequence with individually predetermined optimal VCG delay (right). ROI's were drawn in the left and the right lobe of the liver and in the spleen. ADC values derived from the acquisition without the optimal cardiac triggering (left liver ROI: 2083 ± 728 10^{-6} mm^2/s, right liver ROI:1325 ± 193 10^{-6} mm^2/s, spleen ROI:838 ± 71 10^{-6} mm^2/s) are higher than those obtained from the acquisition using the optimal cardiac triggering delay of 400 ms (left liver ROI: 1406 ± 366 × 10^{-6} mm^2/s, right liver ROI:1217 ± 136 × 10^{-6} mm^2/s, spleen ROI:702 ± 76 × 10^{-6} mm^2/s). The effect is more important in the left liver and indeed the signal loss was manifest in the left liver on the DW images. Interestingly the phenomenon also appears to affect the ADC quantification in the right liver and in the spleen, even if the signal effects on DW images were visually much less evident

variability between three ROI's along five consecutive acquisitions in normal subjects, another study measured a CV of 12.8% in the posterior right liver and 15.4% in the pancreatic head [33]. In malignant hepatic tumours, Kim et al. [34] emphasized the influence of the acquisition technique and of the ADC calculation method. In another study [35], the same group demonstrated that ADC measurements in hepatic malignant tumours were more reproducible in the right liver compared with the left liver and for larger lesions compared with smaller lesions. Moreover the 95% LOA between tumours ADCs measured on repeated respiratory-triggered DW images were 28.7–31.3% of the mean (mean ADC around 1450 × 10^{-6} mm^2/s, with most lesions located in the right liver). The LOA between ADC's measured by two readers were 14.6–22.5% of the mean ADC. Such results are of paramount importance for the use of ADC quantification in longitudinal studies aiming at treatment response assessment. Indeed, a possible increase or decrease in ADC due to treatment response is only detectable and attributable to an actual response if it is larger than the limits of the 95% confidence interval for repeatability in absence of change.

The reproducibility of the micro-perfusion fraction *f*, the pseudo-diffusion coefficient D* and the diffusion coefficient D in colorectal liver metastases was demonstrated to be quite poor [36].

The variability of the upper abdominal organs ADC measurement in different MR systems at different time points has been shown to be significantly improved by using normalized ADC using the spleen as a reference organ [37]. Interestingly, normalizing liver ADC with spleen ADC improves the diagnostic accuracy for detection of liver fibrosis and cirrhosis when using breath-hold diffusion-weighted imaging [38].

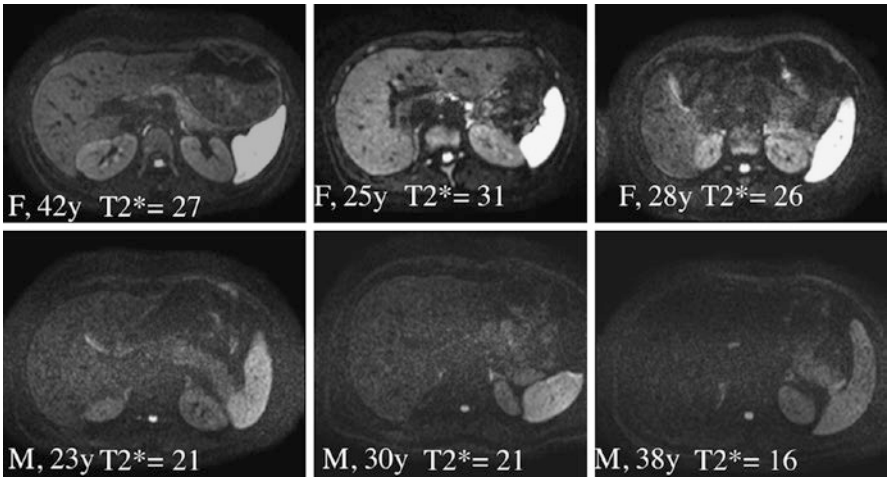

Fig. 1.25 DW images with b 1000 S/mm^2 obtained at 3 T in healthy subjects (top row females, bottom row males) of different ages (in years) and liver T2* values in msec. The normal liver visibility depends dramatically on the age and gender through the liver T2* dependence in the age and the gender. A lower liver visibility corresponds to a poor SNR and the measurement of the ADC provides the artificially low ADC values, with a high standard deviation

More generally, the analysis of ten studies performed with different imaging protocols and patient populations over a period of 10 years at the same institution demonstrated a better ADC repeatability in large tumours than in smaller tumours [39].

Another surprising SNR effect is related to the dual nature of the contrast of DW images (T2-weighted and Diffusion-weighted). The T2* relaxation time of the normal liver is rather low compared to other organs, making its signal relatively lower on DW images because of the T2* weighting of the EPI Stejskal–Tanner diffusion sequence. At high *b* values the signal intensity of the liver is thus quite low. It has been demonstrated that the T2* value of the normal liver is both age and gender dependent and is related to the variable iron content in the normal liver [40] and this dependence does significantly impact the liver signal intensity on DW images (Fig. 1.25) and the corresponding ADC measurements [41]. The ADC value correlates with the individual T2* value, while ADC ROI standard deviation negatively correlated with T2* [41, 42] confirming the gender and age dependency of normal liver parenchyma ADC. Finally, it was demonstrated that IVIM parameters in upper abdominal organ substantially differ across MR systems from different vendors and different magnetic field intensity [43].

1.8 Conclusions

Diffusion-weighted imaging of the upper abdominal area is technically challenging due to the presence of multiple physiologic motions (respiration, cardiac motion), as well as the presence of air in the stomach. In addition, the increased vascularity

of liver, pancreas and spleen is responsible for ADC contamination with microperfusion effects, therefore more complex strategies need to be taken into consideration to minimize these problems. The hardware capabilities of the scanners namely the gradient performance and the presence of high-end RF coils can significantly improve image quality and diagnostic accuracy.

References

1. Paul L. Sur la théorie du mouvement brownien. C R Acad Sci. 1908;146:530–2.
2. Albert E. Über die von der molekularkinetischen Theorie der Wärme geforderte Bewegung von in ruhenden Flüssigkeiten suspendierten Teilchen. Ann Phys. 1905;322(8):549–60.
3. White M, Dale A. Distinct effects of nuclear volume fraction and cell diameter on high b-value diffusion MRI contrast in tumours. Magn Reson Med. 2014;72:1435–43.
4. Carr HY, Purcell EM. Effects of diffusion on free precession in nuclear magnetic resonance experiments. Phys Rev. 1954;94:630–8.
5. Torrey HC. Bloch equations with diffusion terms. Phys Rev. 1956;104(3):563–5.
6. Woessner DE. Effects of diffusion in nuclear magnetic resonance spin-echo experiments. J Chem Phys. 1961;34:2057–61.
7. Stejskal EO, Tanner JE. Spin diffusion measurements: spin echoes in the presence of a time-dependent field gradient. J Chem Phys. 1965;42(1):288–92.
8. Setsompop K, Gagoski BA, Polimeni JR, Witzel T, Wedeen VJ, Wald LL. Blipped-controlled aliasing in parallel imaging for simultaneous multislice echo planar imaging with reduced g-factor penalty. Magn Reson Med. 2012;67(5):1210–24.
9. Obele CC, Glielmi C, Ream J, Doshi A, Campbell N, Zhang HC, Babb J, Bhat H, Chandarana H. Simultaneous multislice accelerated free-breathing diffusion-weighted imaging of the liver at 3T. Abdom Imaging. 2015;40:2323–30.
10. Porter DA, Heidemann R. High resolution diffusion-weighted imaging using readout-segmented echo-planar imaging, parallel imaging and a two-dimensional navigator-based reacquisition. Magn Reson Med. 2009;62:468–75.
11. Le Bihan D, Breton E, Lallemand D, Aubin ML, Vignaud J, Laval-Jeantet M. Separation of diffusion and perfusion in intravoxel incoherent motion MR imaging. Radiology. 1988;168:497–505.
12. Cohen AD, Schieke MC, Hohenwalter MD, Schmainda KM. The effect of low b-values on the intravoxel incoherent motion derived pseudodiffusion parameter in liver. Magn Reson Med. 2015;73:306–11.
13. Ahlgren A, Knutsson L, Wirestam R, Nilsson M, Ståhlberg F, Topgaard D, Lasič S. Quantification of microcirculatory parameters by joint analysis of flow-compensated and non-flow-compensated intravoxelin coherent motion (IVIM) data. NMR Biomed. 2016;29:640–9.
14. Lemke A, Stieltjes B, Schad LR, Laun FB. Toward an optimal distribution of b values for intravoxel incoherent motion imaging. Magn Reson Imaging. 2011;29(6):766–76.
15. Lemke A, Laun FB, Simon D, Stieltjes B, Schad LR. An in vivo verification of the intravoxel incoherent motion effect in diffusion-weighted imaging of the abdomen. Magn Reson Med. 2010;64(6):1580–5.
16. Wetscherek A, Stieltjes B, Laun FB. Flow-compensated intravoxelin coherent motion diffusion imaging. Magn Reson Med. 2015;74(2):410–9.
17. Ozaki M, Inoue Y, Miyati T, Hata H, Mizukami S, Komi S, Matsunaga K, Woodhams R. Motion artifact reduction of diffusion-weighted MRI of the liver: use of velocity-compensated diffusion gradients combined with tetrahedral gradients. J Magn Reson Imaging. 2013;37:172–8.

18. Coenegrachts K, Orlent H, terBeek L, Haspeslagh M, Bipat S, Stoker J, Rigauts H. Improved focal liver lesion detection: comparison of single-shot spin-echo echo-planar and superparamagnetic iron oxide (SPIO)-enhanced MRI. J Magn Reson Imaging. 2008;27(1):117–24.
19. Coenegrachts K, Matos C, terBeek L, Metens T, Haspeslagh M, Bipat S, Stoker J, Rigauts H. Focal liver lesion detection and characterization: comparison of non-contrast enhanced and SPIO-enhanced diffusion-weighted single-shot spin echo echo planar and turbo spin echo T2-weighted imaging. Eur J Radiol. 2009;72(3):432–9.
20. Bennett KM, Schmainda KM, Bennett RT, Rowe DB, Lu H, Hyde JS. Characterization of continuously distributed cortical water diffusion rates with a stretched-exponential model. Magn Reson Med. 2003;50:727–34.
21. Jensen JH, Helpern JA, Ramani A, Lu H, Kaczynski K. Diffusional kurtosis imaging: the quantification of non-Gaussian water diffusion by means of magnetic resonance imaging. Magn Reson Med. 2005;53:1432–40.
22. Panagiotaki E, Walker-Samuel S, Siow B, Johnson SP, Rajkumar V, Pedley RB, Lythgoe MF, Alexander DC. Noninvasive quantification of solid tumor microstructure using verdict MRI. Cancer Res. 2014;74(7):1902–12.
23. Nilsson M, Lätt J, van Westen D, Brockstedt S, Lasič S, Ståhlberg F, Topgaard D. Noninvasive mapping of water diffusional exchange in the human brain using filter-exchange imaging. Magn Reson Med. 2013;69(6):1573–81.
24. Colagrande S, Pasquinelli F, Mazzoni LN, Belli G, Virgili G. MR-diffusion weighted imaging of healthy liver parenchyma: repeatability and reproducibility of apparent diffusion coefficient measurement. J Magn Reson Imaging. 2010;31:912–20.
25. Kyriazi S, Collins DJ, Messiou C, Pennert K, Davidson RL, Giles SL, Kaye SB, Desouza NM. Metastatic ovarian and primary peritoneal cancer: assessing chemotherapy response with diffusion-weighted MR imaging—value of histogram analysis of apparent diffusion coefficients. Radiology. 2011;261(1):182–92.
26. Zhang YD, Wu CJ, Wang Q, Zhang J, Wang XN, Liu XS, Shi HB. Comparison of utility of histogram apparent diffusion coefficient and R2* for differentiation of low-grade from high-grade clear cell renal cell carcinoma. AJR Am J Roentgenol. 2015;205(2):193–201.
27. Becker AS, Wagner MW, Wurnig MC, Boss A. Diffusion-weighted imaging of the abdomen: impact of b-values on texture analysis features. NMR Biomed. 2017;30(1):1–11.
28. Kwee TC, Takahara T, Niwa T, Ivancevic MK, Herigault G, Van Cauteren M, Luijten PR. Influence of cardiac motion on diffusion-weighted magnetic resonance imaging of the liver. MAGMA. 2009;22:319–25.
29. Mürtz P, Flacke S, Traber F, van den Brink JS, Gieseke J, Schild HH. Abdomen: diffusion- weighted MR imaging with pulse-triggered single-shot sequences. Radiology. 2002;224:258–64.
30. Wong O, et al. The effect of respiratory and cardiac motion in liver diffusion tensor imaging (DTI). J Comput Assist Tomogr. 2014;38:352–9.
31. Chen X, Qin L, Pan D, Huang Y, Yan L, Wang G, Liu Y, Liang C, Liu Z. Liver diffusion-weighted MR imaging: reproducibility comparison of ADC measurements obtained with multiple breath-hold, free-breathing, respiratory-triggered, and navigator-triggered techniques. Radiology. 2014;271:113–25.
32. Metens T, Absil J, Denolin V, Bali MA, Matos C. Liver apparent diffusion coefficient repeatability with individually predetermined optimal cardiac timing and artefact elimination by signal filtering. J Magn Reson Imaging. 2016;43(5):1100–10.
33. Braithwaite AC, Dale BM, Boll DT, Merkle EM. Short- and midterm reproducibility of apparent diffusion coefficient measurements at 3.0T diffusion-weighted imaging of the abdomen. Radiology. 2009;250:459–65.
34. Kim SY, Lee SS, Park B, Kim N, Kim JK, Park SH, Byun JH, Song KJ, Koo JH, Choi EK, Lee MG. Reproducibility of measurement of apparent diffusion coefficients of malignant hepatic tumors: effect of DWI techniques and calculation methods. J Magn Reson Imaging. 2012;36(5):1131–8.

35. Kim SY, Lee SS, Byun JH, Park SH, Kim JK, Park B, Kim N, Lee MG. Malignant hepatic tumors: short-term reproducibility of apparent diffusion coefficients with breath-hold and respiratory-triggered diffusion-weighted MR imaging. Radiology. 2010;255:815–23.
36. Andreou A, Koh DM, Collins DJ, Blackledge M, Wallace T, Leach MO, Orton MR. Measurement reproducibility of perfusion fraction and pseudodiffusion coefficient derived by intravoxel incoherent motion diffusion-weighted MR imaging in normal liver and metastases. Eur Radiol. 2013;23:428–34.
37. Song JS, Kwak HS, HeeByon J, Jin GY. Diffusion-weighted mr imaging of upper abdominal organs at different time points: apparent diffusion coefficient normalization using a reference organ. J Magn Reson Imaging. 2017;45:1494–501.
38. Do RK, Chandarana H, Felker E, Hajdu CH, Babb JS, Kim D, Taouli B. Diagnosis of liver fibrosis and cirrhosis with diffusion-weighted imaging: value of normalized apparent diffusion coefficient using the spleen as reference organ. Am J Roentgenol. 2010;195(3):671–6.
39. Winfield JM, Tunariu N, Rata M, Miyazaki K, Jerome NP, Germuska M, Blackledge MD, Collins DJ, de Bono JS, Yap TA, de Souza NM, Doran SJ, Koh DM, Leach MO, Messiou C, Orton MR. Extracranial soft-tissue tumors: repeatability of apparent diffusion coefficient estimates from diffusion-weighted MR imaging. Radiology. 2017; https://doi.org/10.1148/radiol.2017161965.
40. Schwenzer NF, Machann J, Haap MM, Martirosian P, Schraml C, Lie-big G, Stefan N, Haring HU, Claussen CD, Fritsche A, Schick F. T2* relaxometry in liver, pancreas, and spleen in a healthy cohort of one hundred twenty-nine subjects-correlation with age, gender, and serum ferritin. Invest Radiol. 2008;43:854–60.
41. Metens T, Ferraresi KF, Farchione A, Moreno C, Bali MA, Matos C. Normal hepatic parenchyma visibility and ADC quantification on diffusion-weighted MRI at 3 T: influence of age, gender, and iron content. Eur Radiol. 2014;24(12):3123–33.
42. Lavdas I, Rockall AG, Castelli F, Sandhu RS, Papadaki A, Honeyfield L, Waldman AD, Aboagye EO. Apparent diffusion coefficient of normal abdominal organs and bone marrow from whole-body DWI at 1.5T the effect of sex and age. AJR. 2015;205:242–50.
43. Barbieri S, Donati OF, Froehlich JM, Thoeny HC. Comparison of intravoxel incoherent motion parameters across MR imagers and field strengths: evaluation in upper abdominal organs. Radiology. 2016;279(3):784–94.

Benign Liver Lesions

2

Maxime Ronot, Romain Pommier, Anne Kerbaol, Onorina Bruno, and Valérie Vilgrain

2.1 Introduction

Benign liver lesions include a wide variety of solid or cystic entities that are usually found in the absence of any underlying chronic liver disease (Table 2.1). Solid lesions are classified by pathologists based on the cell of origin into epithelial or mesenchymal formations. Furthermore, some lesions correspond to regenerative lesions, while others are truly neoplastic. Epithelial lesions include hepatocellular (focal nodular hyperplasia (FNH) and hepatocellular adenomas (HCAs)) and cholangiocellular tumors (bile duct adenoma and biliary hamartoma). Mesenchymal tumors include hemangiomas, angiomyolipomas, or lipomas. Cystic lesions are frequent and include simple hepatic cysts, biliary hamartoma, also known as Von Meyenburg complex, and biliary cystadenoma.

An accurate diagnosis is clinically important since the management of benign liver lesions is usually conservative. Indeed, these lesions generally remain asymptomatic and follow a very benign course. HCAs, angiomyolipomas, and biliary cystadenomas are an exception, with potentially serious complications that may require more invasive treatment, mainly surgical resection.

Imaging plays a central role in the diagnosis of benign liver lesions. Although various imaging techniques are frequently used sequentially or in combination to obtain the correct diagnosis, magnetic resonance imaging (MRI) is the best technique for both detection and characterization of focal liver lesions. Although

M. Ronot (✉) · R. Pommier · A. Kerbaol · O. Bruno · V. Vilgrain
Department of Radiology, Beaujon Hospital, APHP.Nord, Clichy, Hauts-de-Seine, France

Université de Paris, Paris, France

INSERM U1149, CRI, Paris, France
e-mail: maxime.ronot@aphp.fr; onorina.bruno@aphp.fr; valerie.vilgrain@aphp.fr

C. Matos, N. Papanikolaou (eds.), *Diffusion Weighted Imaging of the Hepatobiliary System*, https://doi.org/10.1007/978-3-319-62977-3_2

Table 2.1 Histological classification of benign liver lesions and main clinical data (in the absence of chronic liver disease)

Epithelial		
– *Hepatocytes*	Hepatocellular adenoma	• Very rare • Associated with oral contraceptives • High rate of complications:(bleeding, malignant transformation)
	Focal nodular hyperplasia	• Rare • Female predominance • No risk of complication
	Nodular regenerative hyperplasia	• Very rare • Associated with systemic diseases and drugs • Portal hypertension
– *Biliary cells*	Bile duct adenoma	• Rare • No risk of complication
	Biliary hamartoma (Von Meyenburg complex)	• Very rare • Development anomaly • No risk of complication
	Simple cyst	• Common • Female predominance • Risk of bleeding
Non-epithelial		
– *Mesenchymal*	Hemangioma	• Common • Female predominance • Very low risk of complication
	Angiomyolipoma	• Rare • Associated with tuberous sclerosis • No risk of complication
	Lipoma, myelolipoma	• Exceptional • No risk of complication
– *Heterotopia*	Adrenal, pancreatic, or spleen tissues	• Exceptional • Very low risk of complication
Other	Inflammatory pseudotumor	• Very rare • Associated with general syndromes • No risk of complication

detection of benign lesions is rarely an issue, characterization is the main challenge. Diffusion-weighted imaging (DWI) has been used for this purpose, mainly to differentiate between benign and malignant lesions in patients with chronic liver disease or extrahepatic cancers. The main differentials in these cases are hepatocellular carcinoma and liver metastases, respectively.

The first part of this chapter reviews the imaging features of the main benign liver lesions on MR imaging with a special focus on DWI. For heuristic purposes, lesions are classified according to their most frequent features of high *b*-value DW images. The second part of chapter reviews and discusses the role of DWI, in particular in clinical cases such as in chronic liver diseases and oncological patients, using a pragmatic diagnostic approach.

2.2 Lesions Showing Marked Hyperintensity on High *b*-Value Images

2.2.1 Hemangioma

Cavernous hemangioma is the most frequent benign solid liver lesion with a prevalence of up to 20% in an autopsy series [1] in the general population. It is found at all ages. The female/male ratio is 2–5 [2, 3]. Except for giant hemangiomas, which may present with symptoms or complications (Bornman syndrome, Kasabach-Merritt syndrome), most lesions are asymptomatic. Their course is benign, and hemangiomas never progress to malignancy [4]. Small hemangiomas may become entirely fibrous and are called "sclerosing hemangiomas."

MR imaging is the key imaging modality to characterize liver hemangiomas [5, 6]. The classic appearance is a homogeneous, well-delineated, strongly hypointense lesion on T1-weighted sequences and a markedly hyperintense lesion on T2-weighted sequences. Dynamic multiphasic T1-weighted sequences following extracellular gadolinium chelate administration show peripheral and globular, then central enhancement, with persistent enhancement of the lesion on delayed sequences [7]. The diagnostic value of MR imaging is good with a sensitivity of 90%, a specificity of 92%, and a global accuracy of 90% [6, 7]. Rapidly filling hemangiomas are usually seen in small lesions (42% of hemangiomas <2 cm in diameter) [8]. MR imaging shows immediate homogeneous enhancement on arterial phase images which makes it difficult to differentiate this entity from other hypervascular tumors. The diagnosis is based on strongly hyperintense T2-weighted images, with enhancement that is parallel to arteries and persists on delayed-phase images using extracellular MR contrast agents (Fig. 2.1). The features of hemangiomas on gadoxetic acid-enhanced MR imaging are similar to those with extracellular contrast agents during the arterial and portal venous phases. However, lesions appear hypointense or have incomplete enhancement compared to the background liver during the transitional phase due to rapid and intense uptake of the contrast agent by hepatocytes. Completely hypointense hepatobiliary phase images, called the "pseudo washout sign," is also usually observed and is most frequent in rapidly enhancing or small hemangiomas [9].

On diffusion-weighted images, there is usually a drop in signal intensity on high *b*-value images because diffusion is not limited to hemangiomas (Fig. 2.1). However, a persistent high signal intensity may be seen on high *b*-value images, known as the "T2-shine through effect." This corresponds to a high signal on DWI images that is not due to restricted diffusion but due to high signal intensity on T2-weighted sequences that "shines through" to the DWI image. In a series of 388 hemangiomas, we observed this effect in approximately half the lesions and in two thirds of the patients [10]. It was significantly more frequent in large hemangiomas and in those with typical enhancement. Thus, radiologists should be familiar with this pattern on DWI in hemangiomas. Careful analysis of the ADC map is needed to confirm this

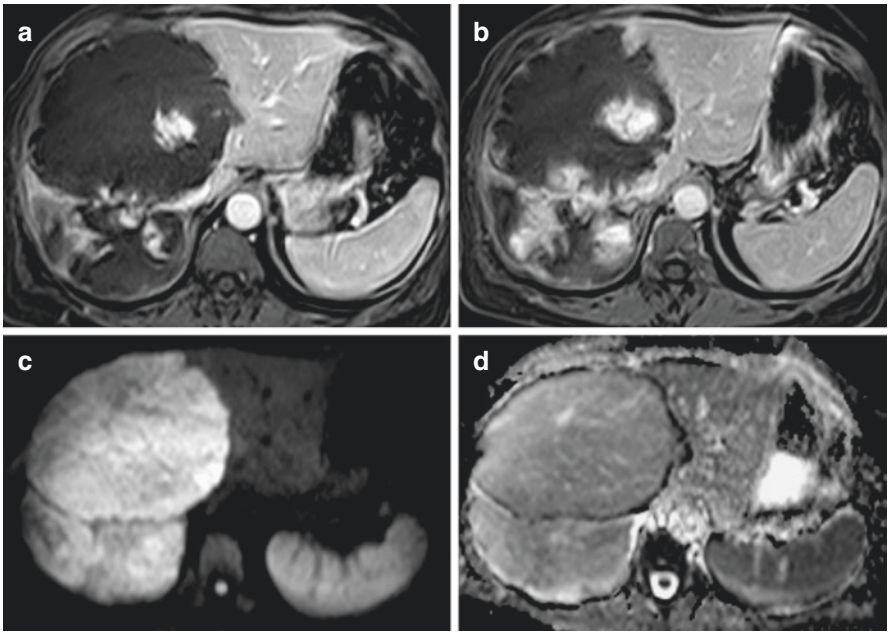

Fig. 2.1 MR imaging of a typical large hemangioma in a 48-year-old woman. (**a**, **b**) The lesion shows nodular peripheral enhancement on post-contrast arterial phase images with progressive enhancement on portal venous phase images. On diffusion-weighted images ($b = 800$), the lesion shows high signal intensity (**c**) and a high ADC value (**d**) corresponding to a "T2-shine-through" effect

pattern since ADC values are high for hemangiomas (above 2×10^{-3} mm^2/s), and the mean ADC value for hemangiomas with the T2 shine-through effect has been shown to be significantly lower than those without [10].

2.2.2 Angiomyolipoma

Hepatic angiomyolipomas are a rare, benign, mesenchymal tumor from the family of lipomatous lesions, like lipoma and myelolipoma. This tumor is now classified as a PECOMA lesion (perivascular epithelioid cell). It is composed of different amounts of fat, epithelioid, and spindled smooth cells and thick-walled blood vessels and occasionally some foci of extramedullary hematopoiesis. Around 15% of patients with hepatic angiomyolipoma have tuberous sclerosis [11], and in these cases, multiple lesions are often present. Women are more affected than men with a ratio W/M (2.5:1). The mean age at diagnosis is 40–50 years, but this tumor can be identified at any age. Most angiomyolipomas are larger than 5 cm in diameter and well circumscribed. Patients are usually asymptomatic, and the tumor is often identified incidentally during a routine ultrasound examination. Blood liver tests are usually normal.

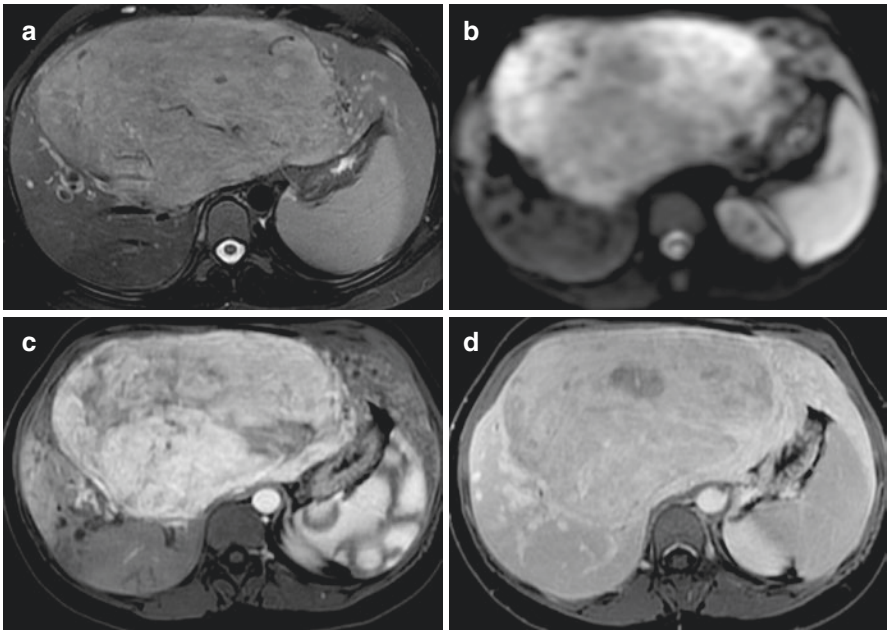

Fig. 2.2 Low-fat containing angiomyolipoma in a 26-year-old woman. On MR imaging, the lesion is heterogeneous, with high signal intensity on T2-weighted images (**a**) and on diffusion-weighted images (**b**). After extracellular contrast agent injection, the images show marked contrast enhancement on arterial phase images (**c**) with mild washout on portal venous phase images (**d**)

The accuracy of the preoperative diagnosis is low because this is a rare tumor with highly variable imaging features due to the presence of the three components. There are two main types:

- *Typical angiomyolipoma* (Fig. 2.2): a heterogenous, well-delineated, single lesion whose size varies. Lesions are hyperintense on T1-weighted sequences (more than 80%) with a drop in signal intensity on fat-suppressed T1-weighted sequences. The fat is usually macroscopic but signal dropout can also be found on chemical shift sequences. The signal varies on T2-weighted sequences depending on the different components. Early enhancement (80%) and an absence of washout are the rules following contrast administration [12]. Large central vessels (so-called macroaneurysms) are highly suggestive of typical angiomyolipomas [12].
- *Angiomyolipoma without fat or with low fat content*. The fat component of angiomyolipomas varies between 10% and 90% but can be less than 5%. Angiomyolipomas with low amount of fat tend to lose typical characteristics and appear hypointense on T1-weighted sequences [13, 14].

On diffusion-weighted images, angiomyolipomas are heterogeneous. A high signal intensity is found for solid tissue, while fat-containing areas are hypointense

because of fat suppression on these sequences. Intratumoral hemorrhage results in an artifact making interpretation difficult.

2.2.3 Solitary Fibrous Tumor

This rare tumor is usually found in the pleura, mediastinum, or respiratory tract. It is more frequent in men (ratio M/W of 2/1) and mainly occurs in adults. Most patients have abdominal pain and even weight loss. A typical solitary fibrotic tumor of the liver is a single, large, heterogenous, well-delineated lesion. There are no suggestive features on MR imaging except progressive enhancement, which can be very strong with extracellular contrast agents during the delayed phase due to abundant collagen [15, 16].

On diffusion-weighted images, a high signal intensity is seen with a low ADC value. DW imaging is not helpful for tumor characterization [17].

2.2.4 Heterotopic Tissue

Several heterotopic tissues may be identified in the liver parenchyma. They are all extremely rare.

- *Adrenal rest tumors* are usually subcapsular and can be difficult to distinguish histologically from HCA.
- *Pancreatic ectopia*.
- *Splenic ectopia* should be considered for the differential diagnosis of hepatic lesions detected after splenectomy.

Most lesions are hypervascular on imaging with washout on portal venous and delayed phase images.

On diffusion-weighted images, there is a marked signal intensity on high b-value images with restricted diffusion and a low ADC value. Diagnosis is therefore difficult, and malignancy is often suggested. The correct diagnosis can be obtained based on the subcapsular location of the lesions and a history of splenectomy.

2.3 Lesions Showing Moderate Signal Intensity on High *b*-Value Images

2.3.1 Focal Nodular Hyperplasia (FNH)

FNH is the most frequent hepatocellular lesion before hepatocellular adenomas (0.4–3% and 0.04%, respectively) [4, 18] and the second most frequent solid benign lesion in the liver after hemangiomas. Mainly found in women, with a ratio of 9/1, FNHs may be identified in all ages but usually occur between 30 and 40 years of age

(80–95% of cases). They are usually asymptomatic and discovered incidentally or during exploration for non-specific symptoms such as abdominal pain or discomfort. They are always benign. Blood liver tests are normal in more than half of the cases, and the only biological abnormalities that may be found are elevated gamma-glutamyl transpeptidase and alkaline phosphatases [19].

The diagnosis of FNH is based on a combination of features, none of which are specific alone. There are five major criteria to obtain a diagnosis [20]:

(a) Attenuation/signal intensity similar to that of the surrounding liver, resulting in a nearly isointense signal on both T1- and T2-weighted images [21, 22].
(b) Homogeneity.
(c) Strong enhancement during the arterial phase without wash-out [22–24]. Lesions show iso- or slight hyperattenuation/signal intensity on portal venous and delayed phase images [21, 22, 25].
(d) Presence of a central scar corresponding to a collection of blood vessels, bile ducts, surrounded by inflammatory cells, encased by a fibrous stroma. This is found on MR imaging in 80% of the cases [24, 25]. The central scar is typically hypointense on precontrast T1-weighted MR images and strongly hyperintense on T2-weighted images (78–84%) [26]. It gradually enhances to become hyperintense on delayed phase contrast-enhanced T1-weighted MR images using extracellular contrast agents due to the accumulation of the contrast medium in the extracellular space of fibrotic tissue [21, 22, 27].
(e) Absence of a capsule (± lobulated aspect).

All these signs must be clearly present to confirm the diagnosis because this combination is highly specific (98%) (Fig. 2.3) [19]. However, the sensitivity of these signs is lower (70%) [19]. It is important to note that these criteria should be applied in the absence of chronic liver disease, extrahepatic cancer, or abnormal liver tests.

Most (>90%) FNHs are iso- or hyperintense during the hepatobiliary phase due to the ability of FNH cells to take up both gadoxetic acid or gadobenate dimeglumine and transport them across the sinusoidal membrane into the primary bile ductules. If the central scar is not visible, hyperintensity is homogeneous during the hepatobiliary phase. A central scar is observed in 60–80% of the cases during this phase [28] and is seen as a central, hypointense area surrounded by the hyperintense signal of the lesion. There may be a slightly heterogeneous appearance in the presence of hypointense fibrous septa. Finally, FNH may have a hyperintense rim-like appearance [29].

On diffusion-weighted images, most FNHs show mild signal hyperintensity on high *b*-value images, with a slightly lower apparent diffusion coefficient (ADC) than the surrounding parenchyma (the ADC ratio (lesion/liver) is less than 15% in most FNHs) (Fig. 2.3). These results may mimic other focal liver lesions, including malignancy [30]. Thus, the signal intensity of DW images is not one of the diagnostic features of FNH.

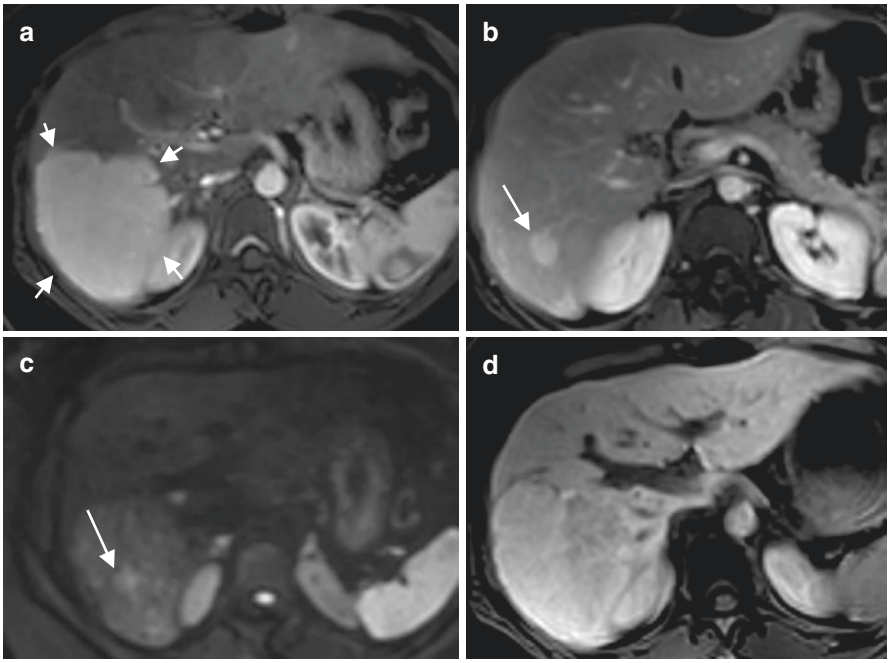

Fig. 2.3 MR imaging of a typical FNH in a 34-year-old woman. (**a**) The lesion shows homogeneous and marked enhancement on arterial phase images (arrows), with a central scar enhancing on delayed imaging (arrow in **b**). On diffusion-weighted images (**c**), the lesion shows mild signal hyperintensity, with higher signal intensity of the central scar (arrow in C). On hepatobiliary phase images (**d**), the lesion shows signal hyperintensity consistent with contrast uptake and retention

2.3.2 Hepatocellular Adenomas

Like FNH, HCAs are a benign proliferation of hepatocytes, with a prevalence in the general population of 0.01–0.004% [4]. They are more frequent in women than in men (ratio 9:1) and involve young women taking oral contraception (OC) in 85% of the cases. The risk of developing an HCA increases with the duration and the estrogen content of OC [31]. HCAs can be associated with other diseases such as diabetes (MODY 3), glycogenosis, and metabolic syndrome or non-alcoholic steatohepatitis [31–33].

Although patients with HCA can present with symptoms, most (80%) are asymptomatic [31, 34]. Nevertheless, HCAs can be revealed by acute abdominal pain due to intratumoral bleeding. Large HCAs may cause a sensation of right upper quadrant fullness or discomfort. Blood liver tests are abnormal in two third of cases and any abnormalities concern cholestatic enzymes (2–10 N) and less frequently transaminases (2–8 N) [31, 34].

HCAs have been classified into several subtypes according to their mutations, each with a different phenotypic expression on pathology and imaging, especially MR imaging:

- *HNF1-α inactivated HCAs* corresponding to 25–35% of all HCAs [34–36]. A biallelic mutation in activating the *TCF1* gene is the main characteristic of this group. This gene codes for HNF1-α, a tumor suppressor. HCAs with TCF1 mutations are diffusely steatotic (>60%) due to increased fatty acid synthesis and impaired transport of fatty acids, resulting in excessive intratumoral lipid accumulation. Inflammatory infiltration and cytological abnormalities are rare. These HCAs are more frequent in women than other subtypes (94–100%) and are quite often multiple [31, 34–36]. Lesions show a diffuse and homogeneous signal dropout on chemical shift in T1-weighted sequences (93%) [37, 38]. This feature has a sensitivity of 87–91% and a specificity of 89–100% [37, 38] (Fig. 2.4).
- *Inflammatory HCAs* are the most common (45–55%) subtype of HCAs [31, 34–36], corresponding to the entity initially described as telangiectatic FNH [39].

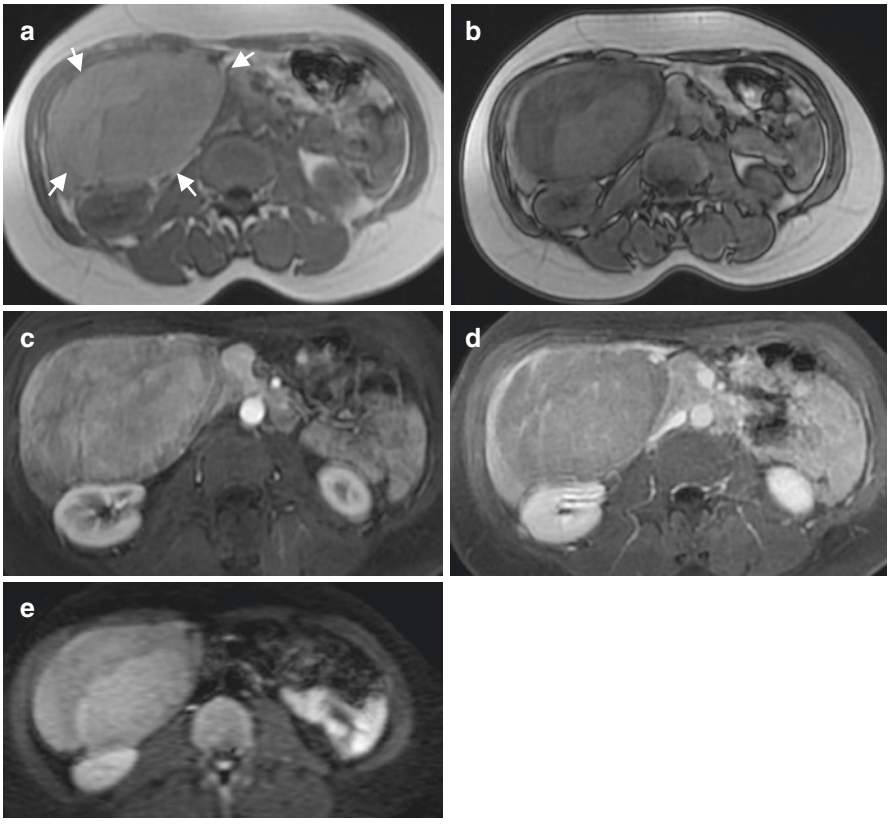

Fig. 2.4 MR imaging aspect of a HNF1a inactivated hepatocellular adenoma in a 41-year-old woman. (**a**, **b**) The lesion is located in the right liver with homogeneous slight hyperintensity on T1 (arrows in **a**) and dramatic signal dropout on chemical shift sequence, (**c**) moderate and (**d**) heterogeneous arterial enhancement with portal and delayed wash out. The lesion is well-delineated. On diffusion-weighted images (e), the lesion shows areas of moderately high signal intensity. The signal intensity is lower by the saturation of fat signal

IL6ST gene mutations have been found. This gene codes for the oncogene gp130. Telangiectatic/inflammatory HCA is composed of inflammatory infiltrates, sinusoidal dilatation, and dystrophic vessels without fibrosis. Cellular atypia and intratumoral steatosis may be present and substantial. Inflammatory HCAs are associated with obesity, hepatic steatosis (40%), and increased serum levels of acute inflammatory markers such as gamma-glutamyl transferase, CRP, SAA [40]. These tumors tend to bleed (one third of cases). A few tumors present an additional β-catenin activation (<10%). Tumoral transformation may be observed in the presence or absence of β-catenin activation in about 11% of cases [31, 41]. MR imaging shows a strong hyperintense signal on T2-weighted images (100%) with a variable iso- to hyperintense signal on T1-weighted sequences. Hyperintensity persists on fat-suppressed and -opposed phase sequences. A sensitivity of 85.2–88.4% and a specificity of 87.5–100% can be obtained by combining two imaging findings (markedly hyperintense signal on T2-weightedsequences and persistent enhancement during the delayed phase) [37, 38] (Fig. 2.5).

- *β-Catenin mutated HCA is* characterized by somatic mutations of the *CTNNB1* gene inhibiting β-catenin phosphorylation. This subtype corresponds to 8–12% of all HCAs [3, 12, 26, 42] and is present in a significantly higher percentage of men than other groups of HCAs (almost 40%) [34, 36]. The main pathological feature is the presence of numerous cytological abnormalities. These HCAs are not steatotic or inflammatory. This subtype has the greatest risk of malignant transformation. These tumors share findings of hepatocellular tumors (mainly arterial enhancement and portal or delayed washout) and may have

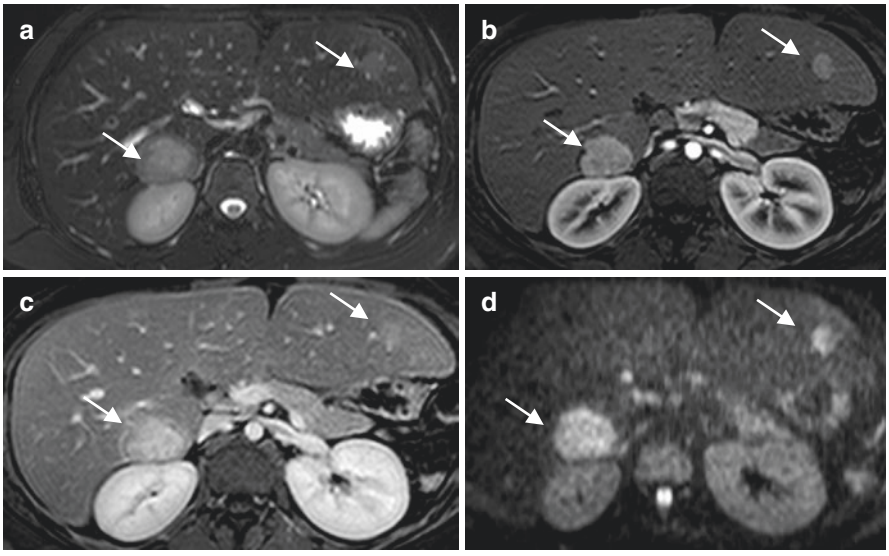

Fig. 2.5 MR imaging aspect of inflammatory hepatocellular adenomas in a 22-year-old woman. (**a**) Lesions show strong hyperintensity on T2-weighted images (arrows), (**b**) homogeneous and marked arterial enhancement with delayed contrast retention (**c**). On diffusion-weighted images (**d**), lesion showed moderate to high signal intensity

heterogeneous content. Imaging cannot reliably identify this entity or differentiate it from HCC.

- *Sonic hedgehog HCA* was recently individualized [34]. This previously considered unclassifiable subtype may account for 4% of all HCAs. Mutations are due to small-sized somatic deletions of INHBE leading to INHBE-GLI1 fusion. This subtype has not been characterized by imaging. It may be more prone to hemorrhage.
- *Other HCAs*, with no associated mutations. These lesions do not have specific imaging features and represent 5–11% of all HCAs [2, 8, 19, 35]. Once again, they have common findings with hepatocellular tumors and cannot be differentiated from HCC.

On diffusion-weighted images, *most* HCAs show mild signal hyperintensity on high *b*-value images, although more than 40% of HNF1-α mutated HCAs are isointense due to the fat suppression on DW sequences [30]. The apparent diffusion coefficient (ADC) is slightly lower than the surrounding parenchyma, thus diffusion-weighted imaging cannot be used to differentiate HCA from other focal liver lesions [30]. Interestingly, the mean ADC value of FNHs is significantly higher than that of HCAs [30]. No significant difference has been found in ADC values among HCA subtypes.

2.3.3 Regenerative Process—Nodular Regenerative Hyperplasia

FNH-like lesions are similar to FNH on pathology and are observed in patients with vascular liver diseases such as Budd–Chiari syndrome, hereditary hemorrhagic telangiectasia, and congenital hepatic fibrosis [43]. They are probably less frequent in patients with agenesis of the portal vein, portosystemic shunts, or portal cavernoma [44, 45]. The common element of all these conditions is a decrease in portal flow with partial compensation by an increase in arterial flow. FNH-like lesions are often multiple and small (typically less than 2 cm). At imaging, they are very similar to FNH but are frequently hyperintense on T1-weighted and hypointense on T2-weighted sequences in congestive livers [43].

On diffusion-weighted images the appearance is close to that of FNH.

Nodular regenerative hyperplasia is a diffuse disorder of the parenchymal organization resulting in a benign, diffuse, micronodular transformation of the liver. It is a distinct disease entity characterized by diffuse involvement of the liver with nodules composed of hyperplastic hepatocytes, which should not be confused with the regenerative nodules of cirrhosis or FNH. Nodules are usually very small (2–3 mm) and develop next to a portal tract, with centrilobular atrophy. Nodular regenerative hyperplasia is observed in myeloproliferative disorders, lymphoproliferative disorders, chronic vascular disorders, rheumatological and collagen vascular diseases (rheumatoid arthritis, Felty's syndrome, polyarteritis nodosa, amyloidosis, and primary biliary cirrhosis), solid organ transplantation (renal and liver transplantation), HIV patients, and following the use of steroids or chemotherapeutic agents.

There are three main presentations on imaging [46]: (1) frequently, unremarkable imaging; (2) portal hypertension without cirrhosis or focal liver lesions; (3)

multiple liver nodules with or without portal hypertension to be distinguished from other hepatocellular tumors. Nodules are small, and they enhance during the arterial phase without washout. They often appear hyperintense on T1-weighted images and iso- or hypointense compared to the normal liver on T2-weighted images [47–49].

On diffusion-weighted images, only the latter presentation shows nodules with mild hyperintense signals on high *b*-value diffusion-weighted images, with a similar or slightly lower mean apparent diffusion coefficient (ADC) than the surrounding parenchyma.

2.3.4 Inflammatory Pseudotumor

Inflammatory pseudotumors are rare, benign tumors usually found in the lung and which can mimic a malignant tumor in the liver. Inflammatory pseudotumors of the liver are reactional fibroblastic proliferations that may be fibrotic with infiltration by inflammatory cells. They correspond to various clinical entities with different morphological and clinical presentations. They are three times more frequent in men than in women and are mostly observed in young adults (mean age at diagnosis is 35 years) [50].

Three different forms can be described according to clinical and morphological presentations [51]:

(a) *Inflammatory form* is revealed by abdominal pain and fever: an inflammatory syndrome is found in half of the patients. At imaging, the lesion is single, ill-defined, large, heterogeneous and hypervascular. It is hypointense on T1-weighted and iso- or hyperintense on T2-weighted sequences (Fig. 2.6).

On diffusion-weighted images, the lesion shows moderate signal intensity on high *b*-value images.

(b) *Encapsulated form also called solitary necrotic nodule of the liver* [52]: This small lesion is discovered incidentally. There is no inflammatory syndrome. On MR imaging, the lesion is well limited, hypointense on T1-weighted images, isointense on T2-weighted images, and surrounded by a capsule that enhances during the delayed phase.

On diffusion-weighted images, signal intensity is mild to absent on high *b*-value images and sometimes high ADC values, corresponding to necrosis.

(c) *Infiltrating periportal form*: frequently revealed by jaundice. MR imaging shows an ill-defined periportal lesion, that is hypo-intense on T1- and moderately hyper-intense on T2-weighted sequences with upstream dilated bile ducts [53]. There is a progressive enhancement on contrast-enhanced sequences. Lymphadenopathy can be observed.

On diffusion-weighted images, periportal inflammatory pseudotumors appear hyperintense on high *b*-value images, mimicking cholangiocarcinoma.

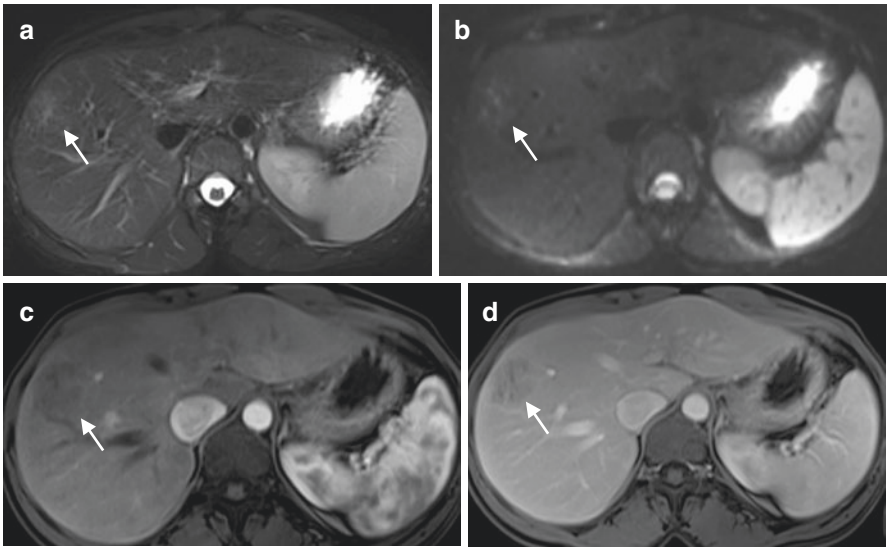

Fig. 2.6 MR imaging of an inflammatory pseudotumor in a 43-year-old woman. The lesion (arrow) shows iso- to high signal intensity on T2-weighted image (**a**) and diffusion-weighted images (**b**) when compared to the surrounding liver. On contrast-enhanced images, the lesion is hypointense and heterogeneous on arterial phase (**c**) with mild heterogeneous washout on portal phase (**d**)

2.3.5 Biliary Cystadenomas

Biliary cystadenomas are slow-growing tumors, representing less than 5% of intrahepatic cystic lesions of biliary origin. Although they are generally intrahepatic (85%), extrahepatic lesions have been reported (extrahepatic bile ducts, gallbladder). Women are mainly affected (8 times out of 10) over 40 years of age. Symptoms are nonspecific and mainly due to the effect of the mass. On MR imaging, these lesions are similar to simple hepatic cysts and appear as large cystic masses with variable signal intensity on the T1- and T2-weighted sequences, depending on the protein concentration. On contrast-enhanced sequences, the presence of enhanced mural nodules and/or inner septa are highly suggestive of the diagnosis [54, 55].

On diffusion-weighted images, the cystic portions show a major drop in signal intensity on high *b*-value images, but mural nodules may be visible as high signals. In case of hemorrhage, signal intensity appears heterogeneous and should not be mistaken with true viable portions.

2.3.6 Focal Fibrosis

Fibrosis deposition is heterogeneous in cirrhotic livers. Some patients may show focal areas of fibrosis called" focal confluent fibrosis". This appears as a focal, wedge-shaped area, radiating from the porta hepatis, that is widest at the capsular

surface with associated capsular retraction, and frequently located in segments IV, VII, or VIII [56]. It can mimic infiltrative HCC because both have ill-defined margins with increased enhancement of fibrosis during the arterial phase. Differentiation from HCC is based on progressive enhancement from the arterial to delayed phase using extracellular contrast agents, due to contrast accumulation in the extracellular compartment, while HCC typically shows washout. On gadoxetic acid-enhanced MR imaging, fibrosis may be more difficult to differentiate from HCC because both are usually hypointense on transitional phase and hepatobiliary phase images compared to the surrounding liver due to the absence of hepatocytes [57].

On diffusion-weighted images, focal fibrosis has the same appearance as fibrosis in general and is mild to moderately hyperintense on high *b*-value images, reflecting restricted diffusion with a lower ADC than the surrounding liver. DW images are helpful to characterize fibrosis, but not to differentiate from other lesions, especially HCC.

2.4 Lesions Not Visible on High *b*-Value Images

2.4.1 Hepatic Cysts

Simple hepatic cysts are benign cystic formations lined by biliary epithelium. They contain serous fluid and do not communicate with the biliary tree. They are usually asymptomatic and discovered incidentally. Ultrasound studies report a prevalence of 3–5% in the general population [58]. More recently, a CT study in adults reported a prevalence of 18% [59], with a higher prevalence in women (ratio 3:2). Simple cysts are solitary in around 70% of cases. The incidence and volume of cysts increase with age, thus large cysts are almost only found in women over 50 years of age. When large, they may be associated with nonspecific symptoms (abdominal pain, dyspepsia, increased abdominal perimeter, nausea, and rarely dyspnea). Blood liver tests are normal in most patients. Intra-cystic bleeding is the most frequent complication [60, 61]. Clinically, hemorrhage usually causes sudden pain in the right upper quadrant due to the increased volume of the cyst.

On MR imaging, cysts are homogeneous, markedly hypointense on T1-weighted and hyperintense on the T2-weighted images (identical to that of the gallbladder and the cerebrospinal fluid) (Fig. 2.7). Cysts do not enhance following gadolinium chelate administration. Hemorrhagic cysts are spontaneously hyperintense on T1- and T2-weighted MR images, with a possible fluid–fluid level [60] (Fig. 2.8). During acute hemorrhage, pericystic contrast uptake can be observed corresponding to the compressed liver parenchyma.

On diffusion-weighted images, the pure liquid content explains the absence of diffusion restriction, and the marked drop in signal on high *b*-value images [62]. Once again, hemorrhage results in cystic heterogeneity.

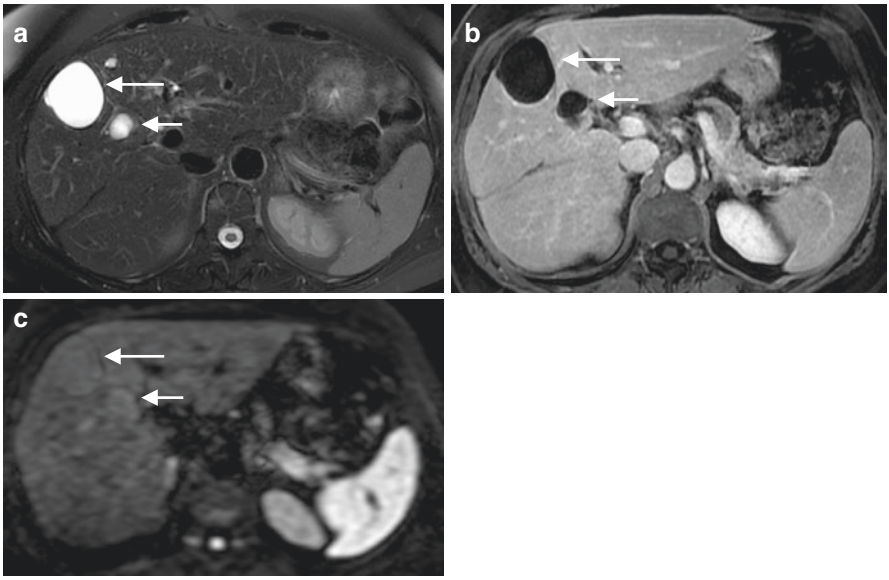

Fig. 2.7 MR imaging aspect of hepatic cysts in a 61-year-old man. Lesions appear markedly hyperintense on T2-weighed images (arrows in **a**), with homogeneous hypointensity on T1-weighted images with no contrast enhancement (**b**). Lesions are not visible on diffusion-weighted images (c, $b = 800$) due to their pure fluid content

2.4.2 Biliary Hamartoma

Also known as the Von Meyenburg complex, biliary hamartomas are a developmental anomaly of the small intrahepatic bile ducts composed of bile ductules, inflammatory cells, and fibrosis. Biliary hamartomas are easily recognizable on heavily T2-weighted MR images such as MRCP and are seen as multiple, small, strongly hyperintense lesions [63]. They do not communicate with bile ducts.

On *diffusion-weighted images*, there is a marked drop in signal on high *b*-value images because of the predominantly cystic structure.

2.4.3 Pseudotumors

2.4.3.1 Focal Steatosis or Focal Fatty Sparing

Steatosis is easily recognizable when it is diffuse. Diffuse steatosis with focal areas of sparing or focal areas of fatty deposition in an otherwise normal liver is more difficult. It is interesting to note that the posterior part of segment 4 is the most common location of uneven steatosis and focal sparing. The key imaging finding of focal steatosis is the signal dropout on opposed phase compared to in-phase T1-weighted GE sequences, while focal sparing shows lack of signal dropout in a fatty liver [64, 65].

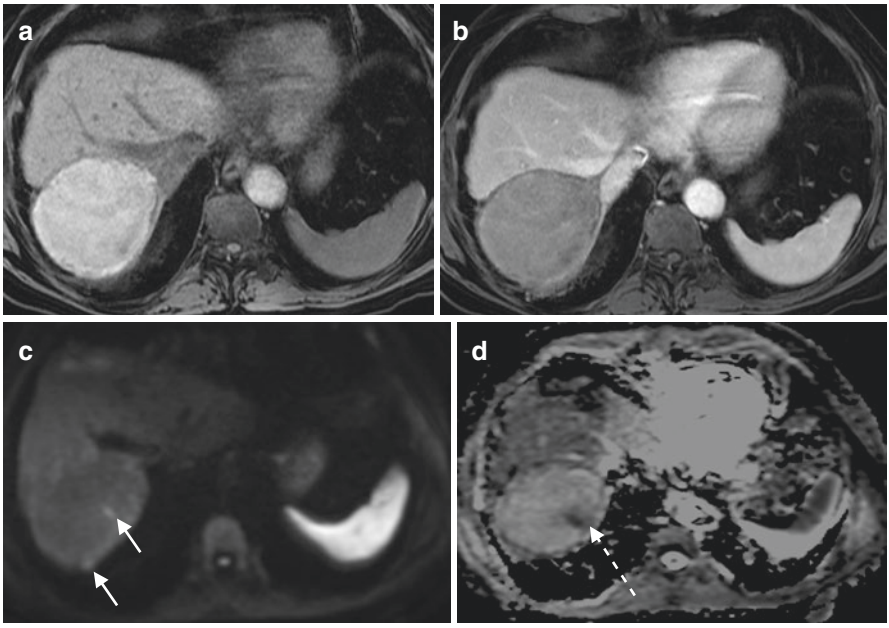

Fig. 2.8 MR imaging aspect of hepatic cysts with history of bleeding in a 73-year-old woman. Lesion appears markedly hyperintense on T1-weighed images (**a**), with no contrast enhancement (**b**). Lesion is isointense on diffusion-weighted images ($b = 800$) with focal hyperintensities (arrow in **c**). On ADC map (d), the lesion shows high ADC value, with lower value in the areas showing signal hyperintensity. This aspect corresponds to artifacts due to hemorrhagic depositions

On diffusion-weighted images, focal fatty sparing or focal fatty steatosis is usually not visible, allowing differentiation with liver tumors.

2.4.3.2 Arterio-Portal Shunts

Arterio-portal shunts are more frequent in patients with advanced fibrosis or cirrhosis due to the modified architecture of the liver parenchyma. These peripheral and triangular shaped lesions are only visible on contrast-enhanced CT and MR images (Fig. 2.9). After contrast administration, there is hyper-enhancement on arterial phase images due to local parenchymal filling of arterial blood. No washout or capsule can be identified on portal venous or delayed phase images. Importantly, they have no mass effect on vessels or bile ducts and are isointense to the surrounding liver parenchyma on hepatobiliary phase images using hepatobiliary MR contrast agents.

Arterio-portal shunts are not visible on *diffusion-weighted images*, which confirms that they are "pseudolesions."

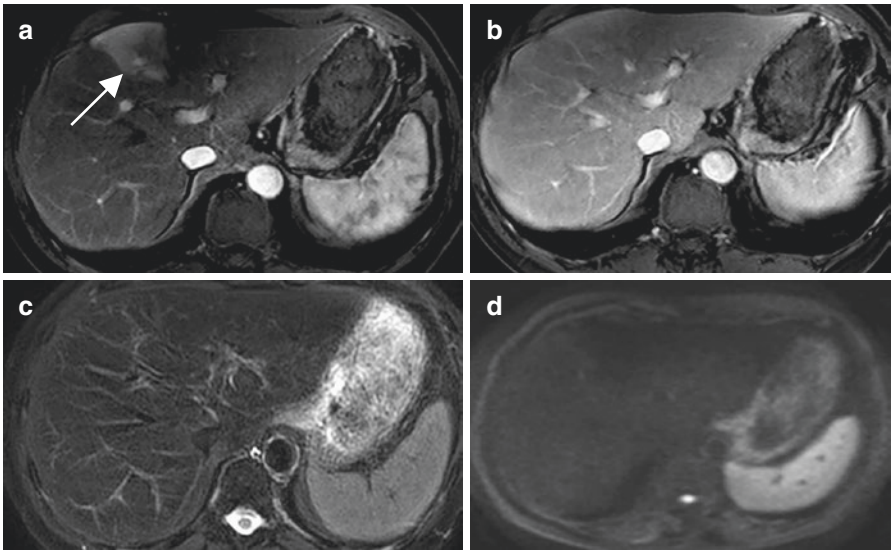

Fig. 2.9 MR imaging aspect of arterio-portal shunt in a 53-year-old woman. (**a**) The shunt appears as a triangular-shaped focal arterial enhancement in segment 4 (arrow) centered by the AP communication. The lesion is not visible on portal and delayed phase (**b**), T2-weighted images (**c**), and diffusion-weighted images (**d**)

2.5 Pragmatic Diagnostic Approach: Specific Contexts

2.5.1 Chronic Liver Disease

Several benign focal liver lesions may be identified in patients with cirrhosis. Some pre-date, and others are a direct consequence of the development of liver fibrosis. Cystic lesions (including hepatic and peribiliary cysts) are easy to differentiate from HCC in most patients. Solid lesions, especially when they hyper-enhance on arterial phase images, may be more challenging. In these cases, diffusion-weighted MR images may be very helpful for specific questions.

2.5.1.1 Ancillary Feature for the Differentiation Between Dysplastic Nodule and Early HCC

HCC is the last step of a complex, multi-step process called hepatocarcinogenesis [66] during which several molecular and histological changes lead to the gradual transformation of nonmalignant liver cells into HCC. When present, regenerative nodules are easy to diagnose because they are numerous and usually smaller than 10 mm. They typically appear isointense on T1- and T2-weighted and DW images and do not contain fat. Because these nodules lack neoangiogenesis, and

hepatocellular function is preserved, enhancement is similar to, or slightly lower than that of the surrounding liver parenchyma after extracellular contrast agent administration. Regenerative nodules appear iso- or hyperintense on hepatobiliary phase MR using hepatobiliary contrast agents compared to the surrounding liver; some may even be strongly hyperintense [67, 68].

Dysplastic nodules (DN) are more difficult to identify. Often multiple, they range from 1 to 15 mm. While low-grade DNs and regenerative nodules share common features, some high-grade DNs resemble early or well-differentiated HCCs and have typical features of HCC, such as intracellular fat, hyper-enhancement on arterial phase images, or even hypointensity on hepatobiliary phase images due to loss of OATP expression. However, there is usually no washout.

Diffusion-weighted images is helpful to differentiate DNs from HCC since most hypervascular high-grade DNs do not show signal hyperintensity on high *b*-value images, while most HCC do [69, 70] (Fig. 2.10).

2.5.1.2 Diagnosis of Cysts and Peribiliary Cysts

The features of hepatic cysts are similar to those in cirrhotic and non-cirrhotic livers. Peribiliary cysts are cystic lesions arising from the extramural glands located in the periductal connective tissue. In non-cirrhotic livers, these glands are not visible on imaging. In cirrhotic livers, the accumulation of fibrosis encases the glands, leading to an increase in size. They are typically located along the large bile ducts, more often left than right, and on both sides of the intrahepatic portal venous branches. This feature differentiates them from bile duct dilatation, which is located on one side of the portal venous branches only [71]. Another important finding is the lack of upstream biliary dilatation. Often numerous, the size and shapes of cysts may vary, but they share common features with simple cysts. They do not communicate with the bile ducts (Fig. 2.11).

Diffusion-weighted images help confirm the cystic nature of lesions, with no visibility on high *b*-value images and high ADC values.

2.5.1.3 Differentiating Hemangiomas from HCC

Hemangiomas have been reported to be less frequent and smaller in patients with cirrhosis [72]. Brancatelli et al. have also reported a smaller size due to the development of cirrhosis [73]. Nevertheless, imaging features are similar to those of hemangiomas observed in patients without cirrhosis. We analyzed more than 230 liver hemangiomas in patients with and without cirrhosis and showed no difference in enhancement patterns or signal intensity on T2-weighted images (fat-suppressed fast spin-echo and single-shot) [72]. Thus, differentiating hemangiomas from HCC is easy in most patients with cirrhosis. It can be more difficult when hemangiomas show flash-filling enhancement. In these cases, a strong T2 signal, lesion enhancement parallel to that of the aorta, and persistent enhancement on delayed phase imaging using extracellular contrast agents are key findings. However, two pitfalls

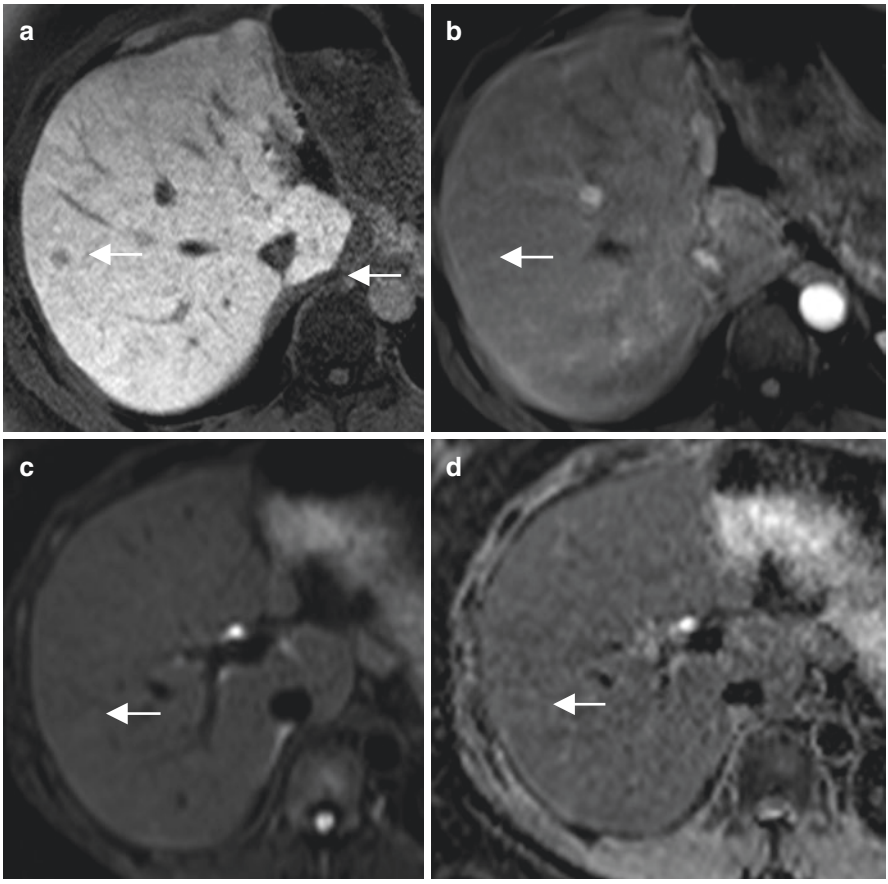

Fig. 2.10 Dysplastic nodule in a 55-year-old woman with HIV infection and HCV-related cirrhosis with history of HCC treated by left hepatectomy. Follow-up MR imaging showed a centimetric nodule showing hypointensity on hepatobiliary phase images (arrow in **a**) without contrast enhancement on arterial phase (b), corresponding to a "hypovascular hypointense nodule." This was consistent with either dysplastic nodule or early HCC. The lesion was not visible on diffusion-weighted images (**c**) or the ADC map (**d**), suggesting the dysplastic nature of the lesion. This was confirmed by percutaneous US-guided biopsy

should be kept in mind. First, small HCCs may have atypical imaging features and lack washout. Also, on gadoxetic acid-enhanced MR imaging, flash-filling hemangiomas appear hypointense on transitional phase images [9] (referred to as "pseudo washout") and markedly hypointense on hepatobiliary phase images [74].

Diffusion-weighted MR sequences is helpful to diagnose difficult cases of hemangioma in cirrhosis by showing high ADC values compared to the surrounding liver (Fig. 2.12).

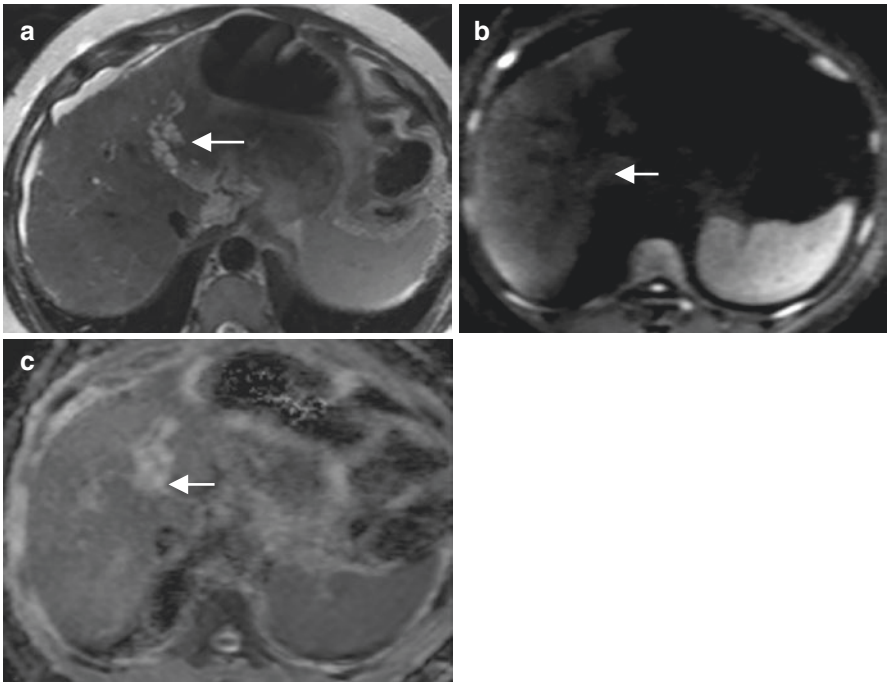

Fig. 2.11 MR imaging aspect of peribiliary cysts in a 49-year-old man with HCV-related cirrhosis. Portal shunt in a 53-year-old female. Lesions appear markedly hyperintense on T2-weighed images (arrows in **a**) along the left portal branch. Lesions are not visible on diffusion-weighted images ($b = 800$) (**b**) and have high ADC values (**c**) due to their pure fluid content

2.5.1.4 Increase the Level of Confidence for the Diagnosis of Intrahepatic Shunts and Transient Perfusion Disorders

As stated above, arterio-portal shunts show hyper-enhancement on arterial-phase images, which could mimic HCC.

They are not visible on *diffusion-weighted images*, which confirms that they are "pseudolesions."

2.5.2 Oncologic Patients

Hepato-specific MR contrast agents and especially gadoxetic acid-enhanced MR imaging during the hepatobiliary phase are now recognized as the best technique for the detection of liver metastases [42].However, due to the rapid entry of gadoxetic acid into hepatocytes, the traditional MR imaging features of liver tumors are modified, especially during the transitional phase (3–5 min after injection). Most lesions that classically accumulate contrast on delayed phase with extracellular contrast

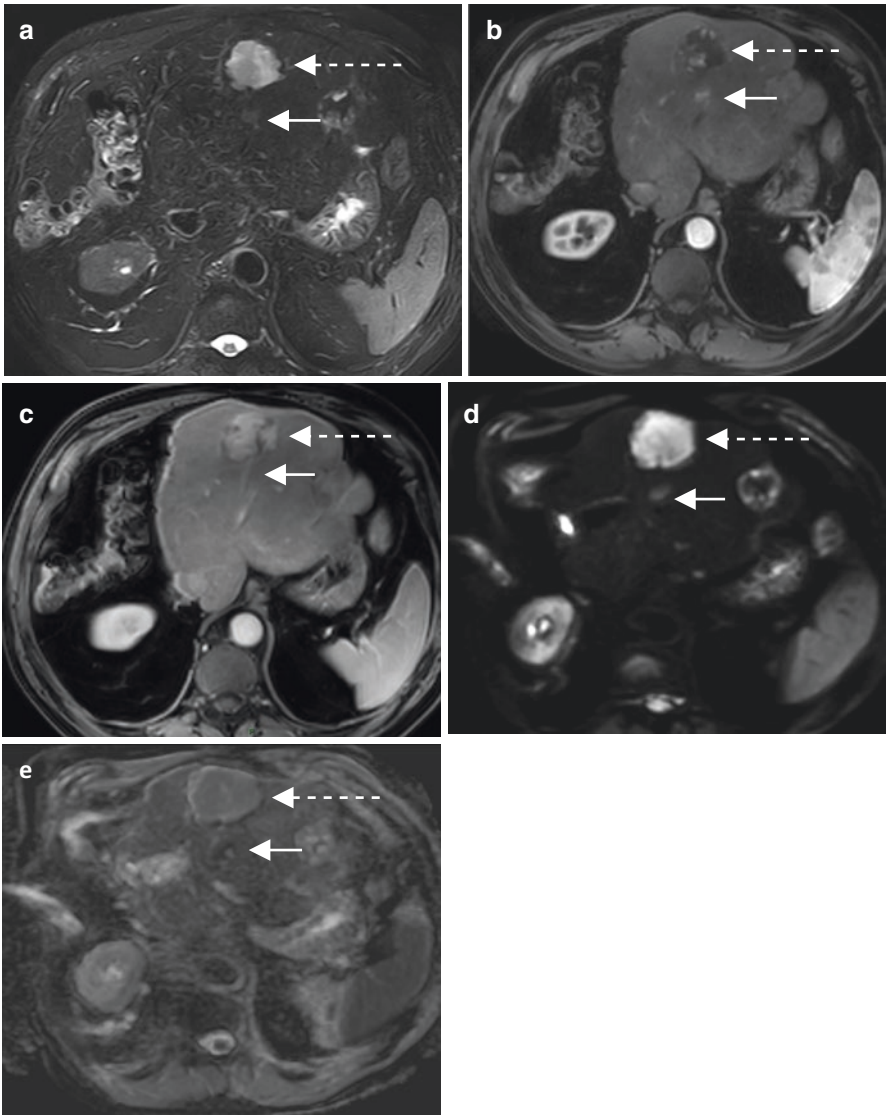

Fig. 2.12 Typical hemangioma (dashed arrows) and hepatocellular carcinoma (arrow) in a 71-year-old male with history of left hepatectomy for hepatocellular carcinoma explored by MR imaging. Hemangioma showed high signal intensity on T2-weighted images (**a**) with peripheral globular enhancement on arterial phase (**b**) with progressive filling on portal and delayed phase images (**c**). HCC showed mild signal hyperintensity on T2-weighted images (**a**), enhancement on arterial phase (**b**), and appeared iso-intense on delayed phase images (**c**). On diffusion-weighted images (d, $b = 800$), both showed signal hyperintensity, but signal of the hemangioma was higher than that of the HCC. Yet, on ADC map (e), HCC had low values while hemangioma has high values (T2-shine-through effect), allowing for the differentiation between both

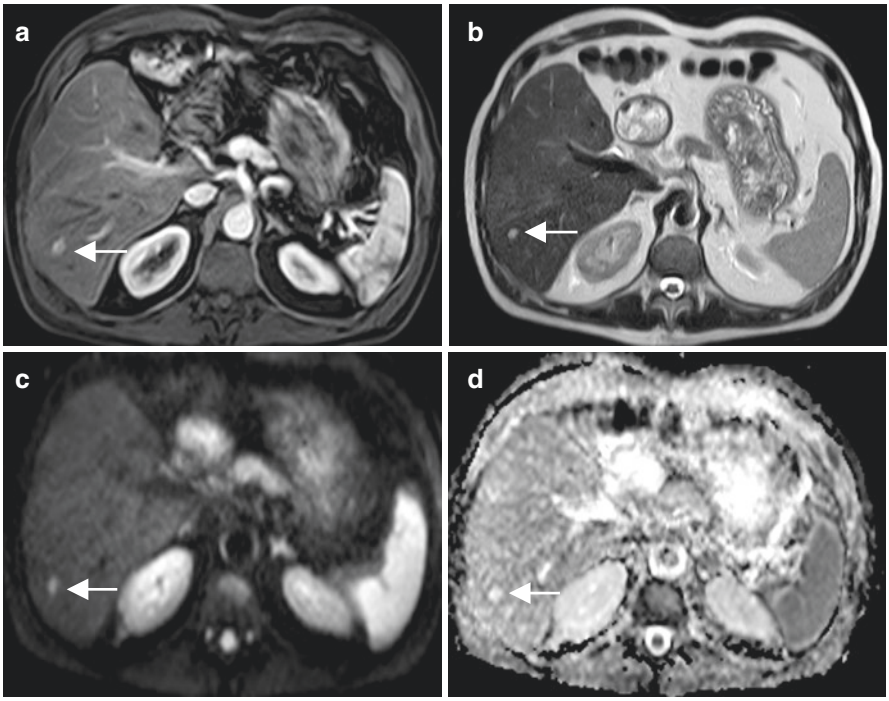

Fig. 2.13 Differentiation between metastasis and hemangioma in a 46-year-old man with resected pancreatic neuroendocrine tumor. The lesion (arrow) showed marked enhancement on arterial phase images (**a**) with high signal intensity on T2-weighted images (**b**). Both could indicate liver metastasis or flash-filling hemangioma. On diffusion-weighted images (c, b = 800), the lesion appears hyperintense, and differentiation cannot be made. ADC map (d) shows high value in the lesion, thus confirming the diagnosis of hemangioma, since metastasis would have shown low ADC values

agents—including benign lesions—are hypointense during the transitional and hepatobiliary phases. Therefore, the differentiation between metastases and preexisting benign lesions may be challenging and may result in an overdiagnosis of metastases. DW imaging is helpful to improve differentiation of both (Fig. 2.13).

Diffusion-weighted images are helpful mainly for:

- Diagnosis of hemangiomas with high ADC values, despite a frequent T2 shine-through effect [10]. Nevertheless, the differential diagnosis can be difficult for very tiny lesions or in mucinous metastases; the choice of the most suitable contrast agent is extremely important to avoid a misdiagnosis [75].
- Diagnosis of focal fat deposition or focal fat sparing, since these pseudolesions do not appear on DW images with high *b*-values.

2.6 Conclusion

DW imaging is rarely used for the detection of benign liver lesions but can be helpful for tumor characterization. We suggest a pragmatic approach based on signal intensity in high *b*-value images (absence of visualization, moderate signal intensity, or marked signal intensity)and on ADC maps (high or low values), to be interpreted according the specific clinical context of each lesion. This should improve the diagnostic evaluation of each lesion and help make differential diagnoses including primary and secondary malignancies. Finally, careful interpretation of all other available sequences—and imaging by other techniques—is extremely important to overcome the difficulties of diagnosis.

Conflict of Interests None of the authors has any conflict of interest or financial ties to disclose.

References

1. Semelka RC, Sofka CM. Hepatic hemangiomas. Magn Reson Imaging Clin N Am. 1997;5(2):241–53.
2. Trotter JF, Everson GT. Benign focal lesions of the liver. Clin Liver Dis. 2001;5(1):17–42, v.
3. Biecker E, Fischer HP, Strunk H, Sauerbruch T. Benign hepatic tumours. Z Gastroenterol. 2003;41(2):191–200.
4. European Association for the Study of the L. EASL Clinical Practice Guidelines on the management of benign liver tumours. J Hepatol. 2016;65(2):386–98.
5. Itai Y, Ohtomo K, Furui S, Yamauchi T, Minami M, Yashiro N. Noninvasive diagnosis of small cavernous hemangioma of the liver: advantage of MRI. AJR Am J Roentgenol. 1985;145(6):1195–9.
6. Stark DD, Felder RC, Wittenberg J, et al. Magnetic resonance imaging of cavernous hemangioma of the liver: tissue-specific characterization. AJR Am J Roentgenol. 1985;145(2):213–22.
7. Semelka RC, Brown ED, Ascher SM, et al. Hepatic hemangiomas: a multi-institutional study of appearance on T2-weighted and serial gadolinium-enhanced gradient-echo MR images. Radiology. 1994;192(2):401–6.
8. Hanafusa K, Ohashi I, Himeno Y, Suzuki S, Shibuya H. Hepatic hemangioma: findings with two-phase CT. Radiology. 1995;196(2):465–9.
9. Kim B, Byun JH, Kim HJ, et al. Enhancement patterns and pseudo-washout of hepatic haemangiomas on gadoxetate disodium-enhanced liver MRI. Eur Radiol. 2016;26(1):191–8.
10. Duran R, Ronot M, Kerbaol A, Van Beers B, Vilgrain V. Hepatic hemangiomas: factors associated with T2 shine-through effect on diffusion-weighted MR sequences. Eur J Radiol. 2014;83(3):468–78.
11. Hooper LD, Mergo PJ, Ros PR. Multiple hepatorenal angiomyolipomas: diagnosis with fat suppression, gadolinium-enhanced MRI. Abdom Imaging. 1994;19(6):549–51.
12. Cai PQ, Wu YP, Xie CM, Zhang WD, Han R, Wu PH. Hepatic angiomyolipoma: CT and MR imaging findings with clinical-pathologic comparison. Abdom Imaging. 2013;38(3):482–9.
13. Yoshimura H, Murakami T, Kim T, et al. Angiomyolipoma of the liver with least amount of fat component: imaging features of CT, MR, and angiography. Abdom Imaging. 2002;27(2):184–7.

14. Kim R, Lee JM, Joo I, et al. Differentiation of lipid poor angiomyolipoma from hepatocellular carcinoma on gadoxetic acid-enhanced liver MR imaging. Abdom Imaging. 2015;40(3):531–41.
15. Nath DS, Rutzick AD, Sielaff TD. Solitary fibrous tumor of the liver. AJR Am J Roentgenol. 2006;187(2):W187–90.
16. Moser T, Nogueira TS, Neuville A, et al. Delayed enhancement pattern in a localized fibrous tumor of the liver. AJR Am J Roentgenol. 2005;184(5):1578–80.
17. Kandpal H, Sharma R, Gupta SD, Kumar A. Solitary fibrous tumour of the liver: a rare imaging diagnosis using MRI and diffusion-weighted imaging. Br J Radiol. 2008;81(972):e282–6.
18. Vilgrain V, Flejou JF, Arrive L, et al. Focal nodular hyperplasia of the liver: MR imaging and pathologic correlation in 37 patients. Radiology. 1992;184(3):699–703.
19. Cherqui D, Rahmouni A, Charlotte F, et al. Management of focal nodular hyperplasia and hepatocellular adenoma in young women: a series of 41 patients with clinical, radiological, and pathological correlations. Hepatology. 1995;22(6):1674–81.
20. Burgio MD, Ronot M, Salvaggio G, Vilgrain V, Brancatelli G. Imaging of hepatic focal nodular hyperplasia: pictorial review and diagnostic strategy. Semin Ultrasound CT MR. 2016;37(6):511–24.
21. Marin D, Brancatelli G, Federle MP, et al. Focal nodular hyperplasia: typical and atypical MRI findings with emphasis on the use of contrast media. Clin Radiol. 2008;63(5):577–85.
22. Brancatelli G, Federle MP, Grazioli L, Blachar A, Peterson MS, Thaete L. Focal nodular hyperplasia: CT findings with emphasis on multiphasic helical CT in 78 patients. Radiology. 2001;219(1):61–8.
23. Shamsi K, De Schepper A, Degryse H, Deckers F. Focal nodular hyperplasia of the liver: radiologic findings. Abdom Imaging. 1993;18(1):32–8.
24. Mortele KJ, Praet M, Van Vlierberghe H, Kunnen M, Ros PR. CT and MR imaging findings in focal nodular hyperplasia of the liver: radiologic-pathologic correlation. AJR Am J Roentgenol. 2000;175(3):687–92.
25. Hussain SM, Terkivatan T, Zondervan PE, et al. Focal nodular hyperplasia: findings at state-of-the-art MR imaging, US, CT, and pathologic analysis. Radiographics. 2004;24(1):3–17; discussion 18–19.
26. Kehagias D, Moulopoulos L, Antoniou A, et al. Focal nodular hyperplasia: imaging findings. Eur Radiol. 2001;11(2):202–12.
27. Grazioli L, Morana G, Federle MP, et al. Focal nodular hyperplasia: morphologic and functional information from MR imaging with gadobenate dimeglumine. Radiology. 2001;221(3):731–9.
28. Gupta RT, Iseman CM, Leyendecker JR, Shyknevsky I, Merkle EM, Taouli B. Diagnosis of focal nodular hyperplasia with MRI: multicenter retrospective study comparing gadobenate dimeglumine to gadoxetate disodium. AJR Am J Roentgenol. 2012;199(1):35–43.
29. Fujiwara H, Sekine S, Onaya H, Shimada K, Mikata R, Arai Y. Ring-like enhancement of focal nodular hyperplasia with hepatobiliary-phase Gd-EOB-DTPA-enhanced magnetic resonance imaging: radiological-pathological correlation. Jpn J Radiol. 2011;29(10):739–43.
30. Agnello F, Ronot M, Valla DC, Sinkus R, Van Beers BE, Vilgrain V. High-b-value diffusion-weighted MR imaging of benign hepatocellular lesions: quantitative and qualitative analysis. Radiology. 2012;262(2):511–9.
31. Dokmak S, Paradis V, Vilgrain V, et al. A single-center surgical experience of 122 patients with single and multiple hepatocellular adenomas. Gastroenterology. 2009;137(5):1698–705.
32. Watkins J, Balabaud C, Bioulac-Sage P, Sharma D, Dhillon A. Hepatocellular adenoma in advanced-stage fatty liver disease. Eur J Gastroenterol Hepatol. 2009;21(8):932–6.
33. Brunt EM, Wolverson MK, Di Bisceglie AM. Benign hepatocellular tumors (adenomatosis) in nonalcoholic steatohepatitis: a case report. Semin Liver Dis. 2005;25(2):230–6.
34. Nault JC, Couchy G, Balabaud C, et al. Molecular classification of hepatocellular adenoma associates with risk factors, bleeding, and malignant transformation. Gastroenterology. 2017;152(4):880–94, e886.
35. Bioulac-Sage P, Balabaud C, Bedossa P, et al. Pathological diagnosis of liver cell adenoma and focal nodular hyperplasia: Bordeaux update. J Hepatol. 2007;46(3):521–7.

36. Zucman-Rossi J, Jeannot E, Nhieu JT, et al. Genotype-phenotype correlation in hepatocellular adenoma: new classification and relationship with HCC. Hepatology. 2006;43(3):515–24.
37. Laumonier H, Bioulac-Sage P, Laurent C, Zucman-Rossi J, Balabaud C, Trillaud H. Hepatocellular adenomas: magnetic resonance imaging features as a function of molecular pathological classification. Hepatology. 2008;48(3):808–18.
38. Ronot M, Bahrami S, Calderaro J, et al. Hepatocellular adenomas: accuracy of magnetic resonance imaging and liver biopsy in subtype classification. Hepatology. 2011;53(4):1182–91.
39. Paradis V, Benzekri A, Dargere D, et al. Telangiectatic focal nodular hyperplasia: a variant of hepatocellular adenoma. Gastroenterology. 2004;126(5):1323–9.
40. Paradis V, Champault A, Ronot M, et al. Telangiectatic adenoma: an entity associated with increased body mass index and inflammation. Hepatology. 2007;46(1):140–6.
41. Laurent A, Dokmak S, Nault JC, et al. European experience of 573 liver resections for hepatocellular adenoma: a cross-sectional study by the AFC-HCA-2013 study group. HPB (Oxford). 2016;18(9):748–55.
42. Vilgrain V, Esvan M, Ronot M, Caumont-Prim A, Aube C, Chatellier G. A meta-analysis of diffusion-weighted and gadoxetic acid-enhanced MR imaging for the detection of liver metastases. Eur Radiol. 2016;26(12):4595–615.
43. Vilgrain VRP-E, Paradis V, Ronot M. Benign and malignant hepatocellular lesions in patients with vascular liver disease. Clin Liver Dis. 2014;3(6):122–5.
44. Handra-Luca A, Paradis V, Vilgrain V, et al. Multiple mixed adenoma-focal nodular hyperplasia of the liver associated with spontaneous intrahepatic porto-systemic shunt: a new type of vascular malformation associated with the multiple focal nodular hyperplasia syndrome? Histopathology. 2006;48(3):309–11.
45. De Gaetano AM, Gui B, Macis G, Manfredi R, Di Stasi C. Congenital absence of the portal vein associated with focal nodular hyperplasia in the liver in an adult woman: imaging and review of the literature. Abdom Imaging. 2004;29(4):455–9.
46. Belghiti J, Cauchy F, Paradis V, Vilgrain V. Diagnosis and management of solid benign liver lesions. Nat Rev Gastroenterol Hepatol. 2014;11(12):737–49.
47. Clouet M, Boulay I, Boudiaf M, et al. Imaging features of nodular regenerative hyperplasia of the liver mimicking hepatic metastases. Abdom Imaging. 1999;24(3):258–61.
48. Casillas C, Marti-Bonmati L, Galant J. Pseudotumoral presentation of nodular regenerative hyperplasia of the liver: imaging in five patients including MR imaging. Eur Radiol. 1997;7(5):654–8.
49. Horita T, Tsutsumi A, Takeda T, et al. Significance of magnetic resonance imaging in the diagnosis of nodular regenerative hyperplasia of the liver complicated with systemic lupus erythematosus: a case report and review of the literature. Lupus. 2002;11(3):193–6.
50. Koea JB, Broadhurst GW, Rodgers MS, McCall JL. Inflammatory pseudotumor of the liver: demographics, diagnosis, and the case for nonoperative management. J Am Coll Surg. 2003;196(2):226–35.
51. Abbey-Toby A, Cazals-Hatem D, Colombat M, Belghiti J, Vilgrain V, Degott C. Inflammatory pseudo-tumor of the liver: is pre-operative diagnosis possible? Gastroenterol Clin Biol. 2003;27(10):883–90.
52. Fang J, Ma X, Yu D, Ma X, Xiang Y, Guo L. Specific imaging characteristic of solitary necrotic nodule of the liver: marked peripheral rim-like enhancement with internal hypointensity on longer delayed MRI. Eur Radiol. 2017;27(9):3563–73.
53. Venkataraman S, Semelka RC, Braga L, Danet IM, Woosley JT. Inflammatory myofibroblastic tumor of the hepatobiliary system: report of MR imaging appearance in four patients. Radiology. 2003;227(3):758–63.
54. Palacios E, Shannon M, Solomon C, Guzman M. Biliary cystadenoma: ultrasound, CT, and MRI. Gastrointest Radiol. 1990;15(4):313–6.
55. Qian LJ, Zhu J, Zhuang ZG, Xia Q, Liu Q, Xu JR. Spectrum of multilocular cystic hepatic lesions: CT and MR imaging findings with pathologic correlation. Radiographics. 2013;33(5):1419–33.

56. Brancatelli G, Baron RL, Federle MP, Sparacia G, Pealer K. Focal confluent fibrosis in cirrhotic liver: natural history studied with serial CT. AJR Am J Roentgenol. 2009;192(5):1341–7.
57. Husarik DB, Gupta RT, Ringe KI, Boll DT, Merkle EM. Contrast enhanced liver MRI in patients with primary sclerosing cholangitis: inverse appearance of focal confluent fibrosis on delayed phase MR images with hepatocyte specific versus extracellular gadolinium based contrast agents. Acad Radiol. 2011;18(12):1549–54.
58. Gaines PA, Sampson MA. The prevalence and characterization of simple hepatic cysts by ultrasound examination. Br J Radiol. 1989;62(736):335–7.
59. Carrim ZI, Murchison JT. The prevalence of simple renal and hepatic cysts detected by spiral computed tomography. Clin Radiol. 2003;58(8):626–9.
60. Vilgrain V, Silbermann O, Benhamou JP, Nahum H. MR imaging in intracystic hemorrhage of simple hepatic cysts. Abdom Imaging. 1993;18(2):164–7.
61. Benzimra J, Derhy S, Rosmorduc O, Menu Y, Poupon R, Arrive L. Hepatobiliary anomalies associated with ABCB4/MDR3 deficiency in adults: a pictorial essay. Insights Imaging. 2013;4(3):331–8.
62. Taouli B, Koh D-M. Diffusion-weighted MR imaging of the liver. Radiology. 2010;254(1):47–66.
63. Tohme-Noun C, Cazals D, Noun R, Menassa L, Valla D, Vilgrain V. Multiple biliary hamartomas: magnetic resonance features with histopathologic correlation. Eur Radiol. 2008;18(3):493–9.
64. Jang JK, Jang HJ, Kim JS, Kim TK. Focal fat deposition in the liver: diagnostic challenges on imaging. Abdom Radiol (NY). 2017;42(6)
65. Vilgrain V, Lagadec M, Ronot M. Pitfalls in liver imaging. Radiology. 2016;278(1):34–51.
66. Choi BI, Lee JM, Kim TK, Dioguardi Burgio M, Vilgrain V. Diagnosing borderline hepatic nodules in hepatocarcinogenesis: imaging performance. AJR Am J Roentgenol. 2015;205(1):10–21.
67. Choi JY, Lee JM, Sirlin CB. CT and MR imaging diagnosis and staging of hepatocellular carcinoma: Part II. Extracellular agents, hepatobiliary agents, and ancillary imaging features. Radiology. 2014;273(1):30–50.
68. Ronot M, Vilgrain V. Hepatocellular carcinoma: diagnostic criteria by imaging techniques. Best Pract Res Clin Gastroenterol. 2014;28(5):795–812.
69. Hwang J, Kim YK, Jeong WK, Choi D, Rhim H, Lee WJ. Nonhypervascular hypointense nodules at gadoxetic acid-enhanced MR imaging in chronic liver disease: diffusion-weighted imaging for characterization. Radiology. 2015;277(1):309.
70. Kim YK, Lee WJ, Park MJ, Kim SH, Rhim H, Choi D. Hypovascular hypointense nodules on hepatobiliary phase gadoxetic acid-enhanced MR images in patients with cirrhosis: potential of DW imaging in predicting progression to hypervascular HCC. Radiology. 2012;265(1):104–14.
71. Baron RL, Campbell WL, Dodd GD 3rd. Peribiliary cysts associated with severe liver disease: imaging-pathologic correlation. AJR Am J Roentgenol. 1994;162(3):631–6.
72. Duran R, Ronot M, Di Renzo S, Gregoli B, Van Beers BE, Vilgrain V. Is magnetic resonance imaging of hepatic hemangioma any different in liver fibrosis and cirrhosis compared to normal liver? Eur J Radiol. 2015;84(5):816–22.
73. Brancatelli G, Federle MP, Blachar A, Grazioli L. Hemangioma in the cirrhotic liver: diagnosis and natural history. Radiology. 2001;219(1):69–74.
74. Dioguardi Burgio M, Ronot M, Paulatto L, Terraz S, Vilgrain V, Brancatelli G. Avoiding pitfalls in the interpretation of gadoxetic acid-enhanced magnetic resonance imaging. Semin Ultrasound CT MR. 2016;37(6):561–72.
75. Pradella S, Lucarini S, Colagrande S. Liver lesion characterization: the wrong choice of contrast agent can mislead the diagnosis of hemangioma. AJR Am J Roentgenol. 2012;199(5):W662.

Malignant Liver Lesions

3

Filipe Caseiro Alves and Francisco Pereira Silva

3.1 Introduction

Imaging techniques applied to medical practice depend on two major characteristics: the ability to consistently define anatomically coherent findings and adequate contrast between tissues. MR diffusion-weighted imaging (DWI) uses the signal loss associated with the random thermal motion of water molecules in the presence of magnetic field gradients to derive a quantitative parameter (the so-called apparent diffusion coefficient—ADC) that directly reflects the translational mobility of the water molecules in the tissues [1]. It is fundamentally different from the conventional morphological and hemodynamically based imaging techniques [2]. Early abdominal applications of DWI were limited due to susceptibility effects, suboptimal fat suppression and artifacts related to random and periodic motion [3, 4]. Many of these issues have not been completely solved but are today minimized considering current hardware and software improvements. As such, DWI has become an indispensable day-to-day tool for liver imaging, proving its value on various clinical scenarios, from focal liver lesion detection to characterization and/or diffuse liver disease assessment. Specific advantages consist on its short examination time, independence of exogenous sources of contrast, and the ability to provide qualitative and quantitative information [5, 6]. The following chapter addresses the most common current clinical applications of DWI in the setting of liver malignancies, considering basic methodologies on how to assess diffusion-weighted images in qualitative and quantitative manner and reviewing clinical results for oncologic applications.

F. C. Alves (✉) · F. P. Silva
Department of Radiology, Faculty of Medicine, Clinical Research CIBIT/ICNAS, University of Coimbra, Coimbra, Portugal

University Hospital of Coimbra (CHUC), Coimbra, Portugal

C. Matos, N. Papanikolaou (eds.), *Diffusion Weighted Imaging of the Hepatobiliary System*, https://doi.org/10.1007/978-3-319-62977-3_3

3.2 Reading DWI: Qualitative Reading

In clinical practice, the information conveyed by DWI is rapidly prone to a qualitative evaluation and, together with the ADC map display is generally sufficient to be used as the reading working strategy. DWI should not be a standalone sequence for interpretation purposes but be integrated and read in conjunction with all the available information arising from the remainder morphological sequences. Tissues with high cellularity such as tumors or abscesses, will display restricted diffusion consisting on hyperintensity on high *b* values (>400–500 s/mm^2) images and low ADC values (less than the normal parenchyma). Conversely, cystic or necrotic tissues will show a signal intensity loss on high *b* value images and return high ADC values. DWI signal intensity, however, depends not only on water diffusivity, but also on the magnetic properties of the tissue itself. Tissues possessing long T2-relaxation times–such as hemangiomas may remain with high signal on high *b* values, and high values on ADC mapping (the so-called T2 shine-through effect). Contrarily, lesions with low-signal intensity on T2-w images may not show hyperintensity on DWI even if they have increased cellularity (the so-called T2-black out effect) [5]. Restricted diffusion is a property commonly seen in malignancy but is by no means specific as described before. As it is well known, several malignant liver tumors will tend to show restricted diffusion such as hepatocellular carcinoma, intrahepatic cholangiocarcinoma, or hepatic metastases [5, 7]. Also, ADC values of solid benign lesion can overlap with ADC values of malignant lesion [7, 8].

A schematic overview of possible signal intensity combinations on T2-w, DWI and ADC is provided in the table below.

	T2 (b=0)	DWI (b>500)	ADC	Examples
Free diffusion	hiper	iso / hipo	hiper	Benign lesion (ex: Cyst / Hemangioma)
T2 shine-through	hiper	hiper	hiper	High T2 signal (Cyst / Hemangioma)
T2 black-out	hipo	hipo	hipo	Paramagnetic substances (e.x., iron), hemorrhage or post-treatment
Restricted diffusion	iso	hiper	iso / hipo	Highly cellular lesions Metastasis
	hiper	hiper	iso / hipo	Tumor Abcess

If iso-intense to liver, with high signal on high b, consider as "low" ADC

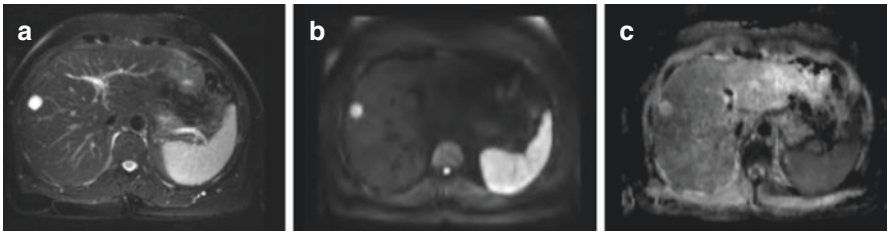

Fig. 3.1 Hemangioma and shine-through effect. (**a**) T2-w fat-suppressed image showing the typical light bulb sign. (**b**) DWI obtained with a *b* value of 800 s/mm^2 reveals pseudo-restriction. (**c**) ADC map confirms a high ADC value compatible with hemangioma

For malignant lesions, DWI is useful in distinguishing the different components of tumors (cystic and/or necrotic vs solid components). False positives for malignancy may occur from T2 shine-through effect, partial volume averaging or misregistration artifacts (Fig. 3.1). False negatives may also result from metastases of mucin-producing tumors (cystic-like behavior), from well-differentiated tumors (no restriction) and from necrotic tumors (either primarily necrotic or secondary to treatment), and finally when image artifacts conceal focal liver lesions [5].

3.3 Reading DWI: Quantitative Reading of ADC

The ADC of the liver calculated from diffusion acquisition can be appraised by either visual assessment of the ADC map or by drawing regions of interest (ROI) on the ADC maps to record the mean or median ADC values in the tissue of interest. Several problems still exist with the latter approach. A wide variation of values dependent of technical issues renders ADC measurements variable and therefore of limited use in the daily clinical practice. It has been shown that values may vary not only among different equipment vendors but also within the same vendor and even within the same patient [9]. Consequently, these problems should be addressed and overcome in order to derive meaningful comparative results in order to use DWI as a routine biomarker especially for evaluation of tumor response. Also, ADC measurements will vary with other confounder factors such as liver iron deposition, fat, fibrosis and/or changes in microcirculation. Most workstations and many clinical studies provide ADC values based on monoexponential models, with considerable variation of the protocols and proposed *b* values [5–8]. These factors also influence the final ADC measurement. As previously stated, diffusion in tissues is more accurately reflected by a bi-exponential model, and thus deriving ADC measurements from monoexponential fitting curves will add to the lack of precision [10–14]. To note that average ADC values does not reflect tumor heterogeneity. Other approaches, such as histogram analysis of a single ROI may prove to be a better depicter of tumor heterogeneity, and it has been investigated as a possible parameter for tumor assessment [15, 16]. Kurtosis, a measurement of the amount of this deviation from

the Gaussian behavior in a dimensionless metric called "excess kurtosis," may assist in the goal of assessing intralesional heterogeneity and has been investigated for tumor follow-up [17].

3.3.1 Lesion Characterization with DWI—A Shift from Classical Qualitative Assessment?

As already stated, DWI interpretation bases itself on the detection of restricted diffusion. This represents an area of high signal on high *b* values. For instants, ADC of hemangiomas or cysts will tend to be significantly higher than ADC of malignant liver lesions, but ADC values did not allow a confident diagnosis among different types of liver malignancies. Published data attempted to test sensitivity and specificity of parameters derived from IVIM (using bi-exponential models) to characterize focal liver lesion [10]. However, use of the perfusion component of DWI (Dfast) using the IVIM approach [13] showed a sensitivity of 90.1% and specificity of 85.2% for the distinction of HCC from intrahepatic cholangiocarcinoma, thus reflecting the different tumor vascularization. To which extent these results are reproducible or additive to clinical decision process remains unknown. Using the same IVIM approach other authors have tried to derive conclusions regarding HCC differentiation and reported a higher accuracy [10] however conflicting data has also been published on this regard [14]. Despite microperfusion information provided by the IVIM approach of derived data with contrast-enhanced studies seem to lack a good correlation [14] or may be lower, meaning that IVIM perfusion assessment needs to be better understood.

3.4 Application of DWI to Hepatocellular Carcinoma

Detection of HCC is improved by DWI [18], with low *b* value DWI showing higher sensitivity due to the vascular signal suppression that increases the conspicuity of nearby lesions. The expected impact of DWI for HCC detection has been proved to be lower than the one reported for liver metastases [19]. As recommended by the LI-RADS classification system from the American College of Radiology, the term "restricted diffusion" should be applied to lesions that are hyperintense relative to the surrounding liver when acquired with at least moderate diffusion weighting (e.g., $b \geq 400$ s/mm^2) and from which the generated ADC map, shows low apparent diffusion coefficient (ADC)—i.e., lower than that of liver by visual estimation. LI-RADS also recommend that if unsure about this feature, it should not be used to perform lesion characterization [20]. In fact, HCC may be difficult to discriminate from the surrounding cirrhotic changes or even dysplastic nodules, as these can have similar behavior and ADC values [6]. Also, it has low sensitivity (range between 62–91%) [21], due to false negatives especially arising from well-differentiated HCC that will tend to show no restriction on DWI in the context of a fibrotic, heterogeneous background liver parenchyma. DWI seems to provide an

additional clue regarding the assessment of tumor aggressiveness. Some studies pinpoint a lower ADC in cases of poorly differentiated HCC [22–24], thus allowing the distinction of low- from high-grade HCC lesions (Fig. 3.2). Association between low ADC value, aggressiveness, and poor response to treatment (such as chemoembolization, thermal ablation, surgical resection, or anti-angiogenic therapy) including a higher recurrence rate after treatment and consequently poor prognosis, has been described [25–28]. DWI can be useful in the diagnosis of macrovascular invasion especially in the infiltrative forms of HCC, with the intravascular tumor casts revealing restricted diffusion and hyperintensity on the high *b* value DWI (Fig. 3.3).

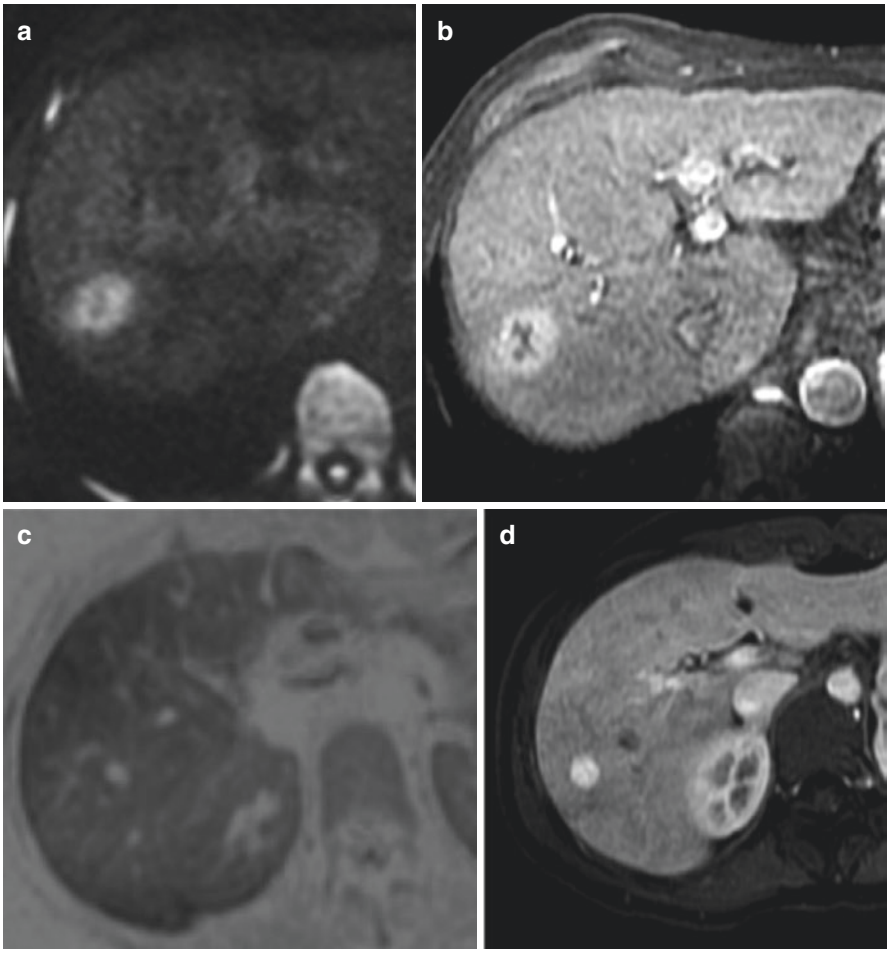

Fig. 3.2 DWI and HCC differentiation. Although sensitivity of DWI to depict HCC remains low, signal intensity on high *b* value DWI tends to be directly proportional to the degree of tumor differentiation. (**a**) Moderately differentiated HCC showing DWI restriction ($b = 800$). (**b**) Late arterial phase depicting typical wash-in. (**c**) Well-differentiated HCC showing absence of DWI restriction. (**d**) Late arterial phase depicting typical wash-in

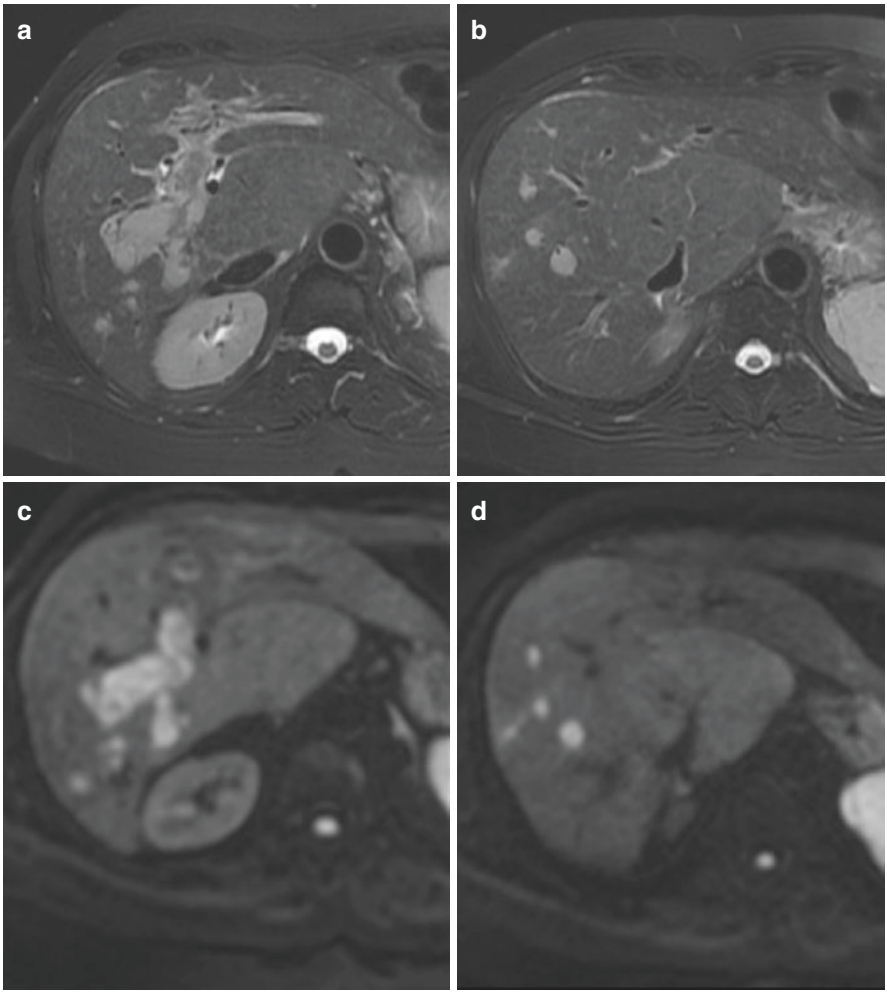

Fig. 3.3 Hepatocellular carcinoma with extensive portal venous invasion. Tumor thrombosis is clearly depicted on DWI images due to its intrinsic high contrast resolution and black blood effect on normal vessels. (**a**) T2-w image with portal vein enlargement and high-signal intensity. (**b**) Tumor casts extending to intrahepatic branches. (**c**, **d**) Corresponding DWI images obtained with high *b* value (*b* = 800)

DWI in the context of HCC can be beneficial once a DWI positive nodule is recognized but lacks the typical wash-in/washout pattern. Until now, and together with other imaging signs, apart from the vascular behavior, high *b* value DWI positivity in a nodule otherwise deemed hypovascular in the dynamic study, is one of the ancillary findings that may trigger a closer follow-up of these patients. Hyperintensity on DWI (using high *b* values) of hypovascular nodules in patients with cirrhosis has been shown to predict progression to hypervascularity, although at a very low rate

[23]. LI-RADS is currently the only western classification system that incorporates DWI in the non-invasive diagnosis of liver nodules in cirrhosis, but only as an ancillary feature. It can be used as a "tie-break" rule pointing toward probable malignancy (as well moderate T2 hyperintensity; microscopic fat-containing nodule, T1 hypointensity on the hepatospecific phase, etc.), allowing the upgrade of a suspicious nodule up to but not beyond LR-4.

3.4.1 Assessment of Tumor Response to Treatment (HCC)

Locoregional treatment of HCC results in dynamic changes and lesion remodeling occurring at the site of treatment. DWI can contribute to the diagnosis of residual tumor and should be interpreted in conjunction with the mRECIST criteria (Fig. 3.4). Residual or recurrent tumor will manifest as area/s of low ADC contrarily to nonviable areas that will display high ADC values. In patients with contra-indications to contrast media injection DWI can be offered as an alternative solution for tumor response evaluation. DWI has also the potential to act as a prognostic indicator in patients with HCC. Low pretreatment ADC has been shown to be a risk factor for early HCC recurrence after surgical resection, and to predict a worse response to transarterial chemoembolization (TACE) [25]. Additionally, ADC changes of tumors following TACE were shown to be an independent predictor of overall survival [11]. An increase in ADC 1 month after TACE or radioembolization (TARE) is indicative of a good prognosis [25, 28]. Deriving the perfusion fraction with IVIM although appealing is still a matter of research as an early predictor of response after chemoembolization [28].

Mean ADC measurements may not be an adequate way to assess tumor heterogeneity after treatment. In this sense, kurtosis calculation may be representing more accurately this feature [17]. Kurtosis after HCC treatment performed better than ADC alone, with better sensitivity (85.7% vs 79.6%) and specificity (98% vs 58.3%), for predicting HCC recurrence.

At the time of this writing there is no clear-cut evidence that ADC quantification for tumor response evaluation is superior or just additive to the mRECIST criteria. In fact, it has been shown that contrast-enhanced MRI with subtraction technique shows a more significant correlation with the histopathologic findings concerning the degree of necrosis estimation after TACE, compared with DWI. Adding for this last topic, advanced quantification of the lesion perfusion with analysis of the Ktrans parameter can also be performed but again its clinical relevance remains to be seen.

3.5 Application of DWI to Intrahepatic Cholangiocarcinoma

Intrahepatic cholangiocarcinoma (IHCCK) is the second most common primary hepatic malignant tumor arising from the epithelium of the bile ducts [29]. Sensitivity is expected to be very high, with series reporting all cholangiocarcinomas to be

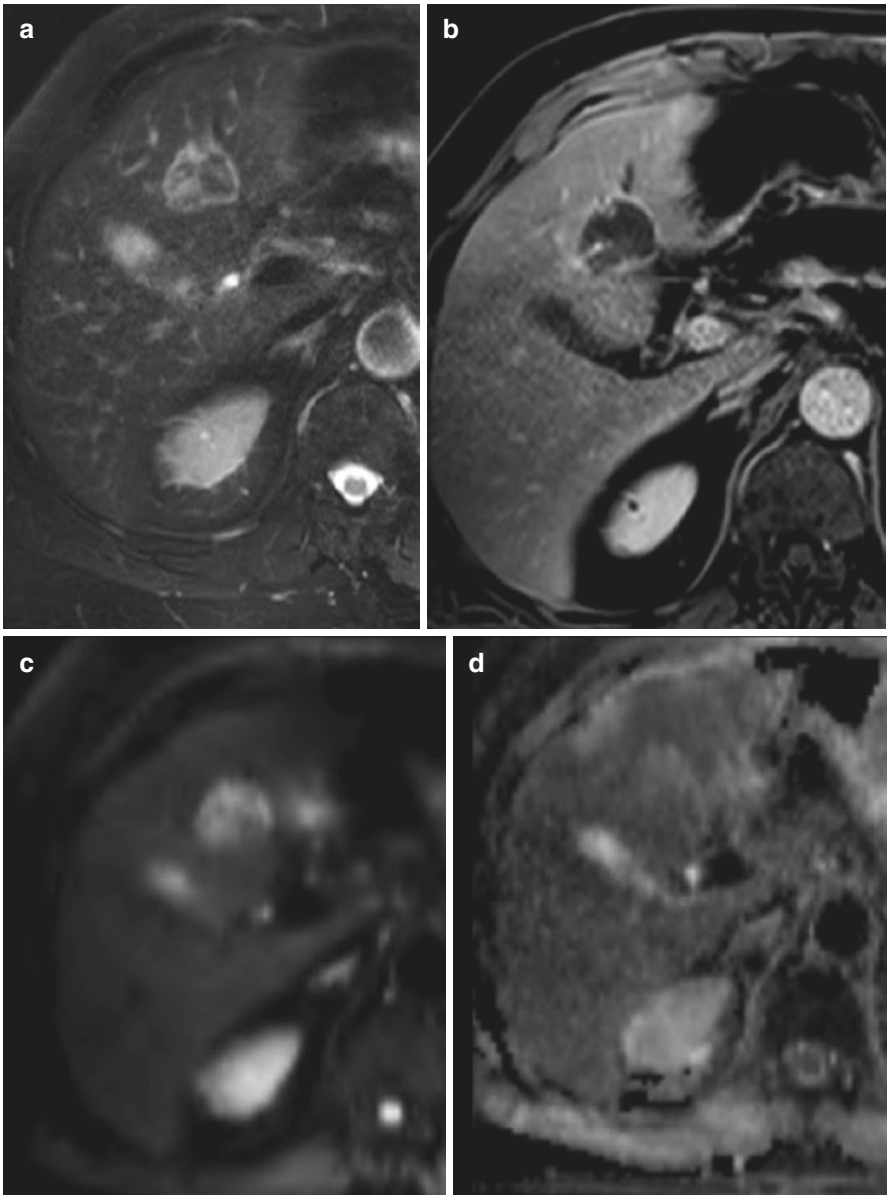

Fig. 3.4 Follow-up MR after thermal ablation of HCC. Despite the high signal intensity of the nodule on the T2-w image, both the dynamic study after contrast administration and DWI (*b* 800 and ADC map) are contributive to affirm complete tumor necrosis. (**a**) T2-w fat-sat FSE. (**b**) 3D T1-w GRE at the late arterial phase of liver enhancement. (**c**) DWI at *b* 800 s/mm^2. (**d**) Corresponding ADC map visually displaying high ADC of the nodule

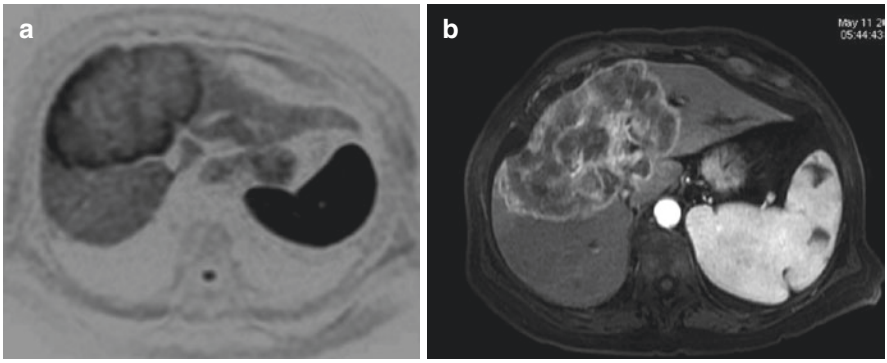

Fig. 3.5 Intrahepatic cholangiocarcinoma typical pattern on contrast-enhanced MR and DWI. The last sequence allows to differentiate the peripheral cellular area showing restriction and the central zone where the less cellular fibrous tumor stroma is predominantly located. (**a**) DWI with $b = 800$ s/mm^2. (**b**) 3D GRE T1-w at the arterial phase of liver enhancement

detectable on DW-MR images with restricted diffusion [30]. In the cirrhotic patient it is fundamental for patient management to recognize and differentiate IHCCK from HCC since the former contraindicates liver transplantation due to its very bad prognosis and early tumor relapse. As a rule of thumb, the majority of IHCCK will show restriction to diffusion and low ADC values. A typical sign that has been associated with this tumor type is the presence of a peripheral rim with high *b* value DWI. In fact, DWI may show a more hyperintense peripheral rim and a larger central hypointense central zone (Fig. 3.5). Pathological correlation reveals that the peripheral rim corresponds to the higher cellularity areas and the inner core to the predominantly fibrotic component of the tumor. This aspect on DWI together with all the remainder imaging descriptors (lobulated contours, rim enhancement in the arterial phase, target appearance on the hepatobiliary phase, capsular retraction, and upstream dilatation of intrahepatic ducts) are consistent with IHCCK. It has been however reported on multivariate logistic regression analysis that only the target appearance on the DWI was a significant and independent variable predictive of ICCK, making it the most reliable imaging feature for distinction of small mass forming IHCC from small HCC [31, 32]. Other ancillary findings (such as capsule or enhancing septa) would favor HCC [32].

3.6 Application of DWI in Liver Metastasis

Hepatic metastases usually demonstrate low ADC except if totally necrotic, calcified (before or after treatment), or derived from mucin-producing tumors (Fig. 3.6) [5, 7, 33].

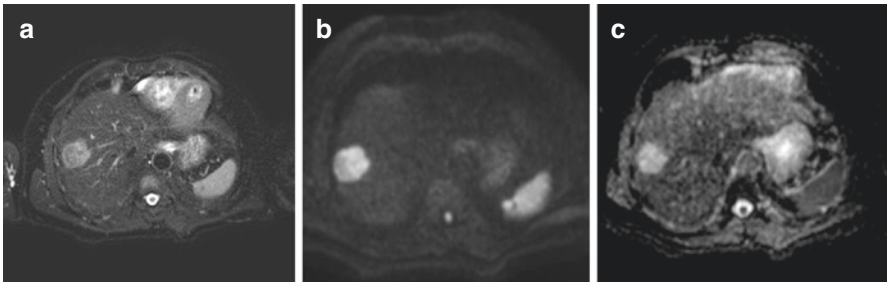

Fig. 3.6 Pseudo-shine-through effect in patient with colorectal cancer liver metastasis. The primary tumor was a mucin-producing adenocarcinoma. (**a**) T2-w fat-sat image showing the right lobe liver metastasis with similar signal intensity to the spleen. (**b**) DWI with *b*800 s/mm^2. (**c**) Corresponding ADC map revealing a high ADC value of the liver metastasis in line with the mucinous content

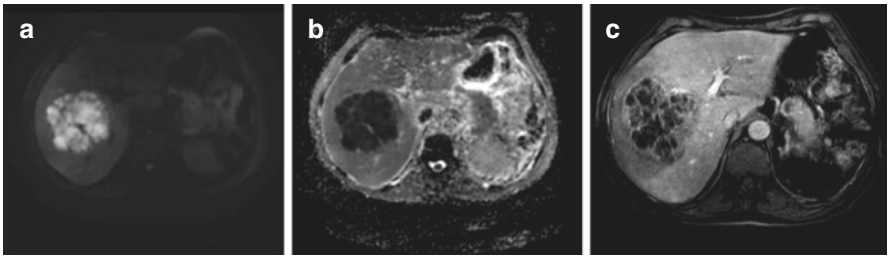

Fig. 3.7 Liver abscess displaying marked restriction on DWI. (**a**) DWI with b = 800 s/mm^2. (**b**) Low-signal intensity on the ADC map. (**c**) GRE T1-w dynamic image showing the typical peripheral enhancement and perilesional perfusion abnormalities

Radiologists should be aware that focal liver abscesses, due to its cellular debris and exudates, will return low ADC values and, in the absence of clinical or laboratory findings, can be confused with metastatic liver disease (Fig. 3.7). There is now abundant evidence of the role of DWI in detection and locoregional staging of metastatic liver disease.

As stated from a recent consensus report from the seventh International Forum for Liver Magnetic Resonance Imaging, the combination of hepatobiliary phase images with DW-MR images yields a higher detection rate, particularly in the setting of sub-centimeter liver metastasis [34]. In a meta-analysis dealing with DWI in liver metastases, there was no difference between DWI and Gd-enhanced studies concerning detection rate [19]. In this study however, Gd-enhanced studies were pooled between extracellular and liver-specific contrast agents. Another meta-analysis, based on 39 articles including a large population (nearly 2000 patients with nearly 4, 000 liver metastases) shows that the sensitivity of combined MR (DWI + Gd-EOB-DTPA) is significantly higher than either of the two techniques interpreted separately [33]. However, and despite its excellent results, DWI alone is less sensitive than gadoxetic acid-enhanced MR imaging for detecting liver

metastases in the sub-centimeter range. Some arguments may be expanded concerning the different DW protocols and *b* values among institutions, that may have impacted results as a potential source of false negative results when compared with the more homogeneous and widespread contrast-enhanced 3D-GRE technique. In fact, highest *b* values ranged from 400 to 1000 s/mm^2, with less than half the studies including low *b* values.

Mean sensibility and specificity for metastasis detection.

	Sensitivity	Specificity
Mean DW-MR	82.2% [(95% CI, 69.4–90.4%)]	90.4% [(95% CI, 82.8–94.8%)]
Gd-EOB-DTPA	91.2% [(95% CI, 83.7–95.4%)]	90.4% [(95% CI, 82.8–94.8%)]
Combined	95.0% [(95% CI, 89.9–97.6%)]	82.4% [(95% CI, 70.5–90.2%)]

When dealing with detection of liver metastases the use of low and high *b* values in DWI (in our institution 50–100 and 800 s/mm^2) is mandatory as low *b* value DWI provide higher SNR, are less prone to motion-induced signal loss and suffer less from eddy current-induced distortions, justifying its greater sensitivity. The "black blood" appearance of vessels on DWI, especially on the more anatomical low *b* value images is an essential component and often, in this setting, DWI is the first sequence to map focal liver lesions. In daily practice a common setting is to use DWI for lesion identification and interpret together low and high *b* values image sets for detection and characterization.

Since 30% of patients with colorectal liver metastases are surgical candidates, three main goals should be considered in order to offer advanced imaging studies such as hepatobiliary-enhanced MRI:

1. to precisely define the tumor burden
2. to provide accurate lesion mapping
3. to verify resection margins around major vessels

DWI deals well with the first two questions while HBCA-MR, due to its superior SNR and 3D spatial resolution capabilities, provides the answer for the last question. To note that in general, the third question addresses the immediate presurgical information while the first two are related to a prior step of patient management (to map and measure lesions before neoadjuvant therapy). Thus, in the initial evaluation of tumor burden and/or tumor response evaluation DWI is a fundamental step and, at this stage, hepatobiliary CA can be skipped.

Special care should be taken not to overlook the so-called "vanishing metastases" corresponding to a dramatic change of metastasis size or signal intensity after chemotherapy. A study addressing patients with this "disappearing" or "tiny residual metastasis" of colorectal cancer after chemotherapy on DWI or Gd-EOB-DTPA, showed an in situ recurrence rate of 15.7% and 33.2%, respectively, at 2 years [35]. So even if not apparent on DWI, the location of prior liver metastases should be carefully inspected and ultimately resected (Fig. 3.8). An ADC transient reduction 24–48 h after initiation of chemotherapy has been described, thought to result from

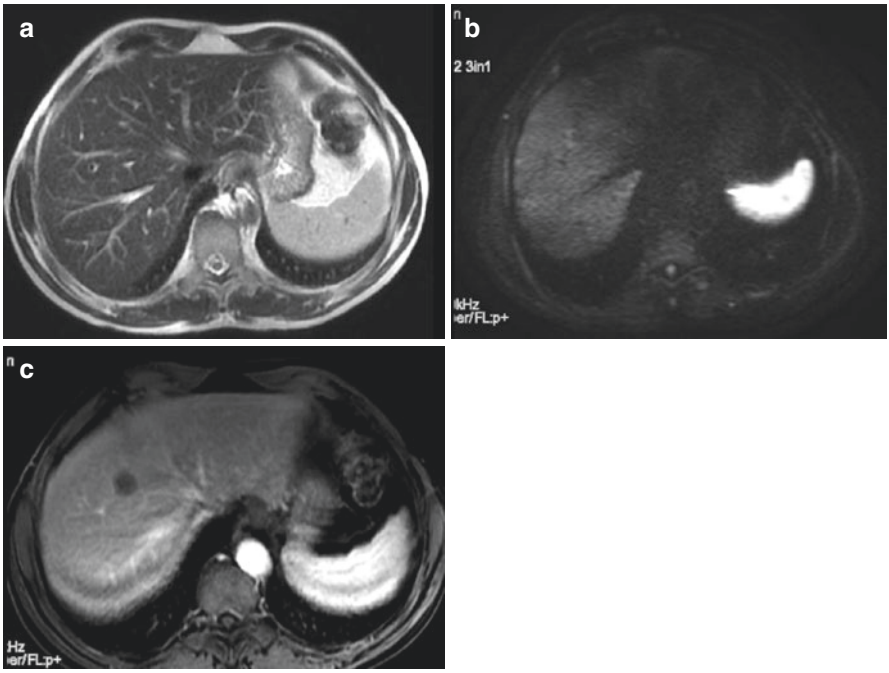

Fig. 3.8 Liver metastasis post-chemotherapy with pathologically proven residual active tumor. The typical imaging findings are lacking, and thus detection and/or characterization may be difficult. Prior comparison is mandatory. (**a**) The T2-w FS sequence is negative. (**b**) DWI with $b = 800$ s/mm^2. The lesion is barely perceptible and only a discrete hyperintense rim is disclosed. (**c**) The metastasis is clearly depicted although tumor viability may be difficult to ascertain

acute cell swelling and/or reduction of interstitial volume. Further ADC decrease along time may correspond to tumor regrowth, fibrosis or tissue remodeling, together with decreased perfusion [36, 37] Thus, in patients submitted to chemotherapy, ADC changes may differentiate between responders and nonresponders, increasing (as expected) in the responders, a finding that may be detected even after the first cycle [38].

For patients with unresectable CRC liver metastases, tumor burden and lower pretreatment ADC values correlate with worst response to radioembolization with 90Yttrium-microspheres. Lower ADC values ($<0.935 \times 10^{-3}$ mm^2/s) were seen in nonresponders before treatment and early ADC changes (within the first 2 months after treatment) meaning increased survival rate [39, 40]. Another interesting observation relates to the histogram analysis of the apparently tumor-free parenchyma. A trend toward larger standard deviation of the parenchyma, and lower ADC values (in the fifth percentile) may be an early predictor of micrometastatic disease [41, 42].

In conclusion, for metastatic liver disease, DWI is highly sensitive for lesion detection, and thus should be routinely and incorporated in every MR liver protocol [43]. DWI increases the accuracy for lesion characterization with the combined

reading of two or more *b* values along with the contrast-enhanced MR study. DWI appears as a potential biomarker for tumor response evaluation albeit unsolved issues such as reproducibility, artifact control and suboptimal SNR.

3.7 Future Directions

Most DW-MR imaging studies have been conducted by using 1.5-T MR systems. 3.0-T are increasingly available, have potential for improved image quality, due to increased SNR provided by 3.0-T fields, which is used to improve spatial resolution, to lower the acquisition time (or both), and enables the use of higher *b* values, which are more sensitive to diffusion and less sensitive to T2 relaxation time.

In DWI, there can be an up to two-fold increase in SNR but with greater magnetic susceptibility artifacts, image distortion and signal loss, greater conspicuity of metal or gas, particularly, with EPI sequences used in DWI, and incomplete fat saturation [44]. There are also reported significant differences between ADC measurements performed at 1.5 and 3 T. Some of these problems can be reduced with a higher receiver bandwidth and parallel imaging techniques.

3.8 Conclusions

DWI can add potentially useful qualitative and quantitative information to conventional imaging sequences. It is quick, can be easily incorporated to existing protocols, is a nonenhanced technique (performed without the use of gadolinium-based contrast media), thus easy to repeat, is useful in patients with severe renal dysfunction at risk for nephrogenic systemic fibrosis.

Variable field strength, number of *b* values used for diffusion-weighted imaging in each study, the "IVIM" effect, contribute for lack of homogeneity of results and lack of external validity. This is mostly true for quantitative approaches do DWI. However, regarding qualitative reading, which is the most thoroughly used in clinical practice, there doesn't seem to be as much variation on the interpretation of findings, on the expected sensibility of detections of malignant lesions (especially metastases). This made it possible for very quick and smooth incorporation of DWI in standard abdominal scanning.

We expect that further standardization will be necessary to ensure reproducibility and implementation of quantitative studies. Furthermore, we believe that more data, other than just ADC values and qualitative parameters will be available. Such data may derive from exploring tumor heterogeneity ("the main reason why we are failing treating cancers after all these years") as was proposed with implementation of kurtosis. There is also the exploit of IVIM and it's still to accurately determine molecular findings, a phenomenon which was initially not taken in account for, but presents with a promising field for ability to discriminate focal liver lesions, to predict its behavior or clinical significance in a follow-up, provided reproducibility is ensured.

References

1. Luypaert R, Boujraf S, Sourbron S, Osteaux M. Diffusion and perfusion MRI: basic physics. Eur J Radiol. 2001;38:19–27.
2. Muhi A, et al. High-b-value diffusion-weighted MR imaging of hepatocellular lesions: estimation of grade of malignancy of hepatocellular carcinoma. J Magn Reson Imaging. 2009;30:1005–11.
3. Chandarana H, Taouli B. Diffusion and perfusion imaging of the liver. Eur J Radiol. 2010;76:348–58.
4. Namimoto T, Yamashita Y, Sumi S, Tang Y, Takahashi M. Focal liver masses: characterization with diffusion-weighted echo-planar MR imaging. Radiology. 1997;204:739–44.
5. Taouli B, Koh D-M. Diffusion-weighted MR imaging of the liver. Radiology. 2010;254: 47–66.
6. Papanikolaou N, Gourtsoyianni S, Yarmenitis S, Maris T, Gourtsoyiannis N. Comparison between two-point and four-point methods for quantification of apparent diffusion coefficient of normal liver parenchyma and focal lesions. Value of normalization with spleen. Eur J Radiol. 2010;73(2):305–9.
7. Gourtsoyianni S, Papanikolaou N, Yarmenitis S, Maris T, Karantanas A, Gourtsoyiannis N. Respiratory gated diffusion-weighted imaging of the liver: value of apparent diffusion coefficient measurements in the differentiation between most commonly encountered benign and malignant focal liver lesions. Eur Radiol. 2008;18(3):486–92.
8. Goshima S, et al. Diffusion-weighted imaging of the liver: optimizing b value for the detection and characterization of benign and malignant hepatic lesions. J Magn Reson Imaging. 2008;28:691–7.
9. Zhu J, et al. Apparent diffusion coefficient normalization of normal liver: will it improve the reproducibility of diffusion-weighted imaging at different MR scanners as a new biomarker? Medicine (Baltimore). 2017;96:e5910.
10. Woo S, et al. Intravoxel incoherent motion diffusion-weighted MR imaging of hepatocellular carcinoma: correlation with enhancement degree and histologic grade. Radiology. 2014;270:758–67.
11. Wu L, et al. ADC total ratio and D ratio derived from intravoxel incoherent motion early after TACE are independent predictors for survival in hepatocellular carcinoma. J Magn Reson Imaging. 2017;46:820. https://doi.org/10.1002/jmri.25617.
12. Guiu B, Cercueil J-P. Liver diffusion-weighted MR imaging: the tower of Babel? Eur Radiol. 2011;21:463–7.
13. Choi IY, et al. Intravoxel incoherent motion diffusion-weighted imaging for characterizing focal hepatic lesions: correlation with lesion enhancement. J Magn Reson Imaging. 2016;45:1589–98.
14. Hectors SJ, et al. Intravoxel incoherent motion diffusion-weighted imaging of hepatocellular carcinoma: is there a correlation with flow and perfusion metrics obtained with dynamic contrast-enhanced MRI? J Magn Reson Imaging. 2016;44:856–64.
15. Drevelegas K, Nikiforaki K, Constantinides M, Papanikolaou N, Papalavrentios L, Stoikou I, Zarogoulidis P, Pitsiou G, Pataka A, Organtzis J, Papadaki E, Porpodis K, Kougioumtzi I, Kioumis I, Kouskouras C, Akriviadis E, Drevelegas A. Apparent diffusion coefficient quantification in determining the histological diagnosis of malignant liver lesions. J Cancer. 2016;7(6):730–5.
16. Liang H-Y, et al. Potential of MR histogram analyses for prediction of response to chemotherapy in patients with colorectal hepatic metastases. Eur Radiol. 2016;26:2009–18.
17. Goshima S, et al. Diffusion kurtosis imaging to assess response to treatment in hypervascular hepatocellular carcinoma. AJR Am J Roentgenol. 2015;204:W543–9.
18. Gluskin JS, Chegai F, Monti S, Squillaci E, Mannelli L. Hepatocellular carcinoma and diffusion-weighted MRI: detection and evaluation of treatment response. J Cancer. 2016;7:1565–70.

19. Wu L-M, Hu J, Gu H-Y, Hua J, Xu J-R. Can diffusion-weighted magnetic resonance imaging (DW-MRI) alone be used as a reliable sequence for the preoperative detection and characterization of hepatic metastases? A meta-analysis. Eur J Cancer. 2013;49:572–84.
20. CT/MRI LI-RADS v2017. Available from: https://www.acr.org/~/media/ACR/Documents/PDF/QualitySafety/Resources/LIRADS/2017/LIRADS_2017_Core.pdf?la=en. Accessed 29 June 2017.
21. Kim YK, Kim CS, Han YM, Lee YH. Detection of liver malignancy with gadoxetic acid-enhanced MRI: is addition of diffusion-weighted MRI beneficial? Clin Radiol. 2011;66:489–96.
22. Sandrasegaran K, et al. The usefulness of diffusion-weighted imaging in the characterization of liver lesions in patients with cirrhosis. Clin Radiol. 2013;68:708–15.
23. Kim YK, et al. Hypovascular hypointense nodules on hepatobiliary phase gadoxetic acid-enhanced MR images in patients with cirrhosis: potential of DW imaging in predicting progression to hypervascular HCC. Radiology. 2012;265:104–14.
24. Chang W-C, et al. Histological grade of hepatocellular carcinoma correlates with arterial enhancement on gadoxetic acid-enhanced and diffusion-weighted MR images. Abdom. Imaging. 2014;39:1202–12.
25. Mannelli L, Kim S, Hajdu CH, Babb JS, Taouli B. Serial diffusion-weighted MRI in patients with hepatocellular carcinoma: prediction and assessment of response to transarterial chemoembolization. Preliminary experience. Eur J Radiol. 2013;82:577–82.
26. Corona-Villalobos CP, et al. Functional magnetic resonance imaging response of targeted tumor burden and its impact on survival in patients with hepatocellular carcinoma. Investig Radiol. 2015;50:283–9.
27. Rhee TK, et al. Tumor response after yttrium-90 radioembolization for hepatocellular carcinoma: comparison of diffusion-weighted functional MR imaging with anatomic MR imaging. J Vasc Interv Radiol. 2008;19:1180–6.
28. Mannelli L, et al. Assessment of tumor necrosis of hepatocellular carcinoma after chemoembolization: diffusion-weighted and contrast-enhanced MRI with histopathologic correlation of the explanted liver. AJR Am J Roentgenol. 2009;193:1044–52.
29. Lee J, et al. Mass-forming intrahepatic cholangiocarcinoma: diffusion-weighted imaging as a preoperative prognostic marker. Radiology. 2016;281:119–28.
30. Fattach H, et al. Intrahepatic and hilar mass-forming cholangiocarcinoma: qualitative and quantitative evaluation with diffusion-weighted MR imaging. Eur J Radiol. 2015;84:1444–51.
31. Park HJ, Kim YK, Park MJ, Lee WJ. Small intrahepatic mass-forming cholangiocarcinoma: target sign on diffusion-weighted imaging for differentiation from hepatocellular carcinoma. Abdom Imaging. 2013;38:793–801.
32. Min JH, et al. Differentiation between cholangiocarcinoma and hepatocellular carcinoma with target sign on diffusion-weighted imaging and hepatobiliary phase gadoxetic acid-enhanced MR imaging: classification tree analysis applying capsule and septum. Eur J Radiol. 2017;92:1–10.
33. Vilgrain V, et al. A meta-analysis of diffusion-weighted and gadoxetic acid-enhanced MR imaging for the detection of liver metastases. Eur Radiol. 2016;26:4595–615.
34. Merkle EM, Zech CJ, Bartolozzi C, et al. Consensus report from the 7th international forum for liver magnetic resonance imaging. Eur Radiol. 2016;26:674–82. https://doi.org/10.1007/s00330-015-3873-2.
35. Kim SS, et al. Disappearing or residual tiny (</=5 mm) colorectal liver metastases after chemotherapy on gadoxetic acid-enhanced liver MRI and diffusion-weighted imaging: is local treatment required? Eur Radiol. 2016;27:3088. https://doi.org/10.1007/s00330-016-4644-4.
36. Nishiofuku H, et al. Increased tumour ADC value during chemotherapy predicts improved survival in unresectable pancreatic cancer. Eur Radiol. 2016;26:1835–42.
37. Wagner M, et al. Assessment of the residual tumour of colorectal liver metastases after chemotherapy: diffusion-weighted MR magnetic resonance imaging in the peripheral and entire tumour. Eur Radiol. 2016;26:206–15.

38. Kim JH, et al. Diffusion-related MRI parameters for assessing early treatment response of liver metastases to cytotoxic therapy in colorectal cancer. AJR Am J Roentgenol. 2016;207:W26–32.
39. Schmeel FC, et al. Prognostic value of pretreatment diffusion-weighted magnetic resonance imaging for outcome prediction of colorectal cancer liver metastases undergoing 90Y-microsphere radioembolization. J Cancer Res Clin Oncol. 2017;143:1531. https://doi.org/10.1007/s00432-017-2395-5.
40. Schmeel FC, et al. Diffusion-weighted magnetic resonance imaging predicts survival in patients with liver-predominant metastatic colorectal cancer shortly after selective internal radiation therapy. Eur Radiol. 2017;27:966–75.
41. Deckers F, et al. Apparent diffusion coefficient measurements as very early predictive markers of response to chemotherapy in hepatic metastasis: a preliminary investigation of reproducibility and diagnostic value. J Magn Reson Imaging. 2014;40:448–56.
42. Lambregts DMJ, et al. Whole-liver diffusion-weighted MRI histogram analysis: effect of the presence of colorectal hepatic metastases on the remaining liver parenchyma. Eur J Gastroenterol Hepatol. 2015;27:399–404.
43. Donato H, França M, Candelária I, Caseiro-Alves F. Liver MRI: from basic protocol to advanced techniques. Eur J Radiol. 2017;93:30–9.
44. Chilla GS, Tan CH, Xu C, Poh CL. Diffusion weighted magnetic resonance imaging and its recent trend-a survey. Quant Imaging Med Surg. 2015;5:407–22.

Diffuse Liver Diseases

4

Sabrina Doblas, Philippe Garteiser,
and Bernard E. Van Beers

Abbreviations

ADC	Apparent diffusion coefficient
AUC	Area under the receiver operating characteristic (ROC) curve
CR	Coefficient of reproducibility
CV	Coefficient of variation
Δ	Gradient separation time
D	Molecular diffusion coefficient
D^*	Perfusion-related diffusion coefficient
DWI	Diffusion-weighted magnetic resonance imaging
EPI	Echo-planar imaging
f	Perfusion fraction
HCV	Hepatitis C virus infection
IVIM	Intravoxel incoherent motion
MR	Magnetic resonance
NAFLD	Nonalcoholic fatty liver disease
NASH	Nonalcoholic steatohepatitis
ROI	Region-of-interest
SNR	Signal-to-noise ratio

S. Doblas · P. Garteiser
Laboratory of Imaging Biomarkers, Center of Research on Inflammation, UMR 1149 Inserm—University of Paris, 75018 Paris, France
e-mail: sabrina.doblas@inserm.fr; philippe.garteiser@inserm.fr

B. E. Van Beers (✉)
Laboratory of Imaging Biomarkers, Center of Research on Inflammation, UMR 1149 Inserm—University of Paris, 75018 Paris, France

Department of Radiology, Beaujon University Hospital Paris Nord, AP-HP, 92110 Clichy, France
e-mail: bernard.van-beers@aphp.fr

C. Matos, N. Papanikolaou (eds.), *Diffusion Weighted Imaging of the Hepatobiliary System*, https://doi.org/10.1007/978-3-319-62977-3_4

TE Echo time
TR Repetition time

4.1 Introduction—Virtual Biopsy of Diffuse Liver Diseases with DWI

4.1.1 Hallmarks of Chronic Liver Diseases

Chronic liver diseases have diverse causes including viral hepatitis, nonalcoholic fatty liver disease (NAFLD), alcohol- and drug-related toxicity, cholestatic and autoimmune diseases and hemochromatosis. Chronic liver diseases can ultimately lead to cirrhosis and its complications, through a process of inflammation and fibrosis [1, 2]. Currently, the two main causes of chronic liver diseases in the Western countries are hepatitis C virus infection (HCV) and NAFLD. In 25% of patients diagnosed with HCV, cirrhosis will develop in a span of 20–40 years after viral infection. The complications of liver cirrhosis, namely portal hypertension, liver failure and hepatocellular carcinoma, occur with a risk of 1–4% per passing year [3].

In developed countries, NAFLD affects about 25% of the population [4]. In 25% of the patients with NAFLD, the excess of lipids in the liver will produce oxidative stress and inflammation (nonalcoholic steatohepatitis or NASH) with stellate cell activation and fibrogenesis, ultimately leading to cirrhosis in 10% of the patients [5]. In patients with type 2 diabetes, the frequency of NAFLD is much higher (about 75%) than in the general population and 60–80% of the NAFLD patients will present NASH [6]. It is estimated that, in a near future, more patients will need liver transplantation because of NAFLD than because of HCV [7].

Additional classical causes of chronic liver diseases are alcohol consumption and hepatitis B virus infection [1]. Less common liver diseases are cholestatic diseases which are due to impaired hepatobiliary production and excretion of bile. Primary biliary cirrhosis and primary sclerosing cholangitis are the two mainly encountered cholestatic liver diseases in adults [8], accounting for nearly 25% of all first liver transplantations in the Western world. Both diseases cause high inflammatory activity and fibrosis, resulting in cirrhosis (in 4–6 years for primary biliary cirrhosis [8]) and its complications (hepatocellular carcinoma for primary biliary cirrhosis (10% of incidence in patients with end-stage disease [8]) and cholangiocarcinoma for primary sclerosing cholangitis (10–15% incidence) [9]). Finally, hemochromatosis is characterized by abnormal iron deposition in the liver (among other sites) and may also lead to cirrhosis [10].

Chronic liver diseases may present common histopathological features, including fibrosis, inflammation, steatosis and iron overload. Fibrosis and inflammation

should be detected and graded because they have prognostic significance [11–13]. For the former, the two main turning points are bridging fibrosis (≥ F2 in the METAVIR classification of HCV and ≥ F3 in the SAF classification of NASH) and cirrhosis (F4). Classically, treatment is started when bridging fibrosis (also called significant fibrosis) is present, although with recent progresses in treatment, there is a trend to perform universal treatment in HCV patients, whatever the fibrosis stage is. Cirrhosis is important to detect because the risk of hepatocellular carcinoma and portal hypertension and the need to start a surveillance programme based on ultrasonography in these patients [14, 15]. Finally, it is important to detect liver inflammation, as inflammatory activity correlates with patient prognosis, such as the rate of progression to cirrhosis [16]. In NAFLD patients, the assessment of lobular inflammation and hepatocyte ballooning will determine if the patient presents NASH instead of simple steatosis [13, 17].

4.1.2 MR Imaging to Provide Virtual Liver Biopsy

The reference examination for the diagnosis of diffuse liver diseases remains histopathological analysis of liver biopsy [18]. However, hepatic biopsy presents some disadvantages, as it necessitates hospitalisation in 3% of the cases [19] and has a 0.01% mortality rate for percutaneous biopsies (0.09% for transvenous biopsies) [20]. Moreover, biopsy only assesses a small portion of the liver, which can lead to sampling errors causing up to 20% false negative results for cirrhosis [20, 21]. Besides, there can be large inter- and intra-observer variability in the interpretation of biopsied tissues [22, 23].

As a result, alternative diagnostic approaches have been proposed. Serological tests (e.g. Fibrotest [24] or Nash Test [25]) can be easily implemented but their diagnostic performance is limited [7]. Imaging markers, and more particularly those obtained with magnetic resonance (MR) imaging, have the particular strength of providing multiparametric information in a noninvasive manner. MR imaging allows virtual liver biopsy, meaning a noninvasive evaluation of the state and functionality of the liver parenchyma [26]. The information can be collected at the organ or regional level, which is important for diseases with heterogeneous distribution of fibrosis [8]. Besides, MR imaging can be easily repeated several times in the disease course to assess its progression and response to treatment.

In particular, diffusion-weighted imaging (DWI) has been proposed to assess diffuse liver diseases, because it does not require complex hardware and post-processing approaches such as MR elastography, is informative on the microstructural state of the tissue and provides information relative to perfusion, using an intravoxel incoherent motion (IVIM) approach, without any use of contrast agents [27].

4.2 Imaging Recommandations for DWI of Diffuse Liver Diseases

The wide range of apparent diffusion coefficient (ADC) and IVIM parameter values reported in the literature, as well as the variability in diagnostic performance for fibrosis and steatosis assessment, can be partly explained by the different acquisition parameters and processing methods used, and by the technical characteristics of the MR imaging system (e.g. gradient and coil systems, pulse sequence design and artefact reduction strategies) [28–31]. It is important that the acquisition and processing parameters are reported to help comparisons between studies and sites.

4.2.1 Guidelines for DWI Acquisition

One prerequisite for sound interpretation of DWI data is to choose acquisition parameters to ensure high signal-to-noise ratio (SNR), limited artefacts (most notably motion and echo-planar imaging (EPI)-induced artefacts) and repeatable data (Table 4.1). Indeed, the ADC values have a strong dependence on the way the acquisition is performed [31]. For example, low SNR increases the uncertainty of parameter determination [32], which can artificially decrease ADC values [33], while motion tends to increase them [34, 35]. Moreover, care must be taken in the choice of *b* values, as it is recognized that the liver parenchyma possesses biexponential behaviour, and as such different sets of *b* values may yield different "weightings" of perfusion information and affect ADC values. All these acquisition choices may explain some of the differences in reported ADC values or reported diagnostic performance of DWI in the literature [31, 36, 37].

Table 4.1 Suggested acquisition parameters and general considerations [27, 38–41]

	Breathhold	Free breathing or respiratory triggering
Field of view	350–400 × 262–300	Same
Matrix size	At least 96 × 96	Same
Repetition time	>1600	2500–6000
Echo time	Minimum (same for all *b* values)	Same
Echo-planar imaging	Single-shot	Same
Phase-encoding direction	Antero-posterior	Same
Parallel imaging acceleration factor	2	Same
Number of signals acquired	2	2–3 (up to 5 for *b* values ≥500 s/mm^2)
Section thickness	7–8	5–7
Number of sections	10	20
Direction of motion-probing gradients	Phase, frequency, section	Same
Fat suppression	Yes	Yes

Repetition time: Long repetition time (TR) is recommended to allow full T1 recovery between shots, avoiding T1-weighting [42] and optimizing SNR.

Echo time: The echo time (TE) must be minimized as much as possible to provide high SNR, which is crucial especially for studies using high *b* values. Minimization of TE also helps getting more accurate measurements of the perfusion fraction *f*. Indeed, when long TE are used, the signal of liver tissue will be dramatically decreased compared to the blood signal, due to their marked difference in T2 (at 1.5 T, 46 ms for liver tissue vs 290 ms for blood) [43, 44]. This will artificially increase *f*, hence compromising comparison between studies [45]. A correction of the IVIM equation has been recommended by including the relaxation times T1 and T2 of the tissue and blood [45].

Dummy scans: It is recommended to have between 1 and 4 dummy scans to be in a steady-state regime (1 for TR above 3000 ms, 4 for TR between 1000 and 3000 ms) [46].

Fasting: Few studies have investigated the effect of eating on the diffusion parameters [47–49]. Overall, fasting is not mandatory as it does not affect ADC, the molecular diffusion coefficient *D*, the perfusion-related diffusion coefficient D^* or *f* values [48, 49]. Some effect on the perfusion-related parameters is sometimes observed [47] as portal venous flow is known to increase after eating, but the changes in diffusion parameters caused by the prandial state are slight and most probably within the reproducibility limits of the parameters [49].

Contrast agent administration: Usually DWI acquisition is performed before contrast agent administration. Indeed, the presence of intravascular contrast agent could affect ADC measurements because of a decrease in signal intensity due to the T2-shortening effect of the agent [50]. Some authors have reported a significant decrease in hepatic parenchyma SNR and ADC after administration of the hepatobiliary contrast agent gadoxetic acid [51].

Number of motion-encoding gradient directions: On clinical MR imaging systems and at clinical resolution, isotropic behaviour of the liver parenchyma has been observed, even in patients with liver cirrhosis [29, 52]. Regardless of the gradient direction (frequency, slice or phase), ADC values were judged similar [52, 53], and fractional anisotropy did not vary among fibrosis stages [54, 55]. This encouraged some authors to use only monodirectional diffusion gradients to gain time during acquisition [52, 56–58].

However, other authors have suggested to treat the fibrotic and cirrhotic hepatic parenchyma as an anisotropic organ, as the deposition of collagen generally forms nodules dimensioned at a scale visible at DWI (i.e. a few millimetres in diameter) [59]. Indeed, fractional anisotropy has been shown to evolve during fibrogenesis in preclinical studies, starting with a decrease in F1–F2 stages when cell necrosis and apoptosis destroy the radially oriented cellular structures of the hepatic parenchyma, and an increase in F3–F4 stages because of extracellular collagen deposition [60–62]. These changes have not been seen in clinical studies [52, 53, 63]. To guarantee that any anisotropic effect which may occur during fibrosis is taken into account, it would be recommended to use three motion-encoding gradient directions during acquisitions [64]. This would also provide beneficial signal averaging in isotropic tissue.

4.2.2 Guidelines for DWI Data Processing

Avoiding vascular structures, artefacts and margins of the liver is needed when choosing regions-of-interest (ROIs). The most common method is manual drawing, which provides suitable interobserver reproducibility [65–67]. Some authors use advanced methods for ROI selection [68, 69]. It has been recommended to avoid ROI placement in the left liver lobe, as dephasing artefacts and image degradation caused by cardiac motion may artificially increase ADC values and worsen the reproducibility [27, 28, 34, 70, 71]. At the exception of the left lobe, ADC values are similar between segments [70, 72] or adjacent slices [53, 61]. Concerning the size of the ROI, averaging several small ROIs (1–2 cm in diameter) from different locations or selecting the largest homogeneous parenchymal area are the best approaches compared to a single small ROI approach [67].

The IVIM approach has some diagnostic advantages relative to the classical ADC approach for fibrosis diagnosis and staging, if acquisition and processing conditions are optimal (sufficient SNR and number of acquired b values). Indeed, the IVIM approach may provide a better diagnostic performance for fibrosis and cirrhosis than conventional ADC, because of the heightened ability of perfusion-related parameters to differentiate fibrotic from non-fibrotic tissues [31, 73]. It has been reported that D^* can better help diagnosing cirrhotic patients [74] or patients with significant to severe fibrosis than ADC [75], and D^* or a combination of the three IVIM parameters provides better fibrosis staging than ADC alone [73, 76].

Diffusion parameters can be determined in two ways: the signal intensity is averaged within a ROI for each b value and the resulting mean intensities are used to calculate the diffusion parameters [77–80] or the parameters can be calculated pixel-by-pixel before being averaged within a ROI [39]. The latter approach allows conserving regional information, but suffers from higher variability than ROI-wide or organ-wide measurements [38], especially for IVIM parameters [81]. Diffuse liver diseases allow working with large ROIs providing robust determination of the diffusion parameters [68, 78]. In research studies, distribution pattern and texture analysis of the pixel-by-pixel signal distribution may provide additional information [66, 82].

4.2.3 Reference Examination

Care must be taken when using histology as reference examination. Liver biopsy is indeed not a true gold standard. Even with optimal sampling conditions (length and number of portal tracts), fibrosis is only correctly categorized in 75–85% of biopsy specimens because of its local heterogeneity [21, 83]. Similarly, the staging of steatosis based on visual estimation of the percentage of hepatocytes containing lipid vacuoles suffers from high interobserver variability [84].

When feasible, the assessment of histological markers, mainly fibrosis and steatosis, should be done quantitatively. Stronger correlations have been demonstrated

between ADC and the percentage of fibrotic areas than between ADC and semi-quantitative staging scores of fibrosis ($r = -0.86$ versus $r = -0.5$) [85]. Similarly for steatosis, correlations are stronger when considering the percentage of lipid areas than the visual assessment of fat-containing hepatocyte number by a pathologist [86]. Digital image analysis techniques have been shown to be more robust in their assessment of steatosis, with stronger correlations with MR imaging data [86–88], and methods for histological quantitative assessment of liver fibrosis, through automated image analysis and texture assessment are available [89]. In animal models, the quantification of hydroxyproline content from extracted liver tissues allows a good depiction of fibrosis content in the whole organ [90].

4.2.4 Reproducibility

To be useful in clinical practice, a prognostic imaging biomarker should have a variability lower than the dynamic range of the grades or stages of the disease of interest. The variability is usually assessed as repeatability, i.e. measurements repeated in the same subject over a given time interval with all conditions kept similar, and reproducibility, i.e. measurements repeated under different conditions [91, 92]. Ideally, the volunteer or patient should be removed from the MR scanner and repositioned before the second examination. Time intervals between examinations range from a short 5 min pause [93] to several months [94]. Attention must be paid when comparing reported reproducibility/repeatability values, because they can be reported in two ways. The first consists in reporting within-subject coefficients of variation (CV), i.e. the standard deviation of the mean values divided by the mean [94–96]. To be judged genuine, a difference between healthy volunteers and patients should be above $1.96 \times CV$ [94]. A second method is to report results from a Bland–Altman analysis, i.e. 95% limits-of-agreement calculated from the standard deviation of differences between measurements [29, 71, 97], also known as coefficient of reproducibility or repeatability (CR) (Fig. 4.1). These CR are around twice as high as CV values, and have direct clinical meaning as they can directly be compared to the difference in value between control and diseased liver obtained with the evaluated biomarker.

The variability originates from image acquisition (variability in hardware and software, level of SNR), from patient-related variability (motion, breathing, eating) and from post-processing (ROI placement, processing algorithm). Technical variability can be apprehended with phantom studies. As phantoms containing tissue-equivalent materials are not readily available and difficult to build, some authors prefer to use fluid-filled phantoms simpler in their conception [98, 99]. In that manner, long-term repeatability and cross-site reproducibility ranging from 4% to 20% have been reported [100, 101]. In vivo sources of variability additionally increase this range (e.g. motion and motion correction schemes, shimming, fat suppression, etc.).

In vivo, ADC and *D* repeatability and reproducibility are generally good. CVs ranging from 2% to 16% have been reported for ADC in healthy hepatic

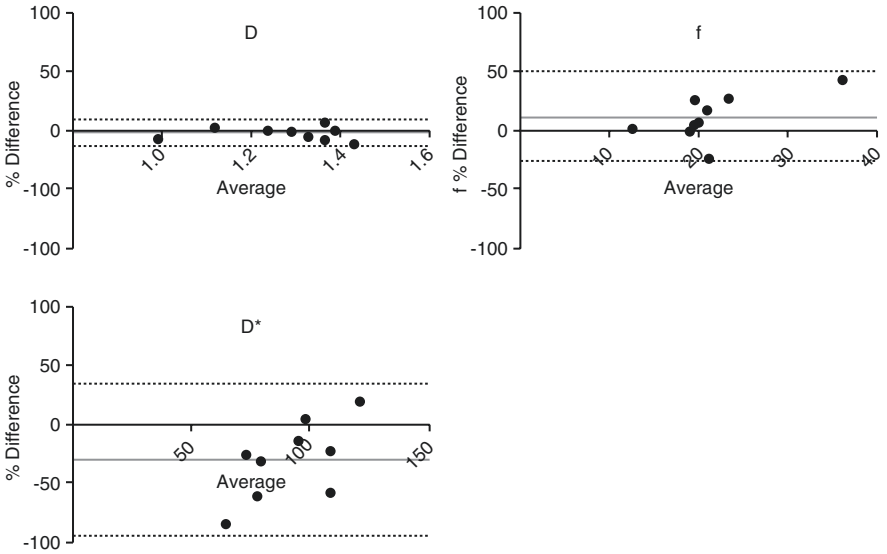

Fig. 4.1 Bland–Altman plots of D, f and D^* calculated in the hepatic parenchyma of nine patients with suspected chronic liver disease and referred for liver biopsy. Data are represented as the percent difference of inter-acquisition measurements (Y-axis) against mean inter-acquisition measurement (X-axis). Mean bias (grey line) and 95% limits-of-agreement (dotted lines) are shown

parenchyma in small animals and humans [77, 93–96, 102], as well as CRs ranging from 4% to 30% [29, 71, 97]. In patients with diffuse liver diseases, ADC variability is similar [99]. Concerning the true diffusion coefficient D, CVs ranging from 5% to 12% and CRs ranging from 5% to 12% have been reported in healthy hepatic parenchyma in small animals and humans, as well as in patients with liver diseases [77, 78, 93, 96, 97, 103]. Perfusion-related parameters, particularly D^*, present worse reproducibility than ADC or D because perfusion only comprises 10–20% of the total DWI signal [104] and because sharp signal loss must be assessed over a relatively short b value dynamic range, making parameter calculation very dependent on SNR [105]. CVs ranging from 8% to 36% have been reported for f in healthy and diseased hepatic parenchyma in small animals and humans [77, 78, 93, 96], as well as CRs ranging from 24% to 32% [97, 103]. D^* is the parameter presenting the worse reproducibility of all diffusion parameters, with reported CVs ranging from 22% to 96% [77, 78, 93, 96] and CRs ranging from 31% to 194% [97, 103].

To limit the variability in determining the diffusion parameters, some authors suggest using an optimized set of b values, as a limited acquisition time would decrease the probability of motion artefacts [103], or using more excitations to improve SNR [71]. D^* variability can be somewhat circumscribed by fixing a range of values for it or use more constraints during the fitting process [103, 104]. However, variability values reported in the literature stay high for this parameter.

4.3 Diffusion-Weighted Imaging for the Diagnosis and Staging of Diffuse Liver Diseases—Rationale and Results

4.3.1 Diagnosis and Staging of Fibrosis

Fibrosis is a consequence of chronic injury within the hepatic parenchyma, and several pathological features occurring during fibrogenesis explain the rationale behind the proposal of using DWI to detect and stage liver fibrosis. First of all, fibrosis results from accumulation of extracellular matrix, and water mobility is hindered by abundant and disorganized glycosaminoglycans, proteoglycans and collagen fibres appearing during fibrogenesis [106]. Capillary functionality is also affected by the increase of collagen fibres and hepatic stellate cells which increase the resistance to blood flow, compress the sinusoids and decrease overall perfusion [107, 108]. As other imaging techniques have shown that perfusion changes during chronic liver diseases [109, 110], the perfusion-related IVIM parameters could be a surrogate marker for fibrosis [39].

Reported results show that liver cirrhosis presents a significantly lower ADC than the healthy hepatic parenchyma with a mean difference in ADC of 20% [39, 52–54, 56, 111–116], with high diagnostic performance (area under the ROC curve (AUC) 0.92–0.96, 93–96% sensitivity, 82–100% specificity [56, 112]). ADC also helps in distinguishing between absence and presence of liver fibrosis in animal models [60, 62, 68, 117], in children with biliary atresia [55, 118] or chronic hepatitis [119, 120] and in patients having chronic liver disease [63, 121], with moderate to good diagnostic performance (mean AUC/sensitivity/specificity of 0.81/82%/72%, ranges of 0.67–0.92, 74–90% and 54–87%, respectively) [54, 63, 66, 72, 117, 120, 122–126].

In addition, worsening of the fibrosis stage is often accompanied by decrease in ADC, with poor to strong correlations reported across studies, ranging from −0.32 to −0.94 [41, 63, 65, 72, 113, 117–136]. Diagnostic performance is moderate to good for predicting significant fibrosis (≥ F2, mean AUC/sensitivity/specificity of 0.83/82%/79%, range of 0.70–0.93, 71–91% and 62–100%, respectively) or advanced fibrosis (≥ F3, mean AUC/sensitivity/specificity of 0.83/85%/78%, range of 0.64–0.93, 65–95% and 64–89%, respectively) [63, 66, 72, 95, 117–127, 129, 131–136] (Fig. 4.2). However, sharp assessment of the fibrosis stage or the severity of cirrhosis is not attained, as nearly all authors report some overlap in ADC values between fibrosis stages or Child–Pugh scores.

Factors explaining this wide range of correlation coefficients and diagnostic performance include the choice of the reference examination (fibrosis staging by a pathologist versus morphometry) and the fact that the percent difference in ADC between fibrosis stages is very close to ADC repeatability. Confounders can also play a role in this discrepancy, as most authors are not taking into account the effect of steatosis. It has been shown that steatosis induces a decrease in ADC [37, 41, 86,

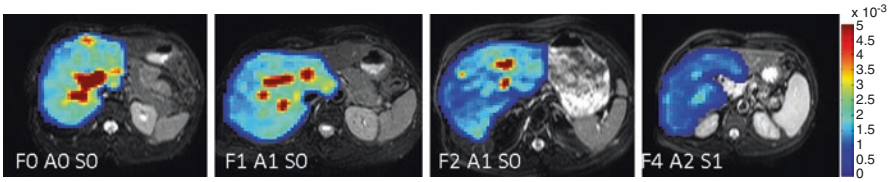

Fig. 4.2 ADC maps superimposed on T2-weighted morphological images in patients with chronic liver disease of varying severity (F: fibrosis, A: activity, S: steatosis scores). ADC decreases with increasing fibrosis stage

137]. Studies using multivariate analysis to separate the effect of fibrosis and steatosis on ADC reported moderate correlation coefficients and AUC/sensitivity/specificity of around 0.8 for predicting moderate and advanced fibrosis [41, 72, 126].

It has also been recommended to exclude patients who underwent hepatectomy, as it is susceptible to affect diffusion parameters because of surgery-induced hepatic vascular alterations [113, 138]. Finally, the acquisition and processing protocols applied throughout these studies greatly vary, especially in their choice and number of *b* values used for ADC calculation, meaning that the perfusion weighting in each reported ADC varies from study to study [27, 139]. Perfusion would be an indicator of fibrosis, and the IVIM approach has been underlined as beneficial at several occasions. For example, Annet et al. [65] showed that the strong correlation that was observed in vivo between ADC and the severity of hepatic fibrosis in a CCl_4 rat model disappeared once the animal was dead. Both Wu et al. [74] and Manning et al. [108] reported differences in IVIM parameters between fibrosis stages, whereas they found no difference in ADC.

To further investigate the effect of fibrosis on diffusion parameters, authors have used the IVIM approach to assess how fibrosis would independently affect the molecular diffusion coefficient and the perfusion-related parameters. For the former, some studies showed a decrease in D when fibrosis increases, in animal models [62, 68, 85] and in patients [78, 140]. However, nearly all of these studies do not take into consideration the potential effect of steatosis on D. In contrast, a lot of studies, some conducted with multivariate analysis or exclusion of steatotic patients [39, 41, 74, 108, 141], do not show significant differences in D between healthy and fibrotic/cirrhotic livers or across fibrosis stages [39, 41, 73, 74, 108, 115, 124, 128, 141].

Regarding perfusion-related parameters, the majority of studies report a change in f or in D^* when fibrosis worsens. The perfusion fraction f was shown to decrease with the progression of fibrosis in animal models [128], in chronic hepatitis C patients [78], in NAFLD [108, 141] and in chronic liver diseases [73, 74, 124], with variable efficacy (reported correlation coefficients from −0.2 to −0.72, AUC around 0.7). The perfusion fraction also helps distinguishing between Child–Pugh classes in cirrhotic patients [115]. The perfusion-related diffusion coefficient D^* has similarly been shown to decrease in liver fibrosis [62, 140] and cirrhosis [39, 115] with

moderate to strong correlation [73, 74] and moderate to high diagnostic performance [73, 140].

The absence of change in perfusion-related parameters observed in some studies may be explained by the high uncertainty of their determination, especially for D^* [78], and in numerous studies it was chosen not to calculate D^*. Finally, the apparent discrepancy between the behaviour of f and D^* for the assessment of fibrosis (very often, one varies while the other does not) might be explained by the fact that these two parameters reflect two different perfusion properties, the vascular volume and the endovascular blood flow velocity, respectively, and that these properties may not be equally affected by fibrogenesis [39, 115, 142]. Stable values of f during fibrogenesis could also be partly explained by the hepatic buffer response, namely a decrease of the portal venous flow inducing arterial vasodilation [143–145].

In conclusion, hepatic fibrosis decreases the ADC and the IVIM perfusion-related parameters, f and D^*. Diagnostic performance for predicting significant and advanced fibrosis is moderate to high, depending on the patient population, the acquisition and processing protocols and the potential influence of confounders (especially steatosis). According to some authors, this diagnostic performance can be similar to the one provided with other imaging techniques, such as transient elastography and acoustic radiation force impulse imaging [74, 95]. However, the applicability of DWI for staging liver fibrosis is mitigated, as overlaps exist between fibrosis stages, with percent change in diffusion parameters very close to repeatability levels.

Both transient elastography [134] and MR elastography [41, 73, 121, 136] generally provide higher diagnostic performance than DWI. Whereas transient elastography may present high variability and is operator-dependent [74], MR elastography is not operator-dependent, is not influenced by the presence of steatosis or ascites [41, 146, 147], and its diagnostic ability for predicting fibrosis stage 2 or above can reach AUC of 0.99, with sensitivity and specificity above 90% [73, 121, 136]. The disadvantage of MR elastography is that it necessitates special hardware and processing algorithms, and is not readily available. In its absence, DWI is an alternative to predict significant and advanced fibrosis and cirrhosis. Multiparametric approaches have also been proposed to stage fibrosis, including ADC as one of the parameters of interest, with diagnostic performances coming close to the one of MR elastography [125, 126].

4.3.2 Assessment of Steatosis

Steatosis, or the accumulation of lipids within the hepatocytes, affects the diffusion parameters in several ways. First, the protons bound to fat molecules have a lower diffusivity than water protons [148] and this decreased diffusivity can affect the ADC. This effect is not prominent as most studies are conducted with fat saturation [27, 149]. However, even when using conventional fat saturation schemes, such as spatial-spectral pulses, fat can still contribute to the observed signal because of the incomplete saturation of the fat peaks between 4.2 and 5.7 ppm, which represent up

to 9% of the total fat signal [150]. Since fat has lower diffusivity than water, this contribution from persistent fat signal will artificially decrease the ADC, and this decrease is more pronounced when the proton density fat fraction is high [37, 151]. Fortunately, this effect remains marginal (at most 10% change in ADC) [108, 141]. Correction of the signal intensities on DW images for fat fraction can be considered to account for incomplete fat suppression [37, 108]. In addition, preliminary studies determining the most adapted fat saturation scheme are recommended, as quality and homogeneity of fat saturation depend on MR field strength and motion compensation scheme [40, 152, 153].

Second, lipid vacuoles within hepatocytes will enlarge the hepatocytes and hinder the diffusion of intracellular and extracellular water [68, 79, 151, 154]. This would result in decreased molecular diffusion.

Third, microcirculation can be modified by swollen, fat-filled hepatocytes narrowing the sinusoids in NAFLD, as well as by sinusoidal capillarization and vasoconstriction in NASH [155–158]. With other imaging methods, decrease in hepatic perfusion because of steatosis has been shown [157, 159, 160].

Overall, the reported results show that all diffusion parameters, ADC, D, f and D^*, decrease when steatosis increases [37, 79, 86, 96, 137].

Decrease of ADC with steatosis has been demonstrated in a NAFLD/NASH rabbit model [96], in patients with NAFLD [41, 108] or viral hepatitis [41] and in patients with chronic liver disease [154, 161]. However, the relationship between ADC and fat fraction is moderate at best ($r^2 = 0.28$ reported by Bulow et al. [154], $r = -0.39$ reported by Poyraz et al. [161]). The lack of strong correlation may be explained by several factors, including a low number of steatotic patients in the total cohort, with less than 20% of the cohort presenting more than 5% steatosis [72, 126, 134], the fact that concomitant factors were not taken into consideration, especially fibrosis [88, 104, 134], and the lack of sensitivity of the composite ADC parameter. Indeed, a significant decrease in D in steatotic patients compared to non-steatotic patients has been shown in two studies, whereas ADC was not affected [137, 141].

Nearly all studies show that D decreases with increasing steatosis, even for small fat fractions (Fig. 4.3). A phantom study demonstrated that D was strongly correlated to phantom fat content, with correlation coefficients above −0.97 [137]. A strong correlation ($r = -0.81$) between D and the percent areas occupied by lipid vacuoles has also been demonstrated in a mouse model of NASH [86]. In diverse

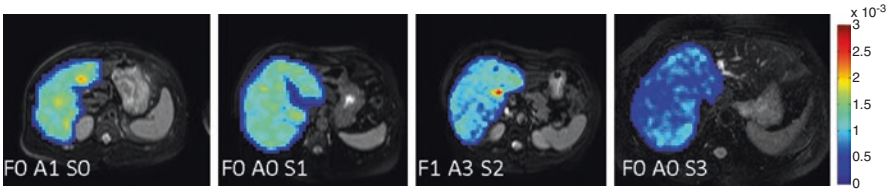

Fig. 4.3 D maps superimposed on T2-weighted morphological images in patients with chronic liver disease of varying severity (F: fibrosis, A: activity, S: steatosis scores). D decreases with increasing grade of steatosis

patient populations (NAFLD, hepatitis, diabetic or general diffuse liver disease), decrease in D occurs when steatosis increases [41, 79, 108, 124, 137, 140, 141], albeit with moderate correlation (r between −0.44 and −0.59) [41, 79, 124, 151]. This relationship was even observed in healthy volunteers across very low levels of steatosis (below 2.75% and between 2.75% and 5.5% of fat content) [151].

Regarding the perfusion-related parameters, few IVIM studies showed a relationship between f or D^* and steatosis [79, 96, 124]. A decrease in f has been observed in a NAFLD/NASH rabbit model, with strong correlation (−0.83) and excellent diagnostic performance (AUC above 0.9 for any grade) [96]. In contrast, in two studies involving diabetic patients and patients with diffuse liver disease, f was found to increase when steatosis increased, with poor to moderate correlation [79, 124]. Only one study reports an effect, namely a decrease, of steatosis on D^* [79]. The fact that the two studies performed in patients reported an increase in f whereas the hepatic perfusion is known to decrease in the presence of steatosis [157] may be explained by several factors. First, a dependence of f on TE has been reported, because of the T2 difference between blood and tissue [45, 79]. Second, differences in NASH between animal models and humans as well as differences in the percentage of NASH patients between studies might also partially explain the discordant results [137, 156].

In contrast, no difference in f or D^* between steatotic and non-steatotic livers was observed in other IVIM studies [41, 104, 108, 137, 140, 141, 151]. Technical factors, including insufficient sampling of the low b values [108, 141, 151] and high variability of the perfusion-related parameters [104] may partially explain these observations.

From the literature, the diagnostic performance of DWI to assess steatosis is moderate at best in patients, and relies on a robust determination of D and, to a lesser extent, of f. More efficient MR methods exist to grade liver steatosis, as for example MR spectroscopy [88]. However, it only provides information from a small volume and necessitates complex post-processing [7]. Chemical-shift-based fat imaging methods with $T2^*$ correction and fat spectrum modelling has become the reference method for assessing fat content within the liver [162, 163], because of its ease of implementation and interpretation, as well as its good agreement with MR spectroscopy and histology [164–167].

While it provides information on the pathological changes occurring in tissue microstructure and microcirculation of liver steatosis, DWI with IVIM approach is not really recommended for the diagnosis and staging of steatosis. However, because of the potential effects of steatosis on ADC and IVIM parameters, steatosis has to be considered as a serious confounding factor in liver DWI studies, especially for the assessment of fibrosis, as we have shown in a recent study performed in patients with chronic liver disease that steatosis was more strongly associated with diffusion parameters than fibrosis did [41].

4.3.3 Assessment of Inflammation and Hepatocyte Degeneration

Activity in chronic liver diseases consists in infiltration of inflammatory cells, hepatocyte ballooning and necrosis, modified regional blood flow and increase in the free water pool (oedema). All these factors are susceptible to affect the diffusion parameters [57, 66, 124]. In the literature, the performance of DWI for diagnosing and grading inflammation goes from null to moderate, regardless of the patient aetiology or the animal model.

A moderate correlation between D and inflammation stage was observed in a methionine-deficient choline-deficient diet mouse model ($r = -0.65$) [86]. In patients with chronic liver disease, ADC was found to be significantly decreased in inflammation [63, 119] with moderate to good diagnostic performance to discriminate ≥ A1 (AUC = 0.83, sensitivity 75%, specificity 79%) and ≥ A2 (AUC = 0.76, sensitivity 67%, specificity 79%) [63, 133]. Moderate correlations between −0.3 and −0.54 have been reported [63, 119, 133]. Results were similar in patients with chronic viral hepatitis, with moderate correlation between ADC and hepatic activity index ($\rho = -0.62$) [130] and good diagnostic performance for diagnosing ≥ A1 (AUC = 0.89, sensitivity 81%, specificity 83%), ≥ A2 (AUC = 0.81, sensitivity 73%, specificity 80%) and = A3 (AUC = 0.84, sensitivity 77%, specificity 83%) [66].

However, all these studies depicting moderate relationships between diffusion parameters and inflammation have in common that they do not consider other factors which effects on diffusion parameters have been clearly demonstrated, namely steatosis and fibrosis. To take into consideration the effects of these confounders on ADC, some authors have used multivariate or subgroup analysis [41, 72, 96, 113, 121, 124, 126]. In these cases, the effect of inflammation on ADC is shown to be weak at best, if not absent. Slight differences in ADC values in the order of 8–16% were reported between A0 and A1–A3 livers in patients with chronic liver disease [121], between A1 and A3 hepatitis patients [54] and between A0–A1 and A2–A3 grades in chronic HCV patients [95]. In patients referred for liver biopsy, ADC weakly correlated with the overall modified hepatic activity index ($\rho = -0.23$) or the modified hepatic activity index 1 score for interface hepatitis ($\rho = -0.31$) in univariate testing. However, multivariate analysis revealed that neither of these two scores contributed to the observed ADC changes [72]. Similarly in diffuse liver disease patients, ADC and f were found differ across inflammation grades, but a factorial "fibrosis-inflammation" analysis of variance revealed that the true effect of these diffusion parameter changes was caused by fibrosis, and not inflammation [124]. In a NAFLD/NASH rabbit model, the perfusion fraction decreased at the onset of NASH but it was demonstrated through multiple regression analysis that this was caused by steatosis, and not inflammation [96]. Finally, several studies have not demonstrated an effect of inflammation on ADC or on IVIM parameters, in animal models [85], in viral hepatitis patients [41, 57, 113, 134] and in NAFLD patients [108, 141].

Initially, noninvasive serological tests have been proposed to replace liver biopsy to detect and quantify hepatic inflammatory activity (such as serum aminotransferases). However, these tests have shown limited diagnostic performance. Several MR methods have also been proposed, including T1 mapping [168], multifrequency MR elastography [169, 170], gadoxetic acid-enhanced imaging [171], MR imaging with ultrasmall superparamagnetic iron oxide particles [172] and $^{1}H/^{31}P$ spectroscopy [173, 174]. The benefit of these approaches in assessing liver inflammation remains to be proven.

4.3.4 Effect of Iron Overload

The presence of iron deposits in the liver parenchyma induces local susceptibility changes and shortens T2 and T2*, hence decreasing the SNR. DW images will be noisier, especially the ones acquired with high *b* values, which may impact ADC calculation [154, 175, 176]. Indeed, several studies have reported lower liver ADC values in patients with moderate and high iron content compared to those without iron deposits [34, 124, 154, 176]. Reports indicate various levels of correlation between ADC and iron concentration, from poor [124] to strong [176]. Other methods have been proven more robust to detect and quantify hepatic iron concentrations, such as approaches involving signal intensity measurements on T2- and T2*-weighted images [177, 178], T2- and T2* relaxation-mapping [179, 180] or susceptibility mapping [181].

Other consequences of iron deposits are that interpretation of DW images and measurement of ADC are not feasible because of a pronounced loss in SNR [182], or that the local magnetic field inhomogeneities induce local shifting in *b* values, hence errors in ADC measurements [176]. It has been recommended to exclude patients with iron overload from DWI studies [66, 161], or to perform T2* imaging for ADC correction in patients with chronic liver diseases [176].

4.3.5 Results in Vascular Liver Diseases and Liver Transplantation

Patients with less common diffuse liver diseases (e.g. Budd–Chiari syndrome, Wilson disease or toxic hepatitis) are generally pooled with viral hepatitis and NAFLD patients in medical imaging studies [28, 72, 124, 176, 183, 184]. The MR methods of choice to assess these diseases are still conventional: T1- and T2-weighted imaging and gadolinium-enhanced MR imaging for Budd–Chiari syndrome, for example [185]. Nevertheless, several studies have investigated the benefit of using DWI in assessing vascular hepatic diseases. While the results are debated for the distinction between benign and malignant portal vein thrombosis [186–188], ADC is affected by hepatic congestion caused by moderate pulmonary hypertension [189], by parenchymal changes induced by chemotherapy [190] and by significant

portal vein stenosis [191]. Moreover, decreased ADC has been shown to reflect the no-reflow zones in a rodent model of reperfused partial liver infarction [192]. Finally, ADC has been reported to decrease following orthotopic liver transplantation when acute or chronic rejection, fibrosis recurrence or fat infiltration was observed [193].

4.4 Future Perspectives

As we saw in the previous paragraphs, diffusion parameters present moderate diagnostic performance, and would scarcely be considered as the first-intent imaging biomarker for staging fibrosis or assessing steatosis and inflammation. However, their relative easy applicability (compared to MR elastography, for example) and the common use of DWI in clinical routine have led some authors to explore new perspectives for using DWI in the diagnosis of diffuse liver diseases.

4.4.1 Texture Analysis

Distribution of fibrosis and inflammation within the liver can be heterogeneous at several scales from the lobule to the lobar level [8]. Similarly, liver fat infiltration can present a heterogeneous pattern within the parenchyma [161]. These patterns can differ between diseases (e.g. between viral hepatitis and NAFLD for fibrosis) [194]. These observations suggest that summarizing the whole parenchyma features into a ROI-based mean ADC may be simplistic and that locoregional information in ADC maps may bring complementary information on the disease.

Histogram features such as median, standard deviation and entropy have been investigated in their ability to detect fibrosis compared with mean ADC [66, 82]. Fujimoto et al. observed that entropy ADC can diagnose fibrosis as early as F1 and inflammatory activity as early as A1, earlier than mean ADC (F2 and A2, respectively) with excellent diagnostic performance (e.g. 91% sensitivity and 92% specificity reported for inflammation) [66].

Moreover, texture analysis provides interesting avenues, as it quantifies the organisation of patterns and sub-patterns within a tissue. However texture analysis of ADC maps of or DW images has been rarely used in diffuse liver diseases [82] as it stays more predominant, albeit scarce, for liver tumour assessment [195–197]. A more widespread use is hindered by the fact that the performance of radiomics features depends on their stability. This can be impacted by numerous acquisition and processing factors, such as the *b* values used for DWI acquisition, the presence of motion artefacts, the level of noise, the image resolution and the method used for grey level quantization [198–200]. Further studies are needed to fully investigate the influence of acquisition and processing parameters on the stability of radiomics features and propose standardized protocols [201].

4.4.2 DWI at Different Spatial Scales

A parameter that could influence the diagnostic performance of DWI for liver fibrosis is the gradient separation time Δ. This parameter dictates the time left to the water molecules to diffuse and encounter obstacles from the microenvironment, i.e. at which length scale the tissue is probed. Obstacles at a subcellular scale can be probed with very short diffusion intervals through the use of motion-probing oscillating gradients rather than pulsed gradients. This technique has been called "OGSE" (for oscillating gradient spin-echo) [202] or "temporal diffusion spectroscopy" [203]. Research groups have shown the potential of this approach to probe cell dimension, differentiate between mitotic and non-mitotic cells [204] or assess nuclear size and organelle integrity [202, 205].

In contrast, using long diffusion intervals directs the sensitivity of DWI towards larger, supracellular obstacles such as collagen fibres [68]. It has been shown that the hepatic ADC and D decrease when the gradient separation time Δ increases [68, 206]. Moreover, with progressively higher Δ, the percentage of change in D between fibrotic stages has been observed to enlarge [68], whereas with conventional diffusion parameters, D does not change significantly with fibrosis stage. ADC and D calculated with a long (186 ms) Δ DWI acquisition have also been shown to provide better diagnostic performance for fibrosis staging than a conventional acquisition (Δ = 35 ms) in CCl_4-induced fibrotic rats, with mean AUC, sensitivity and specificity around 0.92, 88% and 90% for long-Δ DWI versus 0.82, 85% and 78% for conventional DWI [207].

These preliminary studies suggest that long-Δ DWI has the potential for being a more efficient biomarker for fibrosis staging than classical DWI. One caveat is that with long gradient separation times around 180 ms, stimulated-echo acquisition mode DWI is needed to yield sufficient SNR [68, 206].

4.4.3 DWI for Measuring Mechanical Properties

A few years ago, Le Bihan et al. [208] proposed using DWI to assess the mechanical properties of tissues. Indeed, mechanical properties are in large part determined by the concentration of stiff fibre materials such as collagen in the extracellular matrix, and such materials are thought to deviate water diffusivity from its classical Gaussian behaviour. A method sensitive to non-Gaussian diffusivity might be able to probe the fibre content of a tissue [209]. In 15 chronic liver disease patients, Le Bihan et al. showed a correlation between the liver stiffness and ADC calculated with two b values, one being above 1000 s/mm^2, and between liver stiffness and the index of non-Gaussianity [208]. A subsequent study has been performed by the same research group in 74 patients with chronic liver disease, showing that the diffusion-based shear modulus is in good agreement with

the stiffness calculated with MR elastography, with AUC of 0.72 for predicting fibrosis stage 2 and above [210]. However, more studies are needed to validate the diagnostic performance of this method, as MR elastography presents much higher AUCs [73, 121, 136].

4.5 Conclusion

As a noninvasive MR method which does not necessitate complex hardware and processing, DWI has the potential to help assessing diffuse liver diseases because it informs about tissue microstructure and perfusion. Fibrosis significantly decreases ADC, the perfusion fraction f and the perfusion-related diffusion coefficient D^*. While inflammation does not seem to affect diffusion parameters, steatosis and iron are confounding factors which have to be taken into consideration when performing DWI in the liver. Avenues for stabilizing parameter determination and furthering the information brought by DWI are currently explored, to increase its applicability and benefit in clinical work.

References

1. Schuppan D, Afdhal NH. Liver cirrhosis. Lancet. 2008;371(9615):838–51.
2. Gressner AM. The cell biology of liver fibrogenesis – an imbalance of proliferation, growth arrest and apoptosis of myofibroblasts. Cell Tissue Res. 1998;292(3):447–52.
3. Lauer GM, Walker BD. Hepatitis C virus infection. N Engl J Med. 2001;345(1):41–52.
4. Angulo P. Nonalcoholic fatty liver disease. N Engl J Med. 2002;346(16):1221–31.
5. Starley BQ, Calcagno CJ, Harrison SA. Nonalcoholic fatty liver disease and hepatocellular carcinoma: a weighty connection. Hepatology. 2010;51(5):1820–32.
6. Doycheva I, Patel N, Peterson M, Loomba R. Prognostic implication of liver histology in patients with nonalcoholic fatty liver disease in diabetes. J Diabetes Complicat. 2013;27(3):293–300.
7. Taouli B, Ehman RL, Reeder SB. Advanced MRI methods for assessment of chronic liver disease. AJR Am J Roentgenol. 2009;193(1):14–27.
8. Kovac JD, Weber MA. Primary biliary cirrhosis and primary sclerosing cholangitis: an update on MR imaging findings with recent developments. J Gastrointestin Liver Dis. 2016;25(4):517–24.
9. Hirschfield GM, Karlsen TH, Lindor KD, Adams DH. Primary sclerosing cholangitis. Lancet. 2013;382(9904):1587–99.
10. Queiroz-Andrade M, Blasbalg R, Ortega CD, Rodstein MA, Baroni RH, Rocha MS, et al. MR imaging findings of iron overload. Radiographics. 2009;29(6):1575–89.
11. Angulo P, Kleiner DE, Dam-Larsen S, Adams LA, Bjornsson ES, Charatcharoenwitthaya P, et al. Liver fibrosis, but no other histologic features, is associated with long-term outcomes of patients with nonalcoholic fatty liver disease. Gastroenterology. 2015;149(2):389–97, e10.
12. Loomba R, Chalasani N. The hierarchical model of NAFLD: prognostic significance of histologic features in NASH. Gastroenterology. 2015;149(2):278–81.
13. Bedossa P, Patel K. Biopsy and noninvasive methods to assess progression of nonalcoholic fatty liver disease. Gastroenterology. 2016;150(8):1811–22, e4.
14. de Franchis R. Expanding consensus in portal hypertension: report of the Baveno VI consensus workshop: stratifying risk and individualizing care for portal hypertension. J Hepatol. 2015;63(3):743–52.

15. Ghany MG, Strader DB, Thomas DL, Seeff LB. Diagnosis, management, and treatment of hepatitis C: an update. Hepatology. 2009;49(4):1335–74.
16. Yano M, Kumada H, Kage M, Ikeda K, Shimamatsu K, Inoue O, et al. The long-term pathological evolution of chronic hepatitis C. Hepatology. 1996;23(6):1334–40.
17. Bedossa P. Utility and appropriateness of the fatty liver inhibition of progression (FLIP) algorithm and steatosis, activity, and fibrosis (SAF) score in the evaluation of biopsies of nonalcoholic fatty liver disease. Hepatology. 2014;60(2):565–75.
18. Bedossa P, Carrat F. Liver biopsy: the best, not the gold standard. J Hepatol. 2009;50(1):1–3.
19. Saadeh S, Cammell G, Carey WD, Younossi Z, Barnes D, Easley K. The role of liver biopsy in chronic hepatitis C. Hepatology. 2001;33(1):196–200.
20. Rockey DC, Caldwell SH, Goodman ZD, Nelson RC, Smith AD. Liver biopsy. Hepatology. 2009;49(3):1017–44.
21. Regev A, Berho M, Jeffers LJ, Milikowski C, Molina EG, Pyrsopoulos NT, et al. Sampling error and intraobserver variation in liver biopsy in patients with chronic HCV infection. Am J Gastroenterol. 2002;97(10):2614–8.
22. Goldin RD, Goldin JG, Burt AD, Dhillon PA, Hubscher S, Wyatt J, et al. Intra-observer and inter-observer variation in the histopathological assessment of chronic viral hepatitis. J Hepatol. 1996;25(5):649–54.
23. Kleiner DE, Brunt EM, Van Natta M, Behling C, Contos MJ, Cummings OW, et al. Design and validation of a histological scoring system for nonalcoholic fatty liver disease. Hepatology. 2005;41(6):1313–21.
24. Imbert-Bismut F, Ratziu V, Pieroni L, Charlotte F, Benhamou Y, Poynard T. Biochemical markers of liver fibrosis in patients with hepatitis C virus infection: a prospective study. Lancet. 2001;357(9262):1069–75.
25. Poynard T, Ratziu V, Charlotte F, Messous D, Munteanu M, Imbert-Bismut F, et al. Diagnostic value of biochemical markers (NashTest) for the prediction of non alcoholo steato hepatitis in patients with non-alcoholic fatty liver disease. BMC Gastroenterol. 2006;6:34.
26. Van Beers BE, Garteiser P, Leporq B, Rautou PE, Valla D. Quantitative imaging in diffuse liver diseases. Semin Liver Dis. 2017;37(3):243–58.
27. Taouli B, Koh DM. Diffusion-weighted MR imaging of the liver. Radiology. 2010;254(1):47–66.
28. Do RK, Chandarana H, Felker E, Hajdu CH, Babb JS, Kim D, et al. Diagnosis of liver fibrosis and cirrhosis with diffusion-weighted imaging: value of normalized apparent diffusion coefficient using the spleen as reference organ. AJR Am J Roentgenol. 2010;195(3):671–6.
29. Kwee TC, Takahara T, Koh DM, Nievelstein RA, Luijten PR. Comparison and reproducibility of ADC measurements in breathhold, respiratory triggered, and free-breathing diffusion-weighted MR imaging of the liver. J Magn Reson Imaging. 2008;28(5):1141–8.
30. Taouli B, Sandberg A, Stemmer A, Parikh T, Wong S, Xu J, et al. Diffusion-weighted imaging of the liver: comparison of navigator triggered and breathhold acquisitions. J Magn Reson Imaging. 2009;30(3):561–8.
31. Jiang H, Chen J, Gao R, Huang Z, Wu M, Song B. Liver fibrosis staging with diffusion-weighted imaging: a systematic review and meta-analysis. Abdom Radiol (NY). 2017;42(2):490–501.
32. Neil JJ, Bretthorst GL. On the use of Bayesian probability theory for analysis of exponential decay data: an example taken from intravoxel incoherent motion experiments. Magn Reson Med. 1993;29(5):642–7.
33. Dietrich O, Heiland S, Sartor K. Noise correction for the exact determination of apparent diffusion coefficients at low SNR. Magn Reson Med. 2001;45(3):448–53.
34. Bruegel M, Holzapfel K, Gaa J, Woertler K, Waldt S, Kiefer B, et al. Characterization of focal liver lesions by ADC measurements using a respiratory triggered diffusion-weighted single-shot echo-planar MR imaging technique. Eur Radiol. 2008;18(3):477–85.
35. Murtz P, Flacke S, Traber F, van den Brink JS, Gieseke J, Schild HH. Abdomen: diffusion-weighted MR imaging with pulse-triggered single-shot sequences. Radiology. 2002;224(1):258–64.

36. Girometti R, Furlan A, Esposito G, Bazzocchi M, Como G, Soldano F, et al. Relevance of b-values in evaluating liver fibrosis: a study in healthy and cirrhotic subjects using two single-shot spin-echo echo-planar diffusion-weighted sequences. J Magn Reson Imaging. 2008;28(2):411–9.
37. Hansmann J, Hernando D, Reeder SB. Fat confounds the observed apparent diffusion coefficient in patients with hepatic steatosis. Magn Reson Med. 2013;69(2):545–52.
38. Taouli B, Beer AJ, Chenevert T, Collins D, Lehman C, Matos C, et al. Diffusion-weighted imaging outside the brain: consensus statement from an ISMRM-sponsored workshop. J Magn Reson Imaging. 2016;44(3):521–40.
39. Luciani A, Vignaud A, Cavet M, Nhieu JT, Mallat A, Ruel L, et al. Liver cirrhosis: intravoxel incoherent motion MR imaging--pilot study. Radiology. 2008;249(3):891–9.
40. Takayama Y, Nishie A, Asayama Y, Ishigami K, Kakihara D, Ushijima Y, et al. Optimization and clinical feasibility of free-breathing diffusion-weighted imaging of the liver: comparison with respiratory-triggered diffusion-weighted imaging. Magn Reson Med Sci. 2015;14(2):123–32.
41. Leitao HS, Doblas S, Garteiser P, d'Assignies G, Paradis V, Mouri F, et al. Hepatic fibrosis, inflammation, and steatosis: influence on the MR viscoelastic and diffusion parameters in patients with chronic liver disease. Radiology. 2017;283(1):98–107.
42. Nasu K, Kuroki Y, Fujii H, Minami M. Hepatic pseudo-anisotropy: a specific artifact in hepatic diffusion-weighted images obtained with respiratory triggering. MAGMA. 2007;20(4):205–11.
43. Taouli B, Martin AJ, Qayyum A, Merriman RB, Vigneron D, Yeh BM, et al. Parallel imaging and diffusion tensor imaging for diffusion-weighted MRI of the liver: preliminary experience in healthy volunteers. AJR Am J Roentgenol. 2004;183(3):677–80.
44. Stanisz GJ, Odrobina EE, Pun J, Escaravage M, Graham SJ, Bronskill MJ, et al. T1, T2 relaxation and magnetization transfer in tissue at 3T. Magn Reson Med. 2005;54(3):507–12.
45. Lemke A, Laun FB, Simon D, Stieltjes B, Schad LR. An in vivo verification of the intravoxel incoherent motion effect in diffusion-weighted imaging of the abdomen. Magn Reson Med. 2010;64(6):1580–5.
46. Shiehmorteza M, Sirlin CB, Wolfson T, Gamst A, Soumekh AE, Heaton SP, et al. Effect of shot number on the calculated apparent diffusion coefficient in phantoms and in human liver in diffusion-weighted echo-planar imaging. J Magn Reson Imaging. 2009;30(3):547–53.
47. Hollingsworth KG, Lomas DJ. Influence of perfusion on hepatic MR diffusion measurement. NMR Biomed. 2006;19(2):231–5.
48. Pazahr S, Nanz D, Rossi C, Chuck N, Stenger I, Wurnig MC, et al. Magnetic resonance imaging of the liver: apparent diffusion coefficients from multiexponential analysis of b values greater than 50 s/mm^2 do not respond to caloric intake despite increased portal-venous blood flow. Investig Radiol. 2014;49(3):138–46.
49. Jajamovich GH, Dyvorne H, Donnerhack C, Taouli B. Quantitative liver MRI combining phase contrast imaging, elastography, and DWI: assessment of reproducibility and postprandial effect at 3.0 T. PLoS One. 2014;9(5):e97355.
50. Chiu FY, Jao JC, Chen CY, Liu GC, Jaw TS, Chiou YY, et al. Effect of intravenous gadolinium-DTPA on diffusion-weighted magnetic resonance images for evaluation of focal hepatic lesions. J Comput Assist Tomogr. 2005;29(2):176–80.
51. Choi JS, Kim MJ, Choi JY, Park MS, Lim JS, Kim KW. Diffusion-weighted MR imaging of liver on 3.0-Tesla system: effect of intravenous administration of gadoxetic acid disodium. Eur Radiol. 2010;20(5):1052–60.
52. Taouli B, Vilgrain V, Dumont E, Daire JL, Fan B, Menu Y. Evaluation of liver diffusion isotropy and characterization of focal hepatic lesions with two single-shot echo-planar MR imaging sequences: prospective study in 66 patients. Radiology. 2003;226(1):71–8.
53. Girometti R, Esposito G, Bagatto D, Avellini C, Bazzocchi M, Zuiani C. Is water diffusion isotropic in the cirrhotic liver? A study with diffusion-weighted imaging at 3.0 Tesla. Acad Radiol. 2012;19(1):55–61.

54. Tosun M, Inan N, Sarisoy HT, Akansel G, Gumustas S, Gurbuz Y, et al. Diagnostic performance of conventional diffusion weighted imaging and diffusion tensor imaging for the liver fibrosis and inflammation. Eur J Radiol. 2013;82(2):203–7.
55. Liu B, Cai J, Zhu J, Zheng H, Zhang Y, Wang L. Diffusion tensor imaging for evaluating biliary atresia in infants and neonates. PLoS One. 2016;11(12):e0168477.
56. Girometti R, Furlan A, Bazzocchi M, Soldano F, Isola M, Toniutto P, et al. Diffusion-weighted MRI in evaluating liver fibrosis: a feasibility study in cirrhotic patients. Radiol Med. 2007;112(3):394–408.
57. Koinuma M, Ohashi I, Hanafusa K, Shibuya H. Apparent diffusion coefficient measurements with diffusion-weighted magnetic resonance imaging for evaluation of hepatic fibrosis. J Magn Reson Imaging. 2005;22(1):80–5.
58. Yamada I, Aung W, Himeno Y, Nakagawa T, Shibuya H. Diffusion coefficients in abdominal organs and hepatic lesions: evaluation with intravoxel incoherent motion echo-planar MR imaging. Radiology. 1999;210(3):617–23.
59. Fauerholdt L, Schlichting P, Christensen E, Poulsen H, Tygstrup N, Juhl E. Conversion of micronodular cirrhosis into macronodular cirrhosis. Hepatology. 1983;3(6):928–31.
60. Cheung JS, Fan SJ, Gao DS, Chow AM, Man K, Wu EX. Diffusion tensor imaging of liver fibrosis in an experimental model. J Magn Reson Imaging. 2010;32(5):1141–8.
61. Lee Y, Kim H. Assessment of diffusion tensor MR imaging (DTI) in liver fibrosis with minimal confounding effect of hepatic steatosis. Magn Reson Med. 2015;73(4):1602–8.
62. Chow AM, Gao DS, Fan SJ, Qiao Z, Lee FY, Yang J, et al. Liver fibrosis: an intravoxel incoherent motion (IVIM) study. J Magn Reson Imaging. 2012;36(1):159–67.
63. Taouli B, Chouli M, Martin AJ, Qayyum A, Coakley FV, Vilgrain V. Chronic hepatitis: role of diffusion-weighted imaging and diffusion tensor imaging for the diagnosis of liver fibrosis and inflammation. J Magn Reson Imaging. 2008;28(1):89–95.
64. Padhani AR, Liu G, Koh DM, Chenevert TL, Thoeny HC, Takahara T, et al. Diffusion-weighted magnetic resonance imaging as a cancer biomarker: consensus and recommendations. Neoplasia. 2009;11(2):102–25.
65. Annet L, Peeters F, Abarca-Quinones J, Leclercq I, Moulin P, Van Beers BE. Assessment of diffusion-weighted MR imaging in liver fibrosis. J Magn Reson Imaging. 2007;25(1):122–8.
66. Fujimoto K, Tonan T, Azuma S, Kage M, Nakashima O, Johkoh T, et al. Evaluation of the mean and entropy of apparent diffusion coefficient values in chronic hepatitis C: correlation with pathologic fibrosis stage and inflammatory activity grade. Radiology. 2011;258(3):739–48.
67. Colagrande S, Pasquinelli F, Mazzoni LN, Belli G, Virgili G. MR-diffusion weighted imaging of healthy liver parenchyma: repeatability and reproducibility of apparent diffusion coefficient measurement. J Magn Reson Imaging. 2010;31(4):912–20.
68. Zhou IY, Gao DS, Chow AM, Fan S, Cheung MM, Ling C, et al. Effect of diffusion time on liver DWI: an experimental study of normal and fibrotic livers. Magn Reson Med. 2014;72(5):1389–96.
69. Farraher SW, Jara H, Chang KJ, Hou A, Soto JA. Liver and spleen volumetry with quantitative MR imaging and dual-space clustering segmentation. Radiology. 2005;237(1):322–8.
70. Yoshikawa T, Kawamitsu H, Mitchell DG, Ohno Y, Ku Y, Seo Y, et al. ADC measurement of abdominal organs and lesions using parallel imaging technique. AJR Am J Roentgenol. 2006;187(6):1521–30.
71. Chen X, Qin L, Pan D, Huang Y, Yan L, Wang G, et al. Liver diffusion-weighted MR imaging: reproducibility comparison of ADC measurements obtained with multiple breath-hold, free-breathing, respiratory-triggered, and navigator-triggered techniques. Radiology. 2014;271(1):113–25.
72. Bonekamp S, Torbenson MS, Kamel IR. Diffusion-weighted magnetic resonance imaging for the staging of liver fibrosis. J Clin Gastroenterol. 2011;45(10):885–92.
73. Ichikawa S, Motosugi U, Morisaka H, Sano K, Ichikawa T, Enomoto N, et al. MRI-based staging of hepatic fibrosis: comparison of intravoxel incoherent motion diffusion-weighted imaging with magnetic resonance elastography. J Magn Reson Imaging. 2014;42(1):204–10.

74. Wu CH, Ho MC, Jeng YM, Liang PC, Hu RH, Lai HS, et al. Assessing hepatic fibrosis: comparing the intravoxel incoherent motion in MRI with acoustic radiation force impulse imaging in US. Eur Radiol. 2015;25(12):3552–9.
75. Yoon JH, Lee JM, Baek JH, Shin CI, Kiefer B, Han JK, et al. Evaluation of hepatic fibrosis using intravoxel incoherent motion in diffusion-weighted liver MRI. J Comput Assist Tomogr. 2014;38(1):110–6.
76. Hu G, Chan Q, Quan X, Zhang X, Li Y, Zhong X, et al. Intravoxel incoherent motion MRI evaluation for the staging of liver fibrosis in a rat model. J Magn Reson Imaging. 2015;42(2):331–9.
77. Patel J, Sigmund EE, Rusinek H, Oei M, Babb JS, Taouli B. Diagnosis of cirrhosis with intravoxel incoherent motion diffusion MRI and dynamic contrast-enhanced MRI alone and in combination: preliminary experience. J Magn Reson Imaging. 2010;31(3):589–600.
78. Dyvorne HA, Galea N, Nevers T, Fiel MI, Carpenter D, Wong E, et al. Diffusion-weighted imaging of the liver with multiple b values: effect of diffusion gradient polarity and breathing acquisition on image quality and intravoxel incoherent motion parameters--a pilot study. Radiology. 2013;266(3):920–9.
79. Guiu B, Petit JM, Capitan V, Aho S, Masson D, Lefevre PH, et al. Intravoxel incoherent motion diffusion-weighted imaging in nonalcoholic fatty liver disease: a 3.0-T MR study. Radiology. 2012;265(1):96–103.
80. Lemke A, Stieltjes B, Schad LR, Laun FB. Toward an optimal distribution of b values for intravoxel incoherent motion imaging. Magn Reson Imaging. 2011;29(6):766–76.
81. Koh DM, Collins DJ, Orton MR. Intravoxel incoherent motion in body diffusion-weighted MRI: reality and challenges. AJR Am J Roentgenol. 2011;196(6):1351–61.
82. Barry B, Buch K, Soto JA, Jara H, Nakhmani A, Anderson SW. Quantifying liver fibrosis through the application of texture analysis to diffusion weighted imaging. Magn Reson Imaging. 2014;32(1):84–90.
83. Bedossa P, Dargere D, Paradis V. Sampling variability of liver fibrosis in chronic hepatitis C. Hepatology. 2003;38(6):1449–57.
84. Fiorini RN, Kirtz J, Periyasamy B, Evans Z, Haines JK, Cheng G, et al. Development of an unbiased method for the estimation of liver steatosis. Clin Transpl. 2004;18(6):700–6.
85. Anderson SW, Jara H, Ozonoff A, O'Brien M, Hamilton JA, Soto JA. Effect of disease progression on liver apparent diffusion coefficient and T2 values in a murine model of hepatic fibrosis at 11.7 Tesla MRI. J Magn Reson Imaging. 2012;35(1):140–6.
86. Anderson SW, Soto JA, Milch HN, Ozonoff A, O'Brien M, Hamilton JA, et al. Effect of disease progression on liver apparent diffusion coefficient values in a murine model of NASH at 11.7 Tesla MRI. J Magn Reson Imaging. 2011;33(4):882–8.
87. Rawlins SR, El-Zammar O, Zinkievich JM, Newman N, Levine RA. Digital quantification is more precise than traditional semiquantitation of hepatic steatosis: correlation with fibrosis in 220 treatment-naive patients with chronic hepatitis C. Dig Dis Sci. 2010;55(7):2049–57.
88. d'Assignies G, Ruel M, Khiat A, Lepanto L, Chagnon M, Kauffmann C, et al. Noninvasive quantitation of human liver steatosis using magnetic resonance and bioassay methods. Eur Radiol. 2009;19(8):2033–40.
89. Matalka II, Al-Jarrah OM, Manasrah TM. Quantitative assessment of liver fibrosis: a novel automated image analysis method. Liver Int. 2006;26(9):1054–64.
90. Fuchs BC, Wang H, Yang Y, Wei L, Polasek M, Schuhle DT, et al. Molecular MRI of collagen to diagnose and stage liver fibrosis. J Hepatol. 2013;59(5):992–8.
91. Taylor BN, Kuyatt CE. Guidelines for evaluating and expressing the uncertainty of NIST measurement results: National Institute of Standards and Technology; 1994 [updated 5 Oct 2010, Sept 1994].
92. Raunig DL, McShane LM, Pennello G, Gatsonis C, Carson PL, Voyvodic JT, et al. Quantitative imaging biomarkers: a review of statistical methods for technical performance assessment. Stat Methods Med Res. 2015;24(1):27–67.

93. Lee Y, Lee SS, Kim N, Kim E, Kim YJ, Yun SC, et al. Intravoxel incoherent motion diffusion-weighted MR imaging of the liver: effect of triggering methods on regional variability and measurement repeatability of quantitative parameters. Radiology. 2015;274(2):405–15.
94. Braithwaite AC, Dale BM, Boll DT, Merkle EM. Short- and midterm reproducibility of apparent diffusion coefficient measurements at 3.0-T diffusion-weighted imaging of the abdomen. Radiology. 2009;250(2):459–65.
95. Lewin M, Poujol-Robert A, Boelle PY, Wendum D, Lasnier E, Viallon M, et al. Diffusion-weighted magnetic resonance imaging for the assessment of fibrosis in chronic hepatitis C. Hepatology. 2007;46(3):658–65.
96. Joo I, Lee JM, Yoon JH, Jang JJ, Han JK, Choi BI. Nonalcoholic fatty liver disease: intravoxel incoherent motion diffusion-weighted MR imaging-an experimental study in a rabbit model. Radiology. 2014;270(1):131–40.
97. Andreou A, Koh DM, Collins DJ, Blackledge M, Wallace T, Leach MO, et al. Measurement reproducibility of perfusion fraction and pseudodiffusion coefficient derived by intravoxel incoherent motion diffusion-weighted MR imaging in normal liver and metastases. Eur Radiol. 2013;23(2):428–34.
98. Chenevert TL, Galban CJ, Ivancevic MK, Rohrer SE, Londy FJ, Kwee TC, et al. Diffusion coefficient measurement using a temperature-controlled fluid for quality control in multi-center studies. J Magn Reson Imaging. 2011;34(4):983–7.
99. Corona-Villalobos CP, Pan L, Halappa VG, Bonekamp S, Lorenz CH, Eng J, et al. Agreement and reproducibility of apparent diffusion coefficient measurements of dual-b-value and multi-b-value diffusion-weighted magnetic resonance imaging at 1.5 Tesla in phantom and in soft tissues of the abdomen. J Comput Assist Tomogr. 2013;37(1):46–51.
100. Malyarenko D, Galban CJ, Londy FJ, Meyer CR, Johnson TD, Rehemtulla A, et al. Multi-system repeatability and reproducibility of apparent diffusion coefficient measurement using an ice-water phantom. J Magn Reson Imaging. 2013;37(5):1238–46.
101. Malyarenko DI, Newitt D, Wilmes LJ, Tudorica A, Helmer KG, Arlinghaus LR, et al. Demonstration of nonlinearity bias in the measurement of the apparent diffusion coefficient in multicenter trials. Magn Reson Med. 2016;75(3):1312–23.
102. Rosenkrantz AB, Oei M, Babb JS, Niver BE, Taouli B. Diffusion-weighted imaging of the abdomen at 3.0 Tesla: image quality and apparent diffusion coefficient reproducibility compared with 1.5 Tesla. J Magn Reson Imaging. 2011;33(1):128–35.
103. Dyvorne H, Jajamovich G, Kakite S, Kuehn B, Taouli B. Intravoxel incoherent motion diffusion imaging of the liver: optimal b-value subsampling and impact on parameter precision and reproducibility. Eur J Radiol. 2014;83(12):2109–13.
104. Lee JT, Liau J, Murphy P, Schroeder ME, Sirlin CB, Bydder M. Cross-sectional investigation of correlation between hepatic steatosis and IVIM perfusion on MR imaging. Magn Reson Imaging. 2012;30(4):572–8.
105. Pekar J, Moonen CT, van Zijl PC. On the precision of diffusion/perfusion imaging by gradient sensitization. Magn Reson Med. 1992;23(1):122–9.
106. Friedman SL. Seminars in medicine of the Beth Israel Hospital, Boston. The cellular basis of hepatic fibrosis. Mechanisms and treatment strategies. N Engl J Med. 1993;328(25):1828–35.
107. Friedman SL. Mechanisms of hepatic fibrogenesis. Gastroenterology. 2008;134(6):1655–69.
108. Manning P, Murphy P, Wang K, Hooker J, Wolfson T, Middleton MS, et al. Liver histology and diffusion-weighted MRI in children with nonalcoholic fatty liver disease: a MAGNET study. J Magn Reson Imaging. 2017;46(4):1149–58.
109. Van Beers BE, Materne R, Annet L, Hermoye L, Sempoux C, Peeters F, et al. Capillarization of the sinusoids in liver fibrosis: noninvasive assessment with contrast-enhanced MRI in the rabbit. Magn Reson Med. 2003;49(4):692–9.
110. Annet L, Materne R, Danse E, Jamart J, Horsmans Y, Van Beers BE. Hepatic flow parameters measured with MR imaging and Doppler US: correlations with degree of cirrhosis and portal hypertension. Radiology. 2003;229(2):409–14.

111. Kim T, Murakami T, Takahashi S, Hori M, Tsuda K, Nakamura H. Diffusion-weighted single-shot echoplanar MR imaging for liver disease. AJR Am J Roentgenol. 1999;173(2):393–8.
112. Sandrasegaran K, Akisik FM, Lin C, Tahir B, Rajan J, Saxena R, et al. Value of diffusion-weighted MRI for assessing liver fibrosis and cirrhosis. AJR Am J Roentgenol. 2009;193(6):1556–60.
113. Watanabe H, Kanematsu M, Goshima S, Kondo H, Onozuka M, Moriyama N, et al. Staging hepatic fibrosis: comparison of gadoxetate disodium-enhanced and diffusion-weighted MR imaging—preliminary observations. Radiology. 2011;259(1):142–50.
114. Klasen J, Lanzman RS, Wittsack HJ, Kircheis G, Schek J, Quentin M, et al. Diffusion-weighted imaging (DWI) of the spleen in patients with liver cirrhosis and portal hypertension. Magn Reson Imaging. 2013;31(7):1092–6.
115. Zhang J, Guo Y, Tan X, Zheng Z, He M, Xu J, et al. MRI-based estimation of liver function by intravoxel incoherent motion diffusion-weighted imaging. Magn Reson Imaging. 2016;34(8):1220–5.
116. Mo YH, Jaw FS, Ho MC, Wang YC, Peng SS. Hepatic ADC value correlates with cirrhotic severity of patients with biliary atresia. Eur J Radiol. 2011;80(3):e253–7.
117. Li Z, Sun J, Hu X, Huang N, Han G, Chen L, et al. Assessment of liver fibrosis by variable flip angle T1 mapping at 3.0T. J Magn Reson Imaging. 2016;43(3):698–703.
118. Peng SS, Jeng YM, Hsu WM, Yang JC, Ho MC. Hepatic ADC map as an adjunct to conventional abdominal MRI to evaluate hepatic fibrotic and clinical cirrhotic severity in biliary atresia patients. Eur Radiol. 2015;25(10):2992–3002.
119. Razek AA, Khashaba M, Abdalla A, Bayomy M, Barakat T. Apparent diffusion coefficient value of hepatic fibrosis and inflammation in children with chronic hepatitis. Radiol Med. 2014;119(12):903–9.
120. Razek AA, Abdalla A, Omran E, Fathy A, Zalata K. Diagnosis and quantification of hepatic fibrosis in children with diffusion weighted MR imaging. Eur J Radiol. 2011;78(1):129–34.
121. Wang Y, Ganger DR, Levitsky J, Sternick LA, McCarthy RJ, Chen ZE, et al. Assessment of chronic hepatitis and fibrosis: comparison of MR elastography and diffusion-weighted imaging. AJR Am J Roentgenol. 2011;196(3):553–61.
122. Zou LQ, Chen J, Pan L, Jiang JZ, Xing W. Comparison of magnetic resonance elastography and diffusion-weighted imaging for staging hepatic fibrosis. Chin Med J. 2015;128(5):620–5.
123. Hu G, Zhang X, Liang W, Zhong X, Chan Q, Lin X, et al. Assessment of liver fibrosis in rats by MRI with apparent diffusion coefficient and T1 relaxation time in the rotating frame. J Magn Reson Imaging. 2016;43(5):1082–9.
124. Franca M, Marti-Bonmati L, Alberich-Bayarri A, Oliveira P, Guimaraes S, Oliveira J, et al. Evaluation of fibrosis and inflammation in diffuse liver diseases using intravoxel incoherent motion diffusion-weighted MR imaging. Abdom Radiol (NY). 2017;42(2):468–77.
125. Feier D, Balassy C, Bastati N, Fragner R, Wrba F, Ba-Ssalamah A. The diagnostic efficacy of quantitative liver MR imaging with diffusion-weighted, SWI, and hepato-specific contrast-enhanced sequences in staging liver fibrosis—a multiparametric approach. Eur Radiol. 2016;26(2):539–46.
126. Bonekamp D, Bonekamp S, Ou HY, Torbenson MS, Corona-Villalobos CP, Mezey E, et al. Assessing liver fibrosis: comparison of arterial enhancement fraction and diffusion-weighted imaging. J Magn Reson Imaging. 2014;40(5):1137–46.
127. Ayvaz S, Tuncel SA, Can G, Cagli B, Karaca T, Demirtas S, et al. Efficacy of diffusion-weighted magnetic resonance imaging in the evaluation of extrahepatic cholestasis-related hepatic fibrosis. Turk J Med Sci. 2015;45(3):686–93.
128. Zhang Y, Jin N, Deng J, Guo Y, White SB, Yang GY, et al. Intra-voxel incoherent motion MRI in rodent model of diethylnitrosamine-induced liver fibrosis. Magn Reson Imaging. 2013;31(6):1017–21.
129. Li H, Chen TW, Chen XL, Zhang XM, Li ZL, Zeng NL, et al. Magnetic resonance-based total liver volume and magnetic resonance-diffusion weighted imaging for staging liver fibrosis in mini-pigs. World J Gastroenterol. 2012;18(48):7225–33.

130. Bakan AA, Inci E, Bakan S, Gokturk S, Cimilli T. Utility of diffusion-weighted imaging in the evaluation of liver fibrosis. Eur Radiol. 2012;22(3):682–7.
131. Zhu NY, Chen KM, Chai WM, Li WX, Du LJ. Feasibility of diagnosing and staging liver fibrosis with diffusion weighted imaging. Chin Med Sci J. 2008;23(3):183–6.
132. Hong Y, Shi Y, Liao W, Klahr NJ, Xia F, Xu C, et al. Relative ADC measurement for liver fibrosis diagnosis in chronic hepatitis B using spleen/renal cortex as the reference organs at 3 T. Clin Radiol. 2014;69(6):581–8.
133. Taouli B, Tolia AJ, Losada M, Babb JS, Chan ES, Bannan MA, et al. Diffusion-weighted MRI for quantification of liver fibrosis: preliminary experience. AJR Am J Roentgenol. 2007;189(4):799–806.
134. Kovac JD, Dakovic M, Stanisavljevic D, Alempijevic T, Jesic R, Seferovic P, et al. Diffusion-weighted MRI versus transient elastography in quantification of liver fibrosis in patients with chronic cholestatic liver diseases. Eur J Radiol. 2012;81(10):2500–6.
135. Kovac JD, Jesic R, Stanisavljevic D, Kovac B, Banko B, Seferovic P, et al. Integrative role of MRI in the evaluation of primary biliary cirrhosis. Eur Radiol. 2012;22(3):688–94.
136. Hennedige TP, Wang G, Leung FP, Alsaif HS, Teo LL, Lim SG, et al. Magnetic resonance elastography and diffusion weighted imaging in the evaluation of hepatic fibrosis in chronic hepatitis B. Gut Liver. 2017;11(3):401–8.
137. Leitao HS, Doblas S, d'Assignies G, Garteiser P, Daire JL, Paradis V, et al. Fat deposition decreases diffusion parameters at MRI: a study in phantoms and patients with liver steatosis. Eur Radiol. 2013;23(2):461–7.
138. Chandarana H, Taouli B. Diffusion and perfusion imaging of the liver. Eur J Radiol. 2010;76(3):348–58.
139. Aube C. Imaging modalities for the diagnosis of hepatic fibrosis and cirrhosis. Clin Res Hepatol Gastroenterol. 2015;39(1):38–44.
140. Parente DB, Paiva FF, Oliveira Neto JA, Machado-Silva L, Figueiredo FA, Lanzoni V, et al. Intravoxel incoherent motion diffusion weighted MR imaging at 3.0 T: assessment of steatohepatitis and fibrosis compared with liver biopsy in type 2 diabetic patients. PLoS One. 2015;10(5):e0125653.
141. Murphy P, Hooker J, Ang B, Wolfson T, Gamst A, Bydder M, et al. Associations between histologic features of nonalcoholic fatty liver disease (NAFLD) and quantitative diffusion-weighted MRI measurements in adults. J Magn Reson Imaging. 2015;41(6):1629–38.
142. Le Bihan D, Breton E, Lallemand D, Aubin ML, Vignaud J, Laval-Jeantet M. Separation of diffusion and perfusion in intravoxel incoherent motion MR imaging. Radiology. 1988;168(2):497–505.
143. Kubo H, Harada M, Ishikawa M, Nishitani H. Hemodynamic changes with liver fibrosis measured by dynamic contrast-enhanced MRI in the rat. Magn Reson Med Sci. 2006;5(2):65–71.
144. Martin PY, Xu DL, Niederberger M, Weigert A, Tsai P, St John J, et al. Upregulation of endothelial constitutive NOS: a major role in the increased NO production in cirrhotic rats. Am J Phys. 1996;270(3 Pt 2):F494–9.
145. Zipprich A, Steudel N, Behrmann C, Meiss F, Sziegoleit U, Fleig WE, et al. Functional significance of hepatic arterial flow reserve in patients with cirrhosis. Hepatology. 2003;37(2):385–92.
146. Yin M, Talwalkar JA, Glaser KJ, Manduca A, Grimm RC, Rossman PJ, et al. Assessment of hepatic fibrosis with magnetic resonance elastography. Clin Gastroenterol Hepatol. 2007;5(10):1207–13, e2.
147. Talwalkar JA. Elastography for detecting hepatic fibrosis: options and considerations. Gastroenterology. 2008;135(1):299–302.
148. Steidle G, Eibofner F, Schick F. Quantitative diffusion imaging of adipose tissue in the human lower leg at 1.5 T. Magn Reson Med. 2011;65(4):1118–24.
149. Schmid-Tannwald C, Oto A, Reiser MF, Zech CJ. Diffusion-weighted MRI of the abdomen: current value in clinical routine. J Magn Reson Imaging. 2013;37(1):35–47.
150. Hamilton G, Yokoo T, Bydder M, Cruite I, Schroeder ME, Sirlin CB, et al. In vivo characterization of the liver fat (1)H MR spectrum. NMR Biomed. 2011;24(7):784–90.

151. Dijkstra H, Handayani A, Kappert P, Oudkerk M, Sijens PE. Clinical implications of non-steatotic hepatic fat fractions on quantitative diffusion-weighted imaging of the liver. PLoS One. 2014;9(2):e87926.
152. Delfaut EM, Beltran J, Johnson G, Rousseau J, Marchandise X, Cotten A. Fat suppression in MR imaging: techniques and pitfalls. Radiographics. 1999;19(2):373–82.
153. Murtz P, Krautmacher C, Traber F, Gieseke J, Schild HH, Willinek WA. Diffusion-weighted whole-body MR imaging with background body signal suppression: a feasibility study at 3.0 Tesla. Eur Radiol. 2007;17(12):3031–7.
154. Bulow R, Mensel B, Meffert P, Hernando D, Evert M, Kuhn JP. Diffusion-weighted magnetic resonance imaging for staging liver fibrosis is less reliable in the presence of fat and iron. Eur Radiol. 2013;23(5):1281–7.
155. Van Beers BE. Science to practice: can we diagnose nonalcoholic steatohepatitis with intravoxel incoherent motion diffusion-weighted MR imaging? Radiology. 2014;270(1):1–2.
156. McCuskey RS, Ito Y, Robertson GR, McCuskey MK, Perry M, Farrell GC. Hepatic microvascular dysfunction during evolution of dietary steatohepatitis in mice. Hepatology. 2004;40(2):386–93.
157. Rijzewijk LJ, van der Meer RW, Lubberink M, Lamb HJ, Romijn JA, de Roos A, et al. Liver fat content in type 2 diabetes: relationship with hepatic perfusion and substrate metabolism. Diabetes. 2010;59(11):2747–54.
158. Brock RW, Dorman RB. Obesity, insulin resistance and hepatic perfusion. Microcirculation. 2007;14(4–5):339–47.
159. Shigefuku R, Takahashi H, Kobayashi M, Ikeda H, Matsunaga K, Okuse C, et al. Pathophysiological analysis of nonalcoholic fatty liver disease by evaluation of fatty liver changes and blood flow using xenon computed tomography: can early-stage nonalcoholic steatohepatitis be distinguished from simple steatosis? J Gastroenterol. 2012;47(11):1238–47.
160. Balci A, Karazincir S, Sumbas H, Oter Y, Egilmez E, Inandi T. Effects of diffuse fatty infiltration of the liver on portal vein flow hemodynamics. J Clin Ultrasound. 2008;36(3):134–40.
161. Poyraz AK, Onur MR, Kocakoc E, Ogur E. Diffusion-weighted MRI of fatty liver. J Magn Reson Imaging. 2012;35(5):1108–11.
162. Caussy C, Reeder SB, Sirlin CB, Loomba R. Noninvasive, quantitative assessment of liver fat by MRI-PDFF as an endpoint in NASH trials. Hepatology. 2018;68(2):763–72.
163. Middleton MS, Heba ER, Hooker CA, Bashir MR, Fowler KJ, Sandrasegaran K, et al. Agreement between magnetic resonance imaging proton density fat fraction measurements and pathologist-assigned steatosis grades of liver biopsies from adults with nonalcoholic steatohepatitis. Gastroenterology. 2017;153(3):753–61.
164. Bannas P, Kramer H, Hernando D, Agni R, Cunningham AM, Mandal R, et al. Quantitative magnetic resonance imaging of hepatic steatosis: validation in ex vivo human livers. Hepatology. 2015;62(5):1444–55.
165. Kuhn JP, Hernando D, Mensel B, Kruger PC, Ittermann T, Mayerle J, et al. Quantitative chemical shift-encoded MRI is an accurate method to quantify hepatic steatosis. J Magn Reson Imaging. 2014;39(6):1494–501.
166. Meisamy S, Hines CD, Hamilton G, Sirlin CB, McKenzie CA, Yu H, et al. Quantification of hepatic steatosis with T1-independent, T2-corrected MR imaging with spectral modeling of fat: blinded comparison with MR spectroscopy. Radiology. 2011;258(3):767–75.
167. Tang A, Tan J, Sun M, Hamilton G, Bydder M, Wolfson T, et al. Nonalcoholic fatty liver disease: MR imaging of liver proton density fat fraction to assess hepatic steatosis. Radiology. 2013;267(2):422–31.
168. Hoad CL, Palaniyappan N, Kaye P, Chernova Y, James MW, Costigan C, et al. A study of T(1) relaxation time as a measure of liver fibrosis and the influence of confounding histological factors. NMR Biomed. 2015;28(6):706–14.
169. Yin M, Glaser KJ, Manduca A, Mounajjed T, Malhi H, Simonetto DA, et al. Distinguishing between hepatic inflammation and fibrosis with MR elastography. Radiology. 2017;284(3):694–705.

170. Garteiser P, D'Assignies G, Leitao H, Mouri F, Vilgrain V, Sinkus R, et al., editors. The influence of inflammation and fibrosis on multifrequency and monofrequency MR elastography parameters: a study in 47 patients with chronic viral hepatitis. In Joint annual meeting ISMRM-ESMRMB, 2014, Milan, Italy.
171. Chen BB, Hsu CY, Yu CW, Kao JH, Lee HS, Liang PC, et al. Hepatic necro-inflammation and elevated liver enzymes: evaluation with MRI perfusion imaging with gadoxetic acid in chronic hepatitis patients. Clin Radiol. 2014;69(5):473–80.
172. Smits LP, Coolen BF, Panno MD, Runge JH, Nijhof WH, Verheij J, et al. Noninvasive differentiation between hepatic steatosis and steatohepatitis with MR imaging enhanced with USPIOs in patients with nonalcoholic fatty liver disease: a proof-of-concept study. Radiology. 2016;278(3):782–91.
173. Abrigo JM, Shen J, Wong VW, Yeung DK, Wong GL, Chim AM, et al. Non-alcoholic fatty liver disease: spectral patterns observed from an in vivo phosphorus magnetic resonance spectroscopy study. J Hepatol. 2014;60(4):809–15.
174. Kim TH, Jun HY, Kim KJ, Lee YH, Lee MS, Choi KH, et al. Hepatic alanine differentiates nonalcoholic steatohepatitis from simple steatosis in humans and mice: a proton MR spectroscopy study with long echo time. J Magn Reson Imaging. 2017;46(5):1298–310.
175. Bharwani N, Koh DM. Diffusion-weighted imaging of the liver: an update. Cancer Imaging. 2013;13:171–85.
176. Chandarana H, Do RK, Mussi TC, Jensen JH, Hajdu CH, Babb JS, et al. The effect of liver iron deposition on hepatic apparent diffusion coefficient values in cirrhosis. AJR Am J Roentgenol. 2012;199(4):803–8.
177. Tonan T, Fujimoto K, Qayyum A, Kawaguchi T, Kawaguchi A, Nakashima O, et al. Quantification of hepatic iron concentration in chronic viral hepatitis: usefulness of T2-weighted single-shot spin-echo echo-planar MR imaging. PLoS One. 2012;7(3):e33868.
178. Gandon Y, Guyader D, Heautot JF, Reda MI, Yaouanq J, Buhe T, et al. Hemochromatosis: diagnosis and quantification of liver iron with gradient-echo MR imaging. Radiology. 1994;193(2):533–8.
179. Wood JC, Enriquez C, Ghugre N, Tyzka JM, Carson S, Nelson MD, et al. MRI R2 and R2* mapping accurately estimates hepatic iron concentration in transfusion-dependent thalassemia and sickle cell disease patients. Blood. 2005;106(4):1460–5.
180. Storey P, Thompson AA, Carqueville CL, Wood JC, de Freitas RA, Rigsby CK. R2* imaging of transfusional iron burden at 3T and comparison with 1.5T. J Magn Reson Imaging. 2007;25(3):540–7.
181. Sharma SD, Fischer R, Schoennagel BP, Nielsen P, Kooijman H, Yamamura J, et al. MRI-based quantitative susceptibility mapping (QSM) and R2* mapping of liver iron overload: comparison with SQUID-based biomagnetic liver susceptometry. Magn Reson Med. 2017;78(1):264–70.
182. Dyvorne HA, Jajamovich GH, Bane O, Fiel MI, Chou H, Schiano TD, et al. Prospective comparison of magnetic resonance imaging to transient elastography and serum markers for liver fibrosis detection. Liver Int. 2016;36(5):659–66.
183. Kahraman AS, Kahraman B, Ozdemir ZM, Gormeli CA, Ozdemir F, Dogan M. Diffusion-weighted imaging (DWI) of the liver in assessing chronic liver disease: effects of the presence and the degree of ascites on ADC values. Abdom Radiol (NY). 2016;41(1):56–62.
184. Lewis S, Kamath A, Chatterji M, Patel A, Shyknevsky I, Dyvorne HA, et al. Diffusion-weighted imaging of the liver in patients with chronic liver disease: comparison of monopolar and bipolar diffusion gradients for image quality and lesion detection. AJR Am J Roentgenol. 2015;204(1):59–68.
185. Martin DR, Semelka RC. Magnetic resonance imaging of the liver: review of techniques and approach to common diseases. Semin Ultrasound CT MR. 2005;26(3):116–31.
186. Sandrasegaran K, Tahir B, Nutakki K, Akisik FM, Bodanapally U, Tann M, et al. Usefulness of conventional MRI sequences and diffusion-weighted imaging in differentiating malignant from benign portal vein thrombus in cirrhotic patients. AJR Am J Roentgenol. 2013;201(6):1211–9.

187. Ahn JH, Yu JS, Cho ES, Chung JJ, Kim JH, Kim KW. Diffusion-weighted MRI of malignant versus benign portal vein thrombosis. Korean J Radiol. 2016;17(4):533–40.
188. Catalano OA, Choy G, Zhu A, Hahn PF, Sahani DV. Differentiation of malignant thrombus from bland thrombus of the portal vein in patients with hepatocellular carcinoma: application of diffusion-weighted MR imaging. Radiology. 2010;254(1):154–62.
189. Dogan Y, Soylu A, Kilickesmez O, Demirtas T, Kilickesmez KO, Dogan SN, et al. The value of hepatic diffusion-weighted MR imaging in demonstrating hepatic congestion secondary to pulmonary hypertension. Cardiovasc Ultrasound. 2010;8:28.
190. Zhang Q, Yu NN, Wen LJ, Liu GL, Tang J, Yuan ZG, et al. A preliminary study of apparent diffusion coefficient in chemotherapy-induced liver damage. Eur J Radiol. 2012;81(11):2943–6.
191. Moteki T, Horikoshi H. Evaluation of noncirrhotic hepatic parenchyma with and without significant portal vein stenosis using diffusion-weighted echo-planar MR on the basis of multiple-perfusion-components theory. Magn Reson Imaging. 2011;29(1):64–73.
192. Wu X, Wang H, Chen F, Jin L, Li J, Feng Y, et al. Rat model of reperfused partial liver infarction: characterization with multiparametric magnetic resonance imaging, microangiography, and histomorphology. Acta Radiol. 2009;50(3):276–87.
193. Sandrasegaran K, Ramaswamy R, Ghosh S, Tahir B, Akisik FM, Saxena R, et al. Diffusion-weighted MRI of the transplanted liver. Clin Radiol. 2011;66(9):820–5.
194. Faria SC, Ganesan K, Mwangi I, Shiehmorteza M, Viamonte B, Mazhar S, et al. MR imaging of liver fibrosis: current state of the art. Radiographics. 2009;29(6):1615–35.
195. Wang HQ, Yang C, Zeng MS, Rao SX, Ji Y, Weng X, et al. Magnetic resonance texture analysis for the identification of cytokeratin 19-positive hepatocellular carcinoma. Eur J Radiol. 2019;117:164–70.
196. Hui TCH, Chuah TK, Low HM, Tan CH. Predicting early recurrence of hepatocellular carcinoma with texture analysis of preoperative MRI: a radiomics study. Clin Radiol. 2018;73(12):1056.e11–6.
197. Hectors SJ, Lewis S, Besa C, King MJ, Said D, Putra J, et al. MRI radiomics features predict immuno-oncological characteristics of hepatocellular carcinoma. Eur Radiol. 2020;30(7):3759–69.
198. Becker AS, Wagner MW, Wurnig MC, Boss A. Diffusion-weighted imaging of the abdomen: Impact of b-values on texture analysis features. NMR Biomed. 2017;30(1) https://doi.org/10.1002/nbm.3669.
199. Brynolfsson P, Nilsson D, Torheim T, Asklund T, Karlsson CT, Trygg J, et al. Haralick texture features from apparent diffusion coefficient (ADC) MRI images depend on imaging and preprocessing parameters. Sci Rep. 2017;7(1):4041.
200. Peerlings J, Woodruff HC, Winfield JM, Ibrahim A, Van Beers BE, Heerschap A, et al. Stability of radiomics features in apparent diffusion coefficient maps from a multi-centre test-retest trial. Sci Rep. 2019;9(1):4800.
201. Varghese BA, Cen SY, Hwang DH, Duddalwar VA. Texture analysis of imaging: what radiologists need to know. AJR Am J Roentgenol. 2019;212(3):520–8.
202. Colvin DC, Jourquin J, Xu J, Does MD, Estrada L, Gore JC. Effects of intracellular organelles on the apparent diffusion coefficient of water molecules in cultured human embryonic kidney cells. Magn Reson Med. 2011;65(3):796–801.
203. Gore JC, Xu J, Colvin DC, Yankeelov TE, Parsons EC, Does MD. Characterization of tissue structure at varying length scales using temporal diffusion spectroscopy. NMR Biomed. 2010;23(7):745–56.
204. Xu J, Xie J, Jourquin J, Colvin DC, Does MD, Quaranta V, et al. Influence of cell cycle phase on apparent diffusion coefficient in synchronized cells detected using temporal diffusion spectroscopy. Magn Reson Med. 2011;65(4):920–6.
205. Xu J, Does MD, Gore JC. Dependence of temporal diffusion spectra on microstructural properties of biological tissues. Magn Reson Imaging. 2011;29(3):380–90.
206. Zhang H, Sun A, Li H, Saiviroonporn P, Wu EX, Guo H. Stimulated echo diffusion weighted imaging of the liver at 3 Tesla. Magn Reson Med. 2017;77(1):300–9.

207. Zhang H, Yang Q, Yu T, Chen X, Huang J, Tan C, et al. Comparison of T2, T1rho, and diffusion metrics in assessment of liver fibrosis in rats. J Magn Reson Imaging. 2017;45(3):741–50.
208. Le Bihan D, Ichikawa S, Motosugi U. Diffusion and intravoxel incoherent motion MR imaging-based virtual elastography: a hypothesis-generating study in the liver. Radiology. 2017;285(2):609–19.
209. Jensen JH, Helpern JA, Ramani A, Lu H, Kaczynski K. Diffusional kurtosis imaging: the quantification of non-Gaussian water diffusion by means of magnetic resonance imaging. Magn Reson Med. 2005;53(6):1432–40.
210. Kromrey ML, Le Bihan D, Ichikawa S, Motosugi U. Diffusion-weighted MRI-based virtual elastography for the assessment of liver fibrosis. Radiology. 2020;295(1):127–35.

Benign and Malignant Bile Duct Strictures

5

Nikolaos Kartalis and Carlos Valls

5.1 Introduction

Imaging plays a crucial role in the evaluation of patients with biliary strictures, namely in the detection, characterization and treatment planning. For the detection of the presence of intra- or/and extrahepatic bile duct dilatation as well as of the site, length and degree of stricture, the superiority of MRCP is well-documented [1]. In the characterization (i.e. differentiation of benign from malignant causes of biliary strictures) and for treatment planning, MRCP/gadolinium-based contrast-enhanced (CE) MRI has been traditionally widely used. After the implementation of diffusion-weighted imaging (DWI) in clinical protocols, its role has recently been investigated.

In this chapter, the role of DWI [either as stand-alone method or as add-on to conventional MRCP or CE-MRI] in the differentiation of benign from malignant bile duct strictures and in treatment planning will be presented.

5.2 Causes of Bile Duct Strictures

Various benign and malignant entities may cause a biliary stricture [2, 3]. In the benign group, the most commonly seen are chronic pancreatitis, primary sclerosing cholangitis (PSC), IgG4-related sclerosing cholangitis (IgG4-SC), postsurgical complications and fibrostenotic benign stricture whereas other less common causes include ischemia, infection [e.g., recurrent pyogenic, eosinophilic, and acquired immunodeficiency syndrome (AIDS)-related cholangitis], post-radiation and vasculitis. In the malignant group, cholangiocarcinoma (CCA), pancreatic cancer (PC),

N. Kartalis (✉) · C. Valls
Division of Radiology, Department of Clinical Science, Intervention and Technology (CLINTEC), Karolinska Institutet, Stockholm, Sweden

Department of Radiology Huddinge, Karolinska University Hospital, Stockholm, Sweden

C. Matos, N. Papanikolaou (eds.), *Diffusion Weighted Imaging of the Hepatobiliary System*, https://doi.org/10.1007/978-3-319-62977-3_5

ampullary cancer and gallbladder cancer are the most common; hilar lymphadenopathy and intrabilliary growth of hepatocellular carcinoma and metastases are less common causes. Intrahepatic CCA and PC are described in other chapters of this book.

5.3 Common Benign Causes

5.3.1 Primary Sclerosing Cholangitis

PSC is a chronic disease of unknown aetiology. Approximately two-thirds of patients with PSC have associated inflammatory bowel disease (IBD)—predominantly ulcerative colitis—and one fourth of patients has at least one autoimmune disorder outside the gastrointestinal tract [4]; these data in conjunction with genome-wide association studies indicate that autoimmune processes have central role in the pathogenesis of the disease [5, 6]. Inflammation and development of concentric fibrosis around the intra- and/or extrahepatic bile ducts lead to the development of multiple strictures. The patients present with a clinical image and laboratory profile of cholestasis. Imaging findings include multiple, contrast-enhancing short-segment bile duct strictures interchanging with normal or slightly dilated segments (the so-called "beaded" appearance), pruning of peripheral intrahepatic ducts, hypertrophy of the caudate lobe and medial segment/atrophy of the lateral and posterior segments, hilar lymphadenopathy and hepatolithiasis.

Complications that may develop in patients with PSC include cirrhosis, liver failure and development of CCA. Suspicion of CCA is raised when the patient shows one or more of the following [6]:

- progression of symptoms, signs and laboratory profile of cholestasis,
- weight loss,
- elevated levels of carbohydrate antigen 19-9 (CA 19-9), despite the fact that elevated CA 19-9 levels may be present in cases of cholestasis of other aetiology or acute bacterial cholangitis [7] and
- new or progressing prominent high-grade stricture (the term "dominant stricture" is defined at ERC and an equivalent precise definition at MRCP/CE-MRI is lacking), particularly if there is an associated enhancing mass.

In cases where development of CCA is suspected, the initial workout of patients should include ductal sampling such as brush cytology and endobiliary biopsies [6]. In a meta-analysis from 2014, brush cytology was shown to be highly specific (pooled specificity 97%) but not sufficiently sensitive (pooled sensitivity of 43%) [8]. In order to improve sensitivity, fluorescence in situ hybridization (FISH) analysis is helpful in equivocal cases. Interestingly, the triple modality testing (brush cytology, biopsy and FISH) had clearly higher sensitivity 82% compared to brush cytology alone (82% and 42%, respectively) whereas the specificity of both was

100% [9]. In selected cases, the use of cholangioscopy [either peroral or the most recently developed single-operator cholangioscopy-system SpyGlass], intraductal ultrasonography and probe-based confocal laser endomicroscopy may be performed as these techniques have be shown to be potentially useful but still not implemented in the clinical routine [6].

5.3.2 IgG4-Related Sclerosing Cholangitis

IgG4-SC is the manifestation of IgG4-related disease (IgG4-RD) at the bile ducts. The disease aetiology is unknown. Within the spectrum of IgG4-RD are, among others, autoimmune pancreatitis (AIP) type 1, retroperitoneal fibrosis and sialadenitis and it is believed that immune-mediated inflammation has an important role in the pathophysiology of the disease [10]. The clinical presentation and laboratory findings are those of cholestatic disease; often times patients also have associated weight loss and abdominal discomfort/pain, which make the differentiation from CCA challenging.

Imaging findings depend on the type of IgG4-SC. Four types are described in the literature [11]:

- Type 1: stenosis in the lower CBD,
- Type 2: multifocal intrahepatic stenoses with upstream dilatation,
- Type 3: stenosis in the hilum and lower CBD and
- Type 4: stenosis in the hilum.

Depending on the type, the differential diagnosis includes chronic pancreatitis, pancreatic cancer, distal CCA (type 1), PSC (type 2) and perihilar CCA (types 3 and 4).

5.4 Common Malignant Causes

5.4.1 Cholangiocarcinoma

CCA is the second most common primary malignancy of the liver and is the result of malignant transformation of bile duct epithelium [12, 13]. Predisposing factors for the development of CCA are presence of PSC, hepatolithiasis, liver fluke infections, congenital anomalies, cirrhosis, hepatitis (HBV and HCV).

Depending on the location of the tumour, they are classified into the following types [13]:

- Distal tumours, i.e. those that arise between the insertion of the cystic duct in the extrahepatic bile duct and the ampulla of Vater. These tumours represent approximately 40% of all CCA.

- Perihilar tumours, that represent approximately 50% of all CCAs.
- Intrahepatic tumours, that arise in the intrahepatic ducts (i.e. located upstream/peripherally from the secondary biliary confluence) and represent approximately 10% of all CCAs.

Depending on the growth pattern, CCA are classified into periductal infiltrating, mass-forming and intraductal; the most common growth patterns in the perihilar and distal CCA is periductal infiltrating whereas in the in the intrahepatic type the most commons pattern is mass-forming, respectively [14].

In the vast majority of perihilar and distal tumours, the patients present with painless jaundice and laboratory findings of cholestasis. Irrespectively of the tumour location, patients may also have unspecific symptoms such as weight loss, abdominal discomfort, fatigue, etc.

Surgery is the only potentially curative treatment in patients with CCA. In the absence of distant metastases and after complete tumour removal (R0-resection), 5-year survival is reported to be 27%, 30%, and 63% for distal, perihilar and intrahepatic CCAs, respectively. Regarding treatment planning of patients with CCA, information on tumour extend is of utmost importance for the liver surgeon in order to achieve complete tumour removal and, thus, increase the chances for improved patient survival [15–17]. Besides complete tumour removal, prerequisites for successful treatment is the presence of sufficient liver volume (liver volume remnant), adequate circulatory in- and outflow and bile excretion [13]. For this reason, accurate preoperative imaging assessment of both the longitudinal and the radial extension of the tumour as well as its relationship to the major vascular structures in the liver hilum is of particular clinical interest.

5.5 Differentiation of Benign from Malignant Bile Duct Strictures

Accurate differentiation of benign from malignant causes of bile duct stricture is crucial for choice of appropriate treatment and prognosis assessment. In cases of malignant diseases, surgical treatment is usually the only potentially curative treatment in case the preoperative evaluation indicates that complete tumour removal is possible to achieve (R0-resections). In cases of benign biliary stricture aetiology, a variety of nonsurgical options such as medical treatment (e.g. corticosteroids in case of IgG4-SC) and imaging-guided interventions (e.g. stricture dilatation with or without stent placement) are indicated.

5.5.1 Conventional MRCP/Contrast-Enhanced MRI

In conventional MRCP/CE-MRI, various findings have been reported to be useful in the differentiation between benign and malignant strictures [18–27].

Suggestive for malignancy are the presence of the following:

- indistinct outer margins and higher degree of enhancement compared to the liver on post-contrast T1-weighted GRE sequences,
- higher signal intensity compared to the liver on T2-weighted images,
- irregular and asymmetric luminal narrowing with abrupt cut-off and
- strictures longer than 12 mm or with thickness of bile duct wall at the site of stricture greater than 3.1 mm.

On the contrary, findings such as the presence of a short-segment stricture with a progressive, smooth luminal narrowing are indicative of benign disease [18–27].

However, the differentiation of benign from malignant bile duct strictures based on these features is not always possible due to overlapping of imaging findings between benign and malignant diseases. It has been demonstrated that in a substantial number of patients with suspicion of malignant disease, histopathology after surgery revealed a benign entity [3, 28, 29].

5.5.2 DWI

The role of DWI in the differentiation of benign from malignant lesions has been investigated after its implementation in clinical protocols.

In a group-wise evaluation of patients with perihilar and patients with distal extrahepatic strictures, visual evaluation of DWI images with *b*-values of 0 and 500 s/mm^2 and ADC maps demonstrated significantly higher accuracy compared to MRCP for the diagnosis of CCA (DWI vs. MRCP: 96% vs. 73%, respectively) [30]. In all but two cases, the malignant lesions exhibited higher SI on images with *b*-values of 500 s/mm^2 and lower ADC values compared to the surrounding tissues. In the two patients that DWI failed to demonstrate the malignant lesion, the reason was either a very small lesion size or artefacts around the bile duct. In a slightly differently designed study of a patient group with extrahepatic strictures of predominantly non-malignant aetiology, visual assessment of DWI images with *b*-values of 0 and 1000 s/mm^2 together with ADC maps, showed higher sensitivity and accuracy for diagnosis of malignancy compared to a combined reading of MRCP and T2-weighted images [31]. However, in the evaluation of all aetiologies, the overall accuracy of DWI was significantly lower than the combined imaging set of MRCP and T2-weighted images; after the addition of DWI, the overall diagnostic accuracy of the combined imaging set of MRCP and T2-weighted images increased significantly (from 89–93% to 96–98% for two readers) [31]. In a differently designed study of a similar patient group, it was shown that the combined evaluation of DWI (visual assessment of images with *b*-value of 0, 100 and 800 s/mm^2 alongside with ADC maps) and MRCP/hepatobiliary gadolinium-based (gadoxetic acid) CE-MRI resulted in higher accuracy in the differentiation between benign and malignant bile duct strictures compared to MRCP/hepatobiliary gadolinium-based (gadoxetic

acid) CE-MRI alone [32]. However, strictures in patients with recurrent pyogenic cholangitis and IgG4-SC demonstrated impeded diffusion compared to the non-stenotic segments of the bile ducts, which resulted in false positive findings for malignancy. This is also an anecdotal observation from our group where DWI has not been particularly helpful for the differentiation of IgG4-SC from extrahepatic CCA (unpublished data). Contradictory to the main finding of the above studies are results presented in another study where the authors evaluated solely perihilar strictures. They reported that the addition of visual evaluation of high *b*-value DWI images (800 and 1000 s/mm^2) to MRCP/extracellular gadolinium-based CE-MRI protocol did not improve the diagnostic performance for the differentiation of benign from malignant disease for either of two readers [33]. Imaging examples of the role of DWI in patients with perihilar CCA are presented in Figs. 5.1 and 5.2

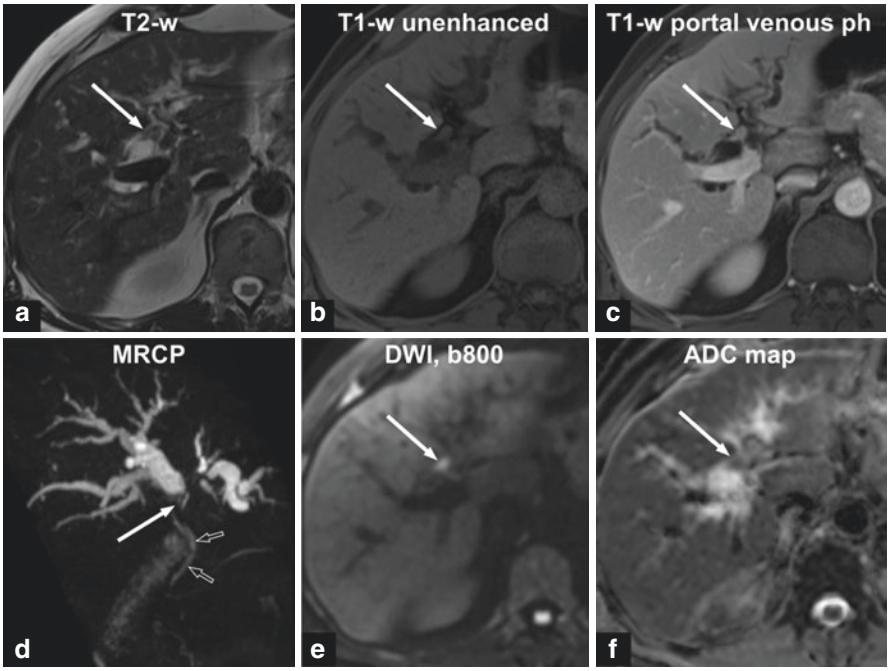

Fig. 5.1 Images of a 53-year-old male with autoimmune hepatitis that presented with worsening cholestasis. In the liver hilum, there is an obstructive soft-tissue lesion (arrow) that has signal intensity (SI) similar to the liver in T2-weighted image (**a**) and shows enhancement (**b**, **c**) after injection of extracellular gadolinium-based contrast agent. On MRCP (**d**), the tumour is seen to involve the common hepatic, left and right hepatic ducts with upstream duct dilatation whereas the common bile duct (open arrows) is thin. On DWI, the lesion shows impeded diffusion with high SI in the image with *b*-value of 800 s/mm^2 (**e**) and dark appearance in the corresponding ADC map (**f**). Findings from intraductal tissue sampling indicated cholangiocarcinoma

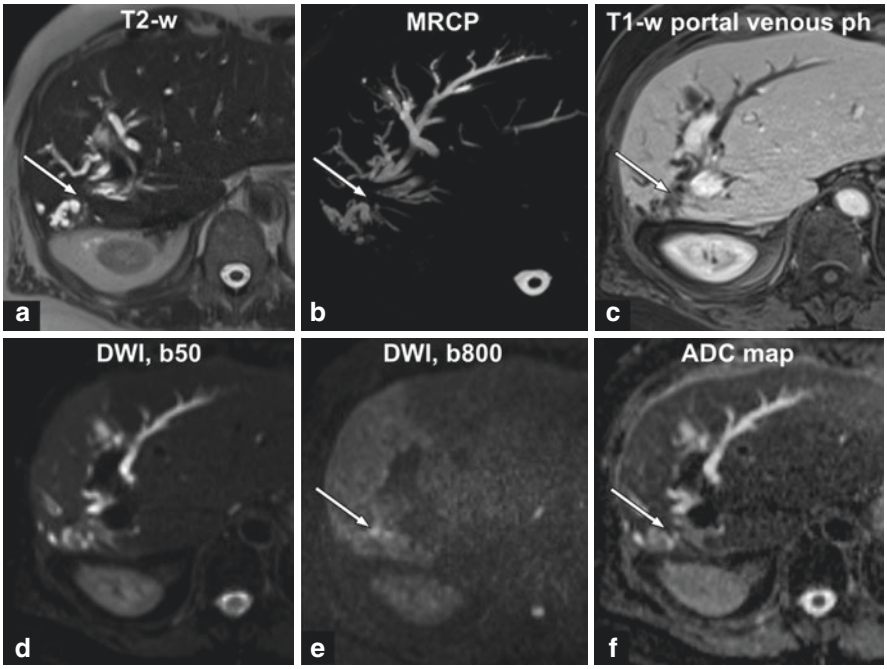

Fig. 5.2 Images of a 70-year-old female patient that presented with painless jaundice 20 years post extended right hemihepatectomy for colorectal cancer liver metastatic disease. In the left hepatic duct, there is obstruction (arrows) with upstream dilatation seen in T2-weighted image (**a**) and axial maximum intensity projection-MRCP (**b**). In the portal venous phase post gadoxetic-acid injection (**c**), there is a suspicious area of low signal intensity that also exhibits impeded diffusion (**d**–**f**). The results of ductal sampling were equivocal and although tumour markers were negative, the findings were suspicious of malignancy. Histopathological findings after atypical hepatectomy showed cholangiocarcinoma

whereas in patients with benign diseases in Fig. 5.3–5.6 (Fig. 5.3: benign fibrotic stricture; Figs. 5.4 and 5.5: PSC; and Fig. 5.6: IgG4-SC).

In the differentiation of benign from malignant strictures in the distal CBD and periampullary region—defined as the area within 2 cm from the ampulla of Vater and encompasses the very distal segment of CBD, ampulla of Vater, parts of duodenum and of pancreatic head—DWI is reported to be particularly helpful. In the combined reading of DWI images (visual assessment of *b*-value of 800 and ADC maps) and MRCP, the accuracy for differentiation of benign from malignant strictures was significantly higher compared to MRCP alone for two readers (92% vs. 71% for both readers) [34]. Similar results, i.e. statistically significant improvement of accuracy of MRCP after the addition of visual assessment of DWI images were

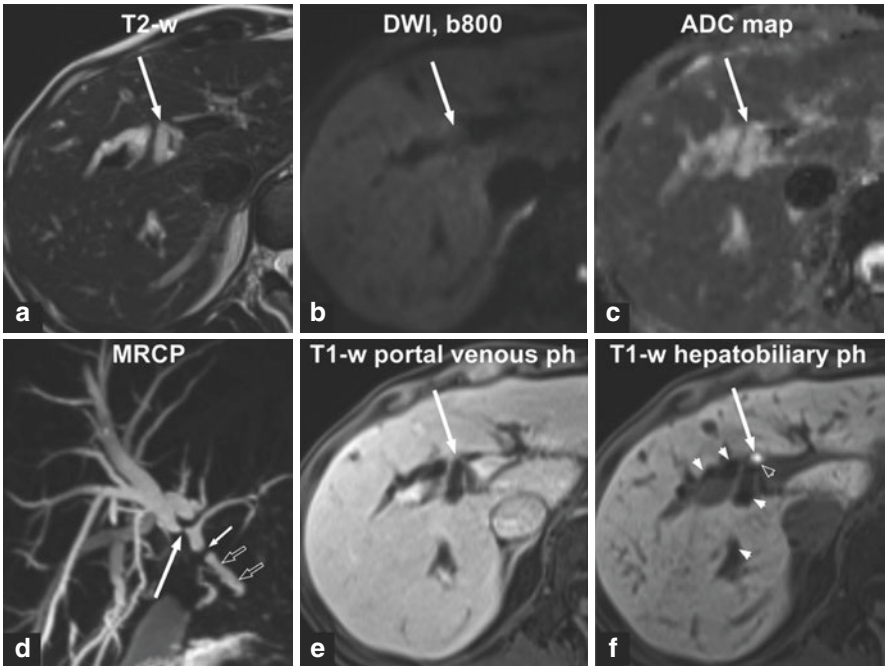

Fig. 5.3 Images of a 66-year-old female that presented with painless jaundice one and a half year post left mastectomy due to breast cancer. A stricture (arrow) affects separately the right anterior and right posterior hepatic ducts and there is upstream duct dilatation seen in T2-weighted image (**a**). No signal intensity changes are observed in the image with *b*-value of 800 s/mm^2 (**b**) or in the corresponding ADC map (**c**). On coronal maximum intensity projection-MRCP image (**d**), the common bile duct is normal (open arrows) and there is compression of the common hepatic duct (CHD) from the crossing right hepatic artery (small white arrow). In the portal venous phase post gadoxetic-acid injection (**e**), there is no abnormal contrast-enhancement in the area that corresponds to the bile duct stricture. In the hepatobiliary phase (**f**), there is no excretion of contrast in the lumen of the affected bile ducts (close arrowheads) whereas the excretion is ordinary in the CHD) (open arrowhead). Brush cytology and single-operator cholangioscopy-system SpyGlass with targeted biopsied were without any signs of malignancy. At 5-year follow-up (not shown), there are still no signs of malignancy and thus the MRI findings are assumed to correspond to nonspecific fibrotic stricture

shown in a more recent work [35]; interestingly, the addition of CE-MRI did not improve the accuracy of the combined set MRCP and DWI for any of the two readers [35]. Further improvements in the differentiation between benign and malignant strictures in the distal CBD have been reported very recently by using novel imaging techniques, such as small field-of-view ZOOMit DWI compared to conventional DWI [values of area under the receiver operating characteristic curves improving from 0.82–0.85 (conventional DWI) to 0.92–0.94 (ZOOMit DWI) for visual assessment of *b*-values of 0, 400, 800 and ADC maps for two reviewers] and MR texture analysis parameters [36].

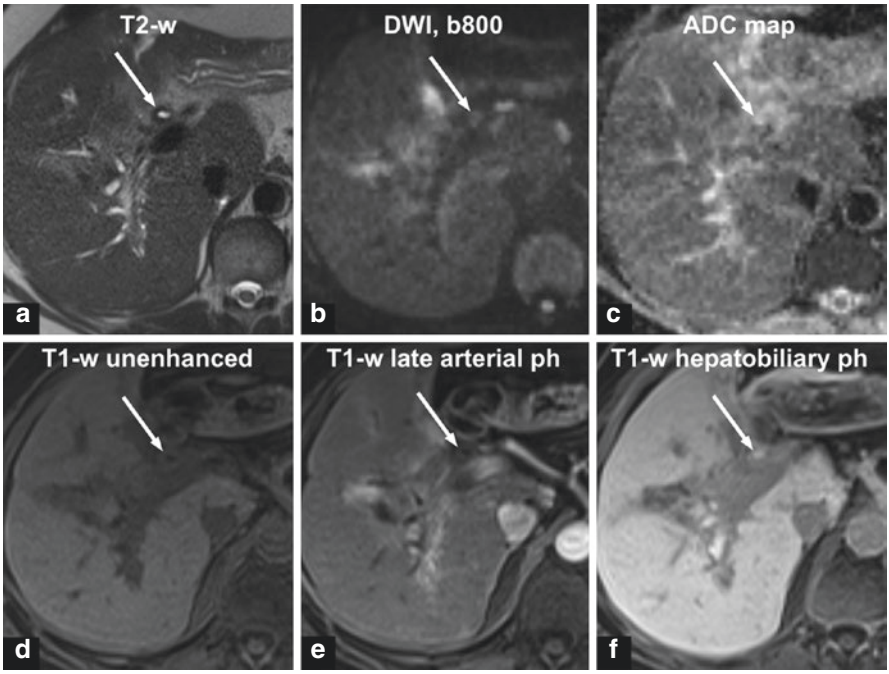

Fig. 5.4 Images of a 61-year-old female with longstanding primary sclerosing cholangitis (PSC). There is thickening of the common hepatic duct (CHD) wall (arrows) that shows signal intensity lower compared to the adjacent liver parenchyma in T2-weighted image (**a**) and no impeded diffusion (**b**, **c**). After the injection of the hepatobiliary contrast agent gadobenate dimeglumine, there is no contrast-enhancement (**d**, **e**); in the hepatobiliary phase 2 h after the administration of the contrast agent (**f**), there is excretion of contrast in the lumen of CHD. Imaging findings indicate fibrotic changes secondary to chronic inflammation

5.6 Treatment Planning

Regarding treatment planning, as stated above, information on tumour extend is of the utmost importance. For this reason, accurate preoperative imaging assessment of both the longitudinal and the radial extension of the tumour as well as its relationship to the major vascular structures in the liver hilum is of particular clinical interest [13]. Data in the literature regarding the role of DWI are contradictory. On the one hand, results from a retrospective study from 2013 showed that the combination of DWI and MRCP/hepatobiliary gadolinium-based (gadoxetic acid) CE-MRI improved the assessment of both the longitudinal and the radial tumour extension of perihilar CCA compared to MRCP/hepatobiliary gadolinium-based (gadoxetic acid) CE-MRI alone, whereas the diagnostic performance for vessel engagement did not improve after the addition of DWI [37]. On the other hand, results from a more recent study (2015) showed that the addition of DWI to MRCP/extracellular

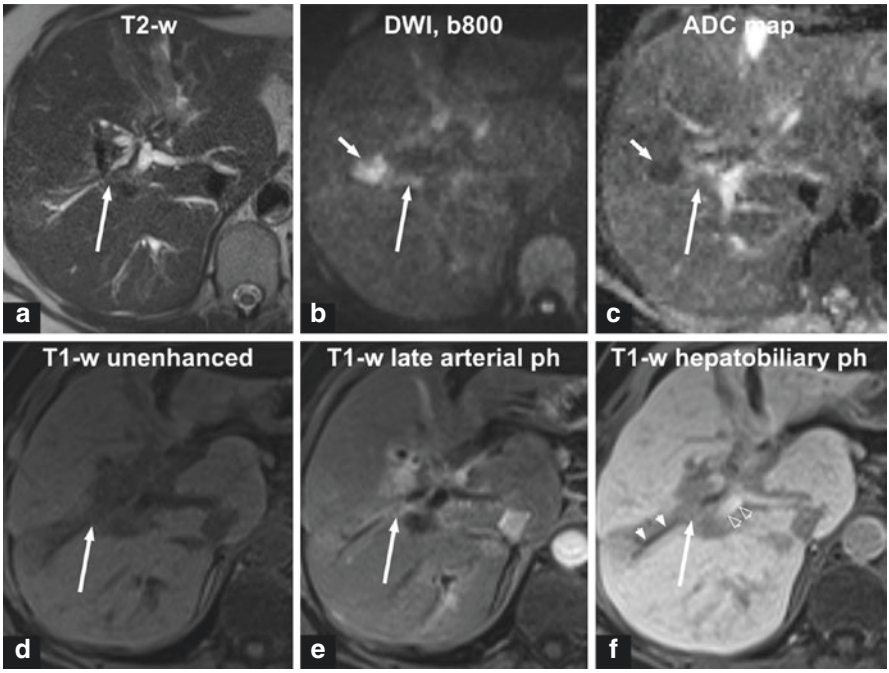

Fig. 5.5 Images of a 61-year-old female with longstanding primary sclerosing cholangitis (PSC), same as in Fig. 5.4. In the inferior/posterior part of liver segment 8, there is a bile duct stricture (arrows) with slight upstream duct dilatation. The thickened wall shows slightly higher signal intensity compared to the adjacent liver parenchyma in T2-weighted image (**a**), impeded diffusion (**b**, **c**) and discrete enhancement after the injection of the hepatobiliary contrast agent gadobenate dimeglumine (**d**, **e**). In the hepatobiliary phase 2 h after the administration of the contrast agent (**f**), there is no excretion of contrast in the lumen of the affected bile duct (close arrowheads) whereas the excretion is ordinary in other non-obstructed bile ducts (open arrowheads). Interestingly, immediately laterally to the stricture, there is a parenchymal area with markedly impeded diffusion (short arrows in **b** and **c**). The imaging findings were suspicious of malignancy but no tumour was identified at ductal sampling. At MR imaging follow-up (not shown), the findings regressed and were, thus, assumed to correspond to active inflammatory changes. At 10-year imaging and clinical follow-up, no signs of tumour have developed

gadolinium-based CE-MRI protocol did not improve the assessment of the longitudinal tumour extend compared to the MRCP/extracellular gadolinium-based CE-MRI protocol alone [33].

In summary, literature data on the role of DWI in the evaluation of patients with bile duct strictures are somehow contradictory. All available studies are retrospectively designed and, in their vast majority, indicate that the addition of DWI to MRCP/gadolinium-based CE-MRI contributes in the differentiation of benign from malignant causes of bile duct strictures as well as in the preoperative assessment of tumour extend. Furthermore, DWI has been shown to perform better than MRCP (and/or T2-weighted sequences) for the diagnosis of bile duct stricture of malignant aetiology.

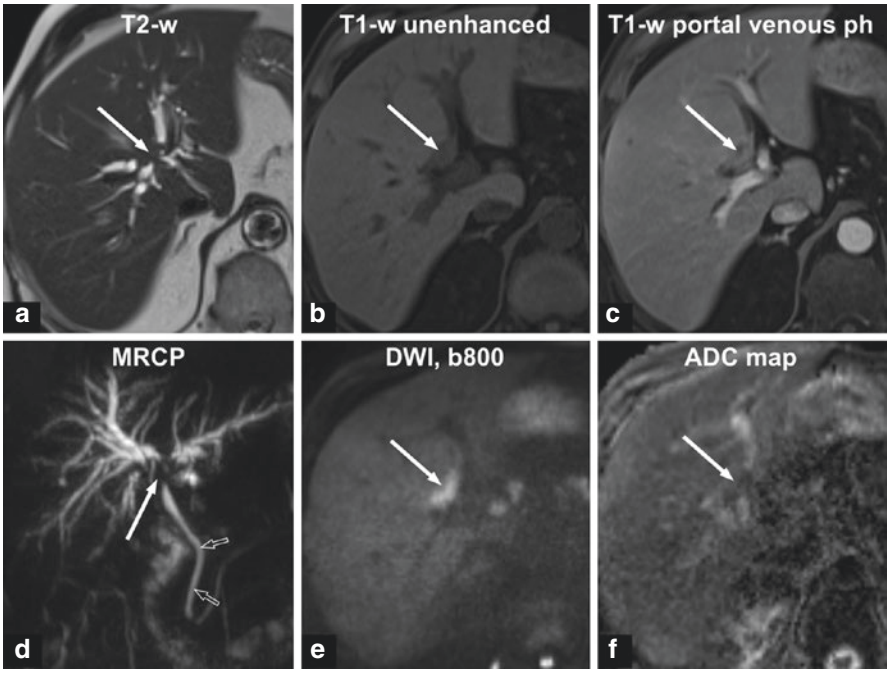

Fig. 5.6 Images of a 72-year-old male that presented with painless jaundice. As seen in Fig. 5.1, there is an obstructive soft-tissue lesion (arrow) in the liver hilum that has signal intensity (SI) similar to the adjacent parenchyma in T2-weighted image (**a**) and shows enhancement (**b**, **c**) after injection of extracellular gadolinium-based contrast agent. Om maximum intensity projection-MRCP (**d**), the obstructing lesion is shown to involve the common hepatic, left, right anterior and right posterior hepatic ducts and results in upstream duct dilatation. The common bile duct (open arrows) is ordinary (**d**). On DWI, the lesion shows markedly impeded diffusion with high SI in the image with *b*-value of 800 s/mm^2 (**e**) and dark appearance in the corresponding ADC map (**f**). Findings were suspicious of malignancy and histopathological findings after extended right hemihepatectomy showed IgG4-related cholangitis

References

1. Katabathina VS, Dasyam AK, Dasyam N, Hosseinzadeh K. Adult bile duct strictures: role of MR imaging and MR cholangiopancreatography in characterization. Radiographics. 2014;34(3):565–86. https://doi.org/10.1148/rg.343125211.
2. Bali MA, Pezzullo M, Pace E, Morone M. Benign biliary diseases. Eur J Radiol. 2017;93:217–28.
3. Bowlus CL, Olson KA, Gershwin ME. Evaluation of indeterminate biliary strictures. Nat Rev Gastroenterol Hepatol. 2016;13(1):28–37.
4. Saarinen S, Olerup O, Broomé U. Increased frequency of autoimmune diseases in patients with primary sclerosing cholangitis. Am J Gastroenterol. 2000;95(11):3195–9.
5. Karlsen TH, Folseraas T, Thorburn D, Vesterhus M. Primary sclerosing cholangitis – a comprehensive review. J Hepatol. 2017;67(6):1298–323.

6. Aabakken L, Karlsen TH, Albert J, Arvanitakis M, Chazouilleres O, Dumonceau JM, Färkkilä M, Fickert P, Hirschfield GM, Laghi A, Marzioni M, Fernandez M, Pereira SP, Pohl J, Poley JW, Ponsioen CY, Schramm C, Swahn F, Tringali A, Hassan C. Role of endoscopy in primary sclerosing cholangitis: European Society of Gastrointestinal Endoscopy (ESGE) and European Association for the Study of the Liver (EASL) Clinical Guideline. Endoscopy. 2017;49(6):588–608.
7. Walker SL, McCormick PA. Diagnosing cholangiocarcinoma in primary sclerosing cholangitis: an "evidence based radiology" review. Abdom Imaging. 2008;33(1):14–7.
8. Trikudanathan G, Navaneethan U, Njei B, Vargo JJ, Parsi MA. Diagnostic yield of bile duct brushings for cholangiocarcinoma in primary sclerosing cholangitis: a systematic review and meta-analysis. Gastrointest Endosc. 2014;79(5):783–9.
9. Nanda A, Brown JM, Berger SH, Lewis MM, Barr Fritcher EG, Gores GJ, Keilin SA, Woods KE, Cai Q, Willingham FF. Triple modality testing by endoscopic retrograde cholangiopancreatography for the diagnosis of cholangiocarcinoma. Ther Adv Gastroenterol. 2015;8(2):56–65.
10. Hubers LM, Maillette de Buy Wenniger LJ, Doorenspleet ME, Klarenbeek PL, Verheij J, Rauws EA, van Gulik TM, Oude Elferink RP, van de Graaf SF, de Vries N, Beuers U. IgG4-associated cholangitis: a comprehensive review. Clin Rev Allergy Immunol. 2015;48(2-3):198–206.
11. Nakazawa T, Shimizu S, Naitoh I. IgG4-related sclerosing cholangitis. Semin Liver Dis. 2016;36(3):216–28.
12. Deoliveira ML, Schulick RD, Nimura Y, Rosen C, Gores G, Neuhaus P, Clavien PA. New staging system and a registry for perihilar cholangiocarcinoma. Hepatology. 2011;53(4):1363–71.
13. Razumilava N, Gores GJ. Classification, diagnosis, and management of cholangiocarcinoma. Clin Gastroenterol Hepatol. 2013;11(1):13–21.e1; quiz e3–4. https://doi.org/10.1016/j.cgh.2012.09.009.
14. Blechacz B, Komuta M, Roskams T, Gores GJ. Clinical diagnosis and staging of cholangiocarcinoma. Nat Rev Gastroenterol Hepatol. 2011;8(9):512–22.
15. Saxena A, Chua TC, Chu FC, Morris DL. Improved outcomes after aggressive surgical resection of hilar cholangiocarcinoma: a critical analysis of recurrence and survival. Am J Surg. 2011;202(3):310–20.
16. Klempnauer J, Ridder GJ, von Wasielewski R, Werner M, Weimann A, Pichlmayr R. Resectional surgery of hilar cholangiocarcinoma: a multivariate analysis of prognostic factors. J Clin Oncol. 1997;15(3):947–54.
17. Igami T, Nagino M, Oda K, Nishio H, Ebata T, Yokoyama Y, Shimoyama Y. Clinicopathologic study of cholangiocarcinoma with superficial spread. Ann Surg. 2009;249(2):296–302.
18. Chang S, Lim JH, Choi D, Kim SK, Lee WJ. Differentiation of ampullary tumor from benign papillary stricture by thin-section multidetector CT. Abdom Imaging. 2008;33(4):457–62.
19. Kim JH, Kim MJ, Chung JJ, Lee WJ, Yoo HS, Lee JT. Differential diagnosis of periampullary carcinomas at MR imaging. Radiographics. 2002;22(6):1335–52.
20. Kim S, Lee NK, Lee JW, Kim CW, Lee SH, Kim GH, Kang DH. CT evaluation of the bulging papilla with endoscopic correlation. Radiographics. 2007;27(4):1023–38.
21. Irie H, Honda H, Shinozaki K, Yoshimitsu K, Aibe H, Nishie A, Nakayama T, Masuda K. MR imaging of ampullary carcinomas. J Comput Assist Tomogr. 2002;26(5):711–7.
22. Kim TU, Kim S, Lee JW, Woo SK, Lee TH, Choo KS, Kim CW, Kim GH, Kang DH. Ampulla of Vater: comprehensive anatomy, MR imaging of pathologic conditions, and correlation with endoscopy. Eur J Radiol. 2008;66(1):48–64.
23. Andersson M, Kostic S, Johansson M, Lundell L, Asztély M, Hellström M. MRI combined with MR cholangiopancreatography versus helical CT in the evaluation of patients with suspected periampullary tumors: a prospective comparative study. Acta Radiol. 2005;46(1):16–27.
24. Chung YE, Kim MJ, Park YN, Lee YH, Choi JY. Staging of extrahepatic cholangiocarcinoma. Eur Radiol. 2008;18(10):2182–95.

25. Kim JY, Lee JM, Han JK, Kim SH, Lee JY, Choi JY, Kim SJ, Kim HJ, Kim KH, Choi BI. Contrast-enhanced MRI combined with MR cholangiopancreatography for the evaluation of patients with biliary strictures: differentiation of malignant from benign bile duct strictures. J Magn Reson Imaging. 2007;26(2):304–12.
26. Kim MJ, Mitchell DG, Ito K, Outwater EK. Biliary dilatation: differentiation of benign from malignant causes—value of adding conventional MR imaging to MR cholangiopancreatography. Radiology. 2000;214(1):173–81.
27. Park MS, Kim TK, Kim KW, Park SW, Lee JK, Kim JS, Lee JH, Kim KA, Kim AY, Kim PN, Lee MG, Ha HK. Differentiation of extrahepatic bile duct cholangiocarcinoma from benign stricture: findings at MRCP versus ERCP. Radiology. 2004;233(1):234–40.
28. Clayton RA, Clarke DL, Currie EJ, Madhavan KK, Parks RW, Garden OJ. Incidence of benign pathology in patients undergoing hepatic resection for suspected malignancy. Surgeon. 2003;1(1):32–8.
29. Gerhards MF, Vos P, van Gulik TM, Rauws EA, Bosma A, Gouma DJ. Incidence of benign lesions in patients resected for suspicious hilar obstruction. Br J Surg. 2001;88(1):48–51.
30. Cui XY, Chen HW. Role of diffusion-weighted magnetic resonance imaging in the diagnosis of extrahepatic cholangiocarcinoma. World J Gastroenterol. 2010;16(25):3196–201.
31. Tsai TH, Hsu JS, Lai ML, Liu GC, Shih MC, Chen CY. Added value of diffusion-weighted imaging to MR cholangiopancreatography for the diagnosis of bile duct dilatations. Abdom Radiol (NY). 2016;41(3):485–92.
32. Park HJ, Kim SH, Jang KM, Choi SY, Lee SJ, Choi D. The role of diffusion-weighted MR imaging for differentiating benign from malignant bile duct strictures. Eur Radiol. 2014;24(4):947–58.
33. Choi KS, Lee JM, Joo I, Han JK, Choi BI. Evaluation of perihilar biliary strictures: does DWI provide additional value to conventional MRI? AJR Am J Roentgenol. 2015;205(4):789–96.
34. Lee NK, Kim S, Seo HI, Kim DU, Woo HY, Kim TU. Diffusion-weighted MR imaging for the differentiation of malignant from benign strictures in the periampullary region. Eur Radiol. 2013;23(5):1288–96.
35. Yoo RE, Lee JM, Yoon JH, Kim JH, Han JK, Choi BI. Differential diagnosis of benign and malignant distal biliary strictures: value of adding diffusion-weighted imaging to conventional magnetic resonance cholangiopancreatography. J Magn Reson Imaging. 2014;39(6):1509–17.
36. Sim KC, Park BJ, Han NY, Sung DJ, Kim MJ, Han YE. Efficacy of ZOOMit coronal diffusion-weighted imaging and MR texture analysis for differentiating between benign and malignant distal bile duct strictures. Abdom Radiol. 2020;45(14) https://doi.org/10.1007/s00261-020-02625-0.
37. Park MJ, Kim YK, Lim S, Rhim H, Lee WJ. Hilar cholangiocarcinoma: value of adding DW imaging to gadoxetic acid-enhanced MR imaging with MR cholangiopancreatography for preoperative evaluation. Radiology. 2014;270(3):768–76.

Diffusion-Weighted Imaging of the Pancreas

6

Carlos Bilreiro and Celso Matos

6.1 Introduction

MRI has become an established imaging modality of the pancreas due to recent technological advances, and diffusion-weighted imaging (DWI) is one major contributor to its success. DWI is sensitive to the Brownian movement of water molecules in tissues, which is a thermally driven process [1, 2]. Different tissues have different degrees of restriction to the Brownian movement of water molecules, due to different intracellular and extracellular compartments' composition and cell density [3, 4]. Thus, in DWI, tissues appear with higher signal intensity depending on the presence of restriction to diffusion. The physics behind DWI are explained in a previous chapter.

DWI is usually performed with a T2-weighted spin-echo echo planar imaging (SE-EPI) sequence, so the images obtained are both sensitive to T2 and diffusion. By increasing the *b* values (usually up to 1000 s/mm^2 in abdominal imaging), the images obtained are increasingly sensitive to water diffusion and less sensitive to T2 [5]. When performing DWI in the clinical setting, an apparent diffusion coefficient (ADC) map is automatically calculated on modern MRI workstations, which provides visual information of quantification of apparent diffusion coefficients in the images obtained, without influence of T2.

Because the pancreas is an organ with high blood perfusion, under low *b* values (<150 s/mm^2), intravoxel incoherent motion (IVIM) due to blood flow in microcirculation network becomes an important source of pseudo diffusion (perfusion), which can be used to derive flowing blood volume fraction, perfusion free diffusion coefficient and perfusion coefficient [6]. Promising results on the use of IVIM have been reported, however, at the present moment, it is not yet implemented in routine clinical practice [7–9].

C. Bilreiro · C. Matos (✉)
Department of Radiology, Champalimaud Centre for the Unknown, Lisbon, Portugal
e-mail: celso.matos@fundacaochampalimaud.pt

C. Matos, N. Papanikolaou (eds.), *Diffusion Weighted Imaging of the Hepatobiliary System*, https://doi.org/10.1007/978-3-319-62977-3_6

6.2 Image Acquisition and Technical Aspects

As stated before, DWI is usually performed over a T2-weighted SE-EPI sequence, preferably using parallel imaging for reduced acquisition times. Fat signal suppression is usually performed, either with spectral fat saturation or spectral adiabatic inversion recovery sequence (SPAIR) [10].

DWI is known for a low in-plane resolution and suffers from susceptibility and motion artifacts [10]. A reduced field of view (FOV) has been shown to improve image quality and reduce these artifacts, however with a reduced signal-to-noise ratio (SNR) [11, 12]. With the increasingly common use of 3 T MRI, one can expect higher SNR with high resolution images [13].

An example of DWI sequence parameters at 3 T is shown in Table 6.1.

6.3 DWI in the Normal Pancreas

The normal disease-free pancreas is basically homogeneous on DWI and should serve as tissue background when identifying focal lesions and abnormalities (Fig. 6.1) [10]. Slightly decreasing ADC values in the different anatomical segments (from head to body to tail) have been reported [14, 15]. However, other studies found variable or no differences in ADC values measured in different pancreatic anatomical segments [10, 16–18].

DWI has been used to evaluate pancreatic exocrine function. Increased and peaking ADC values have been reported, mainly in the pancreatic head, early after secretin administration in healthy subjects, with a subsequent gradual decrease to baseline values [19, 20].

Table 6.1 Suggested parameters for acquiring DWI of the pancreas at 3 T scanners

MR parameters for DWI of the pancreas at 3 T	
Transmission technology	Multi transmit radiofrequency
Body coil	Phased-array 16 channel
FOV	260 × 303 mm
Voxel size	1.8 × 1.8 × 5 mm^3
Sequence	SE EPI DWI
EPI factor	63
B values	0, 150, 1000
Number of signal averages	3 (2, 2, 8)
Parallel imaging	Sense RL 2.6 and POS 1.5 = S total 3.9
Breathing motion	Free breathing with respiratory triggering
TR	1200 ms
TE	82 ms
Fat suppression	SPAIR

Abbreviations: *FOV* field of view, *SE* spin-echo, *EPI* echo planar imaging, *DWI* diffusion weighted imaging, *Sense* sensitivity encoding, *RL* right to left, *TR* repetition time, *TE* echo time, *SPAIR* spectral adiabatic inversion recovery

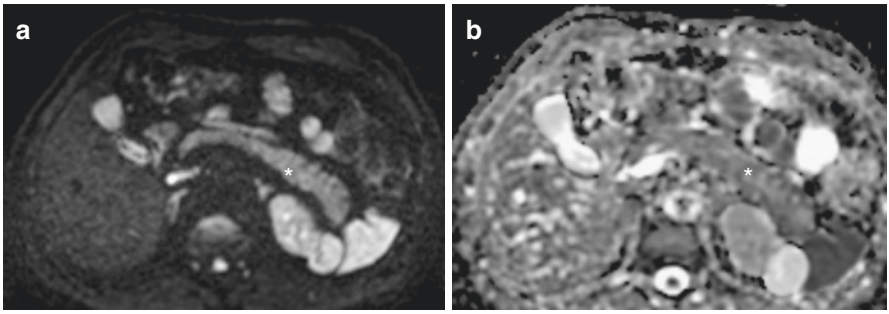

Fig. 6.1 Normal pancreas on DWI b600 (**a**) with respective ADC map (**b**). The healthy pancreatic parenchyma is basically homogeneous (asterisk), serving as tissue background for identification of focal lesions

6.4 DWI of Pancreatic Pathological Conditions

6.4.1 Inflammatory Conditions

6.4.1.1 Acute Pancreatitis

In the setting of acute pancreatitis, the role of DWI is not yet clear. The diagnosis, based on the 2012 revised Atlanta consensus, relies in the presence of two of the following criteria: acute onset of persistent, severe epigastric pain; serum lipase activity (or amylase activity) at least three times greater than the upper limit of normal; characteristic imaging features on contrast-enhanced CT, MRI, or ultrasound [21]. Imaging studies, therefore, are frequently not necessary for the diagnosis and when they are actually performed, MRI is usually not the first option, due to low availability in the emergency setting and higher financial costs.

Acute inflammatory changes in the pancreatic parenchyma have been reported to cause restricted diffusion, with lower ADC values than the healthy pancreatic parenchyma [22]. More importantly, DWI may have a role in identifying infection in acute pancreatic and acute necrotic fluid collections (Figs. 6.2, 6.3 and 6.4). These have been shown to present with restricted diffusion in the collection periphery, a finding reported in one study to have 100% sensitivity and 90.9% specificity when differentiating from sterile collections [23]. The same study reported better DWI MRI performance for this diagnosis when compared to CT (60% sensitivity and 100% specificity). In another study, the addition of DWI to a standard MRI protocol significantly increased diagnostic accuracy for infected pancreatic fluid collections [24]. These authors also suggested a possible increase in diagnostic confidence level for inexperienced readers, probably due to the straightforward nature of DWI interpretation.

6.4.1.2 Chronic Pancreatitis

ADC values of the pancreatic parenchyma have been shown to be lower in chronic pancreatitis compared with healthy pancreas [16, 25]. One study reported an ADC

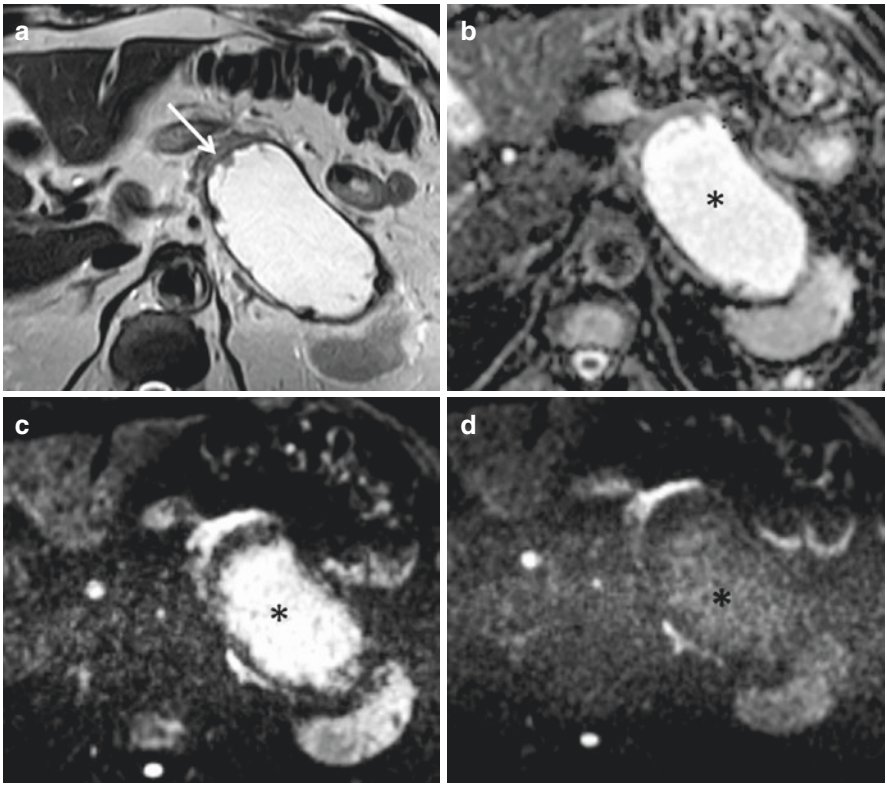

Fig. 6.2 Sterile acute pancreatic fluid collection. There is a large collection in the tail of the pancreas (**a**, arrow), well depicted in T2WI. The lesion shows high signal intensity on DWI b1000, suspicious for possible infection (**c**, asterisk). However, in DWI b1600 the lesion shows low signal intensity (**d**, asterisk), exemplifying the importance of high *b* value DWI to minimize T2 shine-through effects, as confirmed with high ADC values in the lesion (**b**, asterisk)

cutoff value of 2.2×10^{-3} mm^2/s with 100% sensitivity and 73% specificity for this purpose, at 3 T MRI [24]. However, in the same studies, when trying to differentiate between patients with severe and mild chronic pancreatitis, ADC values have not proven useful.

The use of secretin in conjunction with DWI has also been studied for chronic pancreatitis. Delayed and absent peak of ADC values after secretin administration have been correlated with the presence of chronic alcohol abuse and severe chronic pancreatitis, respectively [20].

6.4.1.3 Autoimmune Pancreatitis

Autoimmune pancreatitis may have a variable appearance in MRI studies. The classical description is a diffusely enlarged, "sausage-like" pancreas with decreased signal on T1- and increased signal on T2-weighted images and delayed enhancement after intravenous contrast administration [26–28]. However, different imaging presentations of autoimmune pancreatitis are described, most frequently a focal

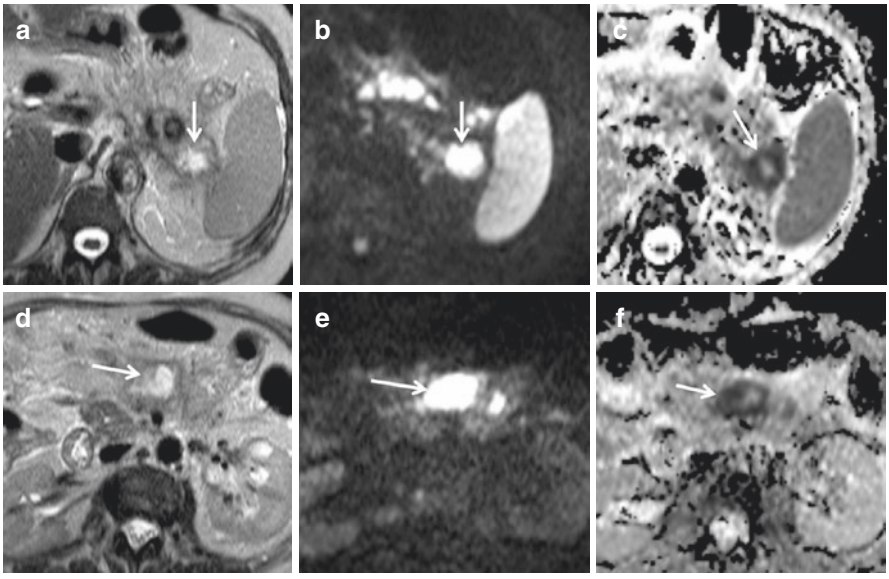

Fig. 6.3 Infected acute pancreatic fluid collections. This patient with acute pancreatitis presented several fluid collections (**a** and **d**, arrows). These collections show restricted diffusion mainly in the periphery, with high signal intensity in b1000 DWI (**b** and **e**, arrows) and low ADC values (**c** and **f**, arrows). These collections were drained and the presence of infection was confirmed

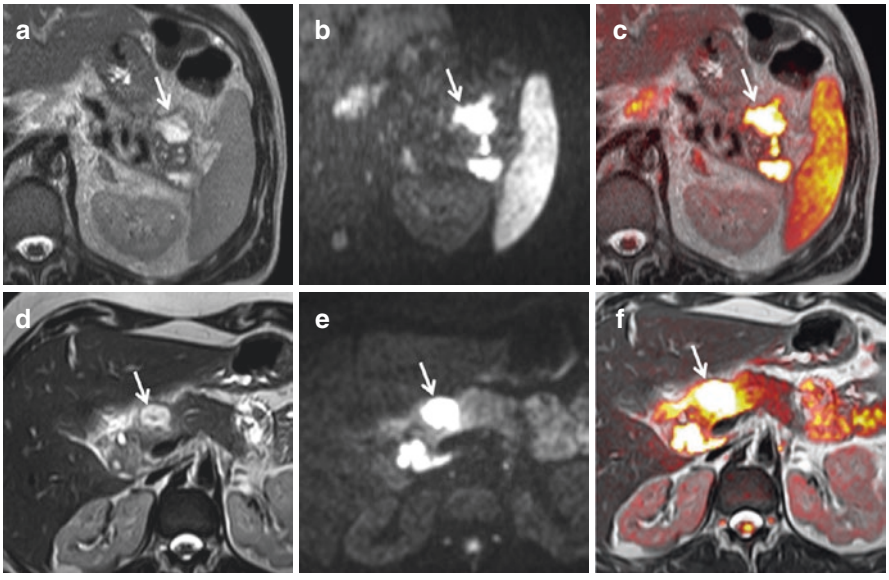

Fig. 6.4 Infected acute pancreatic fluid collections in two different patients (**a**–**c** and **d**–**f**). In both patients, the pancreatic collections (**a** and **d**, arrows) show restricted diffusion with high signal intensity in high *b* value DWI (**b** and **e**, arrows). The T2-DWI fusion images clearly depict the lesions with restricted diffusion (**c** and **f**, arrows)

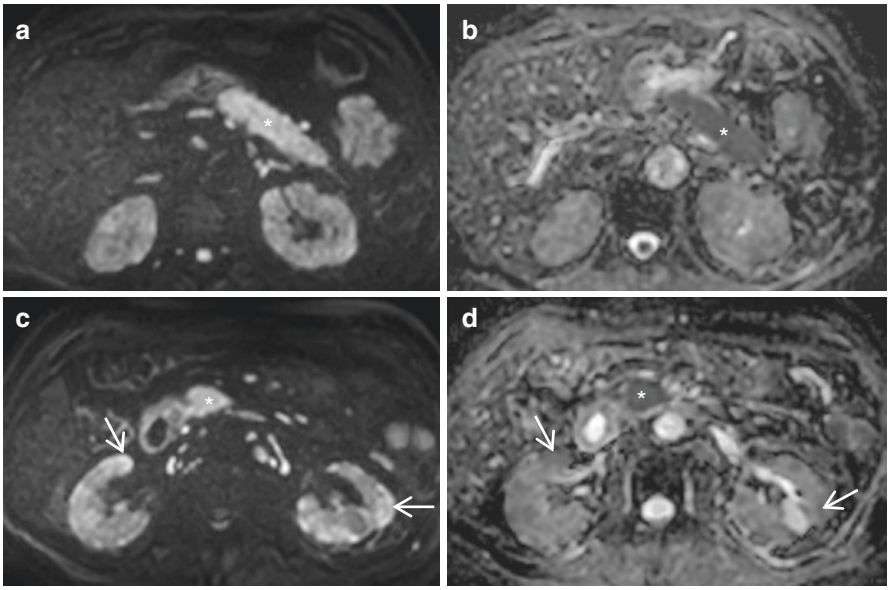

Fig. 6.5 Autoimmune pancreatitis (IgG4-related disease). Note the diffusely enlarged pancreatic parenchyma, with restricted diffusion on DWI b900 (**a** and **c**, asterisks) and consequently low values on ADC map (**b** and **d**, asterisks). There is also bilateral kidney involvement (**c** and **d**, arrows)

mass-like enlargement, which poses a diagnostic challenge. Also, signal changes with absent pancreatic enlargement may be seen, although less frequently [26–28].

DWI may help in the diagnosis of autoimmune pancreatitis (Figs. 6.5 and 6.6). When compared to healthy pancreatic parenchyma, ADC values of autoimmune pancreatitis are known to be lower [29–32]. Also, in the setting of IgG4-related pancreatitis, the involvement of other organs (especially the kidneys) can accurately be detected by DWI, providing additional clues for the differential diagnosis [33].

Another potential role of ADC values in the setting of autoimmune pancreatitis is evaluation of disease activity and response to therapy. One study reported lower ADC values in symptomatic patients when compared with asymptomatic patients [34]. Others reported increasing ADC values correlate with response to steroid administration [35]. IVIM-based models might also help in assessing response to therapy, with perfusion fraction showing progressively increasing values with steroid administration, possibly serving as an imaging biomarker [36].

6.4.1.4 Differentiating Mass Forming Pancreatitis from Pancreatic Adenocarcinoma

An important diagnostic challenge arises when differentiating mass forming pancreatitis from pancreatic adenocarcinoma. ADC values have been studied as a tool to perform the differential diagnosis, however with conflicting success in literature

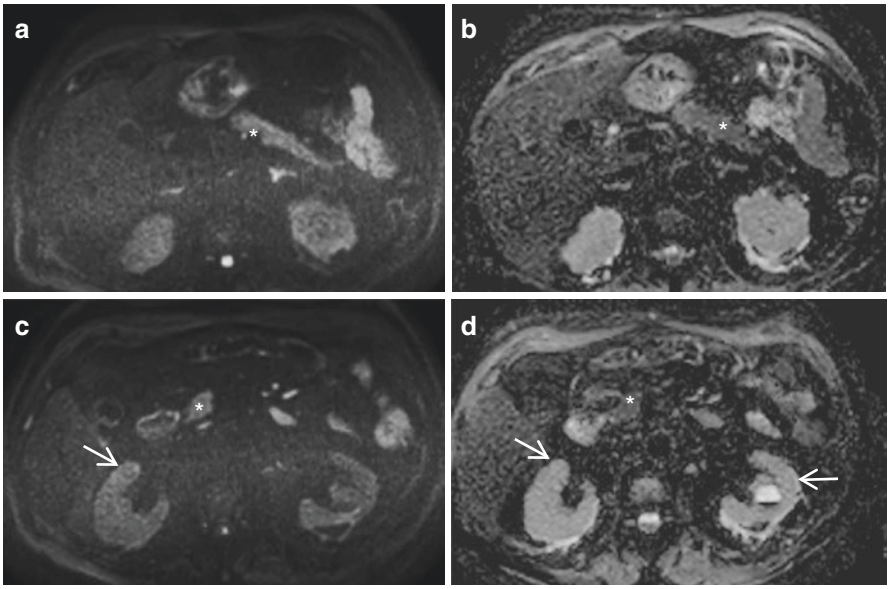

Fig. 6.6 Same patient from Fig. 6.5, after corticosteroid therapy. The pancreatic parenchyma is no longer enlarged and there is no restricted diffusion on DWI b900 (**a**, **c**) with corresponding normal ADC map (**b**, **d**) (asterisks). The kidney lesions seen previously have also resolved with therapy (arrows)

reports. Some studies reported lower ADC values in pancreatic adenocarcinoma than mass forming pancreatitis [29–31]. One study even reported a sensitivity of 100% and a specificity of 98% when using ADC cutoff values of 0.88×10^{-3} mm^2/s together with morphologic findings and delayed parenchymal enhancement [30]. However, others found ADC values unable to differentiate both conditions, or even lower ADC values in pancreatic adenocarcinoma [32, 37]. Due to these conflicting reports, the role of ADC values in differentiating mass forming pancreatitis from pancreatic adenocarcinoma remains unclear.

The use of intravoxel incoherent motion (IVIM)-based models for characterization of pancreatic lesions has been proposed in the differentiation of mass forming pancreatitis and pancreatic adenocarcinoma. The perfusion fraction has been reported as the most valuable IVIM derived parameter for differentiating these entities, with pancreatic adenocarcinoma presenting significantly lower values than pancreatitis [8, 36, 38, 39]. Another study evaluated IVIM-derived parameter maps (diffusivity, perfusion fraction and ADC), reporting good discrimination of pancreatic adenocarcinoma from pancreatitis and neuroendocrine tumors [9]. However, one study reported conflicting results, with perfusion fraction and fast diffusion unable to differentiate these conditions [40]. These results require further studies for clarification, validation and standardization of protocols, before IVIM-based models can be recommended for clinical practice.

6.4.2 Cystic Pancreatic Lesions

Cystic pancreatic lesions include lesions with an invariably benign course (pancreatic fluid collection/pseudocyst, serous cystadenoma, cystic lymphangioma) and lesions with malignant potential (mucinous cystadenoma and intraductal papillary mucinous neoplasm—IPMN).

As discussed previously, DWI may help in the diagnosis of infected pancreatic fluid collection [23, 24]. However, DWI has been reported to be of little value in differentiating pancreatic cystic lesions, with conflicting results in the literature [10]. Several researchers have studied DWI for differentiating mucinous from non-mucinous lesions, malignant from benign lesions and inflammatory from non-inflammatory lesions; however their results were conflicting or showed DWI unable to confidently differentiate these conditions [41–46].

A possible role of DWI with measurement of ADC values in pancreatic cystic lesions might be the differentiation of high-grade/invasive IPMN from low-grade IPMN, with high-grade/invasive lesions presenting significantly lower values than low-grade lesions, as reported in one study (Fig. 6.7) [43]. Another study reported

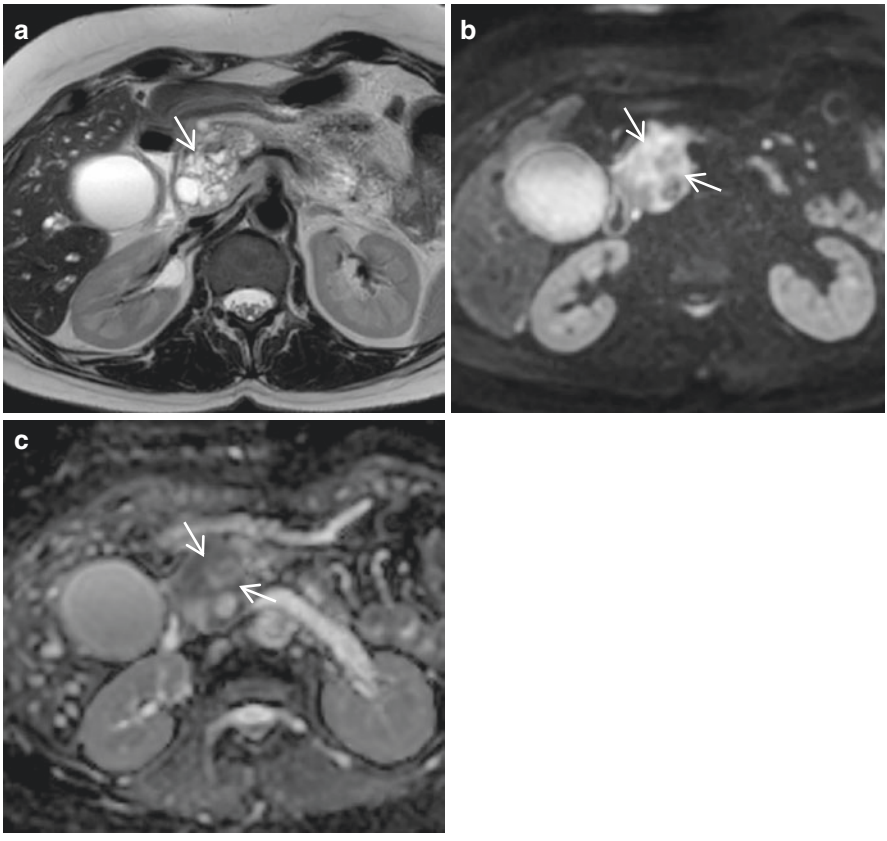

Fig. 6.7 Malignant mixed-type IPMN. There is a large complex cystic lesion in the pancreatic head, as seen on T2 weighted images (**a**, arrow). On DWI b900 (**b**), there are internal septa and solid components with restricted diffusion (arrows) and corresponding low values on ADC map (**c**)

significantly higher specificity for DWI MRI compared with conventional MRI, when differentiating malignant from benign IPMN lesions, mainly due to identification of restricted diffusion on the cyst wall, internal septations, mural nodules or solid components [47]. However, further studies are required to confirm these results.

6.4.3 Pancreatic Ductal Adenocarcinoma

DWI MRI has a major role in diagnosing pancreatic adenocarcinoma, with lesions presenting restricted diffusion (Figs. 6.8 and 6.9). High sensitivity and specificity have been reported (96.2% and 98.6%, respectively) using *b* value of 1000 s/mm^2 [48]. DWI is also comparable to a contrast-enhanced comprehensive MRI for diagnosis of pancreatic adenocarcinoma, with similar accuracy [49].

DWI was studied regarding its ability to evaluate tumor grading, but with conflicting results. One study reported significantly lower ADC values in poorly differentiated adenocarcinoma with dense fibrosis compared to well/moderately differentiated adenocarcinomas [50]. However, another study reported no association between ADC values of pancreatic adenocarcinoma and tumor grade or other adverse pathological features [51].

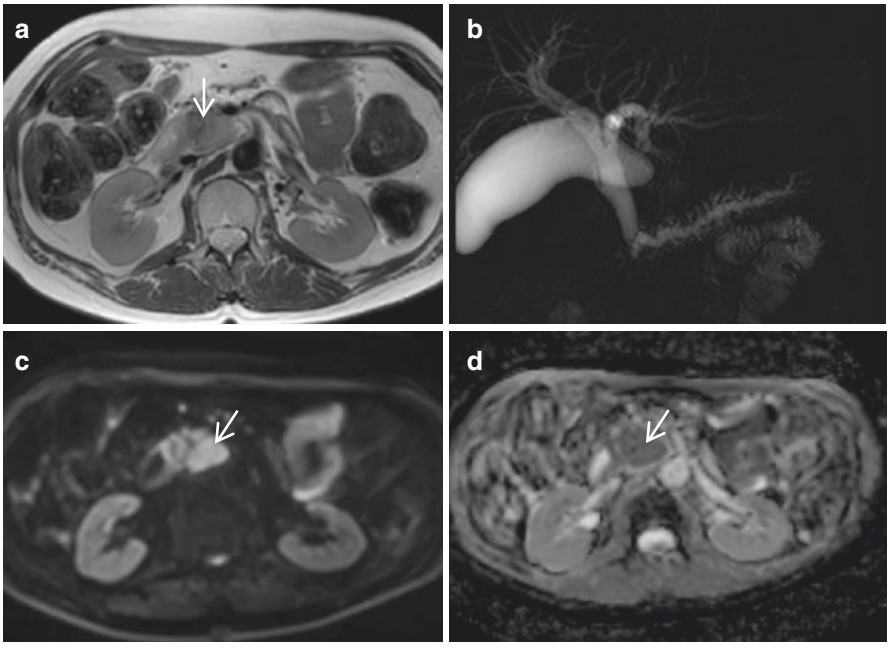

Fig. 6.8 Ductal adenocarcinoma of the pancreatic head. This is a typical case, with a mass in the pancreatic head, identified on T2 weighted images (**a**), causing diffuse dilatation of the biliary tree and the main pancreatic duct, clearly visible on MRCP (**b**). On DWI b900, the mass presents with restricted diffusion (**c**, arrow) with consequent low values on ADC map (**d**, arrow)

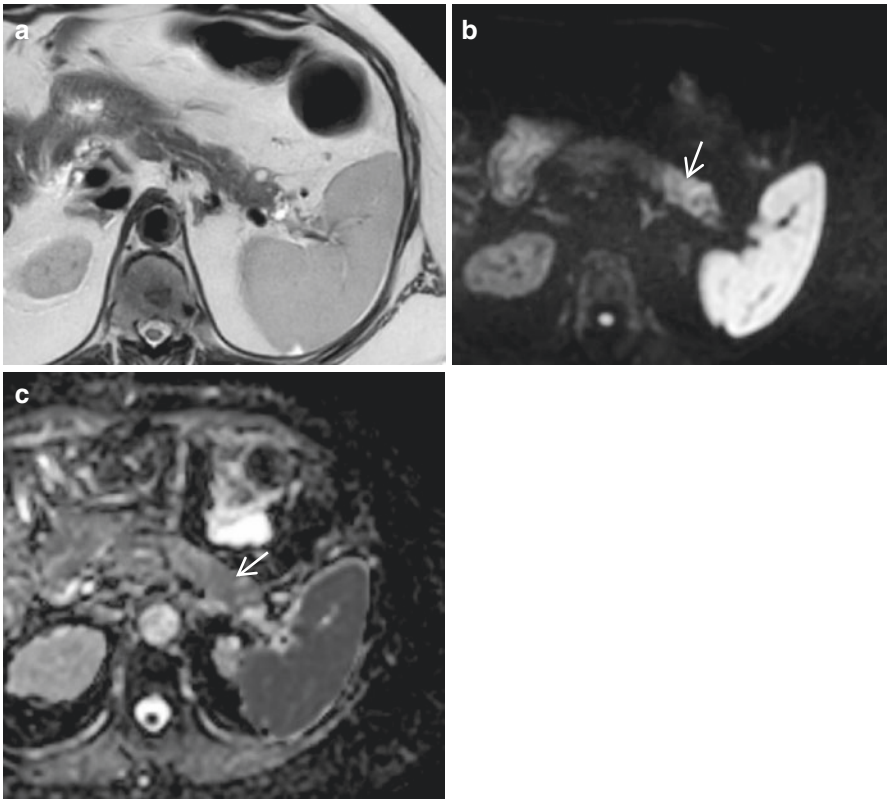

Fig. 6.9 Ductal adenocarcinoma of the pancreatic tail. The tumor is difficult to identify on T2 weighted images (**a**), mainly because of its location in the pancreatic tail, where it doesn't cause typical dilatation of the main pancreatic duct. On DWI b900, it is clearly seen with restricted diffusion (**b**, arrow), with corresponding low values on ADC map (**c**, arrow)

The role of DWI in the diagnostic challenge of differentiating mass forming pancreatitis from pancreatic adenocarcinoma has been discussed previously in this chapter.

DWI may be useful in the prediction of tumor response to neoadjuvant therapy. Two studies reported that tumors of patients without response to neoadjuvant chemotherapy or radio-chemotherapy present lower ADC values, in comparison with patients with response [52, 53].

Another role of DWI may be the imaging assessment of tumor response to neoadjuvant therapy. One study reported reduction of 39% in tumor DW volume (a software assisted DWI tumor volume measurement) as having great performance to assess response to neoadjuvant chemotherapy, with 93% sensitivity and 100% specificity [54]. The same study evaluated IVIM derived parameters and reported increasing diffusivity and ADC values after neoadjuvant chemotherapy in patients with response to therapy, whereas no changes were seen in patients without response

to therapy. Perfusion fraction, however, did not show any significant increase in responding patients, as might have been expected. These are promising results; further studies should help define the role of DWI in assessing response to neoadjuvant chemotherapy.

6.4.4 Pancreatic Neuroendocrine Tumors

Typically, pancreatic neuroendocrine tumors are small lesions with early enhancement in the arterial phase of contrast-enhanced imaging studies [55, 56]. However, variable imaging findings are common, posing diagnostic challenges. DWI MRI has been proposed for the detection and characterization of these lesions. Tumor detection was reported to significantly improve with the addition of DWI to T2-weighted images, with the tumors showing restricted diffusion (Fig. 6.10) [57–59]. One of these studies used fusion T2 and DWI images, reporting improved lesion detection especially for small isointense lesions on T2-weighted images [58].

DWI has also been studied for its ability to predict tumor grade according to the 2010 World Health Organization classification [60]. A recent meta-analysis reviewed nine studies on this topic, more specifically the role of ADC, using cutoff values of $0.95–1.27 \times 10^{-3}$ mm²/s [61–70]. A high diagnostic accuracy was reported, with higher grade tumors (G2 and G3) showing lower ADC values, with pooled sensitivity of 84% and pooled specificity of 87%, when compared with low grade tumors (G1). The same study revealed that 3 T devices had higher sensitivity (93%);

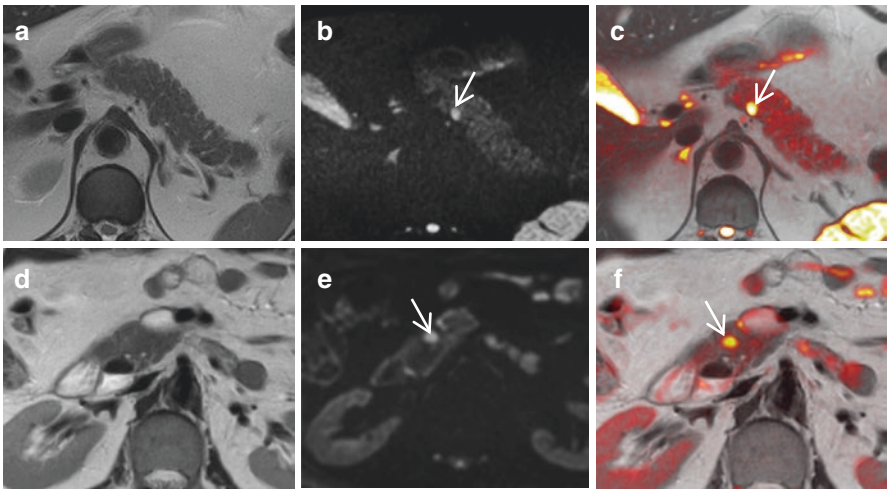

Fig. 6.10 Pancreatic neuroendocrine tumors in two patients (**a**–**c**, **d**–**f**). In both patients, there are no visible pancreatic lesions on T2 weighted images (**a**, **d**). On DWI, a focal lesion is clearly identified in both patients (**b** and **c**, arrows). On fusion T2-DWI images, the lesions are also clearly visible (**c** and **f**, arrows)

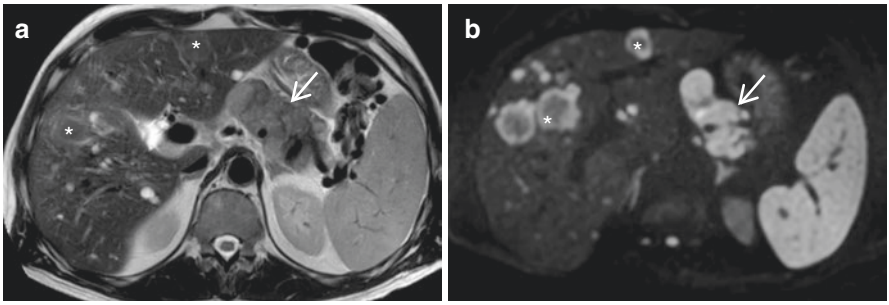

Fig. 6.11 Pancreatic neuroendocrine tumor with liver metastasis. A large mass in the pancreatic body and tail is seen in T2 weighted images and DWI (**a** and **b**, arrows). The liver metastases are visible on T2 weighted images, but badly defined (**a**, asterisks). On DWI, the liver metastases are much clearly depicted (**b**, asterisks)

additionally, using a *b* value of 1000 s/mm^2 and an ADC cutoff of 1.0×10^{-3} mm^2/s had the highest specificity (95%). Once standardized imaging parameters are adopted and validation studies are performed, DWI might be used to predict tumor grade in clinical practice.

When trying to differentiate pancreatic neuroendocrine tumors from pancreatic adenocarcinoma, IVIM based models might prove useful. Perfusion fraction and incoherent microcirculation (fast diffusion) have been reported as the most valuable parameters, with neuroendocrine tumors presenting significantly higher values in comparison with adenocarcinoma [8, 39, 40].

Another role of DWI in the setting of pancreatic neuroendocrine tumors is identification of liver metastasis, with high sensitivity (Fig. 6.11) [10, 71].

6.4.5 Rare Conditions

Rare pancreatic lesions not included in the previous discussions comprise solid pseudopapillary neoplasm and intrapancreatic accessory spleen.

Solid pseudopapillary neoplasm has been reported to present lower ADC vales compared with normal pancreatic parenchyma [18, 72, 73]. However, the role of DWI in diagnosis and management of these tumors remains unclear.

Intrapancreatic spleen is usually diagnosed in MRI by comparing the lesion with the spleen, as signal intensities should be similar in all sequences. DWI may further help in this setting, with two studies reporting excellent diagnostic accuracy by visually comparing findings in the focal pancreatic lesion and the spleen [74, 75].

6.5 Conclusion

DWI MRI is a useful tool for the diagnosis of focal and diffuse pancreatic pathological conditions. DWI may further help evaluating tumor grade (neuroendocrine tumor and IPMN) and predicting and assessing therapeutic response

Table 6.2 Short summary of main aspects for DW MRI of the pancreas

Condition	Relevant aspects
Normal pancreas	Homogeneous DWI signal Peak ADC values after secretin administration, with subsequent gradual decrease to baseline
Acute pancreatitis	Low ADC values in the parenchyma Restricted diffusion in the periphery of fluid collections indicates infection
Chronic pancreatitis	Low ADC values in the parenchyma Delayed or absent peak in ADC values after secretin administration
Autoimmune pancreatitis	Low ADC values in the parenchyma ADC and IVIM perfusion fraction values may correlate with symptoms and response to therapy
Differentiating mass forming pancreatitis from pancreatic adenocarcinoma	ADC values unable to differentiate IVIM-based models appear useful with perfusion fraction as the best parameter
Cystic lesions	DWI unable to differentiate lesions ADC values lower in malignant/high-grade IPMN, especially components of complex lesions
Ductal adenocarcinoma	DWI has high sensitivity and accuracy for diagnosis ADC values and IVIM-based models may help predict and assess response to neoadjuvant therapy
Neuroendocrine tumors	DWI improves tumor detection ADC values correlate with tumor grading IVIM-based models with perfusion fraction and incoherent diffusivity may help differentiate from adenocarcinoma DWI identifies liver metastases
Solid pseudopapillary neoplasm	Low ADC values in the tumor
Intrapancreatic spleen	DWI with identical findings to the spleen

(pancreatic ductal adenocarcinoma and autoimmune pancreatitis). IVIM-based models are promising methods of lesion characterization and may be further developed in the near future. Table 6.2 provides a short summary of key aspects from this chapter.

References

1. Paul L. Sur la théorie du mouvement brownien. C R Acad Sci. 1908;146:530–2.
2. Albert E. Über die von der molekularkinetischen Theorie der Wärme geforderte Bewegung von in ruhenden Flüssigkeiten suspendierten Teilchen. Ann Phys. 1905;322(8):549–60.
3. Stejskal EO, Tanner JE. Spin diffusion measurements: spin-echo in the presence of a time dependent field gradient. J Chem Phys. 1965;42:288–92.
4. Qayyum A. Diffusion-weighted imaging in the abdomen and pelvis: concepts and applications. Radiographics. 2009;29(6):1797–810.
5. Koh DM, Collins DJ. Diffusion-weighted MRI in the body: applications and challenges in oncology. AJR Am J Roentgenol. 2007;188(6):1622–35.

6. Le Bihan D, Breton E, Lallemand D, Aubin ML, Vignaud J, Laval-Jeantet M. Separation of diffusion and perfusion in intravoxel incoherent motion MR imaging. Radiology. 1988;168(2):497–505.
7. Klau M, Mayer P, Bergmann F, Maier-Hein K, Hase J, Hackert T, Kauczor HU, Grenacher L, Stieltjes B. Correlation of histological vessel characteristics and diffusion-weighted imaging Intravoxel incoherent motion-derived parameters in pancreatic ductal adenocarcinomas and pancreatic neuroendocrine tumors. Investig Radiol. 2015;50(11):792–7.
8. Kang KM, Lee JM, Yoon JH, Kiefer B, Han JK, Choi BI. Intravoxel incoherent motion diffusion-weighted MR imaging for characterization of focal pancreatic lesions. Radiology. 2014;270(2):444–53.
9. Concia M, Sprinkart AM, Penner AH, Brossart P, Gieseke J, Schild HH, Willinek WA, Mürtz P. Diffusion-weighted magnetic resonance imaging of the pancreas: diagnostic benefit from an intravoxel incoherent motion model-based 3 b-value analysis. Investig Radiol. 2014;49(2):93–100.
10. Barral M, Taouli B, Guiu B, Koh DM, Luciani A, Manfredi R, Vilgrain V, Hoeffel C, Kanematsu M, Soyer P. Diffusion-weighted MR imaging of the pancreas: current status and recommendations. Radiology. 2015;274(1):45–63.
11. Riffel P, Michaely HJ, Morelli JN, Pfeuffer J, Attenberger UI, Schoenberg SO, Haneder S. Zoomed EPI-DWI of the pancreas using two-dimensional spatially-selective radiofrequency excitation pulses. PLoS One. 2014;9(3):e89468.
12. Thierfelder KM, Sommer WH, Dietrich O, Meinel FG, Theisen D, Paprottka PM, Strobl FF, Pfeuffer J, Reiser MF, Nikolaou K. Parallel-transmit-accelerated spatially selective excitation MRI for reduced-fov diffusion-weighted-imaging of the pancreas. Eur J Radiol. 2014;83(10):1709–14.
13. Ma C, Li YJ, Pan CS, Wang H, Wang J, Chen SY, Lu JP. High resolution diffusion weighted magnetic resonance imaging of the pancreas using reduced field of view single-shot echo-planar imaging at 3 T. Magn Reson Imaging. 2014;32(2):125–31.
14. Ye XH, Gao JY, Yang ZH, Liu Y. Apparent diffusion coefficient reproducibility of the pancreas measured at different MR scanners using diffusion-weighted imaging. J Magn Reson Imaging. 2014;40(6):1375–81.
15. Schoennagel BP, Habermann CR, Roesch M, Hahne JD, Arndt C, Kleibeler L, Petersen KU, Graessner J, Adam G, Herrmann J. Diffusion-weighted imaging of the healthy pancreas: apparent diffusion coefficient values of the normal head, body, and tail calculated from different sets of b-values. J Magn Reson Imaging. 2011;34(4):861–5.
16. Akisik MF, Aisen AM, Sandrasegaran K, Jennings SG, Lin C, Sherman S, Lin JA, Rydberg M. Assessment of chronic pancreatitis: utility of diffusion-weighted MR imaging with secretin enhancement. Radiology. 2009;250(1):103–9.
17. Barral M, Soyer P, Ben Hassen W, Gayat E, Aout M, Chiaradia M, Rahmouni A, Luciani A. Diffusion-weighted MR imaging of the normal pancreas: reproducibility and variations of apparent diffusion coefficient measurement at 1.5- and 3.0-tesla. Diagn Interv Imaging. 2013;94(4):418–27.
18. Barral M, Sebbag-Sfez D, Hoeffel C, Chaput U, Dohan A, Eveno C, Boudiaf M, Soyer P. Characterization of focal pancreatic lesions using normalized apparent diffusion coefficient at 1.5-Tesla: preliminary experience. Diagn Interv Imaging. 2013;94(6):619–27.
19. Wathle GK, Tjora E, Ersland L, Dimcevski G, Salvesen ØO, Molven A, Njølstad PR, Haldorsen IS. Assessment of exocrine pancreatic function by secretin-stimulated magnetic resonance cholangiopancreaticography and diffusion-weighted imaging in healthy controls. J Magn Reson Imaging. 2014;39(2):448–54.
20. Erturk SM, Ichikawa T, Motosugi U, Sou H, Araki T. Diffusion-weighted MR imaging in the evaluation of pancreatic exocrine function before and after secretin stimulation. Am J Gastroenterol. 2006;101(1):133–6.
21. Banks PA, Bollen TL, Dervenis C, Gooszen HG, Johnson CD, Sarr MG, Tsiotos GG, Vege SS, Acute Pancreatitis Classification Working Group. Classification of acute pancreatitis—2012:

revision of the Atlanta classification and definitions by international consensus. Gut. 2013;62(1):102–11.
22. Thomas S, Kayhan A, Lakadamyali H, Oto A. Diffusion MRI of acute pancreatitis and comparison with normal individuals using ADC values. Emerg Radiol. 2012;19(1):5–9.
23. Islim F, Salik AE, Bayramoglu S, Guven K, Alis H, Turhan AN. Non-invasive detection of infection in acute pancreatic and acute necrotic collections with diffusion-weighted magnetic resonance imaging: preliminary findings. Abdom Imaging. 2014;39(3):472–81.
24. Borens B, Arvanitakis M, Absil J, El Bouchaibi S, Matos C, Eisendrath P, Toussaint E, Deviere J, Bali MA. Added value of diffusion-weighted magnetic resonance imaging for the detection of pancreatic fluid collection infection. Eur Radiol. 2017;27(3):1064–73.
25. Akisik MF, Sandrasegaran K, Jennings SG, Aisen AM, Lin C, Sherman S, Rydberg MP. Diagnosis of chronic pancreatitis by using apparent diffusion coefficient measurements at 3.0-T MR following secretin stimulation. Radiology. 2009;252(2):418–25.
26. Irie H, Honda H, Baba S, Kuroiwa T, Yoshimitsu K, Tajima T, Jimi M, Sumii T, Masuda K. Autoimmune pancreatitis: CT and MR characteristics. AJR Am J Roentgenol. 1998;170(5):1323–7.
27. Sahani DV, Kalva SP, Farrell J, Maher MM, Saini S, Mueller PR, Lauwers GY, Fernandez CD, Warshaw AL, Simeone JF. Autoimmune pancreatitis: imaging features. Radiology. 2004;233(2):345–52.
28. Hafezi-Nejad N, Singh VK, Fung C, Takahashi N, Zaheer A. MR imaging of autoimmune pancreatitis. Magn Reson Imaging Clin N Am. 2018;26(3):463–78.
29. Kamisawa T, Takuma K, Anjiki H, Egawa N, Hata T, Kurata M, Honda G, Tsuruta K, Suzuki M, Kamata N, Sasaki T. Differentiation of autoimmune pancreatitis from pancreatic cancer by diffusion-weighted MRI. Am J Gastroenterol. 2010;105(8):1870–5.
30. Muhi A, Ichikawa T, Motosugi U, Sou H, Sano K, Tsukamoto T, Fatima Z, Araki T. Mass-forming autoimmune pancreatitis and pancreatic carcinoma: differential diagnosis on the basis of computed tomography and magnetic resonance cholangiopancreatography, and diffusion-weighted imaging findings. J Magn Reson Imaging. 2012;35(4):827–36.
31. Hur BY, Lee JM, Lee JE, Park JY, Kim SJ, Joo I, Shin CI, Baek JH, Kim JH, Han JK, Choi BI. Magnetic resonance imaging findings of the mass-forming type of autoimmune pancreatitis: comparison with pancreatic adenocarcinoma. J Magn Reson Imaging. 2012;36(1):188–97.
32. Wiggermann P, Grützmann R, Weissenböck A, Kamusella P, Dittert DD, Stroszczynski C. Apparent diffusion coefficient measurements of the pancreas, pancreas carcinoma, and mass-forming focal pancreatitis. Acta Radiol. 2012;53(2):135–9.
33. Pozdzik AA, Matos C, Rorive S, Brocheriou I, Delhaye M, Nortier JL. Diffusion-weighted magnetic resonance imaging: a non-nephrotoxic prompt assessment of kidney involvement in IgG4-related disease. Kidney Int. 2014 Apr;85(4):981.
34. Oki H, Hayashida Y, Oki H, Kakeda S, Aoki T, Taguchi M, Harada M, Korogi Y. DWI findings of autoimmune pancreatitis: comparison between symptomatic and asymptomatic patients. J Magn Reson Imaging. 2015;41(1):125–31.
35. Taniguchi T, Kobayashi H, Nishikawa K, Iida E, Michigami Y, Morimoto E, Yamashita R, Miyagi K, Okamoto M. Diffusion-weighted magnetic resonance imaging in autoimmune pancreatitis. Jpn J Radiol. 2009;27(3):138–42.
36. Klauß M, Maier-Hein K, Tjaden C, Hackert T, Grenacher L, Stieltjes B. IVIM DW-MRI of autoimmune pancreatitis: therapy monitoring and differentiation from pancreatic cancer. Eur Radiol. 2016;26(7):2099–106.
37. Fattahi R, Balci NC, Perman WH, Hsueh EC, Alkaade S, Havlioglu N, Burton FR. Pancreatic diffusion-weighted imaging (DWI): comparison between mass-forming focal pancreatitis (FP), pancreatic cancer (PC), and normal pancreas. J Magn Reson Imaging. 2009;29(2):350–6.
38. Klauss M, Lemke A, Grünberg K, Simon D, Re TJ, Wente MN, Laun FB, Kauczor HU, Delorme S, Grenacher L, Stieltjes B. Intravoxel incoherent motion MRI for the differentiation between mass forming chronic pancreatitis and pancreatic carcinoma. Investig Radiol. 2011;46(1):57–63.

39. De Robertis R, Cardobi N, Ortolani S, Tinazzi Martini P, Stemmer A, Grimm R, Gobbo S, Butturini G, D'Onofrio M. Intravoxel incoherent motion diffusion-weighted MR imaging of solid pancreatic masses: reliability and usefulness for characterization. Abdom Radiol (NY). 2019;44(1):131–9.
40. Kim B, Lee SS, Sung YS, Cheong H, Byun JH, Kim HJ, Kim JH. Intravoxel incoherent motion diffusion-weighted imaging of the pancreas: characterization of benign and malignant pancreatic pathologies. J Magn Reson Imaging. 2017;45(1):260–9.
41. Inan N, Arslan A, Akansel G, Anik Y, Demirci A. Diffusion-weighted imaging in the differential diagnosis of cystic lesions of the pancreas. AJR Am J Roentgenol. 2008;191(4):1115–21.
42. Fatima Z, Ichikawa T, Motosugi U, Muhi A, Sano K, Sou H, Haradome H, Kiryu S, Araki T. Magnetic resonance diffusion-weighted imaging in the characterization of pancreatic mucinous cystic lesions. Clin Radiol. 2011;66(2):108–11.
43. Sandrasegaran K, Akisik FM, Patel AA, Rydberg M, Cramer HM, Agaram NP, Schmidt CM. Diffusion-weighted imaging in characterization of cystic pancreatic lesions. Clin Radiol. 2011;66(9):808–14.
44. Yamashita Y, Namimoto T, Mitsuzaki K, Urata J, Tsuchigame T, Takahashi M, Ogawa M. Mucin-producing tumor of the pancreas: diagnostic value of diffusion-weighted echoplanar MR imaging. Radiology. 1998;208(3):605–9.
45. Mottola JC, Sahni VA, Erturk SM, Swanson R, Banks PA, Mortele KJ. Diffusion-weighted MRI of focal cystic pancreatic lesions at 3.0-Tesla: preliminary results. Abdom Imaging. 2012;37(1):110–7.
46. Schraibman V, Goldman SM, Ardengh JC, Goldenberg A, Lobo E, Linhares MM, Gonzales AM, Abdala N, Abud TG, Ajzen SA, Jackowsky A, Szejnfeld J. New trends in diffusion-weighted magnetic resonance imaging as a tool in differentiation of serous cystadenoma and mucinous cystic tumor: a prospective study. Pancreatology. 2011;11(1):43–51.
47. Jang KM, Kim SH, Min JH, Lee SJ, Kang TW, Lim S, Choi D. Value of diffusion-weighted MRI for differentiating malignant from benign intraductal papillary mucinous neoplasms of the pancreas. AJR Am J Roentgenol. 2014;203(5):992–1000.
48. Ichikawa T, Erturk SM, Motosugi U, Sou H, Iino H, Araki T, Fujii H. High-b value diffusion-weighted MRI for detecting pancreatic adenocarcinoma: preliminary results. AJR Am J Roentgenol. 2007;188(2):409–14.
49. Kartalis N, Lindholm TL, Aspelin P, Permert J, Albiin N. Diffusion-weighted magnetic resonance imaging of pancreas tumours. Eur Radiol. 2009;19(8):1981–90.
50. Wang Y, Chen ZE, Nikolaidis P, McCarthy RJ, Merrick L, Sternick LA, Horowitz JM, Yaghmai V, Miller FH. Diffusion-weighted magnetic resonance imaging of pancreatic adenocarcinomas: association with histopathology and tumor grade. J Magn Reson Imaging. 2011;33(1):136–42.
51. Rosenkrantz AB, Matza BW, Sabach A, Hajdu CH, Hindman N. Pancreatic cancer: lack of association between apparent diffusion coefficient values and adverse pathological features. Clin Radiol. 2013;68(4):e191–7.
52. Cuneo KC, Chenevert TL, Ben-Josef E, Feng MU, Greenson JK, Hussain HK, Simeone DM, Schipper MJ, Anderson MA, Zalupski MM, Al-Hawary M, Galban CJ, Rehemtulla A, Feng FY, Lawrence TS, Ross BD. A pilot study of diffusion-weighted MRI in patients undergoing neoadjuvant chemoradiation for pancreatic cancer. Transl Oncol. 2014;7(5):644–9.
53. Niwa T, Ueno M, Ohkawa S, Yoshida T, Doiuchi T, Ito K, Inoue T. Advanced pancreatic cancer: the use of the apparent diffusion coefficient to predict response to chemotherapy. Br J Radiol. 2009;82(973):28–34.
54. Bali MA, Pullini S, Metens T, Absil J, Chao SL, Marechal R, Matos C, Peerboccus BM, Van Laethem JL. Assessment of response to chemotherapy in pancreatic ductal adenocarcinoma: comparison between diffusion-weighted MR quantitative parameters and RECIST. Eur J Radiol. 2018;104:49–57.
55. Herwick S, Miller FH, Keppke AL. MRI of islet cell tumors of the pancreas. AJR Am J Roentgenol. 2006;187(5):W472–80.

56. Ichikawa T, Peterson MS, Federle MP, Baron RL, Haradome H, Kawamori Y, Nawano S, Araki T. Islet cell tumor of the pancreas: biphasic CT versus MR imaging in tumor detection. Radiology. 2000;216(1):163–71.
57. Schmid-Tannwald C, Schmid-Tannwald CM, Morelli JN, Neumann R, Haug AR, Jansen N, Nikolaou K, Schramm N, Reiser MF, Rist C. Comparison of abdominal MRI with diffusion-weighted imaging to 68Ga-DOTATATE PET/CT in detection of neuroendocrine tumors of the pancreas. Eur J Nucl Med Mol Imaging. 2013;40(6):897–907.
58. Brenner R, Metens T, Bali M, Demetter P, Matos C. Pancreatic neuroendocrine tumor: added value of fusion of T2-weighted imaging and high b-value diffusion-weighted imaging for tumor detection. Eur J Radiol. 2012;81(5):e746–9.
59. Bakir B, Salmaslioğlu A, Poyanli A, Rozanes I, Acunas B. Diffusion weighted MR imaging of pancreatic islet cell tumors. Eur J Radiol. 2010;74(1):214–20.
60. Klimstra DS, Arnold R, Capella C. Neuroendocrine neoplasms of the pancreas. In: Bosman FT, Carneiro F, Hruban RH, Theise ND, editors. WHO classification of tumours of the digestive system. Lyon: International Agency for Research on Cancer (IARC); 2010. p. 322–6.
61. Zong RL, Geng L, Wang X, Xie D. Diagnostic performance of apparent diffusion coefficient for prediction of grading of pancreatic neuroendocrine tumors: a systematic review and meta-analysis. Pancreas. 2019;48(2):151–60.
62. Wang Y, Chen ZE, Yaghmai V, Nikolaidis P, McCarthy RJ, Merrick L, Miller FH. Diffusion-weighted MR imaging in pancreatic endocrine tumors correlated with histopathologic characteristics. J Magn Reson Imaging. 2011;33(5):1071–9.
63. De Robertis R, Cingarlini S, Tinazzi Martini P, Ortolani S, Butturini G, Landoni L, Regi P, Girelli R, Capelli P, Gobbo S, Tortora G, Scarpa A, Pederzoli P, D'Onofrio M. Pancreatic neuroendocrine neoplasms: magnetic resonance imaging features according to grade and stage. World J Gastroenterol. 2017;23(2):275–85.
64. Guo C, Zhuge X, Chen X, Wang Z, Xiao W, Wang Q. Value of diffusion-weighted magnetic resonance imaging in predicting World Health Organization grade in G1/G2 pancreatic neuroendocrine tumors. Oncol Lett. 2017;13(6):4141–6.
65. Pereira JA, Rosado E, Bali M, Metens T, Chao SL. Pancreatic neuroendocrine tumors: correlation between histogram analysis of apparent diffusion coefficient maps and tumor grade. Abdom Imaging. 2015;40(8):3122–8.
66. Kim JH, Eun HW, Kim YJ, Han JK, Choi BI. Staging accuracy of MR for pancreatic neuroendocrine tumor and imaging findings according to the tumor grade. Abdom Imaging. 2013;38(5):1106–14.
67. Jang KM, Kim SH, Lee SJ, Choi D. The value of gadoxetic acid-enhanced and diffusion-weighted MRI for prediction of grading of pancreatic neuroendocrine tumors. Acta Radiol. 2014;55(2):140–8.
68. Kulali F, Semiz-Oysu A, Demir M, Segmen-Yilmaz M, Bukte Y. Role of diffusion-weighted MR imaging in predicting the grade of nonfunctional pancreatic neuroendocrine tumors. Diagn Interv Imaging. 2018;99(5):301–9.
69. Lotfalizadeh E, Ronot M, Wagner M, Cros J, Couvelard A, Vullierme MP, Allaham W, Hentic O, Ruzniewski P, Vilgrain V. Prediction of pancreatic neuroendocrine tumour grade with MR imaging features: added value of diffusion-weighted imaging. Eur Radiol. 2017;27(4):1748–59.
70. Guo C, Chen X, Xiao W, Wang Q, Sun K, Wang Z. Pancreatic neuroendocrine neoplasms at magnetic resonance imaging: comparison between grade 3 and grade 1/2 tumors. Onco Targets Ther. 2017;10:1465–74.
71. d'Assignies G, Fina P, Bruno O, Vullierme MP, Tubach F, Paradis V, Sauvanet A, Ruszniewski P, Vilgrain V. High sensitivity of diffusion-weighted MR imaging for the detection of liver metastases from neuroendocrine tumors: comparison with T2-weighted and dynamic gadolinium-enhanced MR imaging. Radiology. 2013;268(2):390–9.
72. Yao XZ, Yun H, Zeng MS, Wang H, Sun F, Rao SX, Ji Y. Evaluation of ADC measurements among solid pancreatic masses by respiratory-triggered diffusion-weighted MR imaging with inversion-recovery fat-suppression technique at 3.0T. Magn Reson Imaging. 2013;31(4):524–8.

73. Jang KM, Kim SH, Kim YK, Park MJ, Lee MH, Hwang J, Rhim H. Imaging features of small (≤3 cm) pancreatic solid tumors on gadoxetic-acid-enhanced MR imaging and diffusion-weighted imaging: an initial experience. Magn Reson Imaging. 2012;30(7):916–25.
74. Kang BK, Kim JH, Byun JH, Lee SS, Kim HJ, Kim SY, Lee MG. Diffusion-weighted MRI: usefulness for differentiating intrapancreatic accessory spleen and small hypervascular neuroendocrine tumor of the pancreas. Acta Radiol. 2014;55(10):1157–65.
75. Jang KM, Kim SH, Lee SJ, Park MJ, Lee MH, Choi D. Differentiation of an intrapancreatic accessory spleen from a small (<3-cm) solid pancreatic tumor: value of diffusion-weighted MR imaging. Radiology. 2013;266(1):159–67.

Pancreatic Cystic Neoplasms

7

Allen Q. Ye, Camila Lopes Vendrami, Frank H. Miller, and Paul Nikolaidis

7.1 Introduction

Pancreatic cystic neoplasms (PCN) account for 10–15% of all pancreatic cystic lesions and approximately 1% of pancreatic neoplasms. PCN can be divided into mucinous lesions, including intraductal papillary mucinous neoplasms (IPMN) and mucinous cystic neoplasms (MCN), and non-mucinous lesions, which includes serous cystic neoplasms (SCN), solid pseudopapillary neoplasms (SPN), and cystic pancreatic endocrine neoplasms (CPEN) [1]. With an aging population, the widespread use of cross-sectional imaging, as well as better resolution afforded by technical improvements in all imaging modalities, the detection of pancreatic cystic lesions has become very common. The prevalence of PCN varies considerably with the imaging method employed as well as among studies. Ultrasound (US) imaging detects 0.21% of cases of PCN, while computed tomography (CT) and magnetic resonance imaging (MRI) (coupled with magnetic resonance cholangiopancreatography—MRCP) detect 2.6% and 2.4% to 49.1% of these cases, respectively. PCNs are detected in up to 50% of patients according to autopsy studies [2]. Risk factors that predispose patients to developing pancreatic cystic lesions include patient age, diabetes mellitus, non-melanoma skin cancer, hepatocellular carcinoma, and being of Asian descent [3, 4].

Differentiation between the types of PCN is critical since the malignant potential of these types of lesions varies. SCN are usually benign with no need for

A. Q. Ye
Department of Radiology and Biomedical Imaging, University of California San Francisco, San Francisco, CA, USA
e-mail: Allen.ye@ucsf.edu

C. L. Vendrami · F. H. Miller · P. Nikolaidis (✉)
Department of Radiology, Northwestern Memorial Hospital, Northwestern University Feinberg School of Medicine, Chicago, IL, USA
e-mail: Frank.Miller@nm.org; p-nikolaidis@northwestern.edu

C. Matos, N. Papanikolaou (eds.), *Diffusion Weighted Imaging of the Hepatobiliary System*, https://doi.org/10.1007/978-3-319-62977-3_7

surveillance, whereas IPMN, MCN, SPN, and CPEN are considered premalignant lesions and necessitate either surveillance or surgery. PCNs are known precursors of pancreatic cancer [2]. There has been some controversy recently on how to best approach pancreatic cystic neoplasms. Historically, all mucinous pancreatic cysts required resection; however, this does not come without significant risks (up to 2% mortality, 40% morbidity) [5]. Current standard of care advocates a more conservative approach with retrospective data suggesting typically a benign course for pancreatic cystic neoplasms [6, 7]. The overall risk of malignant transformation has been estimated at 0.24% per year [8]. Currently, three guidelines yield recommendations regarding surveillance and surgical resection of PCNs based on symptoms and risk of malignancy: the 2015 American Gastroenterological Association (AGA), the International Association of Pancreatology (IAP, revised in 2017), and the European Study Group on Cystic Tumors of the Pancreas (European, revised in 2018). Surveillance should be considered in asymptomatic patients with cysts presumed to be MCN or IPMN without any concerning characteristics. Concerning characteristics vary with among the different guidelines, though some of these include: pancreatic duct dilatation, presence of a solid component or an enhancing mural nodule, cytology suspicious or positive for malignancy, jaundice, cyst diameter > 40 mm. It has not been established which modality or approach is best, however, and these guidelines provide somewhat different recommendations [2].

In this chapter we will discuss the general MR imaging findings of pancreatic cystic neoplasms, along with the utility and limitations of diffusion weighted imaging (DWI) in assessing cystic lesions of the pancreas. In general, DWI may not be particularly helpful by itself in distinguishing between different cystic lesions and therefore MRI features encountered on other sequences that are obtained as part of a pancreatic protocol MRI will be stressed. These features in conjunction with clinical and demographic data often allow for correct diagnosis on MRI.

7.2 Serous Cystic Neoplasms

Serous cystic neoplasms are typically benign tumors and account for about 1–2% of all exocrine pancreatic neoplasms and approximately 20% of all pancreatic cystic neoplasms [5, 6]. Typically, serous cystic neoplasms occur in older women in the fifth to seventh decade, median age of 65 years [8]. These lesions can be found throughout the pancreas (head, body, and tail) and can grow to span multiple regions [9, 10], though they are often located in the pancreatic head. Mean gross lesion size is 6 cm and typically the lesion is composed of multiple smaller cysts measuring under 2 cm, separated with fibrous septa conglomerating into an area central fibrosis which may also be calcified [11]. The most common subtype is the serous microcystic adenoma, 70% of cases [12], which is lined by glycogen rich epithelial cells and is composed of multiple serous fluid filled cysts [11]. The other two morphologic patterns are: honeycomb pattern (20% of cases), and macrocystic (or oligocystic; 10% of cases) pattern [12], which is composed of larger individual cysts (1–8 cm)

[13]. CT or MRI may often detect the sunburst or stellate appearance of the central scar which may have calcifications (better seen on CT) which is considered pathognomonic for a serous cystic tumor [14]. Chances for malignant transformation are miniscule and symptoms are typically secondary to lesion size and may include a palpable mass, abdominal pain, nausea and vomiting, weight loss, hemorrhage [15], and obstructive jaundice [16].

Other subtypes of serous cystic tumors include von Hippel–Lindau (VHL)-associated cystic neoplasm, serous oligocystic adenoma, solid serous adenoma, and serous cystadenocarcinoma [11]. VHL-associated cystic neoplasms occur in 50–80% of patients with VHL syndrome, without gender predilection, with lesions typically detected at a younger age [17]. Serous oligocystic adenomas are composed of fewer but larger cysts. These lesions can occur in both males and females, are discovered at a younger age (mean age of 50 years) [10]. Solid serous adenomas are even more rare and there are only few case reports of this variant [18, 19]. While they lack the macroscopic cysts typical of serous microcystic adenomas, the cells maintain the same immunohistochemical profile [20]. The malignant variant, serous cystadenocarcinoma, is rare [21].

Serous cystic neoplasms can show wide-ranging appearance on imaging with typical and atypical characteristics, depending on the number of fibrous septa and degree of enhancement [12, 22]. The typical appearance on MRI, is of well-defined grape-like clusters of serous fluid-filled cysts. There should be no evidence of invasion of adjacent organs [23] unless the size of the serous cystic neoplasm becomes excessively large and it begins to show localized adhesion and/or penetration of neighboring organs [24]. On T2-weighted images, the fluid filled cysts should show high signal intensity and the thin fibrous septa associated with these lesions can show delayed enhancement on contrast enhanced T1-weighted images (Fig. 7.1) [25]. While the lesions may appear solid on early phase contrast-enhanced CT or MR from enhancing septations, T2-weighted MR nicely shows the cystic nature of the lesion. There should also be no evidence of invasion into the pancreatic duct or communication with the pancreatic duct in contrast with side branch intraductal papillary mucinous neoplasms (IPMN) which communicate with the duct [26]. As the lesion grows, the central scar may demonstrate a signal void corresponding to the increasing calcification. With regards to diffusion weighted imaging, serous cystadenomas may have higher signal intensity with high b values and lower ADC values due to the fibrous septa. When there is a large cystic component the ADC values should be higher secondary to "T2-shine through." The ADC values vary widely depending on the proportion of fibrous and cystic components and do not allow for differentiation between a nonneoplastic cyst and a cystic neoplasm nor do they allow distinction among different types of cystic neoplasms [13]. It has been suggested that using a threshold of 3.0×10^{-3} mm^2/s for ADC value can differentiate mucin-producing cysts from serous cysts, since mucin-producing ones tend to have higher values, with sensitivity rates of 84–88%, and specificity rates of 66–72% [27]. Atypical characteristics include thick wall, intralesional hemorrhage, portal hypertension secondary to splenic vein obstruction, and communication with main pancreatic duct [12].

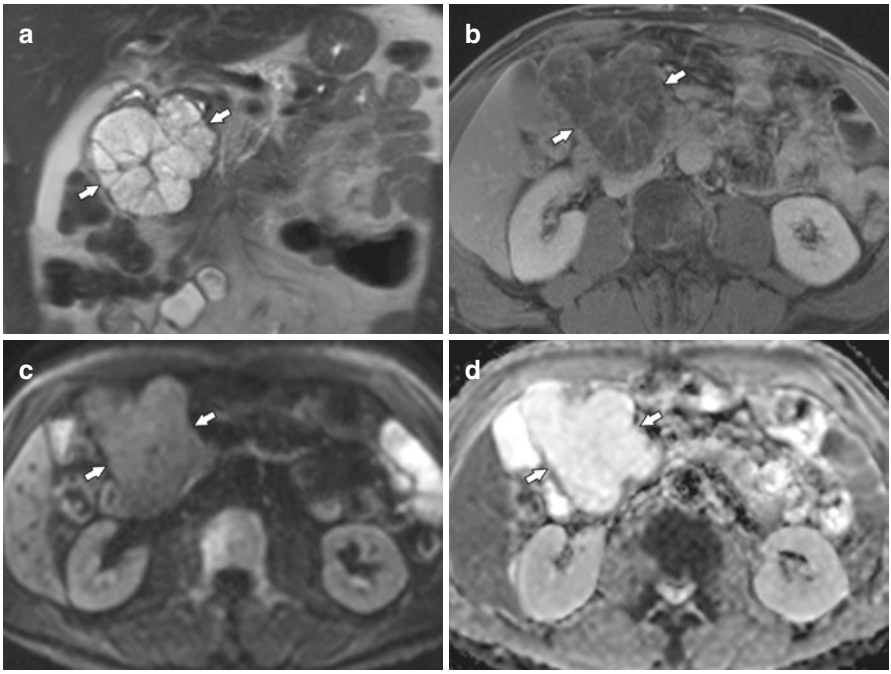

Fig. 7.1 A 60-year-old male presenting for follow-up of a serous cystadenoma. (**a**, **b**) Coronal T2-weighted (**a**) and axial T1 post contrast (**b**) MR images show a lobular T2 hyperintense mass in the pancreatic head (arrows) with internal septations and a stellate central scar. The septations enhance on the postcontrast images (**b**). (**c**, **d**) DWI and ADC images show no restricted diffusion

7.3 Mucinous Cystic Neoplasms

Mucinous cystic neoplasms (MCN) can be divided into two primary categories, mucinous cystadenomas (benign) and mucinous cystadenocarcinomas (malignant) and account for less than 10% of pancreatic cystic neoplasms [6, 7, 28]. Originally they were described as large, septated, thick-walled cysts filled with mucoid and occasionally hemorrhagic material by Compagno and Oertel in 1978 [29]. Histologically, these are lined by an epithelium consisting of tall, mucin-producing columnar cells with varying degrees of atypia [30]. Unique to MCNs, as compared to microcystic or serous cystadenomas, is the presence of a dense cellular ovarian-type stroma surrounding the cyst [9]. The presence of this ovarian stroma has been required to establish the diagnosis of MCN according to the International Association of Pancreatology [31]. Moreover, MCNs do not have communication with the pancreatic ductal system as compared to intraductal papillary mucinous neoplasms. Additional characteristics which often lead to the diagnosis of MCNs include female gender and location in the body or tail of the pancreas with estimates ranging for up to 93–98% for MCNs. Median age for diagnosis was typically in the mid-forties, with age ranges spanning from 16 to 82 [32–34].

Often these lesions are incidentally discovered on imaging studies performed for other indications, however symptoms such as mild abdominal pain, fullness, abdominal masses, or acute pancreatitis have been described [30, 34]. The malignant mucinous cystadenocarcinoma is more rarely diagnosed on biopsy than the mucinous cystadenoma by at most a 1:10 ratio but current guidelines from the International Association of Pancreatology suggest that all MCNs may progress to malignancy and should therefore be routinely resected [31, 35]. In contrast, the American Gastroenterological Association recently endorsed a more conservative approach in those with small lesions (<3 cm) and without solid components, a dilated pancreatic duct, or other symptomatology recommending follow-up MRI scans at 1, 3, and 5 years [36]. Newer approaches include using endoscopic ultrasound-guided alcohol ablation, which may be considered for patients when surgical resection is not an option [37]. After resection, if proven benign, MCNs do not need any follow-up as there is virtually no chance of recurrence, whereas patients with confirmed malignancy should have follow up scanning every 6 months by MRI or CT [32, 38].

MCNs are typically well circumscribed unilocular or mildly septated cystic lesions located in the body or tail of the pancreas without evidence of local invasion or distant metastases and are less likely to be found in the head as compared to serous cystic neoplasms [25, 28]. Because of the fluid content, the lesions are high signal intensity on T2-weighted images and low signal intensity on T1-weighted images (Fig. 7.2) [13]. These cysts are typically larger than 3 cm with the median size reported to be 5–7 cm with ranges up to 23 cm [32, 33]. The thicker walls of the MCNs may show delayed enhancement on fat-suppressed contrast enhanced T1 images which can correlate to fibrotic changes within the walls of the MCN [28]. Calcifications when present are typically peripheral and may result in signal voids [33]. On imaging, the lesions can look similar to walled off necrosis or pseudocysts, so a high index of suspicion is needed especially in middle-aged women without history or clinical findings of pancreatitis. Diffusion weighted imaging in these cases may overlap with non-neoplastic cysts with high signal on low *b*-value images and low signal intensity on high *b*-value DWI and a high ADC within the cysts [13]. Additionally, if soft tissue components are seen within the cysts, there should be increased concern for the presence of a mucinous cystadenocarcinoma [25, 39]. These soft tissue components may have restricted diffusion. Atypical imaging features include internal hemorrhage, upstream chronic obstructive pancreatitis changes (parenchymal atrophy, dilated pancreatic duct, coarse calculi, decreased enhancement in some areas, and decreased signal intensity on fat-saturated unenhanced T1-weighted MR images), and communication with main pancreatic duct related to malignant pancreatic fistula. Features that suggest malignancy include: invasion of adjacent structures, nodal and distant metastases, larger lesion size (cysts <3 cm are usually benign), peripheral calcifications, irregular margins, thick irregular wall, and enhancement of soft tissue component or mural nodules [12].

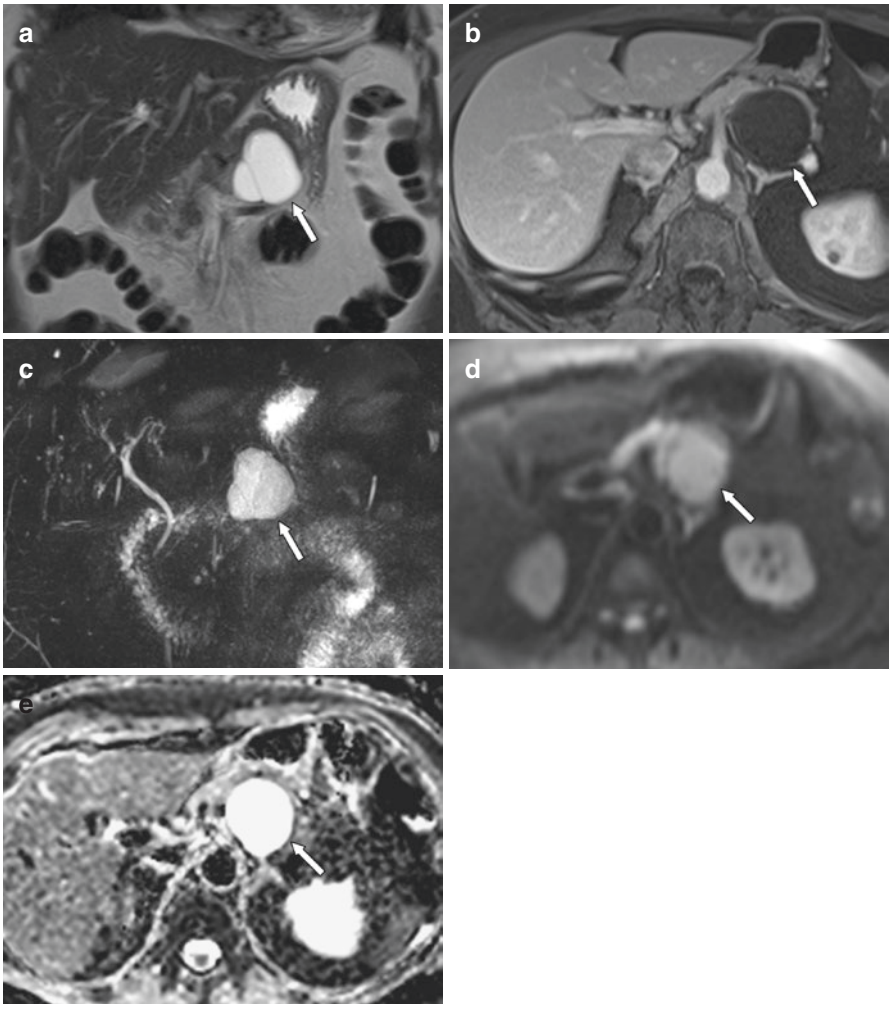

Fig. 7.2 A 67-year-old female with a history of a biopsy-proven mucinous cystic neoplasm (cystadenoma). (**a–c**) Coronal T2-weighted (**a**), axial T1 post contrast (**b**), and MRCP (**c**) images show a cystic lesion (arrow) in the pancreatic body/tail with internal septations. The non-dilated pancreatic duct courses in close proximity to this lesion. (**d**, **e**) DWI and ADC images show no restricted diffusion

7.4 Intraductal Papillary Mucinous Neoplasms

Intraductal papillary mucinous neoplasm (IPMN) is the most common cystic pancreatic neoplasm (20%), accounting for up to 7% of all pancreatic neoplasms [12]. As with many of the other PCNs, IPMNs have demonstrated a growing incidence likely secondary to the increased usage of cross-sectional imaging and increased awareness by radiologists and other physicians. These lesions are potentially

malignant and most often visible; however, the true incidence for these neoplasms is likely underestimated with many early IPMNs being small and asymptomatic [4]. In addition, it is often difficult to determine which lesions are malignant and which are nonaggressive based on imaging studies. If symptoms are present, they may include abdominal pain, jaundice, weight loss, or intermittent pancreatitis-like symptoms [40, 41]. These lesions are lined with mucin-producing columnar cells and can show papillary proliferation, formation of cystic spaces, and different degrees of invasion. Epidemiologically IPMNs are more prevalent in men of older age, most typically occurring in the seventh decade of life [41, 42]. Other risk factors include genetic syndromes with predisposition for pancreatic tumors (Peutz–Jeghers [43], familial adenomatous polyposis [44], familial pancreatic carcinoma syndrome [45]), diabetes [46–48], chronic pancreatitis, family history of IPMNs [49], or history of smoking [46].

There are a few classifications of IPMNs with respect to location and degree of invasion/potential for malignancy. First, IPMNs are subdivided into main duct (MD-IPMN), branch duct (BD-IPMN), or mixed-type (MT-IPMN), depending on the anatomical involvement of the pancreatic duct. MD-IPMNs usually have greater malignant potential than those of BD-IPMNs, with MD-IPMNs more often exhibiting dilation of the pancreatic duct without stricturing, along with dilation of pancreatic duct radicals, and intraductal growth of mucin-producing ductal cells [47]. In comparison, BD-IPMN most often show no or low-grade dysplasia, lack nodular formation, and can show viscous mucin contents [50]. While both forms can occur throughout the pancreas, BD-IPMNs are more likely to be seen in the head and uncinate process while only 30–40% of main duct neoplasms have been shown to involve the body and tail [47, 51].

When assessing the depth of invasion for IPMNs, noninvasive IPMNs can be categorized as adenoma, borderline, or carcinoma in situ. Invasive types can be further characterized as tubular, colloid, mixed, or anaplastic [41]. Of these, the main invasive types encountered on histological examination are tubular adenocarcinomas and colloid carcinomas [50]. Unlike the previously described mucinous cystic neoplasms, IPMNs lack the ovarian type stroma surrounding the cyst and are in communication with the pancreatic ductal system. IPMNs without invasive components have a 5-year survival rate approaching 100% with single digit recurrence rates [51, 52]. In comparison, when invasive components are noted, 5-year survival rates are significantly decreased with estimates ranging from 24 to 60% [51, 53] and median survival in certain studies is estimated at 21 months [54]. In addition, further differentiation between tubular and colloid subtypes also carries prognostic significance as the 2011 study by Yopp et al. showed that tubular carcinoma cases showed no significant survival advantage when compared with pancreatic duct adenocarcinomas when matched stage for stage, while patients with colloid carcinomas fare much better [55].

MR is the modality of choice when imaging IPMNs due to its ability to delineate the pancreatic duct with great detail [56]. Differentiating between MD from BD-IPMNs is of great importance given the differences in prognosis and management. In cases of MD-IPMN, one would expect to see more ductal dilatation from

obstruction and either the entire duct or segmental portions could be dilated [25]. For BD-IPMNs, the lesion itself is typically found in either the head or the neck of the pancreas and dilation of multiple side branches is typically seen on T2-weighted images (Fig. 7.3) [57]. These lesions demonstrate high signal intensity on T2-weighted images and low signal on T1-weighted images [13]. With increased viscosity within noninvasive IPMNs, one would expect to see statistically

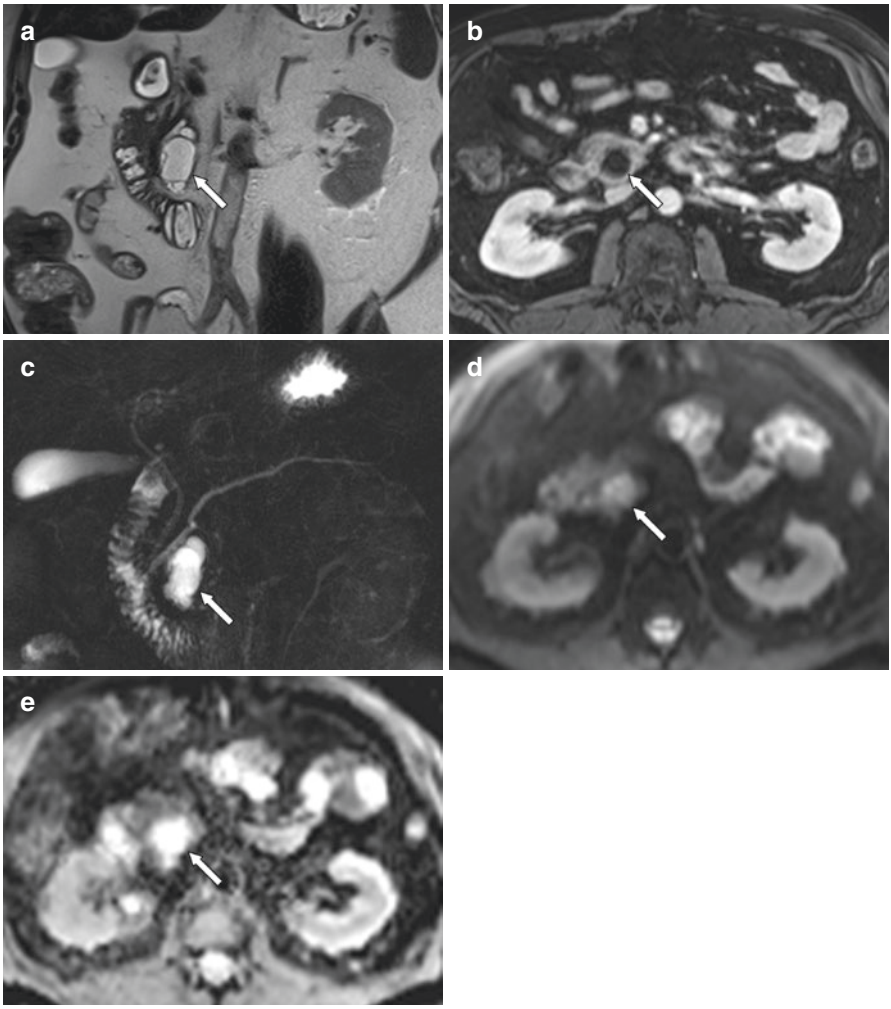

Fig. 7.3 A 65-year-old male with a history of a biopsy-proven pancreatic intraductal papillary mucinous neoplasm. (**a–c**) Coronal T2-weighted (**a**), axial T1 post contrast (**b**), and MRCP images show lobular fluid signal mass in the pancreatic head/uncinate process. There is a connection between this mass and the main pancreatic duct. No enhancing nodular components are identified. There is no pancreatic ductal dilatation. (**d**, **e**) DWI and ADC images show no restricted diffusion

significant lower ADC values within the fluid portion, however, in practice the difference in ADC values is not clinically perceptible and is difficult to rely on [13, 58, 59]. More advanced models of diffusion, especially those with multiple *b*-values, have showed promising results in differentiation between benign and malignant IPMN [60, 61]. Much like other PCNs, additional factors that may cause concern include size >3 cm, thickened or enhancing walls, non-enhancing mural nodules, associated pancreatitis, main duct dilation exceeding 5–9 mm, lymphadenopathy, or an abrupt change in caliber of the pancreatic duct with distal pancreatic atrophy [6].

7.5 Mucinous Nonneoplastic Cyst

While this is a nonneoplastic entity, distinguishing mucinous nonneoplastic cysts (MNC) from other PCNs is difficult even with appropriate clinical, radiographical and biochemical analysis [62]. First described by Kosmahl et al. in 2002, these are unilocular or multilocular thin walled cysts, lined by cuboidal to columnal mucin-producing cells [58]. In comparison to the mucinous cystic neoplasm, the fibrous stromal cells in MNCs lack progesterone positivity. Moreover, unlike IPMNs, MNCs do not exhibit cellular atypia, papillary projections, or ductal communication [7, 13, 63]. More commonly found in women and the elderly, the majority of MNCs occur in the head of the pancreas and are often associated with (or adjacent to) acinar-ductal mucinous metaplasia [62, 63].

On MR imaging, MNCs are typically hyperintense on T2-weighted imaging and hypointense on T1-weighted imaging, consistent with a simple fluid-filled cystic structure [13, 25]. On dynamic contrast-enhanced MR images, there should be no enhancement of fluid or the accompanying soft tissue components [25]. Diffusion weighted imaging could prove useful in supporting the benign nature of the MNC by comparing multiple *b*-values. With these lesions it is expected that signal intensity should drop with increasing *b*-values due to the unhindered environment within the cystic cavity of a MNC as compared to other more complex neoplasms [13]. Conversely, ADC values should be higher.

7.6 Solid Pseudopapillary Neoplasms

Solid pseudopapillary neoplasms are primarily solid but are often complex lesions with cystic, solid, and/or hemorrhagic components surrounded by a capsule. They are rare slow-growing tumors that occur mainly in young women and often asymptomatic at presentation. About 5–15% of solid pseudopapillary neoplasms are more aggressive with metastases and poor prognosis [12]. Their imaging findings are often dictated by the presence of cystic and hemorrhagic degeneration and could overlap those of other cystic pancreatic lesions.

On imaging, these tumors are often well circumscribed with T2 signal that increases with increasing cystic degeneration. Imaging findings may overlap with cystic or degenerated neuroendocrine tumors of the pancreas, however solid

pseudopapillary neoplasms enhance much more slowly on dynamic contrast weighted MRI than neuroendocrine tumors (which show brisk enhancement of their solid components) [25]. As these tumors accumulate more hemorrhagic components, they may show fluid-debris levels and appear hyperintense on T1-weighted images which is often a major distinguishing factor, along with more heterogeneous signal on T2-weighted images (Fig. 7.4) [64, 65]. There have been few reports of diffusion weighted imaging in these neoplasms but some authors have suggested that there are possible ADC thresholds in differentiating pancreatic adenocarcinoma from pseudopapillary tumors from normal pancreatic parenchyma with neoplasms with more solid components having lower ADCs [66]. DWI may be useful and ADCs could help separate solid from hemorrhagic or cystic components in solid pseudopapillary neoplasms [67]. Higher ADCs would be expected in cystic areas of these tumors. Finally, there have been applications of more advanced diffusion models such as intravoxel incoherent motion (IVIM) applied to these tumors which have suggested improved differentiation between malignant and benign entities when using the perfusion-related diffusion coefficient and the perfusion fraction [68]. Nonetheless, in cases of young female patients with a hemorrhagic pancreatic mass that is typically large and without evidence of metastases, solid pseudopapillary neoplasms must

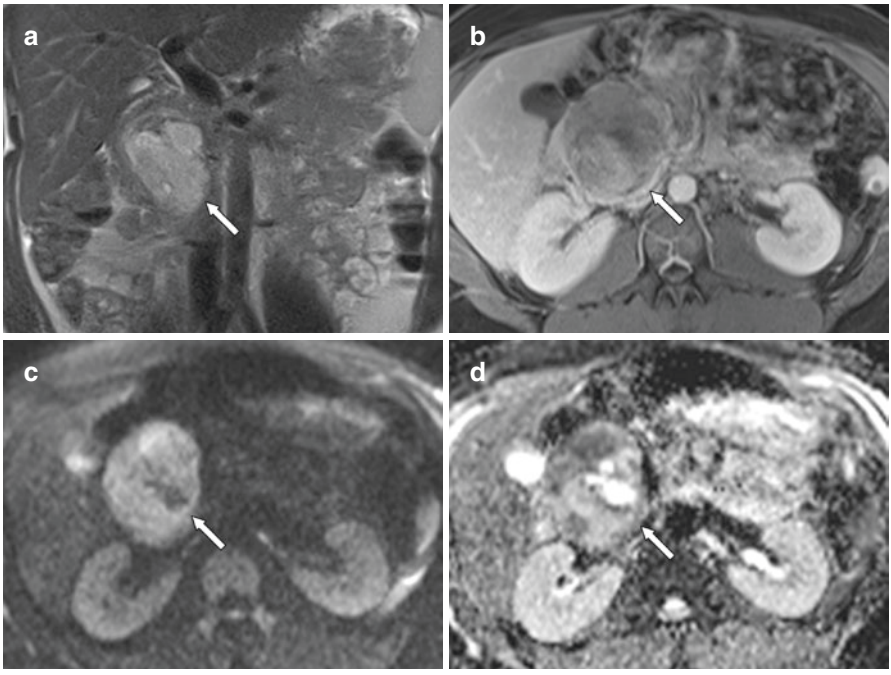

Fig. 7.4 A 25-year-old female with an incidental pancreatic mass that was resected and proven to represent a solid pseudopapillary neoplasm. (**a**, **b**) Coronal T2-weighted (**a**), and axial T1 post contrast (**b**) MR images show an encapsulated heterogeneous enhancing pancreatic head mass with areas of necrosis and internal hemorrhage. (**c**, **d**) DWI and ADC images show restricted diffusion in portions of the pancreatic mass

strongly be considered. Features that are suggestive of malignant solid pseudopapillary neoplasm include: nodal and distant metastases, local invasion of adjacent organs or vessels, extracapsular extension, and ductal dilatation [12].

7.7 Conclusion

In conclusion, the increasing rate of detection of pancreatic cystic neoplasms on MRI makes thorough understanding of these lesions imperative. Throughout this chapter we provide a framework of understanding for the four major classifications of pancreatic cystic neoplasms, as well as a common masquerading entity, the mucinous nonneoplastic cyst. While conventional MRI sequences remain of great importance in the evaluation of these entities, radiologists and clinicians alike should be aware of their appearance on DWI.

Disclosures The authors report no conflict of interest. No funding or grant support was used in the preparation of this manuscript.

References

1. Jana T, Shroff J, Bhutani MS. Pancreatic cystic neoplasms: review of current knowledge, diagnostic challenges, and management options. J Carcinog. 2015;14:3. https://doi.org/10.4103/1477-3163.153285.
2. van Huijgevoort NCM, Del Chiaro M, Wolfgang CL, van Hooft JE, Besselink MG. Diagnosis and management of pancreatic cystic neoplasms: current evidence and guidelines. Nat Rev Gastroenterol Hepatol. 2019;16(11):676–89. https://doi.org/10.1038/s41575-019-0195-x.
3. Moris M, Bridges MD, Pooley RA, Raimondo M, Woodward TA, Stauffer JA, Asbun HJ, Wallace MB. Association between advances in high-resolution cross-section imaging technologies and increase in prevalence of pancreatic cysts from 2005 to 2014. Clin Gastroenterol Hepatol. 2016;14(4):585–593.e583. https://doi.org/10.1016/j.cgh.2015.08.038.
4. Laffan TA, Horton KM, Klein AP, Berlanstein B, Siegelman SS, Kawamoto S, Johnson PT, Fishman EK, Hruban RH. Prevalence of unsuspected pancreatic cysts on MDCT. AJR Am J Roentgenol. 2008;191(3):802–7. https://doi.org/10.2214/AJR.07.3340.
5. Scheiman JM, Hwang JH, Moayyedi P. American gastroenterological association technical review on the diagnosis and management of asymptomatic neoplastic pancreatic cysts. Gastroenterology. 2015;148(4):824–848.e822. https://doi.org/10.1053/j.gastro.2015.01.014.
6. Klimstra DS, Pitman MB, Hruban RH. An algorithmic approach to the diagnosis of pancreatic neoplasms. Arch Pathol Lab Med. 2009;133(3):454–64. https://doi.org/10.1043/1543-2165-133.3.454.
7. Adsay NV. Cystic neoplasia of the pancreas: pathology and biology. J Gastrointest Surg. 2008;12(3):401–4. https://doi.org/10.1007/s11605-007-0348-z.
8. Tseng JF, Warshaw AL, Sahani DV, Lauwers GY, Rattner DW, Fernandez-del Castillo C. Serous cystadenoma of the pancreas: tumor growth rates and recommendations for treatment. Ann Surg. 2005;242(3):413–9; discussion 419–21. https://doi.org/10.1097/01.sla.0000179651.21193.2c.
9. Compagno J, Oertel JE. Microcystic adenomas of the pancreas (glycogen-rich cystadenomas): a clinicopathologic study of 34 cases. Am J Clin Pathol. 1978;69(3):289–98. https://doi.org/10.1093/ajcp/69.1.289.

10. Egawa N, Maillet B, Schroder S, Mukai K, Kloppel G. Serous oligocystic and ill-demarcated adenoma of the pancreas: a variant of serous cystic adenoma. Virchows Arch. 1994;424(1):13–7. https://doi.org/10.1007/BF00197387.
11. Campbell F, Azadeh B. Cystic neoplasms of the exocrine pancreas. Histopathology. 2008;52(5):539–51. https://doi.org/10.1111/j.1365-2559.2007.02856.x.
12. Bollen TL, Wessels FJ. Radiological workup of cystic neoplasms of the pancreas. Visc Med. 2018;34(3):182–90. https://doi.org/10.1159/000489674.
13. Wang Y, Miller FH, Chen ZE, Merrick L, Mortele KJ, Hoff FL, Hammond NA, Yaghmai V, Nikolaidis P. Diffusion-weighted MR imaging of solid and cystic lesions of the pancreas. Radiographics. 2011;31(3):E47–64. https://doi.org/10.1148/rg.313105174.
14. Sahani DV, Kadavigere R, Saokar A, Fernandez-del Castillo C, Brugge WR, Hahn PF. Cystic pancreatic lesions: a simple imaging-based classification system for guiding management. Radiographics. 2005;25(6):1471–84. https://doi.org/10.1148/rg.256045161.
15. Compton CC. Serous cystic tumors of the pancreas. Semin Diagn Pathol. 2000;17(1):43–55.
16. Pyke CM, van Heerden JA, Colby TV, Sarr MG, Weaver AL. The spectrum of serous cystadenoma of the pancreas. Clinical, pathologic, and surgical aspects. Ann Surg. 1992;215(2):132–9. https://doi.org/10.1097/00000658-199202000-00007.
17. Hammel PR, Vilgrain V, Terris B, Penfornis A, Sauvanet A, Correas JM, Chauveau D, Balian A, Beigelman C, O'Toole D, Bernades P, Ruszniewski P, Richard S. Pancreatic involvement in von Hippel-Lindau disease. The Groupe Francophone d'Etude de la Maladie de von Hippel-Lindau. Gastroenterology. 2000;119(4):1087–95. https://doi.org/10.1053/gast.2000.18143.
18. Yamaguchi M. Solid serous adenoma of the pancreas: a solid variant of serous cystadenoma or a separate disease entity? J Gastroenterol. 2006;41(2):178–9. https://doi.org/10.1007/s00535-005-1737-2.
19. Reese SA, Traverso LW, Jacobs TW, Longnecker DS. Solid serous adenoma of the pancreas: a rare variant within the family of pancreatic serous cystic neoplasms. Pancreas. 2006;33(1):96–9. https://doi.org/10.1097/01.mpa.0000226890.63451.c4.
20. Perez-Ordonez B, Naseem A, Lieberman PH, Klimstra DS. Solid serous adenoma of the pancreas. The solid variant of serous cystadenoma? Am J Surg Pathol. 1996;20(11):1401–5. https://doi.org/10.1097/00000478-199611000-00012.
21. Zhang XP, Yu ZX, Zhao YP, Dai MH. Current perspectives on pancreatic serous cystic neoplasms: diagnosis, management and beyond. World J Gastrointest Surg. 2016;8(3):202–11. https://doi.org/10.4240/wjgs.v8.i3.202.
22. Chu LC, Singhi AD, Haroun RR, Hruban RH, Fishman EK. The many faces of pancreatic serous cystadenoma: radiologic and pathologic correlation. Diagn Interv Imaging. 2017;98(3):191–202. https://doi.org/10.1016/j.diii.2016.08.005.
23. Basturk O, Coban I, Adsay NV. Pancreatic cysts: pathologic classification, differential diagnosis, and clinical implications. Arch Pathol Lab Med. 2009;133(3):423–38. https://doi.org/10.1043/1543-2165-133.3.423.
24. Khashab MA, Shin EJ, Amateau S, Canto MI, Hruban RH, Fishman EK, Cameron JL, Edil BH, Wolfgang CL, Schulick RD, Giday S. Tumor size and location correlate with behavior of pancreatic serous cystic neoplasms. Am J Gastroenterol. 2011;106(8):1521–6. https://doi.org/10.1038/ajg.2011.117.
25. Kalb B, Sarmiento JM, Kooby DA, Adsay NV, Martin DR. MR imaging of cystic lesions of the pancreas. Radiographics. 2009;29(6):1749–65. https://doi.org/10.1148/rg.296095506.
26. Martin DR, Semelka RC. MR imaging of pancreatic masses. Magn Reson Imaging Clin N Am. 2000;8(4):787–812.
27. Pozzessere C, Castanos Gutierrez SL, Corona-Villalobos CP, Righi L, Xu C, Lennon AM, Wolfgang CL, Hruban RH, Goggins M, Canto MI, Kamel IR. Diffusion-weighted magnetic resonance imaging in distinguishing between mucin-producing and serous pancreatic cysts. J Comput Assist Tomogr. 2016;40(4):505–12. https://doi.org/10.1097/RCT.0000000000000403.
28. Ku YM, Shin SS, Lee CH, Semelka RC. Magnetic resonance imaging of cystic and endocrine pancreatic neoplasms. Top Magn Reson Imaging. 2009;20(1):11–8. https://doi.org/10.1097/RMR.0b013e3181b4812c.

29. Compagno J, Oertel JE. Mucinous cystic neoplasms of the pancreas with overt and latent malignancy (cystadenocarcinoma and cystadenoma). A clinicopathologic study of 41 cases. Am J Clin Pathol. 1978;69(6):573–80. https://doi.org/10.1093/ajcp/69.6.573.
30. Fernandez-del Castillo C. Mucinous cystic neoplasms. J Gastrointest Surg. 2008;12(3):411–3. https://doi.org/10.1007/s11605-007-0347-0.
31. Tanaka M, Fernandez-del Castillo C, Adsay V, Chari S, Falconi M, Jang JY, Kimura W, Levy P, Pitman MB, Schmidt CM, Shimizu M, Wolfgang CL, Yamaguchi K, Yamao K, International Association of Pancreatology. International consensus guidelines 2012 for the management of IPMN and MCN of the pancreas. Pancreatology. 2012;12(3):183–97. https://doi.org/10.1016/j.pan.2012.04.004.
32. Zamboni G, Scarpa A, Bogina G, Iacono C, Bassi C, Talamini G, Sessa F, Capella C, Solcia E, Rickaert F, Mariuzzi GM, Kloppel G. Mucinous cystic tumors of the pancreas: clinicopathological features, prognosis, and relationship to other mucinous cystic tumors. Am J Surg Pathol. 1999;23(4):410–22. https://doi.org/10.1097/00000478-199904000-00005.
33. Reddy RP, Smyrk TC, Zapiach M, Levy MJ, Pearson RK, Clain JE, Farnell MB, Sarr MG, Chari ST. Pancreatic mucinous cystic neoplasm defined by ovarian stroma: demographics, clinical features, and prevalence of cancer. Clin Gastroenterol Hepatol. 2004;2(11):1026–31. https://doi.org/10.1016/s1542-3565(04)00450-1.
34. Thompson LD, Becker RC, Przygodzki RM, Adair CF, Heffess CS. Mucinous cystic neoplasm (mucinous cystadenocarcinoma of low-grade malignant potential) of the pancreas: a clinicopathologic study of 130 cases. Am J Surg Pathol. 1999;23(1):1–16. https://doi.org/10.1097/00000478-199901000-00001.
35. Wilentz RE, Albores-Saavedra J, Zahurak M, Talamini MA, Yeo CJ, Cameron JL, Hruban RH. Pathologic examination accurately predicts prognosis in mucinous cystic neoplasms of the pancreas. Am J Surg Pathol. 1999;23(11):1320–7. https://doi.org/10.1097/00000478-199911000-00002.
36. Vege SS, Ziring B, Jain R, Moayyedi P, Clinical Guidelines Committee, American Gastroenterology Association. American Gastroenterological Association Institute guideline on the diagnosis and management of asymptomatic neoplastic pancreatic cysts. Gastroenterology. 2015;148(4):819–22; quize812–3. https://doi.org/10.1053/j.gastro.2015.01.015.
37. Oh HC, Seo DW, Song TJ, Moon SH, Park DH, Soo Lee S, Lee SK, Kim MH, Kim J. Endoscopic ultrasonography-guided ethanol lavage with paclitaxel injection treats patients with pancreatic cysts. Gastroenterology. 2011;140(1):172–9. https://doi.org/10.1053/j.gastro.2010.10.001.
38. Sarr MG, Carpenter HA, Prabhakar LP, Orchard TF, Hughes S, van Heerden JA, DiMagno EP. Clinical and pathologic correlation of 84 mucinous cystic neoplasms of the pancreas: can one reliably differentiate benign from malignant (or premalignant) neoplasms? Ann Surg. 2000;231(2):205–12. https://doi.org/10.1097/00000658-200002000-00009.
39. Del Chiaro M, Verbeke C. Cystic tumors of the pancreas: opportunities and risks. World J Gastrointest Pathophysiol. 2015;6(2):29–32. https://doi.org/10.4291/wjgp.v6.i2.29.
40. Zamora C, Sahel J, Cantu DG, Heyries L, Bernard JP, Bastid C, Payan MJ, Sielezneff I, Familiari L, Sastre B, Barthet M. Intraductal papillary or mucinous tumors (IPMT) of the pancreas: report of a case series and review of the literature. Am J Gastroenterol. 2001;96(5):1441–7. https://doi.org/10.1111/j.1572-0241.2001.03689.x.
41. Sohn TA, Yeo CJ, Cameron JL, Hruban RH, Fukushima N, Campbell KA, Lillemoe KD. Intraductal papillary mucinous neoplasms of the pancreas: an updated experience. Ann Surg. 2004;239(6):788–97; discussion 797–9. https://doi.org/10.1097/01.sla.0000128306.90650.aa.
42. Sugiura H, Kondo S, Islam HK, Ito K, Ono K, Morikawa T, Okushiba S, Katoh H. Clinicopathologic features and outcomes of intraductal papillary-mucinous tumors of the pancreas. Hepato-Gastroenterology. 2002;49(43):263–7.
43. Korsse SE, Harinck F, van Lier MG, Biermann K, Offerhaus GJ, Krak N, Looman CW, van Veelen W, Kuipers EJ, Wagner A, Dekker E, Mathus-Vliegen EM, Fockens P, van Leerdam ME, Bruno MJ. Pancreatic cancer risk in Peutz-Jeghers syndrome patients: a large cohort study and implications for surveillance. J Med Genet. 2013;50(1):59–64. https://doi.org/10.1136/jmedgenet-2012-101277.

44. Chetty R, Salahshor S, Bapat B, Berk T, Croitoru M, Gallinger S. Intraductal papillary mucinous neoplasm of the pancreas in a patient with attenuated familial adenomatous polyposis. J Clin Pathol. 2005;58(1):97–101. https://doi.org/10.1136/jcp.2004.020925.
45. Canto MI, Goggins M, Yeo CJ, Griffin C, Axilbund JE, Brune K, Ali SZ, Jagannath S, Petersen GM, Fishman EK, Piantadosi S, Giardiello FM, Hruban RH. Screening for pancreatic neoplasia in high-risk individuals: an EUS-based approach. Clin Gastroenterol Hepatol. 2004;2(7):606–21. https://doi.org/10.1016/s1542-3565(04)00244-7.
46. Matsubayashi H, Maeda A, Kanemoto H, Uesaka K, Yamazaki K, Hironaka S, Miyagi Y, Ikehara H, Ono H, Klein A, Goggins M. Risk factors of familial pancreatic cancer in Japan: current smoking and recent onset of diabetes. Pancreas. 2011;40(6):974–8. https://doi.org/10.1097/MPA.0b013e3182156e1b.
47. Terris B, Ponsot P, Paye F, Hammel P, Sauvanet A, Molas G, Bernades P, Belghiti J, Ruszniewski P, Flejou JF. Intraductal papillary mucinous tumors of the pancreas confined to secondary ducts show less aggressive pathologic features as compared with those involving the main pancreatic duct. Am J Surg Pathol. 2000;24(10):1372–7. https://doi.org/10.1097/00000478-200010000-00006.
48. Tanaka M. Important clues to the diagnosis of pancreatic cancer. Rocz Akad Med Bialymst. 2005;50:69–72.
49. Capurso G, Boccia S, Salvia R, Del Chiaro M, Frulloni L, Arcidiacono PG, Zerbi A, Manta R, Fabbri C, Ventrucci M, Tarantino I, Piciucchi M, Carnuccio A, Boggi U, Leoncini E, Costamagna G, Delle Fave G, Pezzilli R, Bassi C, Larghi A, Italian Association for Study of Pancreas (AISP), Intraductal Papillary Mucinous Neoplasm Study Group. Risk factors for intraductal papillary mucinous neoplasm (IPMN) of the pancreas: a multicentre case-control study. Am J Gastroenterol. 2013;108(6):1003–9. https://doi.org/10.1038/ajg.2013.42.
50. Xiao SY. Intraductal papillary mucinous neoplasm of the pancreas: an update. Scientifica (Cairo). 2012;2012:893632. https://doi.org/10.6064/2012/893632.
51. Salvia R, Fernandez-del Castillo C, Bassi C, Thayer SP, Falconi M, Mantovani W, Pederzoli P, Warshaw AL. Main-duct intraductal papillary mucinous neoplasms of the pancreas: clinical predictors of malignancy and long-term survival following resection. Ann Surg. 2004;239(5):678–85; discussion 685–7. https://doi.org/10.1097/01.sla.0000124386.54496.15.
52. Kench JG, Eckstein RP, Smith RC. Intraductal papillary-mucinous neoplasm of the pancreas: a report of five cases with immunohistochemical findings. Pathology. 1997;29(1):7–11. https://doi.org/10.1080/00313029700169454.
53. Raimondo M, Tachibana I, Urrutia R, Burgart LJ, DiMagno EP. Invasive cancer and survival of intraductal papillary mucinous tumors of the pancreas. Am J Gastroenterol. 2002;97(10):2553–8. https://doi.org/10.1111/j.1572-0241.2002.06022.x.
54. Alexander BM, Fernandez-Del Castillo C, Ryan DP, Kachnic LA, Hezel AF, Niemierko A, Willett CG, Kozak KR, Blaszkowsky LS, Clark JW, Warshaw AL, Hong TS. Intraductal papillary mucinous adenocarcinoma of the pancreas: clinical outcomes, prognostic factors, and the role of adjuvant therapy. Gastrointest Cancer Res. 2011;4(4):116–21.
55. Yopp AC, Katabi N, Janakos M, Klimstra DS, D'Angelica MI, DeMatteo RP, Fong Y, Brennan MF, Jarnagin WR, Allen PJ. Invasive carcinoma arising in intraductal papillary mucinous neoplasms of the pancreas: a matched control study with conventional pancreatic ductal adenocarcinoma. Ann Surg. 2011;253(5):968–74. https://doi.org/10.1097/SLA.0b013e318214bcb4.
56. Song SJ, Lee JM, Kim YJ, Kim SH, Lee JY, Han JK, Choi BI. Differentiation of intraductal papillary mucinous neoplasms from other pancreatic cystic masses: comparison of multirow-detector CT and MR imaging using ROC analysis. J Magn Reson Imaging. 2007;26(1):86–93. https://doi.org/10.1002/jmri.21001.
57. Procacci C, Megibow AJ, Carbognin G, Guarise A, Spoto E, Biasiutti C, Pistolesi GF. Intraductal papillary mucinous tumor of the pancreas: a pictorial essay. Radiographics. 1999;19(6):1447–63. https://doi.org/10.1148/radiographics.19.6.g99no011447.
58. Kang KM, Lee JM, Shin CI, Baek JH, Kim SH, Yoon JH, Han JK, Choi BI. Added value of diffusion-weighted imaging to MR cholangiopancreatography with unenhanced MR imaging

for predicting malignancy or invasiveness of intraductal papillary mucinous neoplasm of the pancreas. J Magn Reson Imaging. 2013;38(3):555–63. https://doi.org/10.1002/jmri.24022.
59. Sandrasegaran K, Akisik FM, Patel AA, Rydberg M, Cramer HM, Agaram NP, Schmidt CM. Diffusion-weighted imaging in characterization of cystic pancreatic lesions. Clin Radiol. 2011;66(9):808–14. https://doi.org/10.1016/j.crad.2011.01.016.
60. Kang KM, Lee JM, Yoon JH, Kiefer B, Han JK, Choi BI. Intravoxel incoherent motion diffusion-weighted MR imaging for characterization of focal pancreatic lesions. Radiology. 2014;270(2):444–53. https://doi.org/10.1148/radiol.13122712.
61. Jang KM, Kim SH, Min JH, Lee SJ, Kang TW, Lim S, Choi D. Value of diffusion-weighted MRI for differentiating malignant from benign intraductal papillary mucinous neoplasms of the pancreas. AJR Am J Roentgenol. 2014;203(5):992–1000. https://doi.org/10.2214/AJR.13.11980.
62. Nadig SN, Pedrosa I, Goldsmith JD, Callery MP, Vollmer CM. Clinical implications of mucinous nonneoplastic cysts of the pancreas. Pancreas. 2012;41(3):441–6. https://doi.org/10.1097/MPA.0b013e318229b9b8.
63. Cao W, Adley BP, Liao J, Lin X, Talamonti M, Bentrem DJ, Rao SM, Yang GY. Mucinous nonneoplastic cyst of the pancreas: apomucin phenotype distinguishes this entity from intraductal papillary mucinous neoplasm. Hum Pathol. 2010;41(4):513–21. https://doi.org/10.1016/j.humpath.2009.05.017.
64. Cantisani V, Mortele KJ, Levy A, Glickman JN, Ricci P, Passariello R, Ros PR, Silverman SG. MR imaging features of solid pseudopapillary tumor of the pancreas in adult and pediatric patients. AJR Am J Roentgenol. 2003;181(2):395–401. https://doi.org/10.2214/ajr.181.2.1810395.
65. Nakatani K, Watanabe Y, Okumura A, Nakanishi T, Nagayama M, Amoh Y, Ishimori T, Dodo Y. MR imaging features of solid-pseudopapillary tumor of the pancreas. Magn Reson Med Sci. 2007;6(2):121–6. https://doi.org/10.2463/mrms.6.121.
66. Lee SS, Byun JH, Park BJ, Park SH, Kim N, Park B, Kim JK, Lee MG. Quantitative analysis of diffusion-weighted magnetic resonance imaging of the pancreas: usefulness in characterizing solid pancreatic masses. J Magn Reson Imaging. 2008;28(4):928–36. https://doi.org/10.1002/jmri.21508.
67. Rodrigues-Duarte H, Torrao H, Coelho P, Noruegas M, Sanches M. Solid pseudopapillary tumor of the pancreas in a child: imaging findings with diffusion-weighted MR imaging. JOP. 2013;14(2):195–8. https://doi.org/10.6092/1590-8577/1185.
68. Kim B, Lee SS, Sung YS, Cheong H, Byun JH, Kim HJ, Kim JH. Intravoxel incoherent motion diffusion-weighted imaging of the pancreas: characterization of benign and malignant pancreatic pathologies. J Magn Reson Imaging. 2017;45(1):260–9. https://doi.org/10.1002/jmri.25334.